Carbon-, Gold- and Iron-based Nanomaterials – Synthesis, Characterization and Potential Applications

By

Lida Hadidi

A thesis submitted in partial fulfillment of the requirements for the degree

Doctor of Philosophy

Department of Chemistry

University of Alberta

Abstract

Nanomaterials are important building blocks of nanotechnology. Their size dependent unique properties (optical, magnetic, electrical, *etc.*) have the potential to revolutionize applications ranging from medicine to electronics. Of the various nanomaterials, carbon-based systems including porous carbon, graphene, graphite nanofibers, and carbon nanotubes (CNTs) have received considerable attention due to their high surface area, limited toxicity, biocompatibility, electronic conductivity, chemical stability, and low density. Despite the development of different synthetic approaches for preparing various carbons, there is still vast interest in developing cost-effective scalable methods for the synthesis of carbon-based materials, in particular mesoporous carbons. Owing to their high surface area, carbon based materials have been extensively studied for catalytic applications. However, important challenges related to material synthesis remain. The research described in this dissertation attempts to address challenges associated with synthesis of mesoporous carbons as well as their prototype catalytic applications. The investigations then shift to the synthesis and applications of iron oxide nanorods coated with N-doped mesoporous carbon core-shell nanostructures as catalyst. Finally, the extension of photothermally responsive hybrid gold/silica nanoparticles into catalytic applications is explored.

The thesis starts with an introduction summarizing the broad field of nanomaterials. Focus then shifts to the materials (*i.e.,* mesoporous carbon, iron oxide nanoparticles and gold nanoparticles) specific to the presented investigation.

Chapter Two outlines on synthesis of hollow mesoporous carbon (HMC) nanostructures using dopamine as carbon precursor. The HMC was fully characterized. The resulting HMC was employed as an electrocatalyst for oxygen reduction/evolution reactions (ORR/OER) in zinc air battery (ZAB). The HMCs exhibited outstanding ORR onset potential and excellent stability comparable to that of precious metal catalyst.

Chapter Three presents the synthesis of high surface area hollow carbon spheres (HCS) using crystalline nanocellulose (CNC) as carbon precursor and a detailed investigation and discussion on the formation mechanism. The synthesized HCS were implemented for catalytic conversion of 4-nitrophenol (4-NP) to 4-aminophenol (4-AP). The catalytic activity was investigated in terms reaction rate and activity parameter. The HCS exhibited remarkable catalytic activity comparable to that of their metallic nanoparticles counterparts.

Chapter Four is extension of previous work where mesoporous carbon is used as a thin shell material. The synthesis of Fe_3O_4 nanorods coated with a nitrogen-doped mesoporous carbon shell (ND-Fe_3O_4@mC) *via* a new microwave-assisted approach is presented. The electrochemical performances of ND-Fe_3O_4@mC with different carbon shell thicknesses are evaluated. The results reveal enhanced ORR catalytic activity for the catalyst with thinnest carbon shell.

The synthesis of different morphologies of gold nanostructures along with hybrid gold/silica nanoparticles is presented in Chapter Five. The optical properties of these structures are investigated in detail and co-related with structure. The

application of silica decorated with gold nanoparticles investigated for catalytic conversion of 4-NP conversion to 4-AP.

Finally, Chapter Six provides a summary of the conclusions of the work and outlines future work.

Preface

This thesis focuses on synthesis, characterization and application of carbon, gold and iron nanomaterials. Some of the research conducted for this thesis is part of valuable research collaborations with Dr. Douglas Ivey's group in Chemical and Materials Engineering Department and Dr. Mark McDermott's group in Chemistry Department at University of Alberta.

Elaheh Davari, PhD candidate in Dr. Ivey's group performed the electrochemistry reported in chapter two and four of this thesis. A version of the research work presented in chapter two has been published with equal contribution:

Hadidi, L.; Davari, E.; Iqbal, M.; Purkait, T. K.; Ivey, D. G.; Veinot, J. G. C., *Nanoscale* **2015**, 7, 20547-20556.

Ahmed Mahmoud, PhD candidate in Dr. Mark McDermott's group performed the catalysis experiments reported in chapter 3 of this thesis. Also, he performed all the Raman measurements reported in this thesis.

I dedicate this thesis to my parents.

تقدیم به پدر و مادر عزیز و مهربانم ...

که در سختی ها و دشواری های زندگی همواره یاوری دلسوز و فداکار و پشتیبانی محکم و مطمئن

برایم بوده‌اند.

Acknowledgements

I still cannot believe that I have made it to this point. It was definitely a long and arduous journey and a big change moving from Iran to Canada. At the outset of my graduate research, it was really hard for me to imagine what I will be accomplishing and what will be my "splash" in the next five years as a PhD student. As I look back, this journey would not have been possible without the help and support of my family members, friends, professors and department staff.

I cannot thank enough all the people whom helped me during the last five years and I hope not miss any of them. First and foremost, I would like to express my deepest gratitude to my supervisor Dr. Jonathan G. C. Veinot for his guidance, support and never losing faith in me during my graduate study.

I would like to thank my examination committee members Drs. Arthur Mar, Steve Bergens, Robert Campbell, and external committee member Dr. Amy Blum from McGill University for their guidance, useful comments and suggestion and support during my PhD study. I would like to thank Dr. Douglas G. Ivey, Dr. Mark T. McDermott, Elaheh Davari and Ahmed Y. Mahmoud for excellent collaborations and valuable guidance.

I would like to thank Veinot group members. You made this path much easier for me. I am sure without your constant support and encouragement, I would not have made it. I would like sincerely thank Ms. Sarah Regli as the first groupmate who introduced me to the lab and trained me work in the lab. I would like to thank Dr. Muhammad Iqbal who always supported me a lot during my hard times in life

and academics. I definitely learnt a lot from him in about many aspect of life. I never forget those golden days working with him in the lab, sharing a laugh while deeply immersed in experiments. I would like to thank Dr. Tapas K. Purkait for his invaluable scientific ideas, encouragement and support. I would like to thank Christina Gonzalez my groupmate, officemate and my awesome friend for her support. We have always supported each other be it the courses, exams, candidacy, or research. Ours is a friendship which made the hectic research days fun. I would like to thank all the group members including Dr. Hosnay Mobarok, Dr. John Washington, Dr. Rhett Clark, Morteza Javadi, Maryam Aghajamali, Regina Sinelnikov, Muhammad Amirul Islam, Christopher Jay Robidillo, Haoyang Yu and Alyxandra Aarbo for all their support and always being there for me.

I would like to thank numerous staff and technicians who helped a lot: during my stay: Wayne Moffat, Ema Sretenovis, Jennifer Jones, Dr. Jason Cooke, Dr. Norman Gee, Greg Popowich, Dr. Kai Cui, Dr. Dimitre Karpuzov, Dr. Shihong Xu, Dr. Nathan Gerein, Peng Li, Diane Caird, Anita Weiler, Bonnie Gover, and Ryan Lewis for their assistance.

I met lots of people from all over the world during these five years and made many great friends who I will cherish always and made my stay worthwhile. I would like to specially thank Ahmed Y. Mahmoud, Amin Moazeni, Elaheh Davari, Ghazaleh Eskandari Sedighi, Hesam Shahin, Krishna Ramachandran, and Nazanin Assempour for their great support during my graduate studies.

Last but not the least, I would like to thank my awesome and loving parents and amazing sisters. They have always supported me through all these years and they are the most precious gift of my life. Maman! You have always encouraged me to do whatever I want to and gave me the strength to tackle challenges and be optimistic. Baba! You have always supported me for all my decisions in life and encouraged me to pursue my endeavors. Jaleh and Jila you both taught me how to fight for my goals and pursue my dreams whatever the odds are. Love you!

Table of Contents

List of Tables

List of Figures

List of Symbols, Nomenclature and Abbreviations

Å	Ångstrom (= 0.1 nm)
AAO	anodic aluminum oxide
AA	ascorbic acid
APTMS	3-aminopropyl-trimethoxysilane
4-AP	4-aminophenol
BET	Brunauer-Emmett-Teller
℃	degree Celsius
CB	carbon black
C_o	bulk concentration of O_2
C_{crit}	critical supersaturation concentration
C_{max}^{nu}	maximun concentration for nucleation
C_{min}^{nu}	minimum concentration for nucleation
cm^{-1}	wavenumber
CMK-1	Carbon Mesoporous Korea-1
CNC	cellulose nanocrystals
CNTs	carbon nanotube
C_s	solubility concentration
C_{60}	buckyball
CTAB	cetyltrimethylammonium bromide
CV	cyclic voltammetry
CVD	chemical vapor deposition
CW	continuous wavelength
1D	1 dimensional
2D	2 dimensional
3D	3 dimensional
D_o	diffusion coefficient of O_2
DCC	dicyclohexylcarbodiimide
DMAP	4-dimethylaminopyridine
DMF	dimethyl formamide
DNA	deoxyribonucleic acid
DSC	dye sensitized solar cell
DSC	differential scanning calorimetry
e^-	electron
EDX	energy-dispersive X-ray spectroscopy
$E_{1/2}$	half-wave potential
EIS	impedance spectroscopy
EOA	triethylorthoacetate
EO	ethylene oxide
E_g	band gap
eV	electronvolt

F	Faraday constant
F127	copolymer of poly(ethylene oxide)-poly(propylene oxide)-poly(ethylene oxide)
fcc	face centered cubic
GC	glassy carbon
GNFs	graphite nanofibers
GNPs	gold nanoparticles
GNRs	gold nanorods
GPa	gigapascal
h	hour
HCS	hollow carbon sphere
HGO	hydrothermally prepared graphene oxide
HIM	helium ion mircroscopy
HMC	hollow mesoporous carbon
HR-TEM	high resolution transmission electron microscopy
ICP	inductively coupled plasma
IR	infrared
IUPAC	International Union of Pure and Applied Chemistry
j_l	diffusion-limiting current density
j_k	kinetic-limiting current density
k	rate constant
K	activity parameter
K-L	Koutecky-Levich
LbL	layer-by-layer
LCT	liquid crystal templating
LH	Langmuir-Hinshelwood
LIBs	lithium-ion battery
LSPR	localized surface plasmon resonance
LSV	linear sweep voltammetry
mC	mesoporous carbon
MCM-48	Mobil Composition of Matter No.48
MΩ	megOhm
mg	milligrams
min	minute (s)
mL	millilitres
mmole	millimole
MPa	megapascal
MPC	mesoporous carbon
MRI	magnetic resonance imaging
n	number of electron transferred
NCs	nanocrystals
ND	nitrogen-doped
nm	nanometer

nM	nanomolar
4-NP	4-nitrophenol
NTs	nanotubes
OER	oxygen evolution reaction
ORR	oxygen reduction reaction
PET	polyethylene terephthalate
PDA	polydopamine
PDS	pore size distribution
PGC	porous glassy carbon
PL	photoluminescent
P123	copolymer of poly(ethylene oxide)-poly(propylene oxide)-poly(ethylene oxide)
PRCVD	plasmon resonance chemical vapor dposition
PS-P4VP	polystyrene-block-poly(4-vinylpyridine)
PVP	polyvinylpyrrolidone
RDE	rotating disc electrode
rpm	rotations per minute
R_u	uncompensated resistance
s	second
SAED	selected area electron diffraction
SBA-15	Santa Barbara Amorphous No.15
SEI	solid electrolyte interphase
SEM	scanning electron microscopy
SNU-1	Seoul National University No.1
STEM	scanning transmission electron microscopy
SWCNTs	single-walled carbon nanotubes
TEM	transmission electron microscopy
TEMPO	(2,2,6,6-tetramethylpiperidin-1-yl)oxyl
TEOS	tetraethoxysilane
TGA	thermogravimetric analysis
TMOS	tetramethoxysilane
TOAB	tetraoctylammonium bromide
UV-vis	ultraviolet-visible (spectroscopy)
υ	kinematic viscosity of the electrolyte
ω	angular velocity
XPS	X-ray photoelectron spectroscopy
XRD	X-ray diffraction
ZAB	zinc-air battery

Chapter 1:

Introduction

1.1 Introduction: Nanomaterials

Nanomaterials have become one of the most active research areas during the last thirty years. There are several reasons for this including the need to fabricate new materials to decrease the cost and increase the speed of information transmission and storage; others include exploiting the unique and enhanced size dependent properties that these materials display.[1]

The typical dimensions of nanomaterials spans from 1 to 100 nanometers.[2] This characteristic dimension could be the particle diameter, crystallite grain size, layer thickness, or even the size of a pore. To put these length scales into perspective, a nanometer is one billionth of a meter (*i.e.*, 10^{-9} m). Something this small is difficult to comprehend; consider that one nanometer is approximately the length of 10 hydrogen or 5 silicon atoms placed in a line. Figure 1-1 shows the range of length scales for some materials in nature, which is useful to develop a physical idea of length scale in nanometer regime.[3]

1.

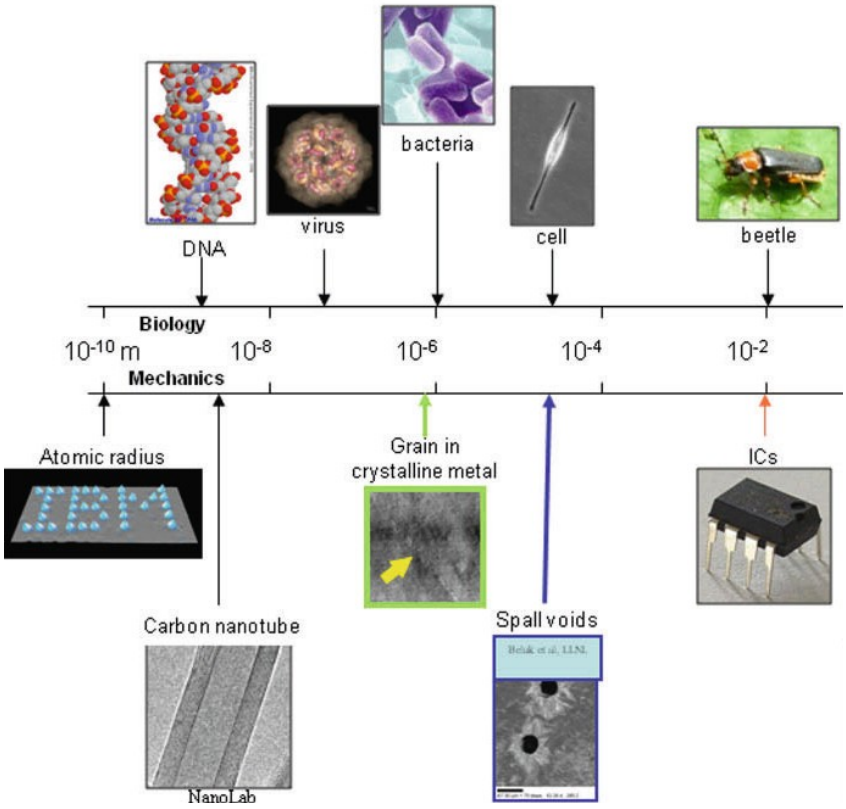

2.

Figure 1-1: Different length scales in mechanics and in biology.[3]

There are many nanomaterial types such as nanoparticles, nanorods and nanowires, as well as thin films. In general, these materials are classified into four broad categories: zero-dimensional nanostructures (*e.g.,* nanoparticles, fullerenes (C_{60}, C_{70}, *etc.*)), one-dimensional nanostructures (*e.g.,* nanowires, nanorods, and nanotubes (NTs)), two-dimensional nanostructures (*e.g.,* thin films, graphene), and special nanostructures (*e.g.,* micro- and meso-porous materials, core-shell

structures, organic-inorganic hybrids, intercalation compounds, nanocomposites, *etc.*).[1]

It is not only the small dimensions of these materials that make them intriguing, their attraction largely comes as a result of their properties that are distinctively different from those of their bulk counterparts. For example, nanoscale crystals have substantially lower melting points (the difference can be as large as 1000 ℃) and reduced lattice constants.[4] As a case in point, the melting point of bulk gold is 1064 ℃. However, when gold particles approach 10 nm in dimension their melting point decreases substantially (Figure 1-2).[5]

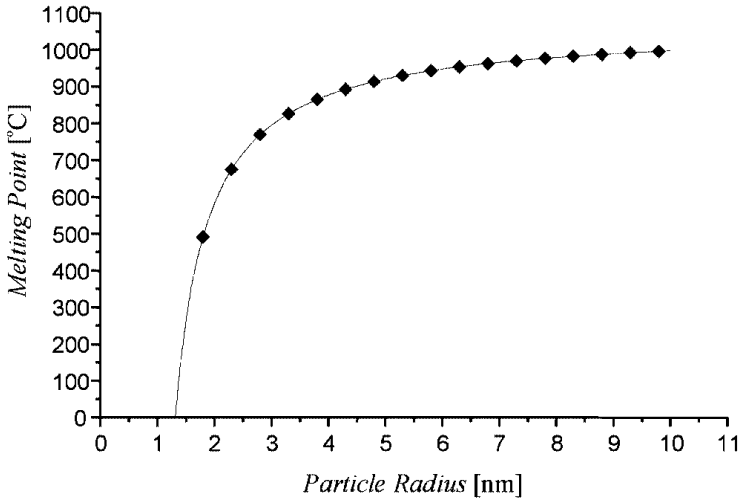

Figure 1-2: Particle size *vs.* melting point for gold nanoparticles.[5] Reprinted (adapted) with permission from ref 5.

The accepted explanation for these observations is nanometer scale particles have tremendously high surface area:volume ratios and the proportionately large number of surface atoms or ions and the resulting surface energy play a significant role.[6]

Another unique aspect of nanomaterials is the stability of crystal structures differs from bulk materials; some are stable at much lower temperatures at nanometer particle sizes – a physical manifestation of this is seen in the structural properties of ferroelectrics and ferromagnetics that can lose or change their ferroelectric behavior and ferromagnetism when prepared at the nanometer scale.[7] Similarly, bulk semiconductors become insulators at the nanoscale while gold nanoparticles exhibit catalytic properties while bulk gold does not.[1]

Methods for preparing nanoparticles fall under two broad classifications: top-down and bottom-up. Attrition (or milling) is a classic example of "top-down" nanomaterial synthesis. Unfortunately, top-down approaches provide limited control over particle morphology and can introduce internal stress, surface defects, and contaminants.[1] Bottom-up approaches may be viewed as those that "build up" a material from its constituent parts (*e.g.*, atom-by-atom, molecule-by-molecule, cluster-by-cluster). There are familiar examples in polymer chemistry that see monomers (*i.e.,* molecular building blocks) come together to form the bulk polymer.[1]

Many bottom-up methods have been developed based on that approach including heterogeneous and homogeneous nucleation. In the former, crystal/particle growth starts with atoms (or molecules) impinging onto the growth substrate and assembling into a crystal structure. Such bottom-up approaches play an important role in the synthesis and processing of nanomaterials and are primarily governed by a reduction in Gibbs free energy, so the final nanostructures are in a state closer to a thermodynamic equilibrium.[1] In homogenous nucleation, nanoparticles are synthesized from a supersaturated growth species away from a surface/substrate. The reduction of Gibbs free energy is the driving force for both nucleation and growth.

Among the large number of theories proposed for the correlation between the nucleation and the growth of particles,[8] the LaMer model has dominated discussions and gives insight into particle formation.[9,10] The LaMer view of particle nucleation and growth is summarized in Figure 1-3.[9,11]

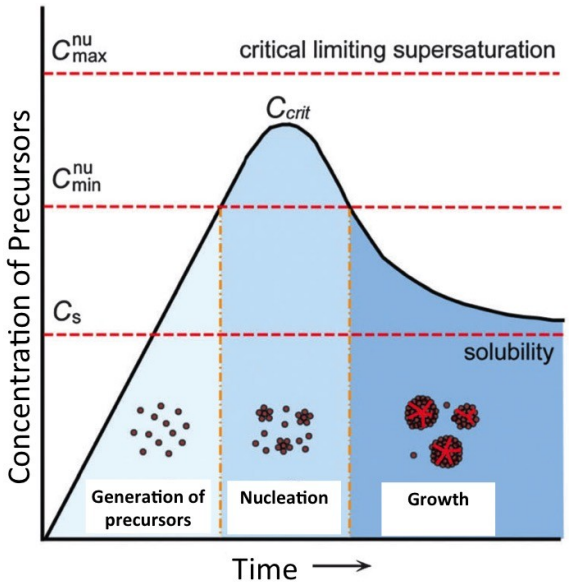

Figure 1-3: Schematic illustration of LaMer model describing nucleation and growth of nanocrystals as a function of reaction time and precursor concentration. (C_s: solubility concentration, $C_{min}{}^{nu}$: minimum concentration for nucleation, C_{crit}: critical supersaturation concentration, $C_{max}{}^{nu}$: maximum concentration for nucleation.[11] Reprinted (adapted) with permission from ref 11.

The LaMer model states that, homogenous nucleation occurs when the solution concentration reaches a certain value above the solution saturation ($C_{\mathrm{min}}{}^{\mathrm{nu}}$). After the initial nucleation occurs, the concentration of the growth species decreases and the Gibbs free energy reduces. When the concentration decreases below this specific concentration ($C_{\mathrm{min}}{}^{\mathrm{nu}}$), no additional nucleation occurs and particle growth continues until the concentration of precursor has reached an equilibrium concentration (C_s).[1] To obtain a narrow size distribution (*i.e.,* monodispersity) of nanoparticles, it is best if all nuclei are formed simultaneously. In these cases,

particles all grow for the same amount of time. In addition, growth can also occurs as a result of Ostwald ripening, where larger particles grow at the expense of smaller particles because of differences in surface energy.[12]

1.2 Carbon-based Nanomaterials

Carbon is the sixth element in the periodic table, fifteenth most abundant in the Earth's crust, and the fourth most abundant in the universe by mass.[13] The best-known allotropes of carbon are diamond, graphite, amorphous carbon, fullerenes (The Noble Prize in Chemistry 1996)[14] (C_{60}, C_{70}, C_{540}), graphene (The Noble Prize in Physics 2010)[15], single-walled carbon nanotubes (SWCNTs), and lonsdaleite (see Figure 1-4).[16,17]

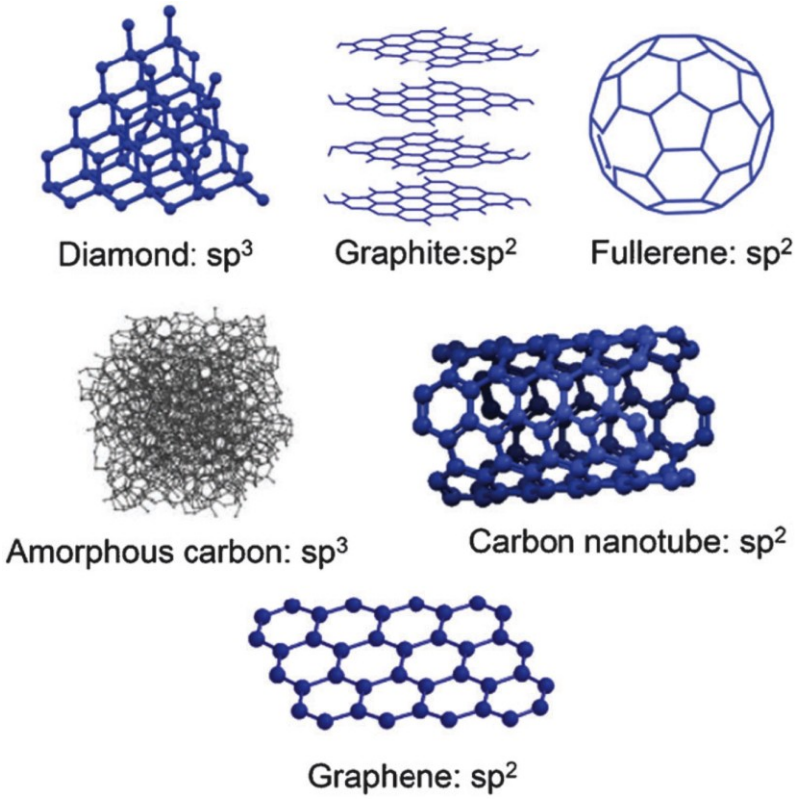

Figure 1-4: A pictorial representation of the allotropes of carbon.[17] Reprinted (adapted) with permission from ref 17.

The properties of these allotropes depend on how the carbon atoms are arranged and bonded together. Graphite is a soft, black, stable form of carbon with strong covalent bonding in the sheet plane and weak van der Waals interactions between the layers – it exhibits metallic electronic properties. In contrast, diamond is hard and transparent with each carbon atom being bonded to four others in a regular structure built up of interconnected tetrahedral – unless doped, it is an electrical insulator. Amorphous carbon does not show extended crystalline order. Buckminster fullerene (C_{60}; buckyball) exhibits a "soccer ball-like structure" consisting of twelve pentagons and twenty hexagons. Buckyball is extremely stable withstanding high pressures and temperatures.[18] It also behaves as an electron deficient alkene, will react readily with electron rich species, and can tolerate six extra electrons in its π-system. Graphene consists of 2D single-atom-thick nanosheets of sp^2-bonded carbon atoms with extraordinary properties including high electrical conductivity (six order of magnitude higher than that of copper), high thermal conductivity (~5000 W m^{-1} K^{-1}), huge specific surface are (2630 m^2 g^{-1}), and a high mechanical strength (Young's modulus ~1100 GPa).[16] Single-walled carbon nanotubes can be viewed as a graphene sheets rolled up into a nanoscale tubes. They exhibit exceptional strength, unique electrical properties, and efficient heat conductivity. Lonsdaleite or hexagonal diamond is another allotrope of carbon with hexagonal unit cell and is simulated to be 58% harder than diamond on the <100> face.[19,20]

1.3 Mesoporous Carbons: Properties and Applications

Porous materials are important because of their interaction with atoms, ions and molecules at their surfaces and throughout the bulk materials.[21] Traditionally, porous materials have been used in ion exchange, adsorption (separation), and catalysis.[21] According to IUPAC (International Union of Pure and Applied Chemistry) *nanoporous* materials are classified into three categories based on their pore size: *microporous* (2 nm < pore size), mesoporous (2 nm < pore size < 50 nm), and *macroporous* (pore size > 50 nm).[22] The pore shapes, size distribution and volume directly affect material function. For example, zeolites are a naturally occurring microporous solid widely used as an adsorbent to separate different sizes of molecules.[21] Material composition is also important: hydrophilic porous materials (*e.g.,* aluminosilicates) will selectively adsorb water from organic solvents while hydrophobic systems (*e.g.,* pure silica) adsorb organic components from water.

Porous carbon is of practical and scientific interest because of its high surface area, limited toxicity and biocompatibility, as well as physical properties (*e.g.*, including electronic conductivity, thermal conductivity, chemical stability, and low density).[23] These characteristics make various porous carbons ideal for applications including: catalysis, separation, electronics.[24]

Activated carbons and carbon molecular sieves are conventional porous carbons that exhibit broad pore-size distributions in the micro- and meso-pore regimes; they find uses in adsorption, separation, and catalysis.[25] In 1987, Huang *et*

al.[26] reported the adsorption of heavy metal ions (*e.g.,* Cu^{2+}, Pb^{2+}, Ni^{2+}, Zn^{2+}) onto the hydrous activated carbon surface. The carbon type, pH, and surface loading were the most important factors affecting the extent of metal ion removal. They proposed the metal adsorption occurred *via* formation of a surface complex. Sircar *et al.* also applied activated carbon in gas separation and storage.[25] These authors used different precursors and formed a series of materials with a wide range of pore structures and surface chemistries.

Mesoporous carbon (MPC) microparticles have been used as sensing platforms for nucleic acids.[27] The MPC microparticles adsorb and quench the photoluminescence of dye-labeled single-strand DNA probes; subsequent hybridization of the probe with its target produces double-stranded DNA that no longer interacts strongly with the carbon substrate and detaches from it. Upon detachment, the florescence will be recovered (Figure 1-5). This sensing platform allowed differentiation between "perfect" complementary and mismatched targets.

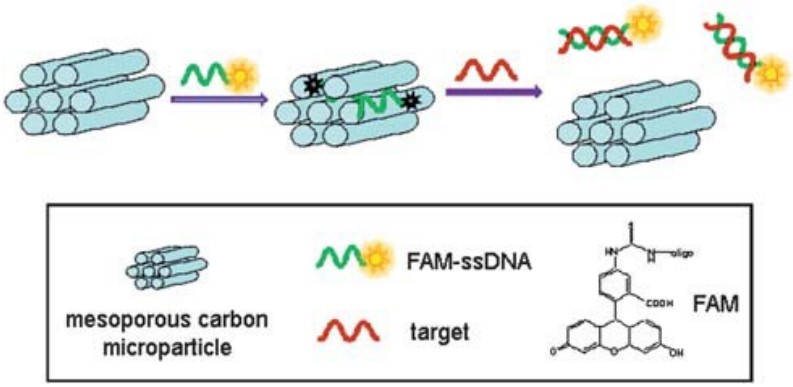

Figure 1-5: MPC microparticles as a sensing platform for fluorescence-enhanced nucleic acid detection.[27] Reprinted (adapted) with permission from ref 27.

Other applications of MPC include electronic devices,[28] bioimaging agents,[23] and catalysis.[29] MPC containing sulfur in its pores was studied as a carbon-sulfur composite electrode for lithium-sulfur (Li-S) batteries.[30] MPC materials are also considered as efficient catalyst supports in fuel cell systems.[31] Ryoo *et al.* initiated the application of ordered MPC materials as support for fuel cell system.[32] The ordered MPC materials were used to support platinum nanoparticles *via* wetness impregnation of Pt precursor (H_2PtCl_6) and subsequent reduction with H_2 gas.

1.4 Preparation of MPCs

Conventional porous carbon materials that exhibit broad pore-size distributions (*e.g.,* activated carbon and carbon molecular sieves) are typically prepared *via* high temperature pyrolysis and physical/chemical activation of organic precursors such as coal, wood, polymers, or fruit shells.[33,34] Microporous

materials prepared using these procedures suffer from three main limitations: 1) small pore sizes that limit mass transport, 2) surface functional groups and defects that lead to low electrical conductivity, and 3) porous structures (microporosity) that collapse during high-temperature treatments or during graphitization.[24]

A variety of approaches have been explored in attempts to overcome these limitations; they include: 1) carbonization of carbon precursors consists of thermosetting and thermally stable components,[35,36] 2) a high degree of physical and chemical activation (a series of processes performed to render high surface area carbon) methods,[22,34,37,38] 3) activation of carbon precursors with metal (oxide) or organometallic compounds,[38–41] and 4) carbonization of aerogels or cryogels.[42,43] Although each of these methods results in MPC materials, pore-size distributions (PSD)-remain broad and the materials possess considerable microporosity.

1.4.1 Preparation of MPCs Using Hard-templates

The general approach for preparing MPCs using hard templates (mesoporous silica) method involves the infiltration of the template with appropriate carbon precursor followed by carbonization (< 1000 °C). Finally, the template is removed *via* dissolution (Figure 1-6).[44]

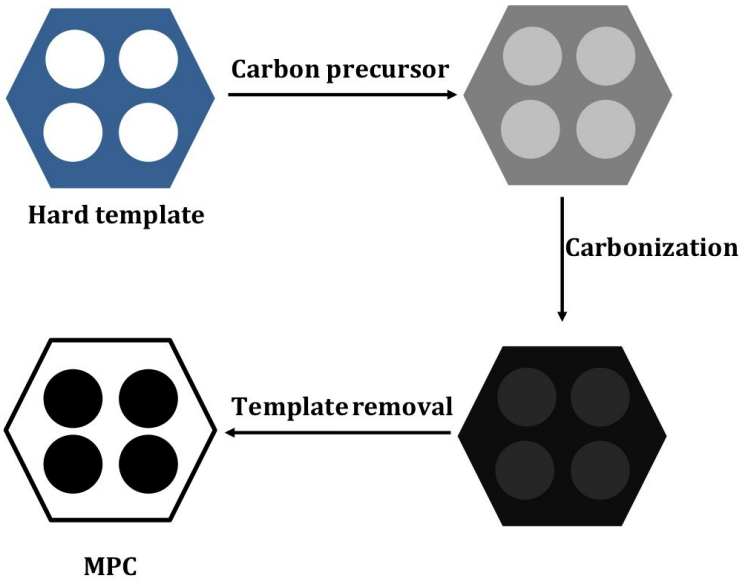

Figure 1-6: Schematic illustration of hard template method for MPC synthesis.

Knox *et al.* reported the synthesis of MPC materials using silica gel as a hard template.[45,46] A mixture of phenol-hexamine (*i.e.,* the carbon precursor) was added to the template. Following polymerization, carbonization of the phenolic resin and subsequent dissolution of the template resulted in rigid and spherical MPCs (Figure 1-7).[45] Brunauer-Emett-Teller (BET) surface area analysis of the resulting materials afforded areas on was 450 - 600 m^2g^{-1}. Subsequent graphitization at 2500 °C in Ar removed micropores and the final specific surface area was reported to be 150 m^2g^{-1}. These materials exhibit unique retention characteristics in liquid chromatographic separation and have been commercialized under the trade name "Hypercarb".[45,46]

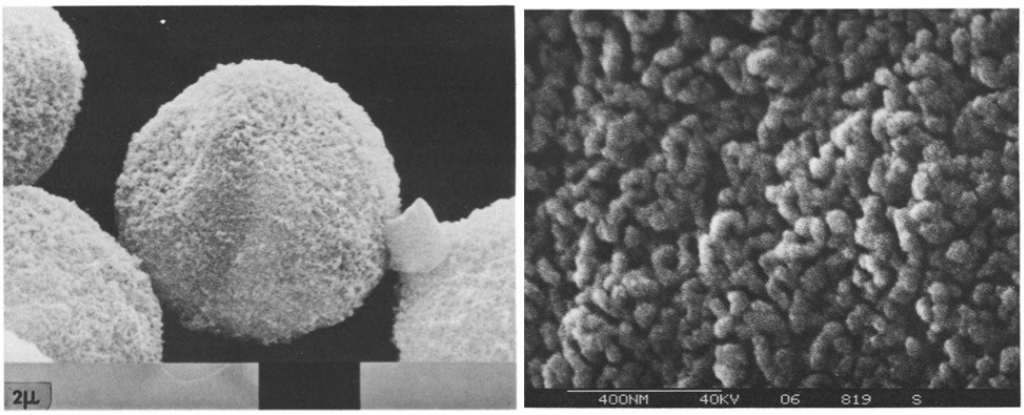

Figure 1-7: SEM images of porous glassy carbon (PGC) at different magnifications.[45] Reprinted (adapted) with permission from ref 45.

Following the example of Knox's pioneering work, other researchers attempted to synthesize porous carbon using zeolite templates – unfortunately the fine structure of zeolite was not replicated.[47,48] Exploration of other hard templates for porous carbon preparation was spurred by the discovery of the M41S family of nanostructured mesoporous materials by Mobil researchers in 1992 (Figure 1-8).[49–51]

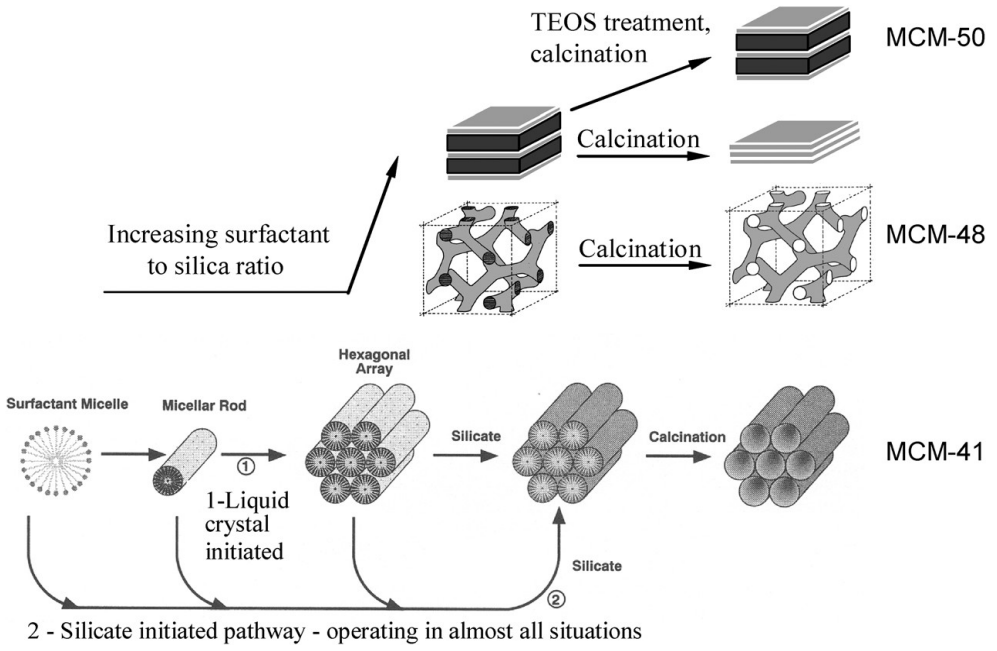

Figure 1-8: Liquid crystal templating (LCT) mechanism and M41S family of mesoporous molecular sieves including MCM-41, MCM-48, and MCM-50.[51] Reprinted (adapted) with permission from ref 51.

In 1999 Ryoo *et al.* reported the preparation of highly ordered MPC, CMK-1; the published method used mesoporous silica molecular sieves (*i.e.*, MCM-48) as a hard template and sucrose as the carbon precursor.[52] The general procedure involved impregnating the mesoporous silica template with an aqueous solution of sucrose and sulfuric acid followed by heating to 800 - 1100 °C under in inert atmosphere or under vacuum. Under these conditions, sulfuric acid catalyzes sucrose carbonization. The resulting cubic MPC (*i.e.*, CMK-1) obtained after removal of the template contains 3 nm pores and a surface area of 1380 m^2g^{-1} (Figure 1-9).[52]

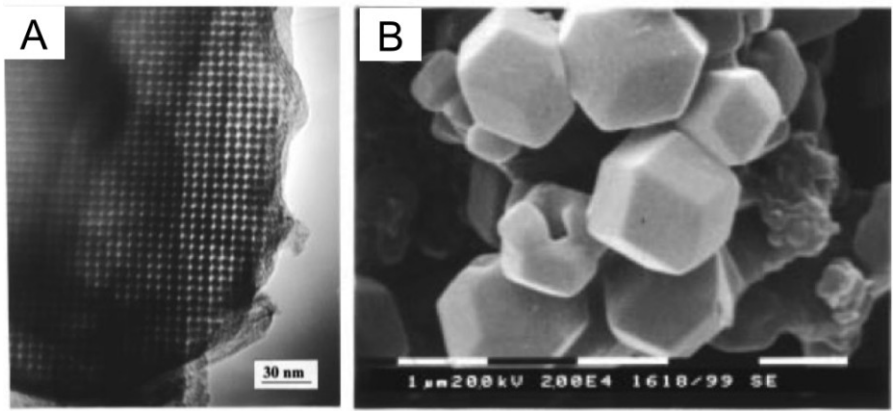

Figure 1-9: (A) TEM image of the ordered carbon molecular sieve CMK-1 (B) SEM image of a CMK-1.[52] Reprinted (adapted) with permission from ref 52.

Despite providing a MPC, the procedure used by Ryoo *et al.* did not provide a true inverse replica of the template; MCM-48 has a cubic structure bearing *Ia3d* symmetry, while the CMK-1 exhibited symmetry of $I4_1/a$. This somewhat surprising structural change can be understood in the context of a displacement model in which the relative position of the two non-interconnecting filled mesopore networks change after the template was removed.[53] Hyeon *et al.* also prepared ordered MPC (SNU-1) with regular three-dimensionally interconnected pore channels using the MCM-48 template and phenolic resin.[28] Their results showed that the carbon network is strong enough to keep its structure even after template removal.

Chemical vapor deposition (CVD) provides another approach to introduce carbon into hard templates and Ryoo *et al.* applied it to use acetylene as the carbon

source with MCM-48 templates. This procedure provided CMK-4 which posses the same symmetry as the template.[53] Another well-ordered hexagonal mesoporous silica structures (*i.e.*, SBA-15) originally prepared by Stucky *et al.*[54] were used by Ryoo and coworkers to template the synthesis of a highly ordered hexagonally structure MPC (*i.e.,* CMK-3) *via* sucrose decomposition. The final product bare a surface area of 1520 m^2g^{-1} and was a true inverse replica of the template.[55]

1.4.2 Preparation of MPCs Using Soft-templates

Another approach for preparing MPCs bypasses the preparation of a hard template and aims to use amphiphilic molecules (*e.g.*, surfactants, block copolymers) bearing hydrophilic and hydrophobic (lipophilic) similar to those used as soft-templates for the synthesis of ordered mesoporous oxides directly.[49] Despite notable successes in employing molecular ordering of this kind to achieve MPC materials, direct transfer to MPCs is non-trivial. There are four important criteria that must be met when preparing MPCs in this way if the synthesis is to be achieved:[24]

1) Precursor components must self-assemble into nanostructures,

2) Two components (pore-forming and one carbon-yielding) are needed,

3) The pore-forming component must be stable toward the carbonization conditions required of carbon-yielding component,

4) The carbon-yielding component must provide a highly cross-linked polymeric material that maintains its structure during the decomposition and removal of the pore-forming material.

In 1999, Moriguchi *et al.* reported their attempts to prepare ordered MPCs using the surfactant cetyltrimethylammonium bromide (*i.e.,* $(C_{16}H_{33})N(CH_3)_3Br$; CTAB) as the soft template and phenolic resin the carbon source.[56] While various mesophases including lamella, hexagonal, and disordered structures were achieved by defining the ratio of phenolic resin to CTAB, these structures collapsed upon aging at 200 °C (Figure 1-10).

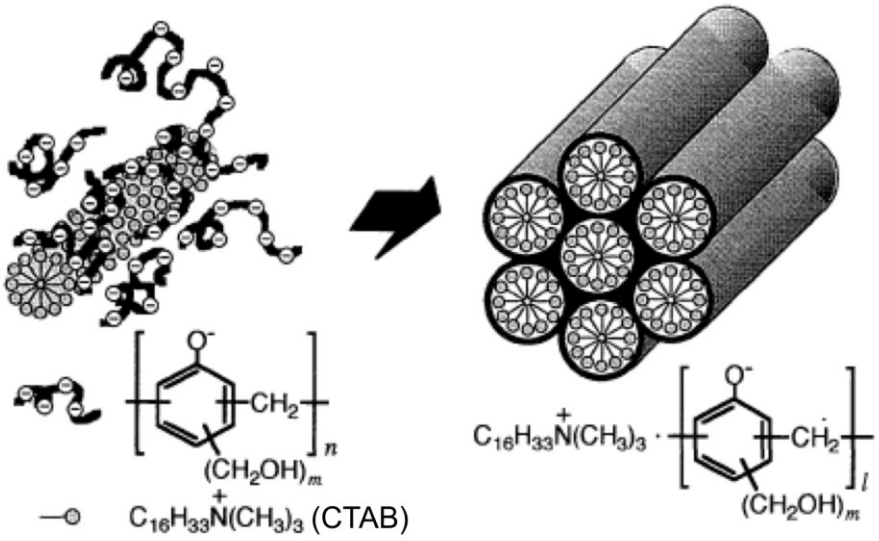

Figure 1-10: Schematic illustration for synthesis of MPC using a soft template approach. CTAB was used as soft template.[56] Reprinted (adapted) with permission from ref 56.

Zhao *et al.* tried a similar approach by replacing CTAB with ethylene oxide-based surfactant (*i.e.,* Brij; $C_nH_{2n+1}(EO)_x$; (EO = ethylene oxide)), but the resulting carbonized materials did not possess mesoporous structure.[57]

Unfortunately, block copolymers alone are not suitable for direct synthesis of MPCs because the nanostructures assembled by linear block copolymers are not resistant to carbonization and the carbon yield is too low.[58] Combinations of block copolymers as pore-forming/structure-directing reagents and appropriate carbon precursors have been used to synthesize ordered MPCs. The driving force for the self-assembly of the template is often the interaction between it and the carbon precursor (*e.g.*, hydrogen bonding). Commonly thermoset polymers are used to "lock in" the mesoporous structure of the template. The first report that applied this type of approach to the preparation of MPCs appeared in 2004.[59] In this early study, polystyrene-*block*-poly(4-vinylpyridine) (PS-P4VP) templated the carbonization of resorcinol-formaldehyde. Assembly within this template/precursor pairing was driven by hydrogen bonding (Figure 1-11 and Figure 1-12).[60]

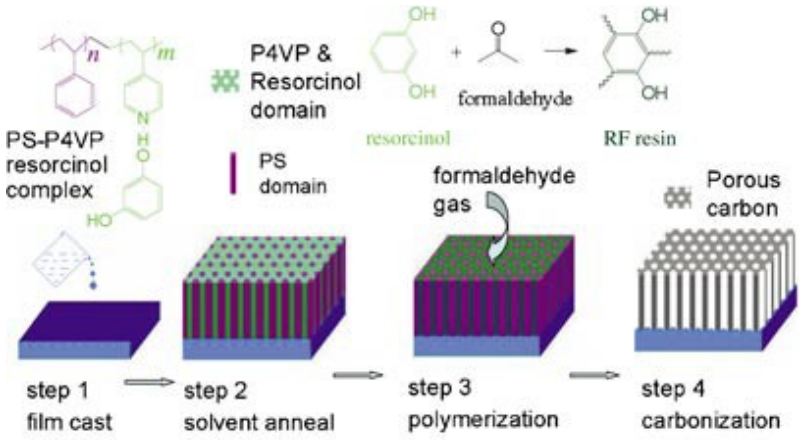

Figure 1-11: Pictorial representation of the synthesis protocol used to prepare well-defined carbon nanostructures using the PS-P4VP/resorcinol–formaldehyde system.[60] Reprinted (adapted) with permission from ref 60.

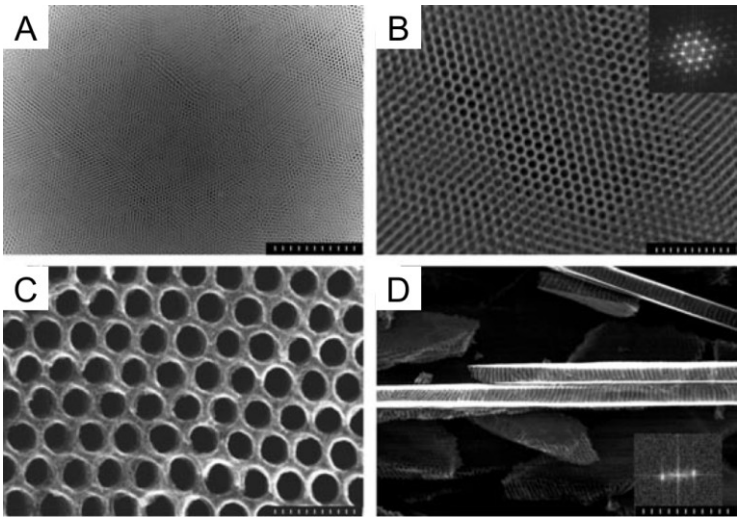

Figure 1-12: TEM images of the carbon film obtained using the PS-P4VP/resorcinol–formaldehyde system. (A) Z-contrast image of the large-scale homogeneous carbon film in a 4×3 μm area. The scale bar is 1 μm. (B) Z-contrast image with higher magnification. The scale bar is 300 nm. (C) High-resolution SEM image of the surface of the carbon film that reveals uniform hexagonal-pore array. The scale bar is 100 nm. (D) SEM image of the film cross-section. The scale bar is 100 nm.[60] Reprinted (adapted) with permission from ref 60.

Another block copolymer soft template (*i.e.,* Pluronic F127; triblock-copolymer of poly (ethylene oxide)-poly (propylene oxide)-poly (ethylene oxide)(PEO-PPO-PEO)) was demonstrated by Tanaka *et al.* (see Figure 1-14).[61] In this case, the carbon coprecursors were resorcinol-formaldehyde copolymer and triethylorthoacetate (EOA) (see Figure 1-13). The authors found that by defining the carbonization temperature carbon content could be maximized, and the pore size as well as surface area (600 - 1300 m^2g^{-1}) could be defined.

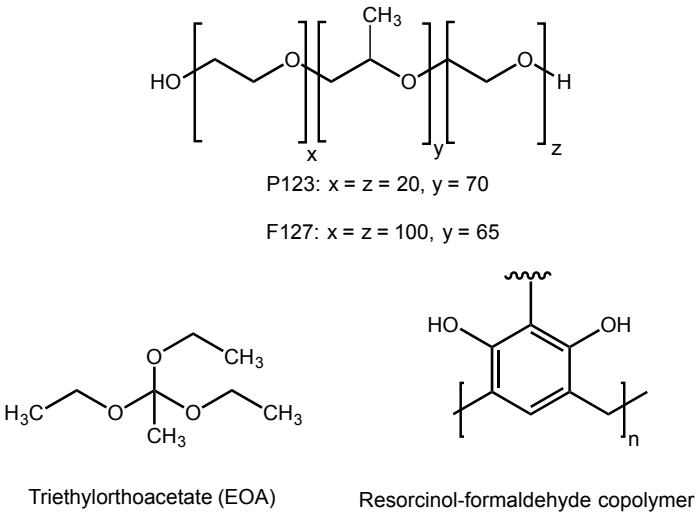

Figure 1-13: Chemical structures of pluronic P123 and F127, resorcinol-formaldehyde copolymer and triethylorthoacetate (EOA).

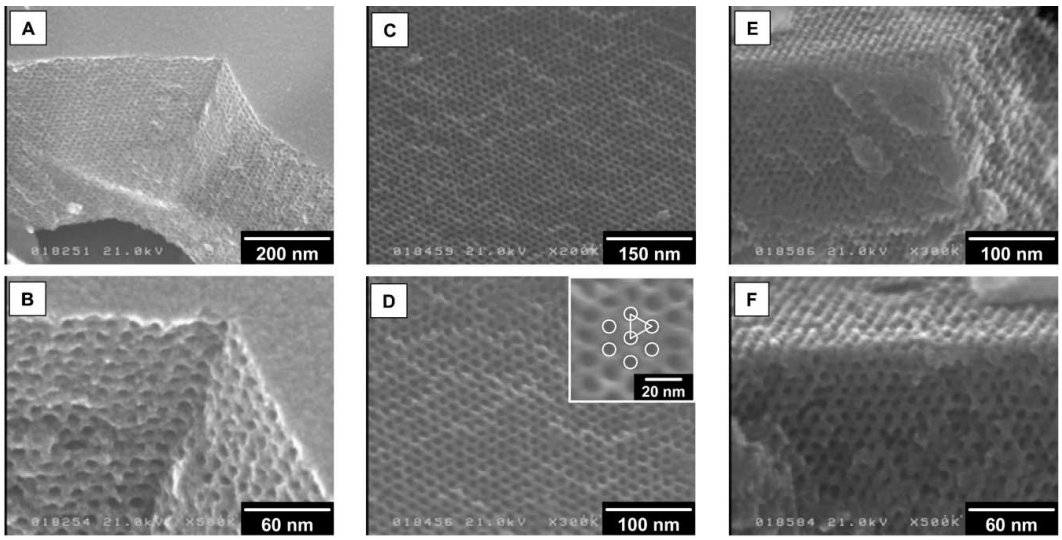

Figure 1-14: Field emission SEM images of carbonized mesoporous carbons with ordered channel structure at different carbonization temperatures: (A, B) 400 °C, (C, D) 600 °C and (E, F) 800 °C.[61] Reprinted (adapted) with permission from ref 61.

Zhao's group made advances using PEO-PPO-PEO soft templates. They used variety of block copolymers as templates (F127 and P123) (see Figure 1-13) for the synthesis of mesoporous polymers and carbons.[57,62–64] They found that there are three experimental parameters that must be considered while using this class of soft templates:

1) Volume ratio between PEO to PPO in the block copolymer surfactants,

2) Ratio of carbon source to the surfactants

3) Carbonization conditions (*i.e.*, temperature, time, rate of heating, atmosphere).

Similar to the work noted previously that employed PVP-derived templates, the self-assembly driving force is interactions between the template of choice and carbon precursor (*e.g.,* hydrogen bonding). Therefore, the choice of the carbon precursor and its hydrogen bonding capacity with the soft template are important.

This template/precursor interplay is illustrated by carbohydrates such as turanose (disaccharide), raffinose (trisaccharide) (see Figure 1-15), and glucose that have been used as carbon precursors in porous anodic aluminum oxide (AAO) and poly(styrene)-*block*-poly(4-vinylpyridine) (PS-P4VP) as template (see Figure 1-16).[65] The carbohydrates possess multiple hydrogen bonding sites that can interact with PVP moieties of the template. The PS moieties of the surfactant decompose during carbonization. After removing AAO by chemical etching, porous carbon nanotubes were formed (see Figure 1-17).

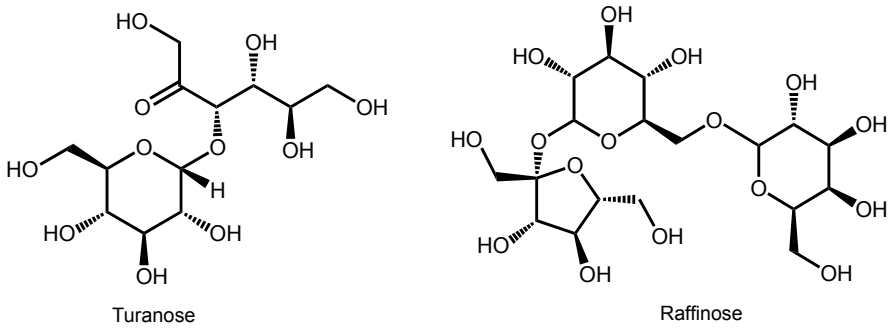

Figure 1-15: Chemical structures of turanose and raffinose.

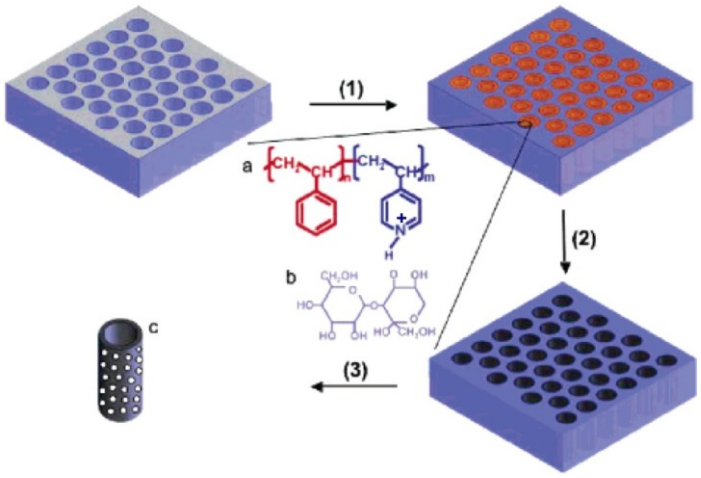

Figure 1-16: Synthesis of nanoporous carbon nanotubes. (1) Filling the AAO templates with the polymer and carbohydrate dimethylformamide (DMF) solution; (2) carbonization under inert atmosphere (argon); (3) Template removal. (a) poly(styrene)-block-poly(4-vinylpyridine)(PS-P4VP) and (b) are carbohydrates such as turanose, raffinose, glucose, *etc*.[65] Reprinted (adapted) with permission from ref 65.

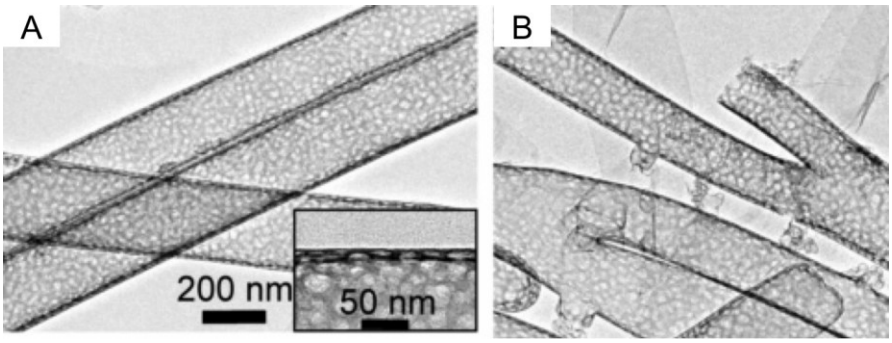

Figure 1-17: (A) TEM image of nanoporous carbon nanotubes (inset is the magnified image). (B) TEM image of branched nanoporous carbon nanotubes.[65] Reprinted (adapted) with permission from ref 65.

1.4.3 Nitrogen-doped Carbon Nanostructures

Doping carbon nanostructures with nitrogen changes properties and adds another degree of freedom when tailoring nano-carbon;[66–70] catalytic activity, conductivity, and structure can be affected. N-doped carbon-based catalysis has a long history. As early as 1926, Rideal and Wright reported the effect of nitrogen dopants derived from urea on the catalytic activity of carbon while investigating the oxidation of oxalic acid.[71] They showed that nitrogen doping results in an increase of the total surface area of carbon that possibly affects the catalytic activity of it. More recently N-doped CNTs showed enhanced catalytic activity toward the oxygen reduction reaction (ORR) important for fuel cell development and applications.[72–74] N-doping also improves catalyst durability.[75–79]

The influence of nitrogen atoms on the catalytic activity of carbon can be traced to its effect on the material electronic structure; it lowers the band gap,

increases electron mobility and decreases the electron work function at carbon/liquid (gas) interface.[70] It also improves surface wettability, as well as adsorption properties that facilitate an electrochemical reaction on the carbon surface.[80] Doping carbon nanostructures with nitrogen can be achieved *via in-situ* processes during synthesis or post-treatment with nitrogen containing species (*e.g.,* N_2, NH_3, *etc.*).[81] Common *In-situ* methods used to synthesize nitrogen-doped carbons include high-temperature arc-discharge[82,83] and laser ablation,[84,85] as well as low-temperature CVD,[86–91] and solvothermal procedures.[92,93] Post-treatments are normally performed in an atmosphere containing the nitrogen source at high temperatures (*i.e.*, 600-900 °C).[73,94–96]

The choice of nitrogen precursor in both methods depends on the experimental conditions and desired degree of doping. If a doping concentration is favored, a nitrogen-enriched precursor is preferred. For example, polyacrylonitrile, tetracyanoquinodimethane, ethylenediamine, 1,2-phenylenediamine, hydrogen phthalocyanine, pyrrole and their derivatives,[97–99] and also gases such as NH_3[100] or acetonitrile[101] are commonly used as nitrogen precursors to obtain different levels of nitrogen doping (see Figure 1-18).

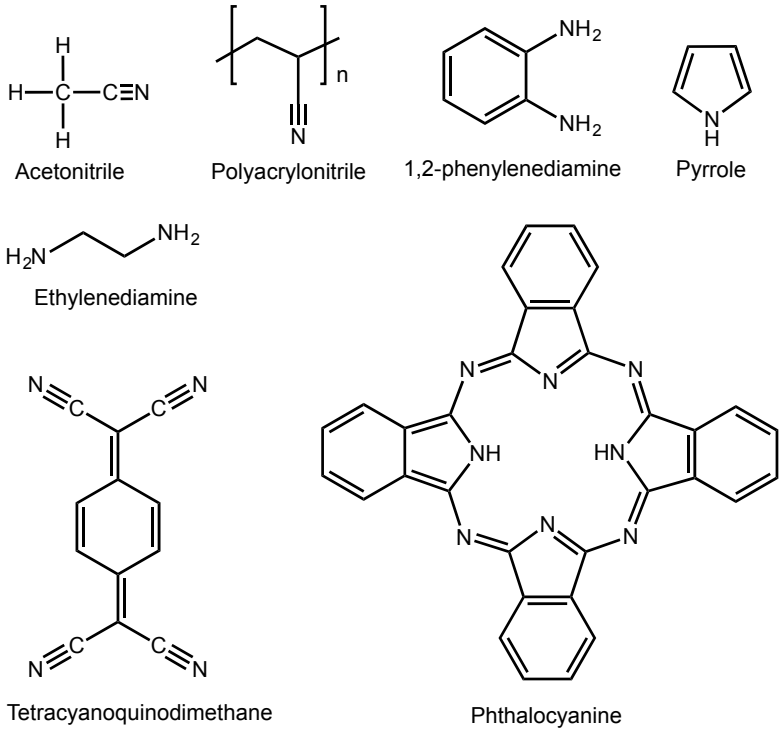

Figure 1-18: Chemical structures of selected common nitrogen precursors.

N-doped carbon nanostructures can also be prepared starting with a nitrogen-containing carbon precursor such as dopamine. Dopamine (*i.e.,* 4-(2-aminoethyl)benzene-1,2-diol) is biomolecule and a neurotransmitter. Dopamine contains catechol and amine functional groups (catecholamine) that are key to their targeted reactivity (Figure 1-19).

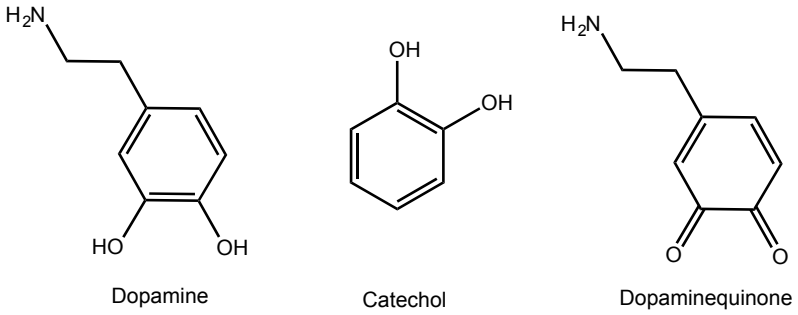

Figure 1-19: Dopamine, catechol and dopaminequinone chemical structures.

Dopamine undergoes self-polymerization under basic conditions to form a polymer (*i.e.,* polydopamine) that possesses a complex and poorly understood structure.[102] It is has been proposed that the catechol functional group is deprotonated and subsequently oxidizes to form dopaminequinone, which subsequently rearranges *via* intramolecular cyclization to leukodopaminechrome. Further oxidation and rearrangement leads to 5,6-dihydroxyindole, whose further oxidation causes inter-molecular cross-linking to yield a polymer (see Figure 1-20).[103,104] This process facilitates film formation on support surfaces *via* covalent bonds and other strong intermolecular interactions such as hydrogen-bonding, metal chelation and π-π interactions.[104–107] Figure 1-21 highlights the interaction mechanism of polydopamine with silanols groups on the surface of silica *via* hydrogen bonding.[108] Interactions similar to those shown are exploited using other precursors (*vide supra*) and provide a basis for using silica-based templates to form N-doped carbon nanostructures.

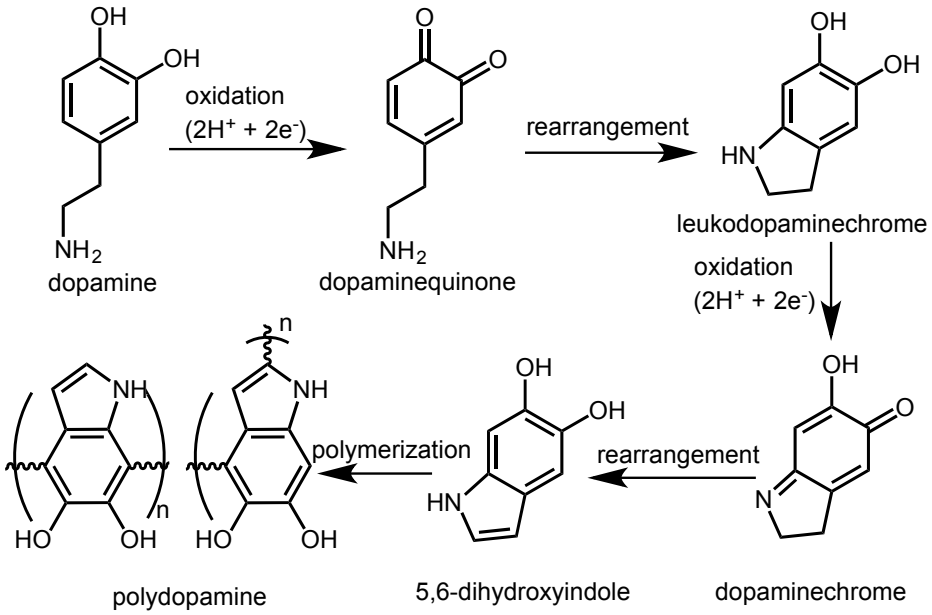

Figure 1-20: Oxidative polymerization of dopamine and proposed structure for polydopamine.

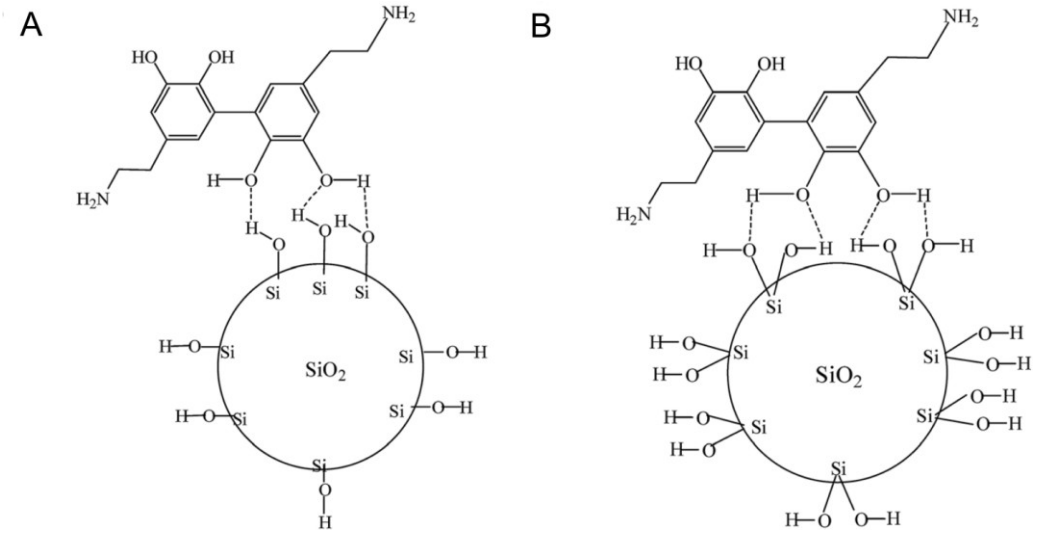

Figure 1-21: Illustration of the interaction mechanism of (A) isolated and (B) geminal silanols groups on the surface of silica with catechol group in polydopamine molecule.[108] Reprinted (adapted) with permission from ref 108.

Dai *et al.* reported the first application of dopamine (or polydopamine) as a carbon precursor to coat silica nanosphere (d ~ 400 nm) templates (see Figure 1-22 A).[107] The dopamine coating was formed by direct polymerization onto the silica particles under basic conditions. Subsequently, the polymer-coated silica was carbonized in an inert atmosphere. Finally the silica template was removed by HF etching to afford hollow carbon spheres (see Figure 1-22 B and C).[107]

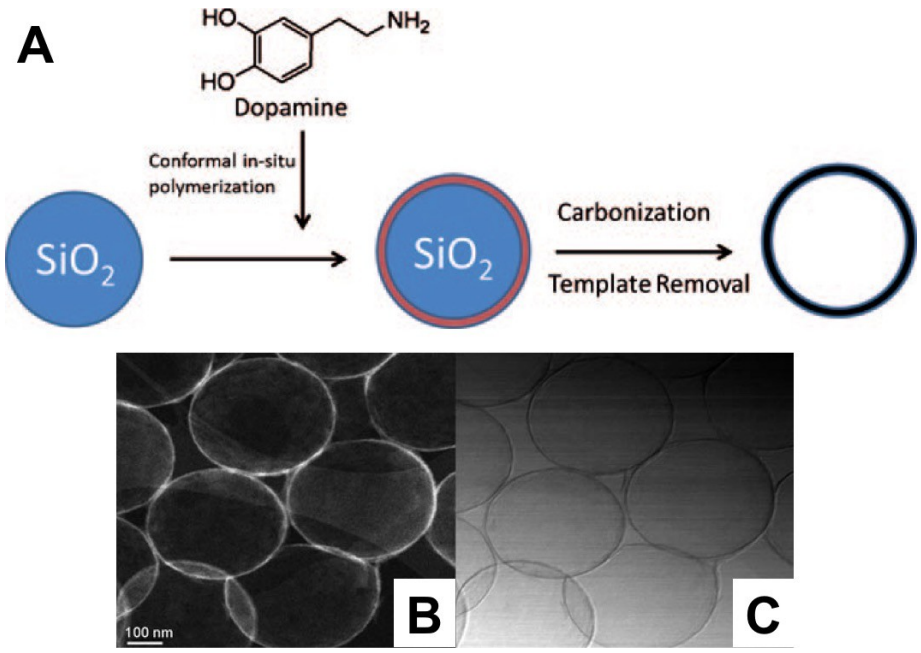

Figure 1-22: Illustration of synthesis of hollow carbon spheres. (A) Silica spheres (blue) are used as the template and dopamine (red ring) is used as the carbon precursor. STEM images of the resulting hollow carbon spheres: (B) Z-contrast, (C) bright field.[107] Reprinted (adapted) with permission from ref 107.

1.4.4 Cellulose Nanocrystals as Carbon Precursor

Cellulose is the most abundant natural biopolymer on the earth.[109] Cellulose nanocrystals (CNC; Figure 1-23) are an emerging renewable nanomaterial that holds potential in a variety of applications including personal care, chemicals, foods (texturizing agent and fat replacer), pharmaceuticals (tablet binder), as well as additive in paper and composites applications.[109,110]

Rånby first reported the production of CNC in 1951 and used sulfuric acid-catalyzed degradation of cellulose fibers derived from wood and rayon.[111–113] CNC differ from common cellulose because of their nanoscale dimension, high specific strength and modulus (Young's modulus of 100-140 GPa), high tensile strength (7500 MPa), high surface area (150-250 m^2/g), and unique optical properties.[114] CNCs are rod-like particles exhibiting diameters of 10-20 nm and lengths of a few hundred nanometers.[115] CNC morphology depends on the natural source material (*e.g.,* tunicate, green algae, wood, cotton) and the hydrolysis conditions employed.[115]

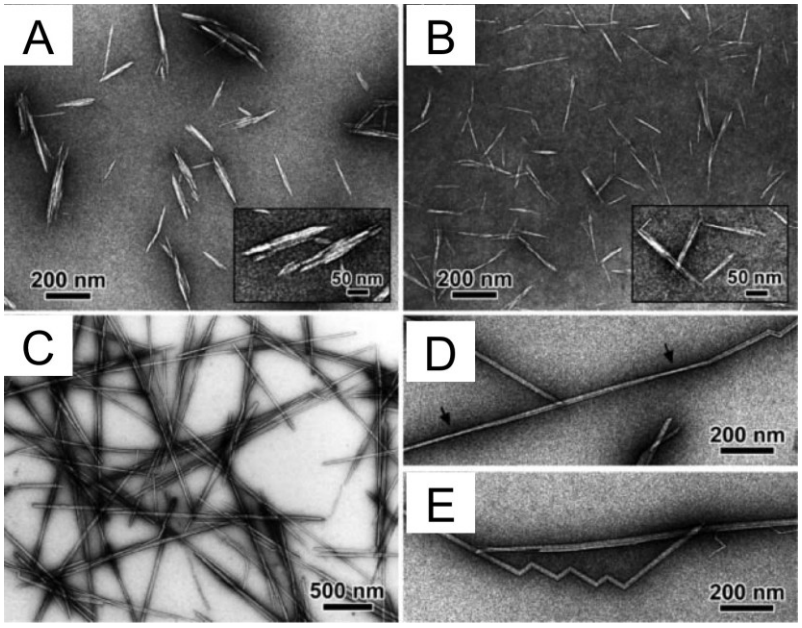

Figure 1-23: TEM images of CNC particles obtained from the sulfuric acid hydrolysis from different sources; (A) cotton (B) avicel (C-E) tunicate cellulose.[115] Reprinted (adapted) with permission from ref 115.

CNC surface chemistry also influences its properties. Those prepared using sulfuric acid hydrolysis possess negatively charged surfaces resulting from the formation of sulfate ester groups during acid treatment; this surface results in materials that are compatible with aqueous conditions and facilitates the formation of stable colloids (see Figure 1-24).

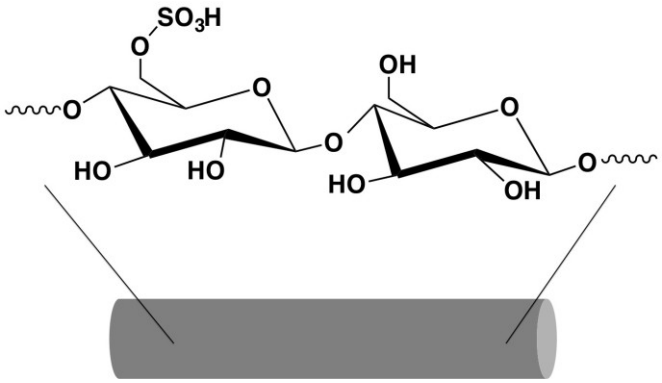

Figure 1-24: Illustration of CNC surface feature.

In addition, the presence of hydroxyl groups on CNC surfaces provides a reactive platform on which chemical modification may be performed *via* esterification (Figure 1-25)[116] and oxidation *via* TEMPO (2,2,6,6-tetramethylpiperidin-1-yl)oxyl mediated oxidation (Figure 1-26).[117] Noncovalent surface modifications such as adsorbing surfactants and polymer coating are also possible.[118] All these surface modifications methods are exploited to render a much stable dispersion of CNC. Also, they improve its compatibility for further modification/functionalization.

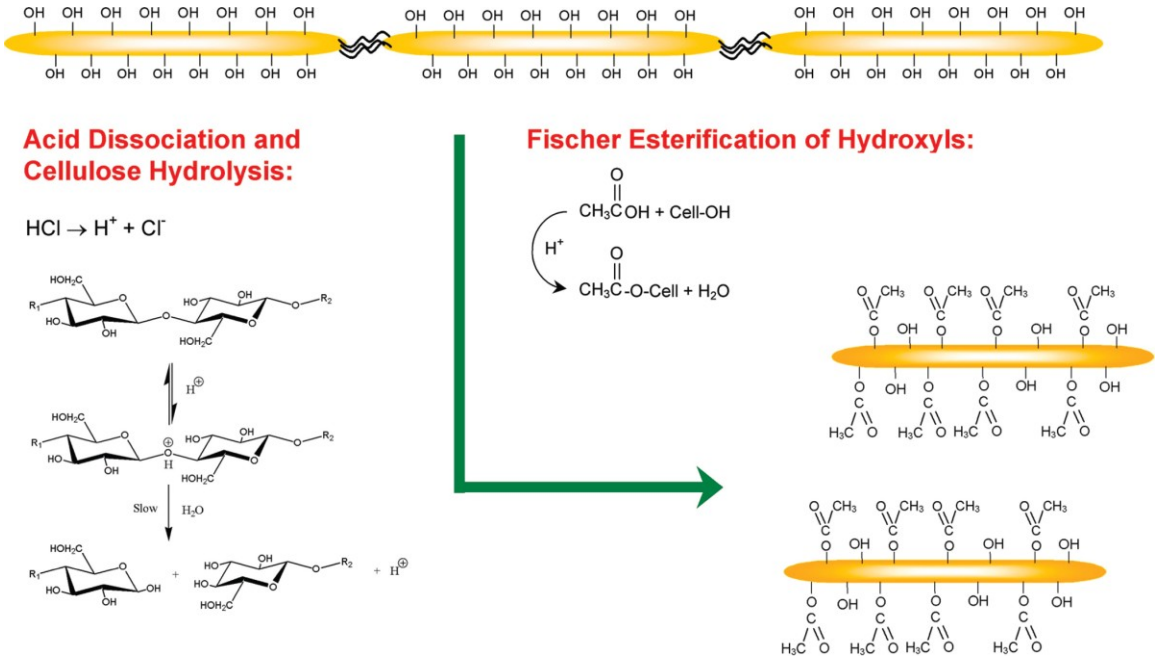

Figure 1-25: Illustration of simultaneous cellulose hydrolysis and esterification of hydroxyl groups using a mixture of acetic and hydrochloric acid as example.[116] Reprinted (adapted) with permission from ref 116.

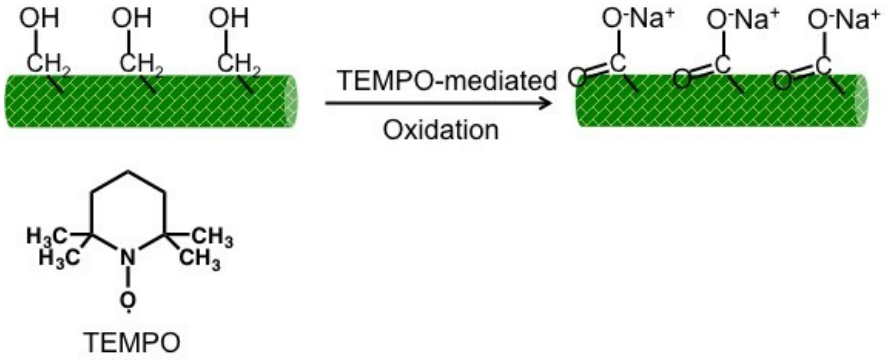

Figure 1-26: Schematic representation of TEMPO-mediated oxidation of CNC.

CNCs have been employed as an additive to impart useful material properties (*e.g.,* strength, optical response). It was first used as a reinforcing filler in poly(styrene-*co*-butyl acrylate) (poly(S-*co*-BuA))-based nanocomposites by Favier *et al.*[119] It has also been used as a templating agent in the synthesis of mesoporous materials. Shin *et al.* presented a synthetic protocol for porous titania that relied on cellulose nanocrystals templates.[120] Similarly, another report saw the formation of a three-dimensional template of self-assembled CNCs that was subsequently filled with a polymer.[121,122] This later procedure exploited the hydrogen-bonding characteristics of the CNC; the researchers used solvent exchange and a homogeneous aqueous dispersion of CNCs to form a gel template structure into which a polymer of choice could be incorporated.

Another report by the MacLachlan group described a similar CNC templating approach to prepare freestanding mesoporous silica films with tunable chiral nematic structures.[123] In this fabrication procedure, common silica precursors, $Si(OEt)_4$ (TEOS) or $Si(OMe)_4$ (TMOS) were added to an aqueous suspension of CNCs at a defined pH to obtain a homogeneous mixture; the mixture was left undisturbed in order to form a chiral nematic phase. After air-drying, the cellulose template was removed upon calcination in air. This general approach was extended by the same group to prepare chiral nematic MPC.[124] In this case the CNC-silica composite was pyrolyzed in an inert atmosphere to obtain a carbon-silica composite that was freed of the silica template upon exposure to aqueous NaOH (Figure 1-27).[124]

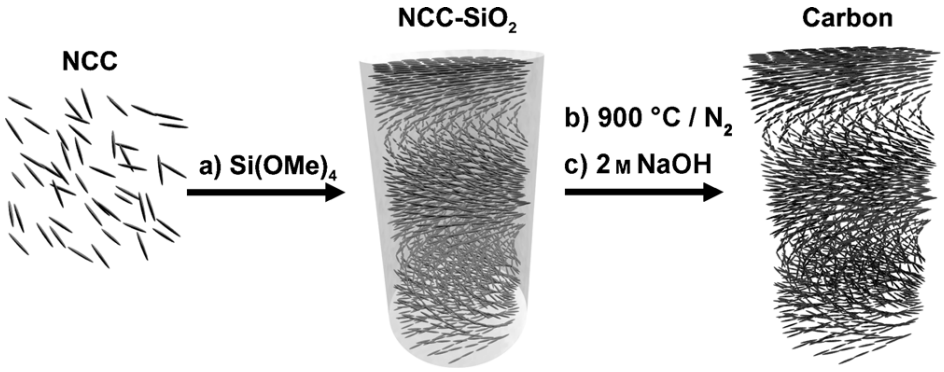

Figure 1-27: Schematic representation of synthesis of chiral nematic MPC. a) CNC is mixed with TMOS and slowly evaporated to form chiral nematic CNC–silica composite films. b) Pyrolysis in an inert atmosphere at 900 °C. c) Silica removal using 2 M NaOH to generate chiral nematic MPC.[124] Reprinted (adapted) with permission from ref 124.

Table 1-1 summarizes the synthetic methods for preparing MPCs outlined in Section 1.4. The choice of carbon precursor and template (hard or soft) along with the synthetic conditions (*i.e.,* carbonization temperature/time/heating rate, *etc.*) all affect the MPC structural properties (*i.e.,* surface area, pore size, pore volume), morphology (*i.e.,* size and shape), and chemical properties. Because porosity generally is generated by the release of small molecules (*e.g.,* H_2O, CO, CO_2, and NO_x) during carbonization and template removal, the pore diameters of MPCs can be understood in the context of the thermal stabilities of different carbon precursors (*i.e.,* aromatic > aliphatic), carbonization yield, and also the interactions between template and carbon precursor.[125]

Table 1-1: Summary of various methods for preparing MPCs.

Carbon precursor	Template	Surface area (m^2g^{-1})	Reference
Phenol-hexamine	Silica gel	450 - 600	Ref 45,46
Poly(acrylonitrile)/ poly(furfuryl alcohol)	Zeolite	2000	Ref 47
Phenol-formaldehyde	Zeolite Y	488	Ref 48
Sucrose	MCM-48	1380	Ref 52
Sucrose	SBA-15	1520	Ref 55
Resorcinol-formaldehyde	PS-P4VP	ND*	Ref 61
Resorcinol-formaldehyde/ triethylorthoacetate	F127	600-1300	Ref 60
Turanose/raffinose/glucose	PS-P4VP	ND*	Ref 65
Dopamine	Silica	ND*	Ref 107
CNC	CNC/silica	1460	Ref 124

* ND: not determined.

1.5 Iron Oxide-based Nanomaterials

Iron oxide nanoparticles are widely studied.[126,127] Broadly speaking, most iron oxide nanomaterials possess the hematite (α-Fe_2O_3) or magnetite (Fe_3O_4) crystal structure. Hematite is the most thermodynamically stable phase of iron oxide and is an n-type semiconductor (E_g = 2.1 eV).[128] Hematite exhibits a rhombohedral symmetry (Figure 1-28).[129,130] It has been used in a wide range of applications including pigments, magnetic devices, anticorrosive agents, catalysts, gas sensors, photoanodes for photo-assisted electrolysis, lithium-ion batteries, and water treatment.[131–141]

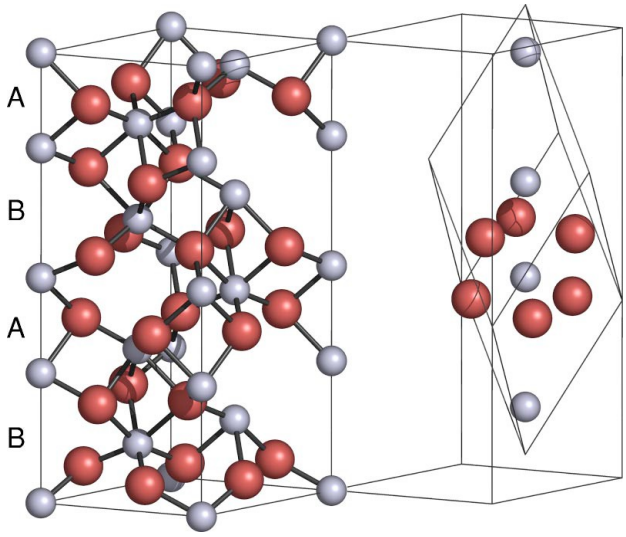

Figure 1-28: Hexagonal unit cell of α-Fe_2O_3 (left) rhombohedral primitive cell (right). Grey spheres display Fe atoms; red spheres represent the O atoms.[130] Reprinted (adapted) with permission from ref 130.

Magnetite, Fe_3O_4, is the common magnetic iron oxide with a cubic inverse spinel structure with oxygen atoms forming a face centered cubic (fcc) closest packing and Fe cations occupying interstitial tetrahedral sites and octahedral sites (Figure 1-29).[129,142] In this configuration, electrons can jump between Fe^{2+} and Fe^{3+} ions in octahedral sites at room temperature, rendering magnetite an important class of "half-metallic" (conductive) material.[143] Magnetic nanoparticles have been developed and find use in many technological applications including magnetic, biosensing, targeted drug delivery, magnetic resonance imaging (MRI) contrast agents, magnetic inks, catalysis, and batteries.[144–152]

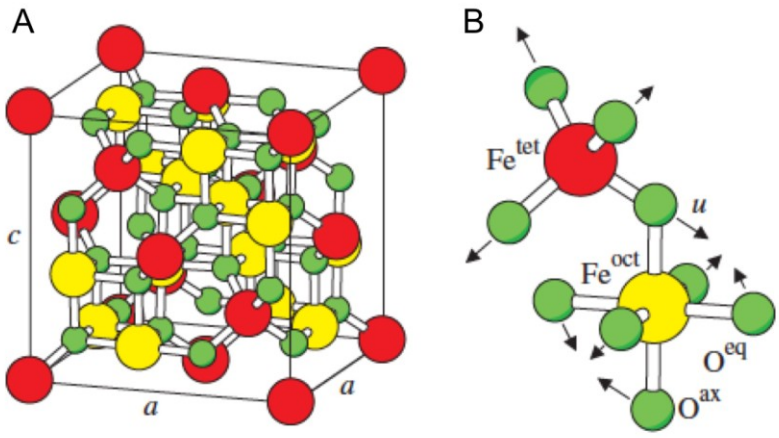

Figure 1-29: (A) Schematic illustration of face-centered cubic inverse spinel structure of magnetite. (B) Higher magnification of an octahedron and a tetrahedron sharing an oxygen atom. Fe^{2+} cations occupy octahedral holes and Fe^{3+} cations occupy tetrahedral holes and the remaining octahedral ones.[142] Reprinted (adapted) with permission from ref 142.

1.5.1 Iron Oxide Nanorod Synthesis

A variety of synthetic methods have been used to prepare α-Fe_2O_3 nanoparticles with different morphologies including, nanospheres, nanowires, nanaotubes, cubes, and nanorods. This section focuses primarily on synthetic methods that provide α-Fe_2O_3 nanorods because of their relevance to the presented work. For descriptions of methods affording particles with different morphologies/crystal structures the reader is directed to the following references.[153,154] Sol-gel mediated synthesis is a common approach toward α-Fe_2O_3 nanorods.[155,156] Woo *et al.* reported α-Fe_2O_3 nanorods prepared *via* a sol-gel reactions within reverse micelles (Figure 1-30 A).[156] In general, a gelation promoter agent (*e.g.*, propylene oxide) is used during the synthesis. After gelation is complete the powder undergoes a crystallization phase that involves refluxing in a high boiling point, reducing solvent. It has been proposed that during this crystallization step the partially crystallized monolithic gel particles fuse in an end-to-end manner yielding nanorods (Figure 1-30 B).[156] As shown in Figure 1-30 B the nanorods are poorly defined and aggregated. The resulting dimensions (diameter × length) was 6.8 nm × 24.3 nm.

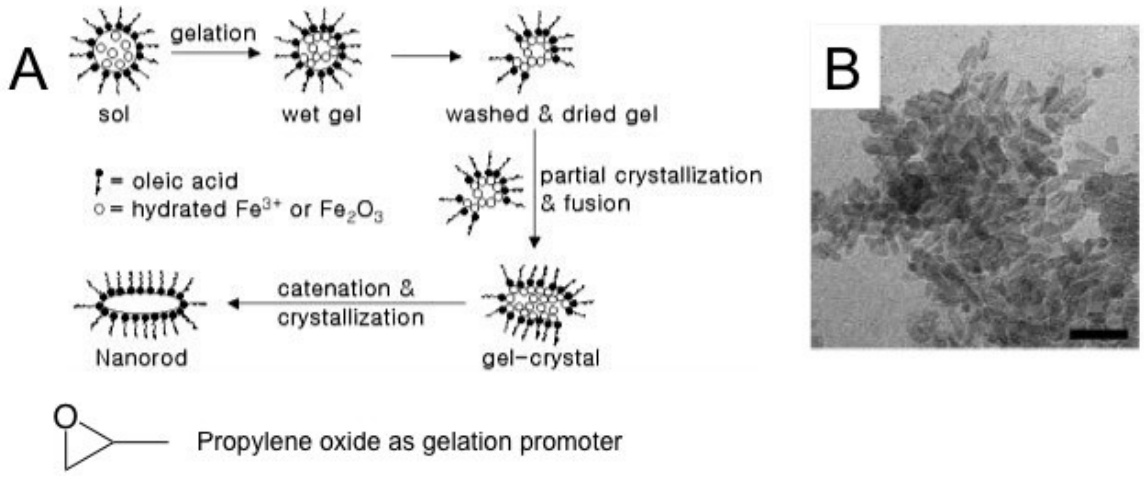

Figure 1-30: (A) A representation of materials transformation in a reverse micelle followed by crystallization by reflux. (B) TEM image of α-Fe_2O_3 nanorods (scale bar is 30 nm).[156] Reprinted (adapted) with permission from ref 156.

Zhu *et al.* reported the preparation of single-crystal hexagonal α-Fe_2O_3 nanorods *via* an iron-water reaction at 350 - 450 °C (Figure 1-31).[157] Spherical iron nanoparticles were employed as a precursor and were housed within a quartz reaction tube. Varying amounts of water vapor were introduced at predetermined temperatures for different reaction times.

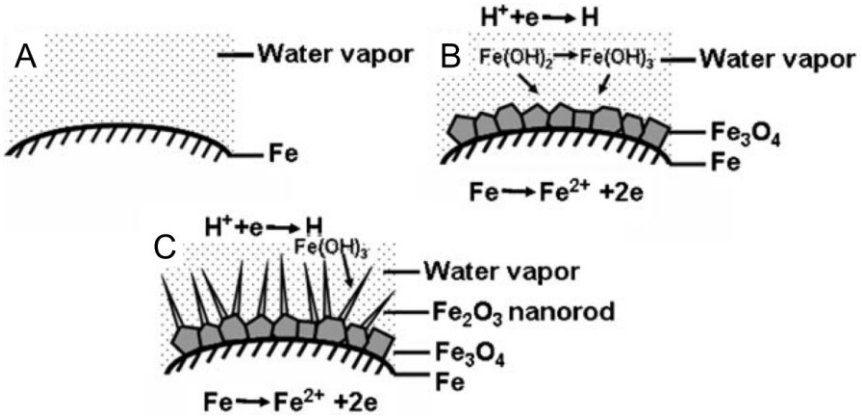

Figure 1-31: A scheme of the nanorod growth. At the beginning, iron particle and water vapor are both present (A) then a layer of Fe_3O_4 formed on the particle surface (B) in the last step Fe_2O_3 nanorods grown on the surface of the Fe_3O_4 layer (C).[157] Reprinted (adapted) with permission from ref 157.

Figure 1-32 shows the nanorods are poorly defined and some are broken at both tip and base. Most nanorods have a diameter less than 100 nm and terminate with a sharp tip (20 nm).

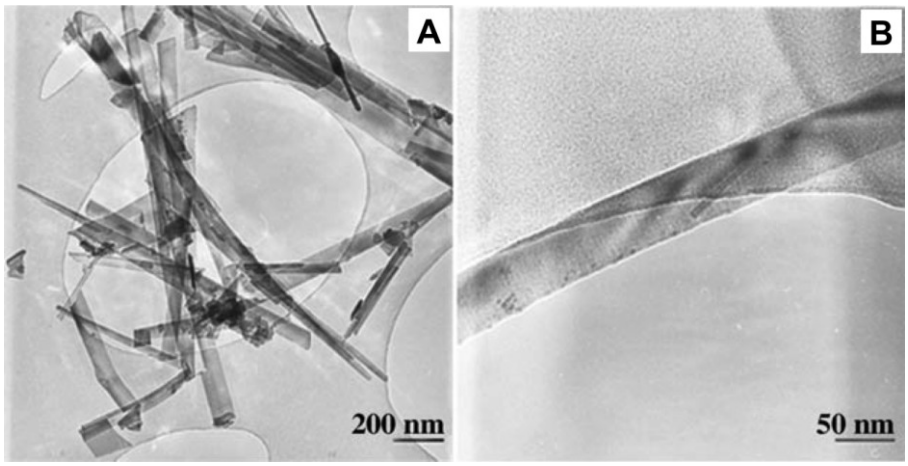

Figure 1-32: (A) TEM image of α-Fe_2O_3 nanorods prepared *via* iron-water reaction at 350 °C for 3 h. (B) A single nanorod.[157] Reprinted (adapted) with permission from ref 157.

Among the reported methods for iron oxide nanorod preparation, hydrothermal synthesis is one of the most promising.[158,159] Hydrothermal syntheses generally involve crystal synthesis and/or growth at high temperatures and water pressures.[160] Advantages of this approach include: 1) control of size, morphology, and degree of agglomeration, 2) limited introduction of impurities, 3) low reaction temperatures (< 300 °C), 4) cost-effectiveness, and 5) environmental compatibility.[153] Zheng *et al.* reported the hydrothermal synthesis of α-Fe_2O_3 with various morphologies (*i.e.*, nanoparticles, nanopolyhedra, microcubes; See Figure 1-33). The reaction was performed in Teflon-lined stainless steel autoclaves at 180 °C. By varying the reaction time and solvent particle morphologies were tailored.[153]

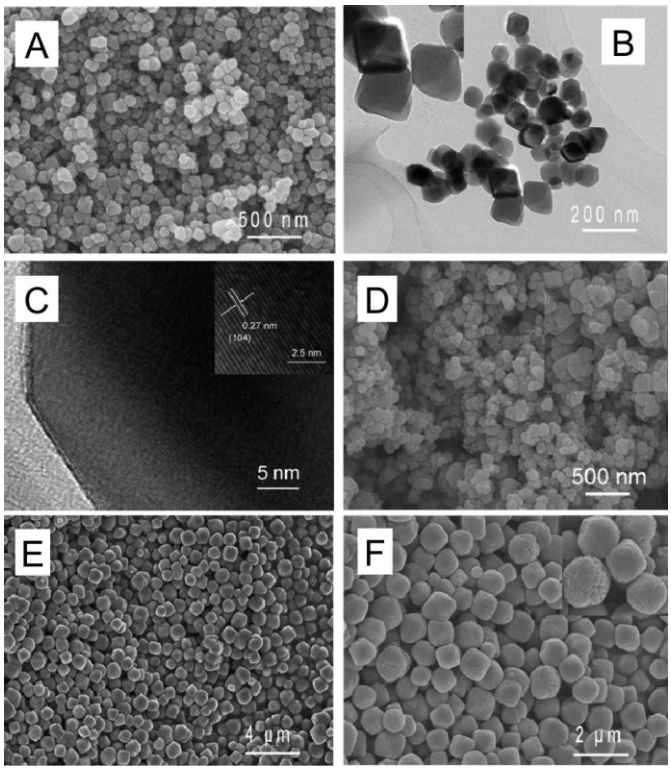

Figure 1-33: Representative electron microscopy images of different morphologies of α-Fe_2O_3 prepared *via* hydrothermal synthesis. (A, B, C) α-Fe_2O_3 nanopolyhedra; (D) α-Fe_2O_3 nanoparticles; (E and F) nanoparticles-aggregated α-Fe_2O_3 microcubes.[153] Reprinted (adapted) with permission from ref 153.

Brown *et al.* also reported the hydrothermal synthesis of α-Fe_2O_3 nanorods using phosphate anion (PO_4^{3-}) capping agents. Again, the reaction time, temperature, and capping agent concentration were investigated with the goal of optimizing the yield of α-Fe_2O_3 nanorods.[161] Representative TEM images (Figure 1-34) illustrate the effect of increasing hydrothermal synthesis temperature from 120 - 240 °C on the shape of nanoparticles. A fully crystalline oval α-Fe_2O_3 nanorod

(aspect ratio of ~7) formed at 200 °C. Curiously, these authors also identified the presence of a β-FeOOH intermediate at lower hydrothermal temperature and short time and suggested that its presence was fundamental to the supply of Fe^{3+} required for the nucleation and growth of α-Fe_2O_3. A detailed process map is shown in Figure 1-35 illustrating the complexity of the hydrothermal products and development of the shape and phases at different experimental conditions.

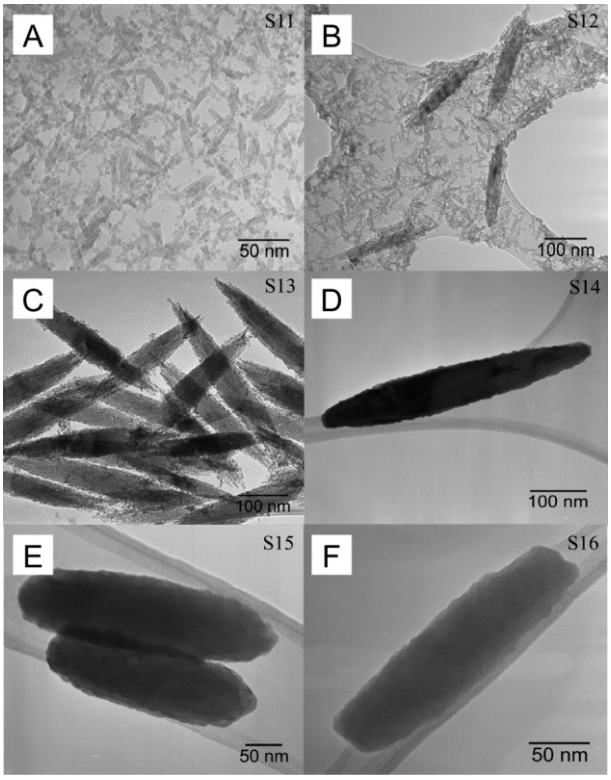

Figure 1-34: TEM images of different particles obtained hydrothermally after a reaction time of 120 min at different Fe^{3+}-PO_4^{3-} molar ratio of 31.5. (A) 120, (B) 140, (C) 180, (D) 200, (E) 220, and (F) 240 °C.[161] Reprinted (adapted) with permission from ref 161.

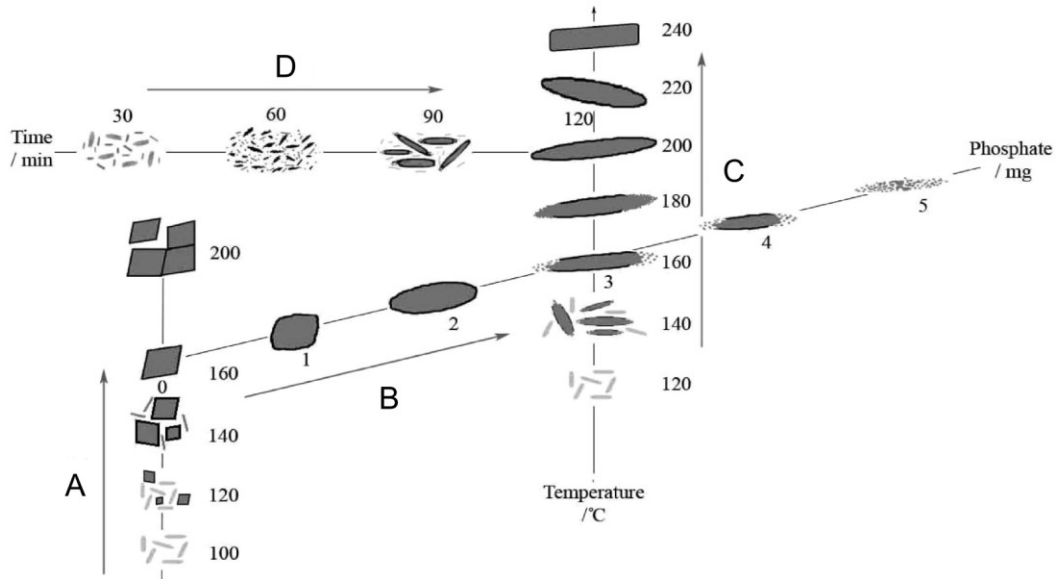

Figure 1-35: Schematic illustration of different shapes and phases evolution during hydrothermal synthesis using 0.2 mL of 45% pure $FeCl_3$ in 40 mL water, as a function of temperature, time, and phosphate concentration. (A) In this stage, β-FeOOH precipitation and dissolution is dominant and α-Fe_2O_3 precipitation will happen subsequently as a result of increase in hydrothermal synthesis temperature no surfactant is present in this stage; (B) By introducing PO_4^{3-} with different concentrations α-Fe_2O_3 shape changes at an hydrothermal synthesis processing temperature of 160 °C; (C) By increasing hydrothermal synthesis temperature at an Fe^{3+}-PO_4^{3-} molar ratio of 31.5, β-FeOOH precipitation and dissolution would occur and α-Fe_2O_3 nanorod will grow subsequently; (D) By increasing reaction time and keeping the temperature constant (200 °C), β-FeOOH precipitation and dissolution would occur and subsequently α-Fe_2O_3 nanorod will precipitate and grow.[161] Reprinted (adapted) with permission from ref 161.

Microwave heating provides yet another convenient approach for preparing iron oxide nanomaterials that offers short reaction times and good yields. Brachais *et al.* reported the microwave-assisted one-step hydrothermal synthesis of pure iron oxide nanoparticles and synthesized three major iron oxide phases: magnetite, maghemite, and hematite from alcohol/water solutions of chloride salts ($FeCl_2$ and $FeCl_3$) in the presence of sodium hydroxide.[162] This impressive control of crystal structure was achieved by rationally varying the ratio of Fe^{2+}/Fe^{3+}, NaOH and microwave treatment parameters including time and temperature. They showed that the synthesis realized with $FeCl_3$ as the single precursor led to the production of pure hematite phase. However, when $FeCl_2$ was used as the single precursor, magnetite or maghemite nanoparticles were produced depending on the drying process used. They also showed that pure maghemite phase could be synthesized in a very short time (6 min) using an ethanol/water mixture of chloride salts ($FeCl_2$ + $FeCl_3$). Also, they showed that size of particles could change depending on experimental conditions (Figure 1-36).[162]

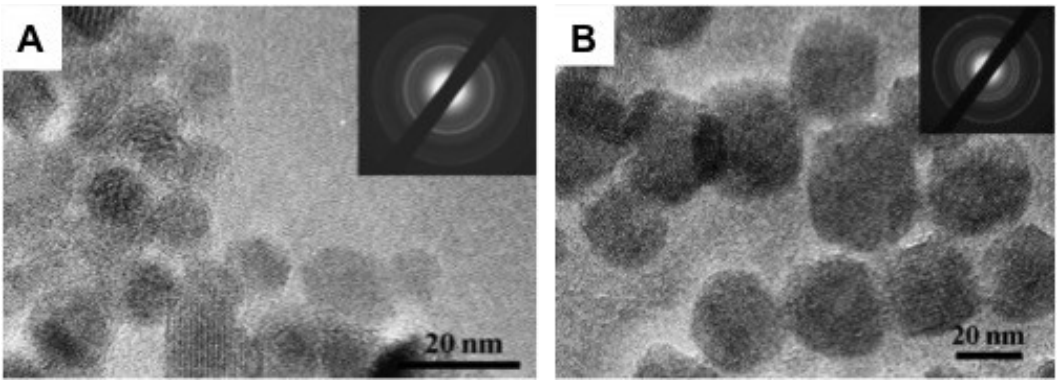

Figure 1-36: TEM images of nanoparticles synthesized *via* microwave-assisted hydrothermal method with different Fe^{2+}/Fe^{3+} molar ratios; (A) 1 (maghemite), (B) ∞ (magnetite or maghemite).[162] Reprinted (adapted) with permission from ref 162.

In 2011, Suib *et al.* also reported the synthesis of nanosized α-Fe_2O_3 powder *via* a microwave-assisted hydrothermal reaction of $Fe(NO_3)_3$ and urea at 120 °C for 30 min.[136] As shown in Figure 1-37, particles are about 5 nm in size and the lattice fringes are separated by ~0.25 nm. The as synthesized particles were further tested as catalyst for the oxidation of CO to CO_2.

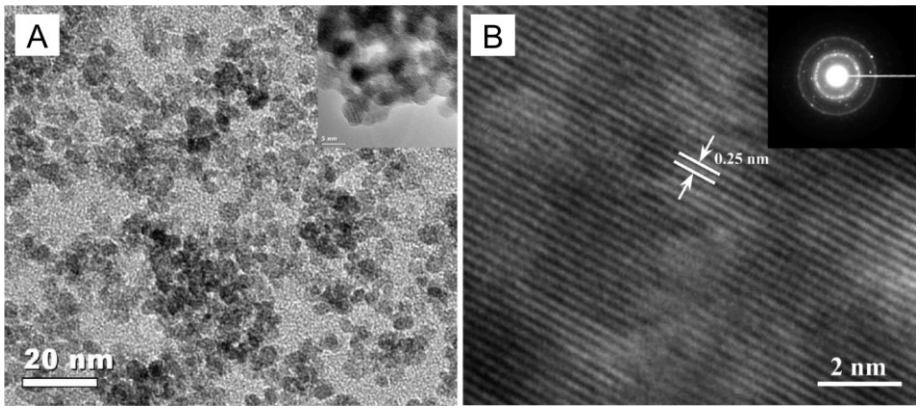

Figure 1-37: TEM images (A) and HRTEM image and SAED patterns (inset) (B) of the α-Fe_2O_3 powder synthesized *via* microwave-assisted hydrothermal method.[136] Reprinted (adapted) with permission from ref 136.

1.6 Gold Nanomaterials

Gold is a precious metal with a unique yellow color, but gold nanoparticles (d < 100 nm) properties, including color is distinct from their bulk counterpart. As early as the fourth century, gold flakes were introduced into glass to tailor optical properties – this is illustrated well by the Lycurgus Cup whose appearance varies depending on the angle of exposure to light (see Figure 1-38 A and B). This same type of coloring was employed in the preparation of stained glass for church windows (see Figure 1-38 C).[163] The first scientific report of the synthesis of gold nanomaterials was the work of Michael Faraday in 1857 where he provides an account of gold colloids produced by reduction of an aqueous solution of gold salt (*i.e.,* $HAuCl_4$) with phosphorus dissolved in carbon disulfide.[164] These colloids exhibited a ruby red color totally different from the known golden yellow color of

bulk gold (see Figure 1-38 D).[165] It is now known that these colloids can be engineered to show optical absorption properties spanning the entire visible spectrum (see Figure 1-38 E).[166]

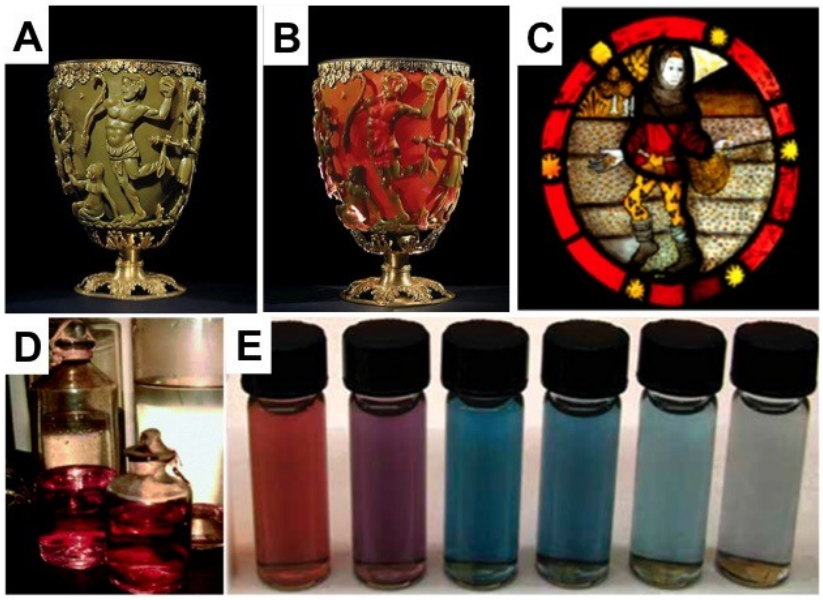

Figure 1-38: The Lycurgus Cup, (A) in reflected light, (B) in transmitted light. (C) Ancient church windows as indicated by the striking red stain containing Au nanoparticles, (D) aqueous suspensions of nanoparticles synthesized by Faraday, and (E) gold nanocages (size ~ 50 nm) with different gold percentage and as a result distinctive different colors.[163-166] Reprinted (adapted) with permission from refs 163, 164, 165 and 166.

1.6.1 Optical Properties of Gold Nanomaterials

In 1908, a German physicist named Gustav Mie proposed the characteristic red color observed by Faraday originated from the absorption and scattering of light by the gold nanoparticles (GNPs).[167] He suggested that when incident light hits GNPs, the free electrons of the gold (metal) are influenced by the electromagnetic field and will oscillate collectively relative to the lattice of positive ions at the same frequency as the incident light. This phenomenon is known as localized surface plasmon resonance (LSPR) (see Figure 1-39).[168,169]

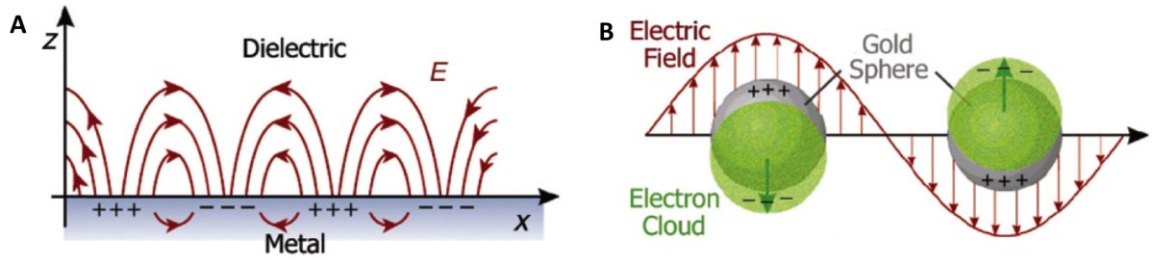

Figure 1-39: Pictorial illustration of the SPR for (A) a metal–dielectric interface and (B) a spherical GNP.[168,169] Reprinted (adapted) with permission from refs 168 and 169.

This phenomenon can occur in any nanomaterial containing a high density of free electrons (*e.g.,* metal nanoparticles, heavily doped semiconductors).[169–173] Two types of light-matter interactions are considered in this phenomenon: absorption and scattering. These two processes together lead to extinction (scattering +

absorption) or attenuation in intensity of the incident light. There are several parameters that influence the LSPR properties of gold nanostructures including the morphology (size and shape) and the environment surrounding the surface of the nanostructure.[170] When the dielectric constant of the medium is changed, the LSPR of the gold nanostructure will be shifted. As shown in Figure 1-38E, the LSPR peaks of these gold nanocage samples could be tuned from 450 to 1200 nm depending on the gold percentage. The ability to engineer gold properties by tuning the size, shape, and structure all without altering its elemental composition makes it an excellent example of a multifunctional nanomaterials.

Different synthetic methods have been developed to synthesize different morphologies of gold nanostructures. One of the most interesting one is gold nanorod that posses an anisotropic shape. The LSPR positions of these nanorods are highly sensitive to the aspect ratio.[174–176]

1.7 Thesis Outline

The work described in this thesis has four foci involving developing three different classes of nanomaterials based upon carbon, iron, and gold for catalysis applications. Chapter two focuses on the synthesis, characterization, and prototype application of N-doped carbon mesostructures obtained from the carbonization of polymerized dopamine. The as-synthesized N-doped carbon mesostructures exhibit high oxygen reduction (ORR) and oxygen evolution (OER) activities as well as

superior stability in alkaline electrolytes when compared with baseline Pt/C catalysts. The unique structures of the porous shell provide abundant active sites for oxygen adsorption and desorption and facilitate the diffusion of reactants during the catalytic processes. More importantly, when used as a bifunctional catalyst to construct an air electrode for ZAB, N-doped carbon mesostructures outperforms the state of-art Pt/C counterpart. The high surface area and N-doped active sites boost the diffusion-limiting current and long-term stability.

The other carbon precursor that has been used in this thesis work to prepare carbon nanostructures is cellulose nanocrystals (CNC). Chapter Three reports the synthesis of hollow carbon spheres (HCSs) prepared using nanocrystalline cellulose as carbon precursor, trisodium citrate as the mediator, and pluronic F127 as surfactant. The presented study provides the first example of using CNC as a carbon precursor to generate MPC hollow spheres. We demonstrate that the use of citrate and pluronic are necessary to make MPC using CNC as carbon precursor. The resulting structure was fully characterized and evaluated as catalyst for 4-nitrophenol reduction reaction.

Microwave irradiation heating methods are clean, cheap, and convenient that can solve the problem of inhomogeneity in heating. Moreover, microwave heating can enhance reaction rates and product yields in much shorter reaction time in comparison to conventional heating methods. Chapter Four reports the microwave-assisted synthesis of crystalline N-doped carbon coated Fe_3O_4 nanorods. The as-synthesized α-Fe_2O_3 nanorods are coated with dopamine as carbon

precursor and then are transferred to Fe_3O_4 coated with N-doped MPC *via* carbothermic reduction. The as-synthesized Fe_3O_4 nanorods coated with N-doped carbon are then evaluated as electrocatalyst for ORR.

Chapter Five reports the synthesis of gold nanorods of differing lengths *via* seed mediated method. The as-synthesized nanorods were then coated with porous and non-porous silica shells. Also, the synthesis of silica particles coated with gold nanoparticles is discussed and the catalytic activity of these particles is investigated for 4-nitrophenol reduction reaction.

Finally, Chapter Six outlines the significant advances resulting from the presented research and provides a brief outlook of possible future research directions and potential applications of as-synthesized nanomaterials.

Chapter 2:

Spherical Nitrogen-doped Hollow Mesoporous Carbon as an Efficient Bifunctional Electrocatalyst for Zn–air Batteries[1]

[1] A version of this chapter has been published:
Hadidi, L.; Davari, E.; Iqbal, M.; Purkait, T. K.; Ivey, D. G.; Veinot, J. G. C., *Nanoscale* **2015**, 7, 20547-20556.
Lida Hadidi and Elaheh Davari have made equal contribution to the work described in the published contribution.
The reported electrochemistry was performed by Davari, E.

2.1 Introduction

Recent estimates suggest that fossil fuels could be depleted this century if the rates of population growth, energy demand, and the associated exploitation of the energy stored in fossil fuels continue unchecked.[177] Energy storage systems play key roles in energy management because they mitigate the mismatch rate between energy supply and energy demand.[178]

Battery technology has made significant advances in recent years seeing new electrochemical systems and new battery materials being developed. To keep pace with developments in electronics and transportation demands, theoretical (and practical) limits regarding the amount of electrical energy that can be delivered by batteries must be addressed. Developing new batteries that meet all the requirements including availability, reasonable cost, safety and environmentally compatibility for a commercial product is the focus of battery research and development.[178]

Batteries are generally classified as primary (non-rechargeable) or secondary (rechargeable). The operation of a battery is relatively straightforward. During discharge, when the battery is connected to an external load, electrons flow from the anode to the cathode. Simultaneously in the electrolyte the flow of anions to the anode and cations to the cathode complete the circuit. Under a charging condition, this process is reversed.[178]

Of the available electrical storage technologies, secondary electrochemical batteries are one of the most reliable and efficient. To date, Li-ion batteries (LIBs) have dominated the market; however, their low theoretical energy density (*ca.* 400 Wh kg^{-1}) is insufficient to meet the demands of large-scale applications such as electric vehicles. Metal–air batteries, such as Zn-air batteries (ZABs), offer a promising alternative boasting theoretical energy densities of up to 1084 Wh kg^{-1}.[179] Adding to the appeal of ZABs, the cost to manufacture them is approximately two orders of magnitude lower than LIBs partly because working with Zn is more straightforward than working with Li. In addition, because ZABs employ an air-breathing cathode the weight of the cell is decreased.

Metal-air batteries (*e.g.,* ZABs) produce electricity via a redox reaction of metallic anode with oxygen in air.[179–181] Figure 2-1 illustrates the processes involved in the operation of a typical ZAB.[182] The battery consists of three components: Zn metal anode, air electrode cathode, and a separator. The air-cathode consists of a gas diffusion layer and a catalytic active layer. The pressure difference between the interior and exterior of the cell promotes diffusion of atmospheric oxygen into the electrode.

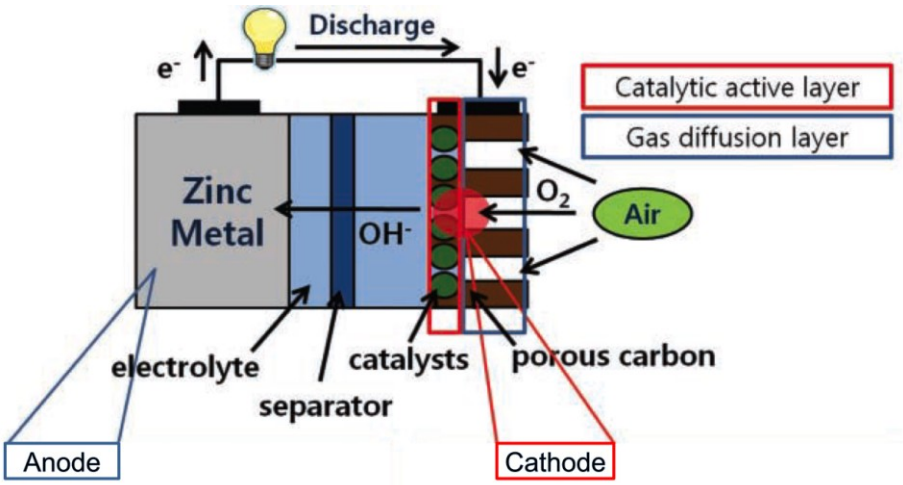

Figure 2-1: A pictorial representation of a typical ZAB. The red circle highlights the location where reaction between oxygen, catalyst and electrolyte occurs.[182] Reprinted (adapted) with permission from ref 182.

The general electrochemical reactions occuring in alkaline solution ZAB are summarized below:

Anode:

$$Zn \longrightarrow Zn^{2+} + 2e^- \quad (2\text{-}1)$$

$$Zn^{2+} + 4OH^- \longrightarrow Zn(OH)_4^{2-} \quad (E^o = -1.25 \text{ V } vs. \text{ NHE}) \quad (2\text{-}2)$$

$$Zn(OH)_4^{2-} \longrightarrow ZnO + H_2O + 2OH^- \quad (2\text{-}3)$$

Cathode:

$$O_2 + 2H_2O + 4\bar{e} \longrightarrow 4OH^- \quad (E^o = 0.4 \text{ V } vs. \text{ NHE}) \quad (2\text{-}4)$$

Overall:

$$2Zn + O_2 \longrightarrow 2ZnO \quad (E^o = +1.65 \text{ V}) \quad (2\text{-}5)$$

Despite their aforementioned benefits of ZABs, a major hurdle in realizing optimized devices is the development of highly active bifunctional electrocatalysts that facilitate oxygen reduction and oxygen evolution reactions (ORR/OER) at the cathode.[181] While the equilibrium potential of a ZAB is 1.65 V (Equation 2-5) there is a large overpotential to generate hydroxide ions (Equation 2-4) lowering the working voltage of the cell. New electrocatalysts can help address this limiation.[179]

Currently, the most efficient ORR and OER catalysts are based upon Pt and Ir, respectively.[181] Unfortunately noble metals are scarce and costly; clearly, the development of cost-effective precious metal-free bifunctional electrocatalysts is of paramount importance to the advancement and wide scale use of metal–air batteries.[182–184] Carbon is an ideal electrocatalyst;[185] it is electronically conductive, resistant to corrosion, straightforward to modify, easily separated from catalytic metals, abundant, and cost-effective. Many carbon systems, including porous carbon,[186–188] graphite nanofibers (GNFs), and carbon nanotubes (CNTs),[189,190] have been explored as catalysts for ORR and oxidation of small organic molecules (*e.g.,* alcohol and ether).[185]

Despite the potential of these materials, there is continued interest in developing durable cost-effective catalysts exhibiting high activity. Porous carbon has received substantial attention because of its high surface area and physicochemical properties (*e.g.,* electronic conductivity, thermal conductivity, chemical stability, and low density).[24] As a result, its potential applications are far reaching and include support materials for catalytic processes, sorbents for

separation processes, gas storage, and purification, as well as electrode materials for batteries, fuel cells, and supercapacitors.[191] Porosity is one of the most important attributes of these carbon materials because it dictates surface area and facilitates mass transport.[192]

Mesoporous carbon (mC) is often preferred for electrochemical applications because of its comparatively high surface area and efficient ion mass transport.[192] Common synthetic approaches for preparing mC have been discussed in detail in Chapter 1, Section 1.4. Doping of carbon nanostructures with N can induce/improve favorable properties (*e.g.*, catalytic activity and conductivity).[66,70,193,194] Of particular note here, nanostructures of N-doped carbon frequently exhibit enhanced bifunctional catalytic activity with and without metals.[72–74,195] Although the exact catalytic mechanism remains the subject of debate, it has been proposed that N within carbon nanostructures influences catalytic properties because N decreases the material band gap facilitating higher electron (charge) mobility and affords a lower work function at the carbon/liquid (gas) interface.[70] Doping carbon nanostructures with N can be achieved during (*in situ*) or following preparation via post treatment with N-containing species (*e.g.*, N_2 and NH_3).[185] Polydopamine (PDA) is a biomimetic adhesive polymer and an excellent carbon source that affords direct N-doping.[196] The general polymerization of dopamine has been outlined in Chapter 1, Section 1.4.3. Of particular interest for ZABs solid sub-micrometer carbon spheres fabricated using PDA show excellent thermal stability as well as ORR catalytic activity.[197]

In this chapter, a facile method that affords high surface area, hollow N-doped mesoporous carbon (HMC) is presented. These well-defined carbon shells show comparable ORR/OER catalytic activity to that of the commercial 40 wt% Pt/C catalysts. The presented materials exhibit a high electron transfer number (~ 4) and high ORR stability when compared with the baseline materials. Furthermore, ZAB performance of metal-free N-doped HMC outperforms the Pt/C catalyst over repeated charge–discharge cycling. In addition, N-doped HMC synthesized in this study could act as a general building block for fabricating other transition metal–HMC hybrid materials as bifunctional electrocatalysts for metal–air batteries.

2.2 Experimental

2.2.1 Reagents and Materials

Dopamine hydrochloride, pluronic F127, 2-amino-2-hydroxymethyl-propane-1,3-diol (Tris), hexadecyltrimethylammonium bromide (CTAB) (≥99%), and tetraethoxysilane (TEOS) (≥99%) were purchased from Sigma-Aldrich and used as received. Ammonium hydroxide (30%) was purchased from Caledon Laboratories. Electronic grade hydrofluoric acid (HF, 49% aqueous solution) was purchased from J. T. Baker. Pt/C (40%), Nafion solution (5% w/w in water), and 1-propanol (99.99%) were purchased from Alfa Aesar. Potassium hydroxide was purchased from Fisher and used as received. Carbon-coated, 200-mesh Cu grid was purchased from Electron Microscopy Sciences.

2.2.2 Preparation of Stöber Silica Spheres

Spherical silica particles were prepared via the Stöber method using tetraethoxysilane (TEOS) as the silica source.[198] For a typical synthesis, 40 mL of 0.2 M TEOS was added to a solution of 50 % ethanol (80 mL) and ammonium hydroxide (28 %, 4 mL) and stirred for 3 hours at ambient temperature. The solution was centrifuged three times at 10000 rpm for 30 min to collect the particles and upon drying a white powder was obtained.

2.2.3 Synthesis of silica@mC Particles

For a typical synthesis, 15 mg of Stöber silica (170 ± 10%), 7.5 mg (6×10^{-4} mmole) of triblock copolymer pluronic F127, and 2-amino-2-hydroxymethyl-propane-1,3-diol (Tris) (4.5 mg; 0.04 mmole) were dispersed/dissolved in deionized water (4 mL). Subsequently, dopamine hydrochloride (15 mg; 0.01 mmole) was added and the mixture followed by stirring at room temperature for 24 hours. The resulting polydopamine coated silica particles were collected by centrifugation at a speed of 10000 rpm for 30 min. The particles were washed three times using ethanol (25 mL) and dried under vacuum. The resulting black powder was placed in a quartz boat in a tube furnace and heated to 400 °C (heating rate of 1 °C min^{-1}) and the peak temperature was maintained for 2 h. The temperature was subsequently raised (heating rate of 5 °C min^{-1}) to 800 °C, maintained for 3 h and then the sample was cooled to room temperature.[199] All heating and cooling were performed in flowing Ar.

2.2.4 Synthesis of Hollow Mesoporous Carbon Particles (HMC)

As-synthesized silica@mC particles (*ca.* 0.2 g) were placed in a polyethylene terephthalate (PET) beaker. Water (2 mL), ethanol (2 mL), and aqueous 49% HF (2 mL) were subsequently added sequentially and the mixture was stirred for 1 h at room temperature. (Caution! HF is dangerous and must be handled with extreme care). The particles were recovered via vacuum filtration and washed with water (60 mL) and ethanol (60 mL). The resulting black powder was finally dried under

vacuum. The HMC product was characterized using transmission and scanning electron microscopy (TEM and SEM), Raman and infrared (IR) spectroscopy, X-ray photoelectron spectroscopy (XPS), and N_2 adsorption/desorption measurements.

2.2.5 Preparation of Polydopamine Beads (PDA)

Dopamine (0.3 mg mL^{-1}) was dissolved in Tris-HCl buffer (10 mM and pH = 8.8) and the resulting solution was stirred for 12 h. The black suspension was centrifuged at 14000 rpm for 30 min. The clear supernatant was decanted and discarded. The black precipitate was washed three times in water (~60 mL) with sonication followed by recovery by centrifugation. Finally, the sample was dried under vacuum and heated in an Ar atmosphere in a tube furnace, as outlined for the silica@mC particles (*vide supra*).

2.2.6 Electrochemical Measurements

All electrochemical measurements were performed using a Bio-Logic SP-300 potentiostat/galvanostat. Linear sweep voltammetry (LSV) half-cell experiments were performed using a rotating disc electrode (RDE) (Pine Instruments Co, AFMSRCE). A three-electrode cell configuration was employed with a catalyst coated glassy carbon (5 mm diameter) working electrode, Pt coil counter electrode, and Hg/HgO (1 M NaOH, 0.098 V *vs.* NHE at 25 °C) reference electrode. The electrolyte used for all measurements was a 0.1 M KOH aqueous solution. It has been shown that there are sub-ppm levels of Fe in KOH electrolyte that might interfere the

performance of the catalyst.[200] Although not done in this work, trace Fe can be removed from KOH electrolyte using high-purity $Ni(OH)_2$ as Fe absorbent. More details about this procedure can be found in Boettcher *et al.* report.[200] A catalyst "ink" was prepared by ultrasonic mixing of 20 mg of the catalyst of choice, 2 ml of 5 % Nafion solution (5% w/w in water and 1-propanol dispersion, ≥ 0.92 meq g^{-1} exchange capacity), and 1-propanol for 30 min. A 5 μL aliquot of the "ink" was drop coated on a glassy carbon disc and dried in air to yield a film with catalyst loading of 0.10 mg cm^{-2}. CV was performed at a scan rate of 10 mV s^{-1} in Ar and O_2-saturated electrolytes. The Ar-saturated electrolyte was prepared by purging a 0.1 M KOH aqueous solution with high purity (i.e., > 99.99%) Ar for 20 min. After testing, the solution was purged with O_2 (> 99.5%) for 10 min at a constant flow rate. In this work, the onset potential is defined as the potential at which the current density is 10% of that at the potential of −0.4 V for ORR and 0.65 V for OER in LSV curves at 1600. LSV curves were obtained using a rotating working electrode at predefined rotation rates (400, 900, 1600, and 2500 rpm) and a scan rate of 10 mV s^{-1}.

The ZAB was assembled with a laboratory made Zn–air cell using an air cathode with HMC or commercial Pt/C (40% Pt) as the catalyst. The battery performance was evaluated at ambient air conditions without introducing an additional O_2 source. A polished Zn plate was used as the anode and 6 M KOH (containing 2 % ZnO to facilitate the reversible Zn electrochemical reactions by forming zincate ions; $Zn(OH)_4^{2-}$) was used as the electrolyte. The current density used for battery testing was normalized to the geometric surface area of the catalyst film. The charge–

discharge pulse cycling was tested by the galvanic pulse method using an applied current of 10 mA with each cycle consisting of 5 min discharge followed by 5 min charge for 102 cycles.

2.2.7 Materials Characterization and Instrumentation

FT-IR was performed on a Nicolet Magna 750 IR spectrometer by drop coating an ethanol dispersion of particles on a piece of Si wafer. Raman spectroscopy Raman spectra of the particles were measured with a Renishaw inVia Raman microscope. The excitation wavelength was 514 nm. Samples were prepared by mounting the powder on aluminum foil.

Conventional transmission electron microscopy was performed using a JEOL 2010 TEM equipped with a LaB6 thermionic emission filament operated at an accelerating voltage of 200 kV. Samples for TEM analysis were prepared by placing a drop of a dilute ethanol suspension of the material of interest onto a carbon-coated, 200-mesh Cu grid and drying at room temperature. High-resolution (HR) TEM images were acquired using a Hitachi-9500 TEM operated at an accelerating voltage of 300 kV and processed using Image J software (version 1.48v).

Scanning electron microscopy (SEM) was carried out with a JEOL 6301F field emission SEM operated at an acceleration voltage of 5 kV. Samples were prepared by drop casting samples of choice from dilute ethanol suspensions onto a clean Si (100) wafer.

X-ray photoelectron spectroscopy (XPS) was performed using a Kratos Axis Ultra instrument with a monochromatic Al Kα source (λ = 8.34 Å) with an energy hν = 1486.6 eV. Survey spectra were collected with analyzer pass energy of 160 eV and a step size of 0.3 eV. For high-resolution spectra, the pass energy was 20 eV and the step size was 0.1 eV with a dwell time of 200 ms. The base pressure in the sample analytical chamber was lower than 1 Å ~ 10−9 Torr. Binding energies were calibrated by using the C 1s peak as a reference (284.6 eV). CASA XPS Version 2.3.13 software was used to accomplish the background subtraction and curve fitting.

Nitrogen adsorption–desorption isotherms were measured at −196 °C with a Quantachrome Autosorb-1 adsorption analyzer. Prior to adsorption measurements, samples were degassed at 250 °C under vacuum for 2 h. The data were analyzed using Brunauer–Emmett–Teller (BET) theory and Barret-Joyner-Halenda (BJH) method.[201] The specific surface area was determined from the linear portion of the BET data and the total pore volume was calculated from the amount adsorbed at a relative pressure of about P/P_o = 0.995. The pore size was determined using BJH method.

2.3 Results and Discussion

HMC, silica@mC, and PDA beads were prepared using straightforward dopamine polymerization followed by carbonization. The resulting structures were characterized and evaluated as bifunctional electrocatalysts in alkaline solution. Stöber silica particles templates used in the present study were prepared by exploiting standard sol–gel processing. As-synthesized Stöber silica particles (diameter = 170 nm ± 10%) were coated with dopamine and triblock copolymer PEO–PPO–PEO (F127); this layer was polymerized under basic conditions.[202] Finally, the polymer layer was carbonized upon heating in Ar at 400 °C for 2 h and at 800 °C for 3 h. Figure 2-2 shows representative electron microscopy images of coated Stöber silica particles before and after carbonization. After heating at 800 °C (Figures 2-2 B and D) the particle structure remains intact. PDA beads (d = 121 μm ± 28%; Figure 2-6) were also prepared via oxidative polymerization of dopamine in a Tris-HCl buffer solution.[202,203] Carbonization was achieved using the same conditions outlined for HMC (*vide supra*).

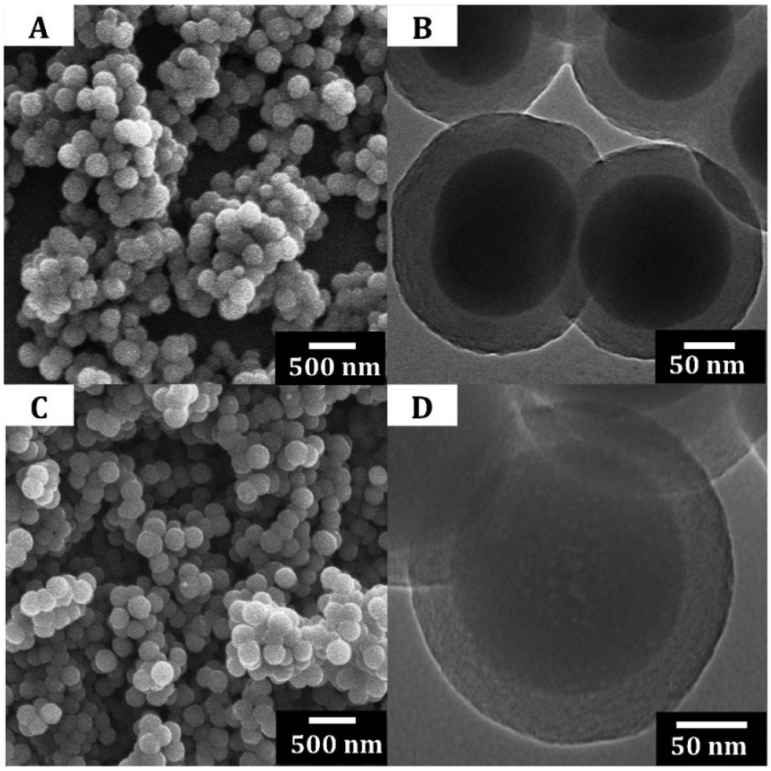

Figure 2-2: Secondary electron SEM images of coated silica before (A) and after (C) carbonization. Bright field TEM images of carbon-coated silica before (B) and after (D) carbonization.

The shell thickness after carbonization is ca. 21 nm ± 28%. Etching with alcoholic hydrofluoric acid provided a convenient method for removing the silica template. Consistent with a porous structure (*vide infra*), one hour of etching provided hollow uniformly shaped hollow mesoporous spheres (Figures 2-3 A and B). EDX and XPS analysis suggests these spheres contain trace of silica (See Figures

2-4 and 2-5). Evaluation of the carbon shells using high resolution TEM (HRTEM) revealed graphitic (Figures 2-3 C and D) and amorphous domains.

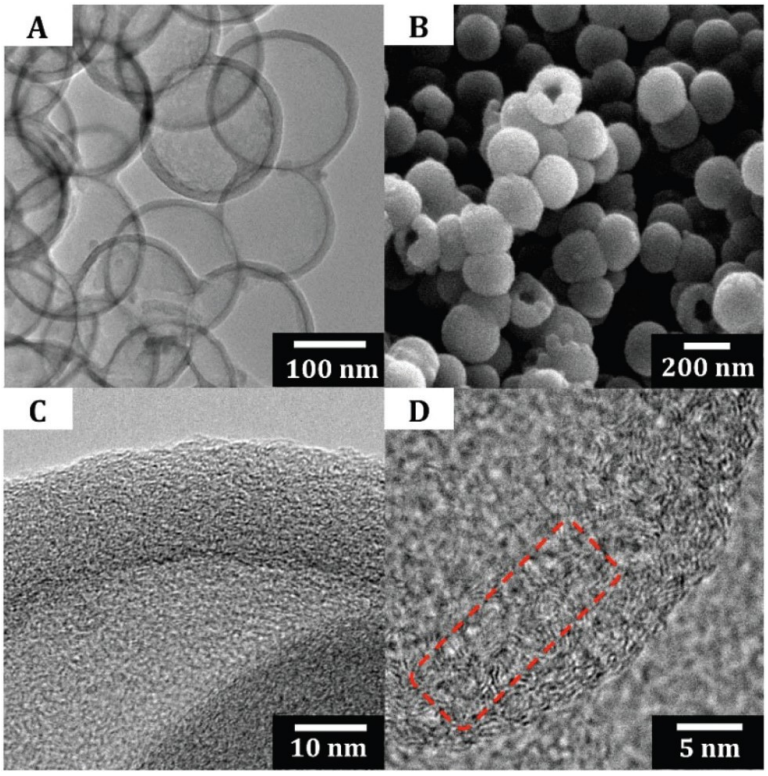

Figure 2-3: (A) Bright field TEM image of HMC. (B) Secondary electron SEM image of HMC. (C) and (D) HR-TEM images of HMC.

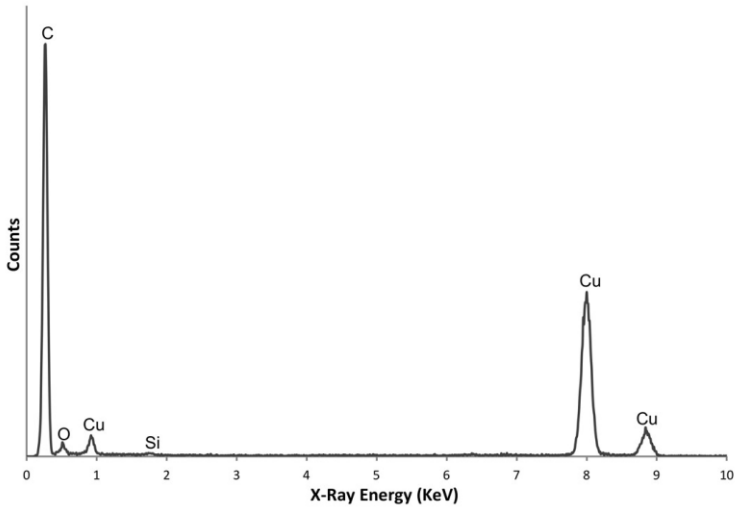

Figure 2-4: Energy dispersive X-ray spectrum for HMC.

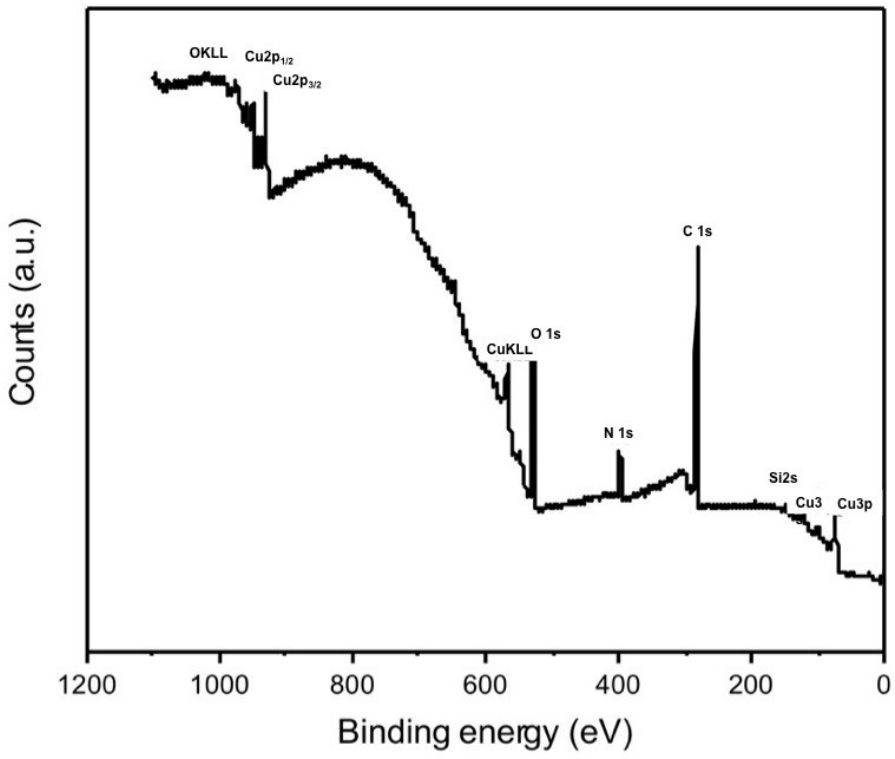

Figure 2-5: XPS survey spectrum for HMC.

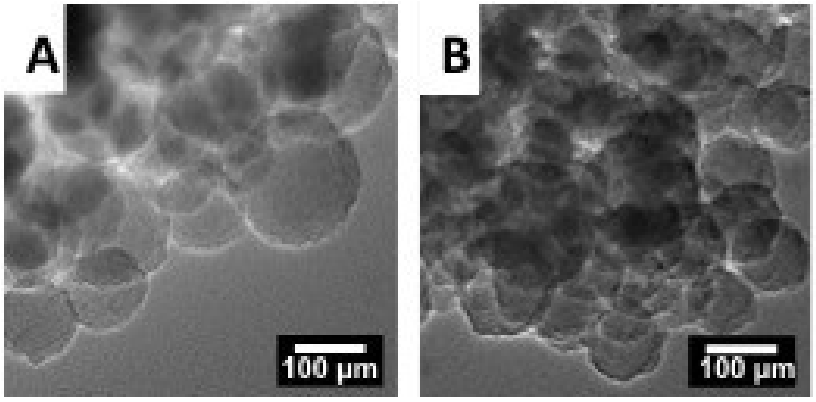

Figure 2-6: TEM bright field images of polydopamine beads (A, B).

The present carbonaceous materials were further characterized using XPS, FTIR, and Raman spectroscopy. The N 1s XPS spectra provide insight into the environment of the N atoms in silica@mC, HMC, and PDA beads. Representative spectra for silica@mC and HMC are shown in Figure 2-7; peak deconvolution indicates two components centered at 398.2 and 400.3 eV, corresponding to pyridinic N and pyrrolic N, respectively. Similar analysis of PDA beads shows pyrrolic N with only minor contributions from pyridinic N approaching the sensitivity limits of the XPS method. Speciation of the N content in silica@mC, HMC, and PDA beads is summarized in Table 2-1. The survey XP spectrum showed no evidence of metals at the sensitivity of this method. The Cu signal observed in the spectrum arises from the sample substrate (Figure 2-5).

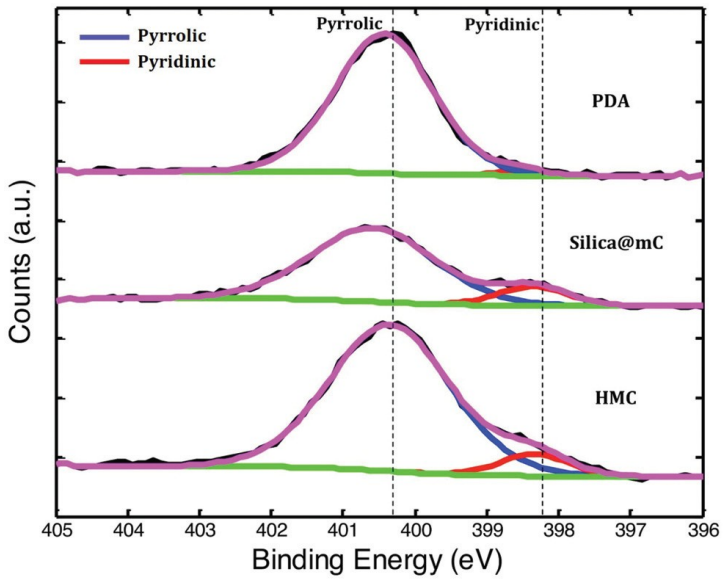

Figure 2-7: Representative high-resolution XP spectra of N 1s region for PDA beads, silica@mC, and HMC.

Table 2-1: Relative atomic ratio of nitrogen species for HMC, silica@mC, and PDA beads

Catalyst	N content (at %)	Pyridinic N (at %)	Pyrrolic N (at %)
HMC	7.08	0.58	6.5
Silica@mC	4.34	0.56	3.80
PDA beads	4.90	0.08	4.81

FTIR spectra for PDA beads, silica@ mC, and HMC are shown in Figure 2-8. The PDA beads spectrum shows an absorption at 2921 cm^{-1}, which is assigned to C–H stretching modes. Another feature at 1431 cm^{-1} arising from heterocyclic

stretching (C–N bonds).[202] The peak at 1161 cm^{-1} is the result of heterocyclic N–H in-plane deformation breathing.[202] In addition, a feature associated with C–N bending is found at ca. 1500 cm^{-1} and appears to be merged with the heterocyclic stretching feature at 1431 cm^{-1}.[202] The peak at 3800 cm^{-1} is due to the O-H stretch of water. The IR spectrum for silica@mC shows a strong band at 1103 cm^{-1}, which is assigned to the Si–O–Si stretching mode. As expected, this feature is not obvious after HF etching (HMC). A feature associated with C–N bending is observed for silica@mC and HMC at ca. 1570 cm^{-1}.

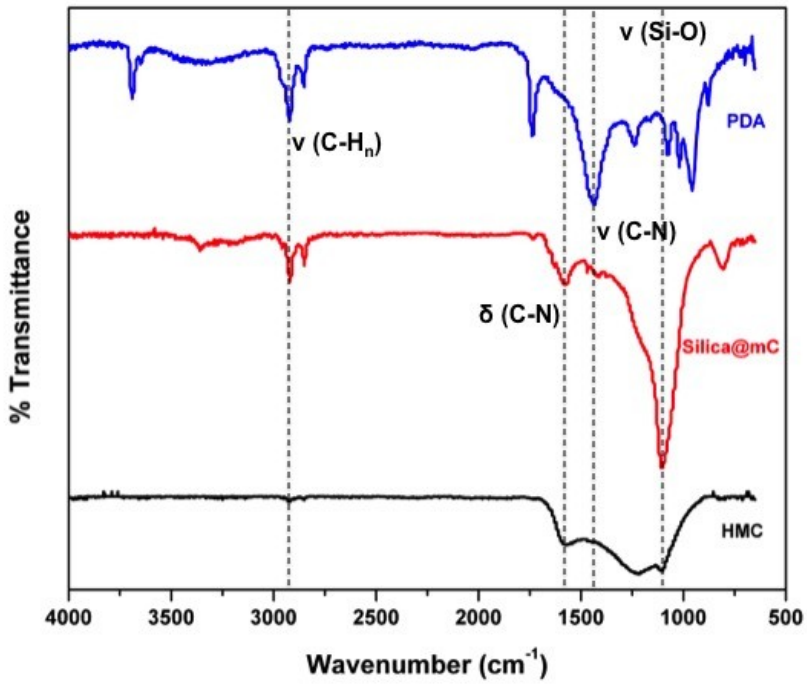

Figure 2-8: FTIR spectra for PDA beads, silica@mC, and HMC.

The Raman spectra for silica@mC, HMC, and PDA beads (Figure 2-9) show two features at 1331 and 1578 cm^{-1} that correspond to the D band and G band, respectively. The D band arises from the A1g breathing mode from sp^3 carbon components, while the G peak corresponds to in-plane stretching of bonds involving sp^2 carbon atoms.[202] Based upon these observations and the HR-TEM data (*vide supra*), we conclude that all the present materials contain a mixture of graphitic and amorphous carbon.

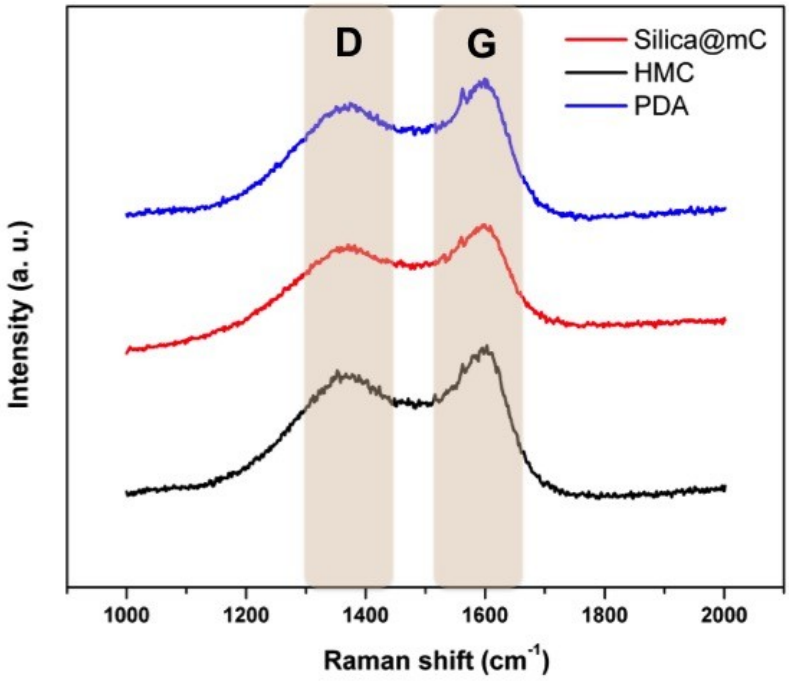

Figure 2-9: Raman spectra for PDA beads, silica@mC, and HMC.

Nitrogen sorption analysis was used to evaluate the specific surface area, pore volume, and average pore diameter of the silica@mC, HMC, and PDA beads. The corresponding isotherms (Figures 2-10, 2-11, and 2–12) show a distinct hysteresis loop at high relative pressure, consistent with mesoporous materials as defined by IUPAC.[199] Analysis of HMC indicates it possesses porosity consisting of uniformly sized mesopores (*ca*. 30 nm). Silica@mC and PDA beads show pore sizes of about 50 nm and 10 nm, respectively. Of the three materials, HMC exhibits the highest BET surface area (*i.e.,* 340 $m^2 g^{-1}$) and pore volume (2.5 $cm^3 g^{-1}$) followed by silica@mC and then PDA beads (Table 2-2).

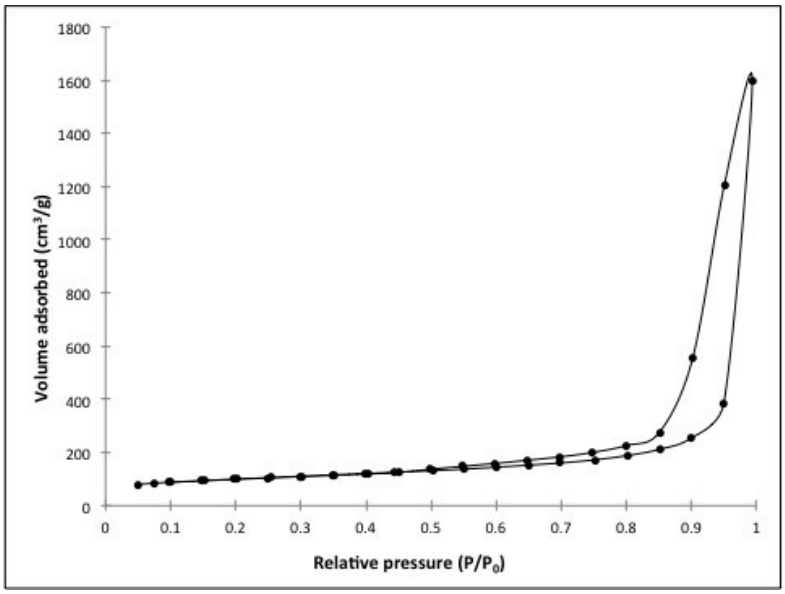

Figure 2-10: Nitrogen adsorption-desorption isotherms for HMC.

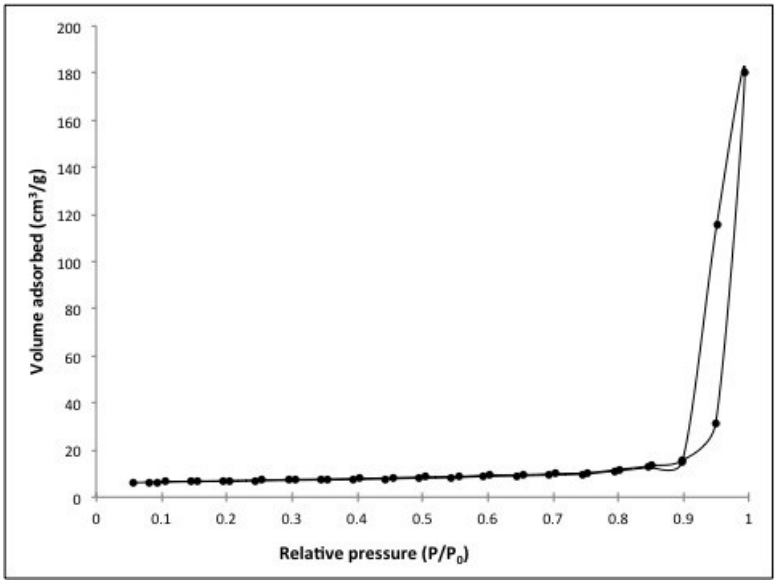

Figure 2-11: Nitrogen adsorption-desorption isotherms for silica@mC spheres.

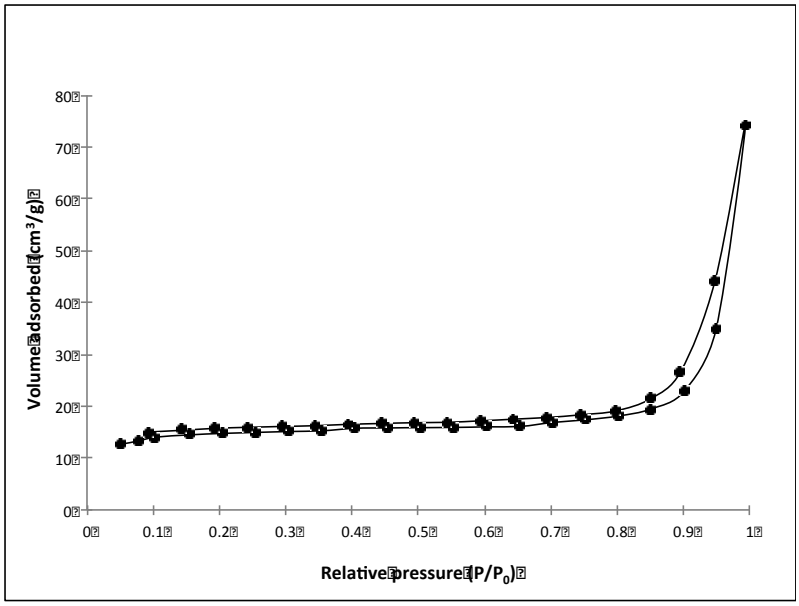

Figure 2-12: Nitrogen adsorption-desorption isotherms for polydopamine beads.

Table 2-2: Textural properties of HMC, silica@mC and PDA beads.

Catalyst	BET surface area ($m^2 g^{-1}$)	Pore diameter (nm)	Pore volume ($cm^3 g^{-1}$)
HMC	340	30	2.5
Silica@mC	22	50	0.28
PDA beads	45	10	0.10

The ORR catalytic activity of HMC was explored using a conventional three-electrode system within Ar- or O_2-saturated 0.1 M KOH as the electrolyte. Cyclic voltammetry (CV) experiments were performed after removal of dissolved oxygen from the solution. The CV curve for HMC (Figure 2-13) shows a featureless capacitive current in the Ar-saturated electrolyte. After purging the electrolyte solution with O_2, an irreversible cathodic current at −0.23 V, indicative of ORR occurring at the HMC surface, appears.

To evaluate the ORR performance of HMC, linear sweep voltammetry (LSV) was conducted from −0.8 to 0.05 V *vs*. Hg/HgO using predefined electrode rotation rates (400, 900, 1600, and 2500 rpm) and a scan rate of 10 mV s^{-1} in O_2-saturated 0.1 M KOH solution (Figure 2-14 A). LSV curves for silica@mC and PDA beads are shown in Figures 2-15 A and Figure 2-16 A. In both cases the $E_{1/2}$ (half-wave potential) shifted to more positive values in comparison to that of HMC. This shows higher ORR overpotential for silica@mC and PDA beads, which results in slower kinetic and probably mixed two and four electron transfer ORR reaction path. As presented in table 3, the number of electron transfer is smaller for silica@mC and

PDA as opposed to baseline Pt/C and HMC.

The ORR polarization curve for HMC can be divided into three regions: i) kinetically controlled (*ca.* −0.1 to −0.3 V), ii) kinetic–diffusion controlled (*ca*. −0.3 to −0.6 V), and iii) mass diffusion controlled (less than −0.6 V) (Figure 2-14 A). ORR is commonly evaluated using Koutecky–Levich (K–L) plots (Figure 2-14 B).[204]

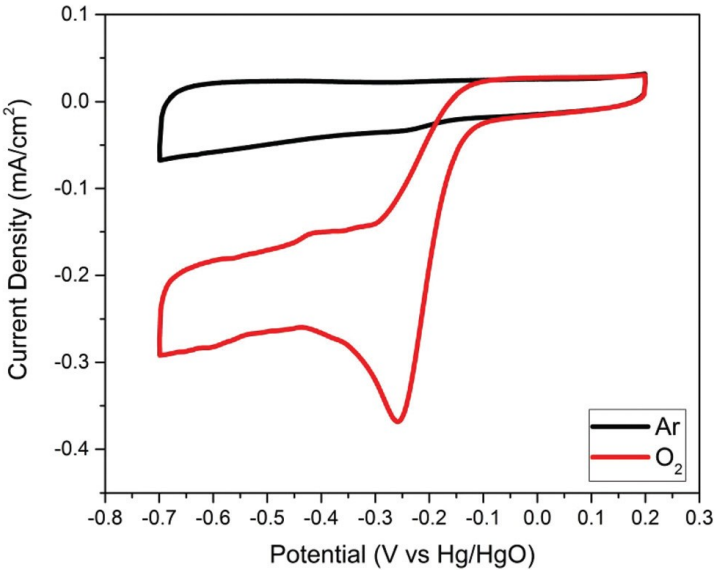

Figure 2-13: Cyclic voltammograms for HMC in Ar- (black trace) and O_2- (red trace) saturated 0.1 M KOH with a scan rate of 10 mV s^{-1}.

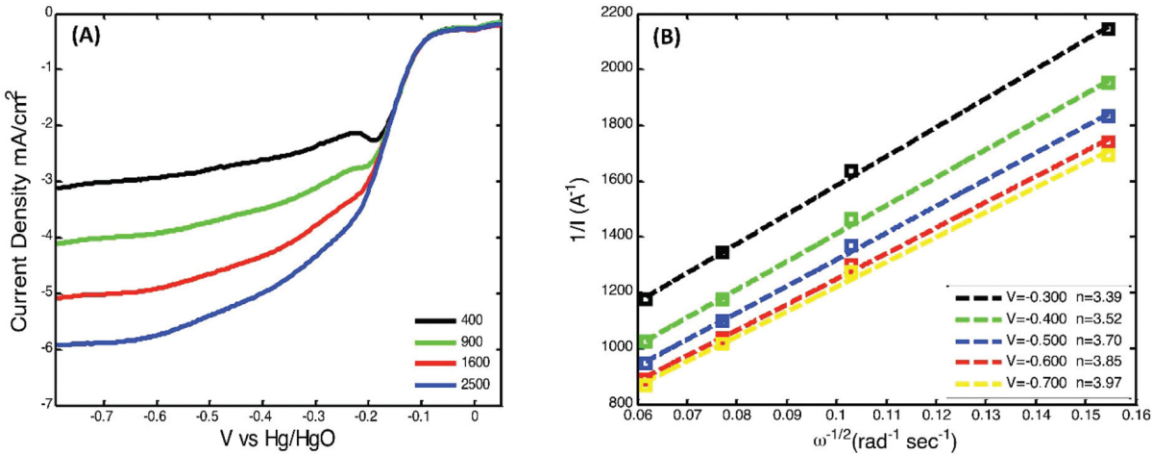

Figure 2-14: (A) ORR LSV curves for HMC in an O_2-saturated 0.1 M KOH solution at indicated rotational rates and a scan rate of 10 mV s^{-1}. (B) K–L plots for HMC in the potential range of −0.3 to −0.7 V *vs.* Hg/HgO.

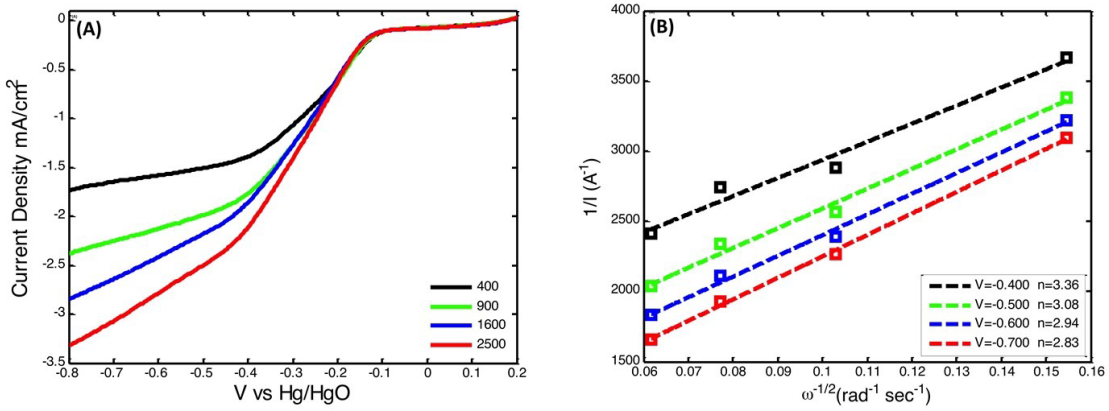

Figure 2-15: (A) LSV curves for silica@mC in an O_2-saturated 0.1 M KOH solution at indicated rotational rates and a scan rate of 10 mV s^{-1}. (B) K-L plots for silica@mC in the potential range of -0.3 to -0.7 V *vs.* Hg/HgO.

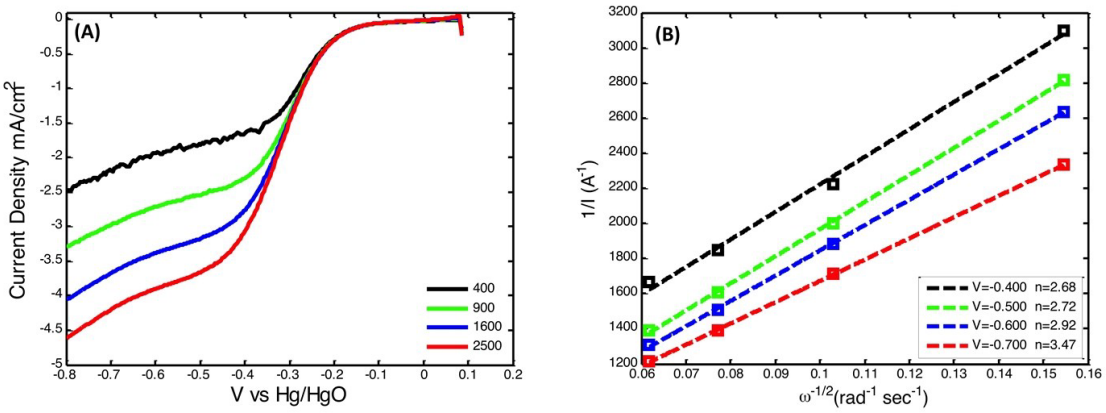

Figure 2-16: (A) LSV curves for PDA beads in an O_2-saturated 0.1 M KOH solution at indicated rotational rates and a scan rate of 10 mV s^{-1}. (B) K-L plots for PDA beads in the potential range of -0.3 to -0.7 V *vs.* Hg/HgO.

The overall current density can be separated into diffusion and kinetic currents by applying the K–L equations:[205]

$$\frac{1}{j} = \frac{1}{j_k} + \frac{1}{j_l} = \frac{1}{B\omega^{1/2}} + \frac{1}{j_k} \qquad (2\text{-}6)$$

$$B = 0.62nFC_o(D_o)^{2/3}\nu^{-1/6} \qquad (2\text{-}7)$$

$$j_k = nFkC_o \qquad (2\text{-}8)$$

where, j, j_k, and j_l are the measured, kinetic-, and diffusion-limiting current densities, respectively, ω is the angular velocity of the electrode (ω = 2πN, N is the linear rotation), n is the number of electrons transferred during ORR, F is the Faraday constant (F = 96,485 $Cmol^{-1}$), C_o is the bulk concentration of O_2 ($C_o = 1.2 \times 10^{-3}$ mol L^{-1}), D_o is the diffusion coefficient of O_2 in the KOH electrolyte ($D_o = 1.9 \times 10^{-5}$ cm^2 s^{-1}), ν is the kinematic viscosity of the electrolyte (ν = 0.01 cm^2 s^{-1} in 0.1 M KOH),

and *k* is the electron-transfer rate constant. The limiting current density increases with oxygen flux to the electrode surface. Consistent with first-order kinetics of ORR with respect to the concentration of dissolved O_2, the *K–L* plots for HMC (Figure. 13B) show linear relationships for I^{-1} as a function of $(\omega)^{-1/2}$. The non-zero intercept shows that O_2 reduction is under kinetic control.

Oxidation–reduction in alkaline solutions proceeds by an indirect two-electron (equations (2-9) and (2-10)) or a direct four-electron pathway (equation (2-11)),[204] with the following simplified overall reactions:

$$O_2 + H_2O + 2\bar{e} \longrightarrow HO_2^- + OH^- \quad (2\text{-}9)$$

$$HO_2^- + H_2O + 2\bar{e} \longrightarrow 3OH^- \quad (2\text{-}10)$$

$$O_2 + 2H_2O + 4e^- \longrightarrow 4OH^- \quad (2\text{-}11)$$

Applying the *K–L* relationships to the present systems yields the number of electrons transferred (*n*) as *ca.* 4 for the potentials investigated. The electron transfer number increases at more negative potentials, which indicates the further reduction of hydrogen peroxide (equation (2-10)) to hydroxide in this potential range. These results indicate the electrocatalytic process of HMC proceeds *via* the four-electron mechanism and is appropriate for ORR.[206]

The ORR LSV curves for the candidate catalysts, obtained at 1600 rpm, are shown in Figure 2-17 A. The catalysts were initially cycled 40 times at 10 mV s^{-1} in 0.1 M KOH O_2-saturated electrolyte in order to stabilize the system. HMC shows the highest ORR kinetic-limiting current density (−4.95 mA cm^{-2}) of the carbon-based catalysts investigated. This value exceeds the current density for Pt/C (−4.39 mA

cm^{-2}), which is the benchmark catalyst for ORR. The ORR onset potential for HMC (*ca.* −0.055 V) is the most positive of the catalysts studied in this work and is ca. 54 mV more negative than the ORR onset potential for commercial 40% Pt/C (ca. 0.001 V). The ORR onset potential and current density of the HMC particles is superior to that of other mesoporous carbons (*ca.* −0.06 V, 1.7 mA cm^{-2}).[207] The half-wave potential ($E_{1/2}$) (the potential where the current density reaches half the limiting current), provides insight into the capability of catalysts to decrease the ORR overpotential. The $E_{1/2}$ for HMC is only 170 mV more negative than that of 40% Pt/C. From this data, we conclude that HMC exhibits excellent electrocatalytic activity.

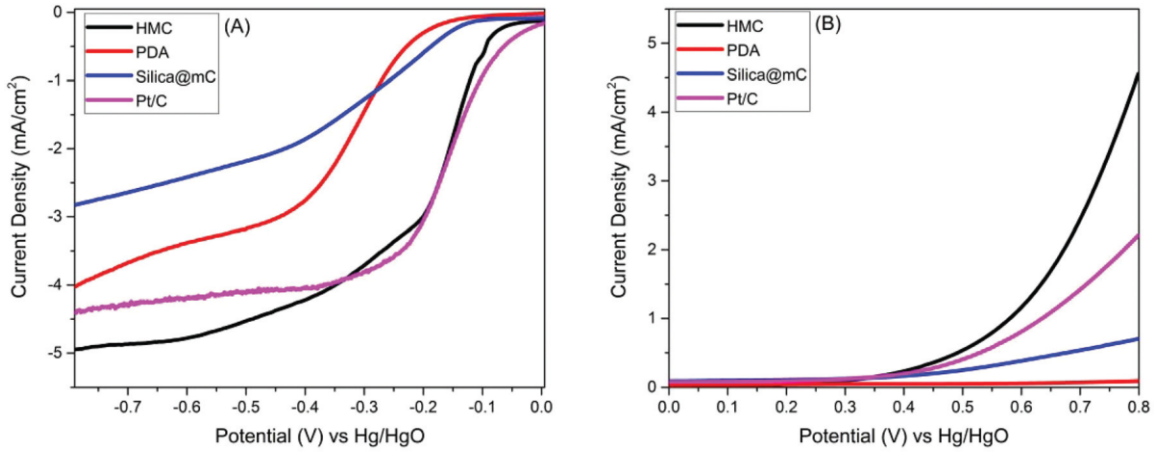

Figure 2-17: (A) ORR LSV curves for HMC, silica@mC, PDA beads, and Pt/C in an O2-saturated 0.1 M KOH solution at 1600 rpm. (B) OER LSV curves for HMC, silica@mC, PDA beads, and Pt/C in 0.1 M KOH solution at 1600 rpm.

The catalytic activity of cycled HMC for OER was tested using LSV. Figure 2-17 B shows a large anodic current due to the oxidation of water. Clearly the OER

activity of the present HMC is superior to that of the other carbon-based materials and the 40% Pt/C material. Table 2-3 summarizes the bifunctional oxygen activity of HMC, silica@mC, and PDA beads. To assess the overall oxygen catalytic activity, the difference between ORR and OER onset potentials was tabulated. A smaller difference indicates better catalytic behavior for the bifunctional electrode. Based upon this metric, HMC particles have an onset potential difference of 420 mV, which compares favorably to 40% Pt/C material.[208] In addition, a summary of ORR activity in 0.1 M KOH for HMC and other carbon-based electrocatalysts is presented in Table 2-4. It is shown that the ORR activity of metal-free N-doped HMC is comparable to that of other carbon-based ORR catalysts. ORR–OER bifunctional catalytic activity depends upon the surface area and N content of the structure.[209]

Table 2-3: Oxygen electrode catalyst activities

Catalyst	ORR onset (V)	j_l (mA cm^{-2})	n at -0.7 V	OER onset (V)	j_l (mA cm^{-2})	E_{OER}-E_{ORR} (V)
HMC	-0.055	-4.95	3.97	0.365	4.53	0.420
Silica@mC	-0.112	-2.85	2.83	0.373	0.68	0.485
PDA beads	-0.165	-4.05	3.47	0.463	0.08	0.628
Pt/C	0.001	-4.39	4.00	0.430	2.18	0.429

j_l: limiting current density. n: number of electrons transferred. $E_{1/2}$: half-wave potential.

Table 2-4: Comparison of the ORR activity of HMC with various non-precious metal catalysts in the recent literature

References	Materials	Onset potential (V)	Cathodic ORR peak potential (V)	Max current density at 1600 rpm (mA cm^{-2})	Mass loading (mg cm^{-2})
This study	Nitrogen doped-HMC	-0.050	-0.230	4.95	0.1
Nanoscale, 2015, 7, 1501	Fe/N/C hollow nanospheres	ND	-0.070	ND	0.2
Nanoscale, 2014, 6, 15080	Co nanoparticles in N-doped carbon	-0.040	-0.140	5.29	0.2
Angew. Chem. 2013, 125, 3192-3198	N-doped graphene	-0.319	-0.389	2.42	ND
Adv. Mater. 2013, 25, 998-1003	N-rich PD Abased carbon	-0.001	-0.120	ND	ND
J. Am. Chem. Soc. 2012. 134, 16127	P—doped ordered mesoporous carbons	-0.060	ND	1.70	0.7
Chem. Commun., 2015, 51, 8841	Eggplant-derived microporous carbon sheets	-0.003	-0.120	2.45	ND
Nature Communication, 2014, 1-24	N-doped hierarchically porous carbon	ND	-0.140	4.32	0.5
Nanoscale, 2014, 6, 3540	$NiCo_2S_4$	-0.050	-0.120	4.30	0.7

ND: Not determined.
*All the potential are expressed vs. the Hg/HgO reference electrode.

According to the data summarized in Table 2-1, the present HMC has the highest N content of the samples investigated. The N bonding environment (*e.g.*, pyridinic, pyrrolic, and graphitic) influences catalytic activity; the literature suggests that the proportion of pyridinic and pyrrolic N plays key roles.[72,208–211] Still, conflicting reports exist regarding the precise relationship between catalytic activity

and N speciation.[210] Comparison of HMC, silica@mC, and PDA beads shows differences in specific surface area, pore size, pore volume, and N speciation. The specific surface area of HMC is the highest (340 m^2 g^{-1}) of the studied structures (Table 2-1). Furthermore, the pore volume of HMC particles is an order of magnitude higher than that of both silica@mC and PDA beads, which is consistent with the electrochemical performance of HMC. The mesoporous nature of HMC provides more active sites for ORR and OER. These factors, along with the type of N doping contribute to the different electrochemical performances. Therefore, the synergistic effect of high surface area and N doping improves the bifunctional electrocatalytic activity of HMC.

The short-term durability of HMC was evaluated by chronoamperometry at a constant potential of −0.2 V *vs*. Hg/HgO for 3 h in O_2-staurated 0.1 M KOH at 1600 rpm. The chronoamperometric results are shown in Figure 2-18. The HMC catalyst exhibits higher relative current over time than 40% Pt/C. After 3 h, 40% Pt/C retained 54.7% of the initial current, whereas HMC retained 70.1% of its initial current. This shows the good stability of the HMC in addition to its promising bifunctional activity. The gradual decay of the reduction current may be due to insufficient gas flux or slow catalyst removal from the electrode surface during testing. Activity degradation of 40% Pt/C catalysts in alkaline solutions has been observed previously and it is attributed to the dissolution or aggregation of Pt nanoparticles.[181]

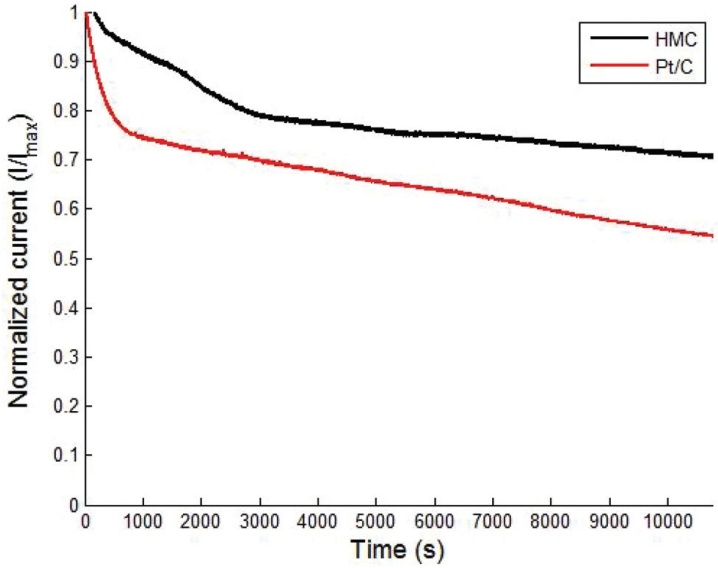

Figure 2-18: Chronoamperometric responses for ORR for HMC and Pt/C catalysts at −0.2 V *vs.* Hg/HgO in O_2-saturated 0.1 m KOH solution at a rotational rate of 1600 rpm.

The stability of HMC was confirmed by extended cycling of the catalysts. This is shown in Figure 2-19 where HMC has been exposed to repeated potential cycles from **−**0.8 to 0.7 V *vs*. Hg/HgO in O_2-saturated electrolyte at 100 mV s^{-1}. After 1000 cycles, only minimal changes to ORR kinetics are observed. In fact there is a slight increase in the magnitude of the current density with cycling. The good stability is attributed to the nature of HMC active sites, which are N doped, and the corrosion resistant nature of the HMC particles. The high stability and rapid kinetics may arise from the high surface area and multiple active sites for oxygen adsorption.[212]

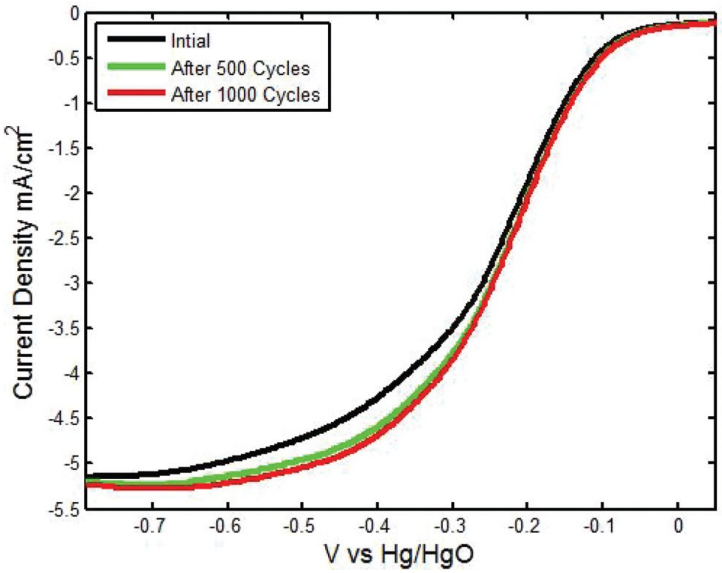

Figure 2-19: LSV ORR curves measured during cycling of HMC in O_2-saturated 0.1 M KOH at 1600 rpm (potential range −0.8 – 0.7 V *vs.* Hg/HgO at 100 mV s^{-1}).

RDE measurements are generally insufficient in their prediction of the performance of the catalyst because the KOH concentration is 0.1 M KOH is much lower than the concentration usually used in a battery system (6 M KOH). Therefore, it is necessary to characterize the bifunctional activity under conditions that approach those of a "real world" ZAB. A ZAB is typically consists of a Zn electrode, a separator, and an air cathode. The ZAB investigated here was fabricated using a polished Zn plate anode, 6 M KOH with 2 wt% ZnO electrolyte, and HMC or 40 wt% Pt/C as the active material in the air electrode. Galvanostatic charge–discharge at a current density of 2 mA cm^{-2} gave a discharge voltage of 1.24 V and a charge voltage of 2.05 V at the initial stage for HMC (Figure 2-20 A).

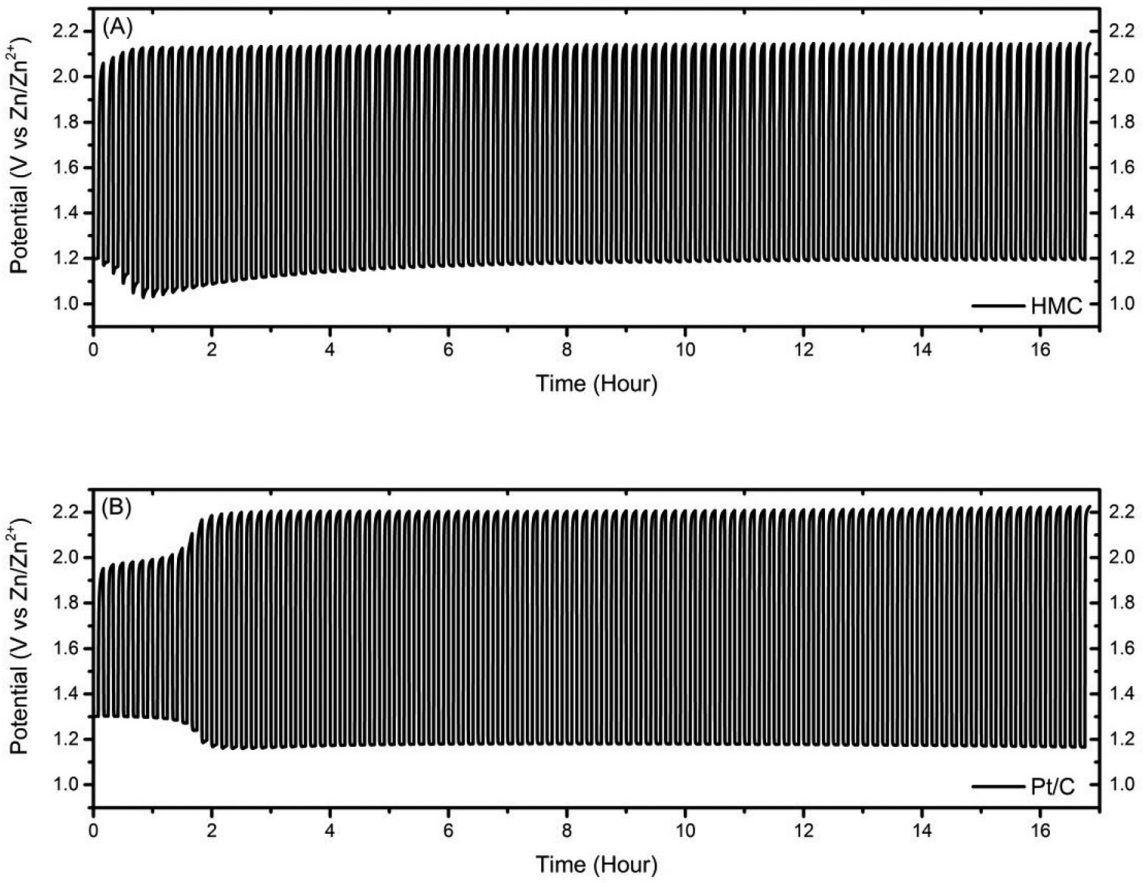

Figure 2-20: ZAB cycling test data for (A) HMC-based ZAB at 2 mA cm^{-2} and (B) Pt/C based ZAB at 2 mA cm^{-2}. One cycle includes 5 min of charge followed by 5 min discharge.

The charge–discharge potential gap for HMC increased from 0.85 to 0.89 V (~10%) after 3 cycles. For the Pt/C based air cathode ZAB, the initial potential gap is smaller compared with HMC (0.65 V *vs*. 0.85 V). However, the potential gap for Pt/C increases to 1.05 V (~60%) after 12 cycles (Figure 2-20 B). This clearly shows the HMC is a more stable catalyst than Pt/C in highly alkaline electrolytes. The

charge and discharge potentials after 12 cycles are compared with other bifunctional catalysts in Table 2-5, which highlights the superior performance and stability of HMC. These results will open new avenues to develop cost effective and high performance metal free electrocatalysts applied in advanced energy storage devices.

Table 2-5: Comparison of the rechargeable ZAB performance of HMC with various non-precious metal catalysts in the recent literature

References	Materials	Charge potential (V)	Discharge potential (V)	Mass loading (mg cm^{-2})
This study	Nitrogen- doped HMC	2.13	1.24	1
This study	Pt/C	2.20	1.15	1
Nat.nano, 2015, 5, 444-452	N and P co-doped mesoporous nanocarbon	~2.5	~0.95	0.50
Chem. Commun., 2015, 51, 8841	Eggplant-derived microporous carbon sheets	~2.2	1.23	*ND
Nano Lett. 2012, 12, 1946–1952	$LiNO_3$/CNT	2.33	0.94	0.72

*ND: Not determined.

2.4 Conclusions

The synthesis and characterization of N-doped carbon mesostructures obtained from the carbonization of polymerized dopamine have been reported. N-doped HMC exhibits high ORR and OER activities as well as superior stability in alkaline electrolytes when compared with baseline Pt/C catalysts. The unique structures of the porous shell provide abundant active sites for oxygen adsorption and desorption and facilitate the diffusion of reactants during the catalytic processes. More importantly, when used as a bifunctional catalyst to construct the air electrode for ZAB, N-doped HMC outperforms the state-of-art Pt/C counterpart. The high surface area and N-doped active sites boost the diffusion-limiting current and long-term stability. As a result, HMC is a promising high performance alternative to precious metal bifunctional electrocatalysts in Zn–air batteries (ZAB).

Chapter 3:

Synthesis of Cellulose Nanocrystals (CNC)-derived Hollow Mesoporous Carbon Spheres and Their Application as Metal-free Catalyst for 4-Nitrophenol Reduction[2]

[2] The reported catalysis experiment was performed by Mahmoud A. Y.

3.1 Introduction

Cellulose nanocrystals (CNC) derived from cellulose have gained considerable attention during the past decade due to their natural abundance and unique features such as, nanoscale dimensions, high mechanical strength, high surface area, and unique optical properties.[110,213] The properties and applications of CNC were outlined in Chapter 1, Section 1.4.4. Currently, CNC is considered as a platform for a wide variety of applications including polymer reinforcement,[119] nano-composite formulation,[214] enzyme immobilization,[215] drug delivery,[216] biomedical application, personal care, foods,[217] pharmaceuticals[218] and as a support matrix for metallic nanoparticle synthesis.[219]

There are few examples that use CNC as carbon precursor and a template to prepare mesoporous carbon structures. It is known that CNC suspensions organize into chiral nematic phases that can be preserved upon air-drying.[220] Researchers have exploited this property to prepare chiral nematic mesoporous carbon films by using CNC as carbon precursor within a freestanding mesoporous silica host.[123,124] Recently, cage-like microcapsules of CNC nanoparticles with a highly porous shell morphology were synthesized *via* layer-by-layer (LbL) assembly onto silica microspheres.[221] The work presented here extends these previous demonstrations to prepare ultrathin, mesoporous carbon structures by carbonization of CNC on silica particle templates.

Expanding the range of materials that provide catalytic activity is the goal of many research labs. The most widely known and studied catalysts are based on metallic or organometallic centers. However, the development of metal-free catalysts is an active area of research due to the potential of these materials exhibiting lower cost, better stability, a higher degree of biocompatibility and a lower environmental impact. Carbon nanomaterials are receiving more attention as metal-free catalyst as they meet all the above mentioned benefits.[222]

In this Chapter, we report the synthesis of CNC-derived hollow mesoporous carbon spheres (HCS). CNC particles are self-assembled onto silica spheres that have been coated with a pluronic block copolymer. Subsequent carbonization under inert atmosphere generates an ultrathin mesoporous carbon film on the silica spheres. Removal of the silica core through etching results in generation of hollow mesoporous carbon spheres. This study, to the best of our knowledge, provides the first example of using CNC as a carbon precursor along with a soft template to generate mesoporous carbon hollow spheres. We have found that addition of sodium citrate as a mediating agent and the pluronic block copolymer are necessary for the optimal formation of HCS. Once the spheres were prepared we investigated their catalytic activity in the reduction of 4-nitrophenol (4-NP) to 4-aminophenol (4-AP) by sodium borohydride ($NaBH_4$). The chemical principles related to this reaction are further discussed in Chapter 5, Section 5.3.

3.2 Experimental

3.2.1 Reagents and Materials

Freeze-dried cellulose nanocrystals (CNC) derived from cotton were provided by Alberta Innovates Technology Futures (AITF). Pluronic F127, trisodium citrate dihydrate, tetraethoxysilane (TEOS) (≥99%), 4-nitrophenol (4-NP) and sodium borohydride were purchased from Sigma-Aldrich and used as received. Electronic grade hydrofluoric acid (HF, 49% aqueous solution) was purchased from J. T. Baker. Ammonium hydroxide (30%) was purchased from Caledon Laboratories. Carbon-coated, 200-mesh Cu grids were purchased from Electron Microscopy Sciences. Milli-Q water (18.2 MΩ) was used for making all the solutions.

3.2.2 Preparation of Stöber Silica Particles

Spherical silica particles were prepared using the Stöber method and tetraethoxysilane (TEOS) as the silica source.[223] For a typical synthesis, 40 mL of 0.2 M TEOS was added to a mixed solution of 50% ethanol (80 mL) and ammonium hydroxide (28%, 4 mL) and then stirred for 3 hours at ambient temperature. The reaction mixture was purified by centrifugation and washing with ethanol three times at 10,000 rpm for 30 min to collect the particles and upon drying a white powder was obtained.

3.2.3 Synthesis of Hollow Carbon Spheres

For a typical synthesis, 400 mg of Stöber silica (500 nm ± 10%) was dispersed in 100 mL DI water. Then, 200 mg (0.02 mmol) of triblock copolymer pluronic F127 was added. After it dissolved, 120 mg (0.5 mmol) of trisodium citrate dehydrate was added. At the end, 400 mg (0.4 wt. %) of CNC was added and the mixture was stirred overnight at room temperature. The resulting coated silica particles were collected by centrifugation at 10000 rpm for 30 min. The particles were washed three times using ethanol (25 mL) and then dried under vacuum. The resulting white powder was placed in a quartz boat in a tube furnace and heated to 400 ˚C (heating rate of 1 ˚C/min) and held for 2 h. The temperature was then raised (heating rate of 5 ˚C/min) to 800 ˚C and held for 3 h and then cooled to room temperature. All heating and cooling procedures were performed in a flowing Ar atmosphere.

As-synthesized coated silica particles (*ca.* 0.2 g) were placed in a polyethylene terephthalate (PET) beaker. Water (2 mL), ethanol (2 mL), and aqueous 49% HF (2 mL) (Caution! HF is dangerous and must be handled with extreme care) were added sequentially and the mixture was stirred for 1 hour at room temperature. The particles were recovered *via* vacuum filtration and washed with water (60 mL) and ethanol (60 mL). The resulting black powder was dried under vacuum. The HCS product (0.05 mg) was characterized using transmission electron microscopy (TEM), Helium ion microscopy (HIM), Raman, infrared (IR) and

X-ray photoelectron spectroscopies (XPS), X-ray diffraction (XRD) and N_2 adsorption/desorption measurements.

3.2.4 Catalytic reaction

A stock solution of HCS was prepared with the aid of sonication in a bath sonicator (0.1 mg/mL). In a quartz cuvette, 1 mL of 1 x 10^{-4} M 4-NP was mixed with 0.9 mL of HCS (0.1 mg/mL) and 20 µl of 0.5 M sodium borohydride. The volume was adjusted to 2 mL with water and the UV-vis measurements were taken just after mixing the sodium borohydride solution. The molar ratio between 4-NP and sodium borohydride was kept at 1:100. All water used for the catalytic reaction experiments was Milli-Q water (18.2 MΩ).

3.2.5 Materials Characterization and Instrumentation

FT-IR spectroscopy was performed using a Nicolet Magna 750 IR spectrometer by drop coating an ethanol dispersion of particles on a piece of Si wafer.

Conventional transmission electron microscopy was performed using a JEOL 2010 TEM equipped with a LaB_6 thermionic emission filament operated at an accelerating voltage of 200 kV. Samples for TEM analysis were prepared by placing a drop of a dilute ethanol suspension of the material of interest onto a carbon-coated, 200-mesh Cu grid and drying at room temperature.

High-resolution (HR) TEM images were acquired using a Hitachi-9500 TEM operated at an accelerating voltage of 300 kV and processed using Image J software (Version 1.48v).

Helium ion microscopy (HIM) imaging was carried out by Zeiss Orion Helium Ion Microscope operated at an acceleration voltage of 30 kV. Samples were prepared as outlined above for TEM.

XPS was performed using a Kratos Axis Ultra instrument with a monochromatic Al Kα source (λ = 8.34 Å) with an energy hν = 1486.6 eV. Survey spectra were collected with analyzer pass energy of 160 eV and a step of 0.3 eV. For high-resolution spectra, the pass energy was 20 eV and the step was 0.1 eV with a dwell time of 200 ms. The base pressure in the sample analytical chamber was lower than 1×10^{-9} torr. Binding energies were calibrated by using the C 1s peak as a reference (284.6 eV). CASA XPS Version 2.3.13 software was used to accomplish the background subtraction and curve fitting.

Perkin-Elmer Lambda 35 UV/vis spectrometer was used to collect the UV/vis spectra of solutions.

Nitrogen adsorption-desorption isotherms were measured at -196 ˚C with a Quantachrome Autosorb-1 adsorption analyzer. Prior to adsorption measurements, samples were degassed at 250 ˚C under vacuum for 2 h. The data were analyzed using Brunauer-Emmett-Teller (BET) theory and Barret-Joyner-Halenda (BJH) method. The specific surface area was determined from the linear portion of the BET data and the total pore volume was calculated from the amount adsorbed at a

relative pressure of about P/P_o=0.995. The pore size was determined using BJH method.

Raman spectra of the particles were measured with a Renishaw inVia Raman microscope. For HCS sample, 514 nm laser was used for 300 seconds using a 5× objective. The laser power at the sample was approximately 1.93 ± 0.04 mW. However, for CNC and silica coated samples that were not annealed, a 785 nm laser was used for 10 seconds with 10 accumulations using a 5× objective. The laser power at the sample was approximately 92.7 ± 0.5 mW. Samples were prepared by mounting the powder on gold substrate. Wire 3.4 was used for Raman spectra smoothing and background subtraction.

XRD was performed using an INEL XRG 3000 X-ray diffractometer equipped with a Cu Kα radiation source (λ = 1.54 Å). Samples were mounted on a low-intensity background Si (100) holder.

3.3 Results and Discussion

Hollow mesoporous carbon spheres (HCS), were prepared using CNC as carbon precursor. Sodium citrate is used as mediator, and pluronic F127 as a surfactant. The resulting structure was characterized and evaluated as a catalyst for the reduction of 4-NP to 4-AP by $NaBH_4$ (Figure 3-1).

Figure 3-1: Synthesis of HCS using CNC as a carbon precursor and subsequent catalytic activity for reduction of 4-nitrophenol (4-NP).

Stöber silica particles, used as sacrificial templates in the formation of HCS, were prepared by exploiting standard sol-gel processing. As-synthesized Stöber silica particles (diameter = 500 nm ± 10%) were first coated with the triblock copolymer PEO-PPO-PEO (Pluronic F127) soft template. Subsequently, trisodium citrate is adsorbed to the pluronic coated particles. This interaction is presumably

promoted by the formation of hydrogen bonds between carboxyl and hydroxyl groups of trisodium citrate and the available surface OH groups of F127 and silica. We have found that the presence of both sodium citrate and pluronic is necessary for the formation of HCS. We believe that citrate ions facilitate anchoring of CNC to silica in the subsequent step. After addition of the solid CNC, the mixture was allowed to stir for ~12 hours. The resulting white powder was collected, dried and carbonized (annealed) upon heating in an Ar atmosphere at 400 °C for 2 h and then at 800 °C for 3 h to yield a black powder.

The surface features of coated silica spheres before and after carbonization were evaluated using a Helium-ion microscope (Figure 3-2). As a result of low contrast of carbon and charging issues it is difficult to discern the coating before annealing (Figure 3-2A and B). Some distinct "bubble shaped" features emerged on the surface of silica particles after annealing (Figure 3-2C and D) which were not present before annealing. Further, the bright features observed on the surface of silica (Figure 3-2D) may be a qualitative indication of particle coating, however no definitive conclusion is possible.

Optical spectroscopy provides some evidence of coating. The Raman spectrum of coated silica particles before annealing exhibited characteristic features of CNC at 380, 437, 458, and 521 cm^{-1} (C-C and C-O bending modes), 1096 and 1120 cm^{-1} (C-C and C-O stretching modes), and 1340 and 1380 cm^{-1} (H-C-C, H-C-O and H-O-C bending modes, respectively).[224,225] Moreover, the FTIR spectrum of coated silica particles before annealing Figure (3-4B) shows the appearance of CNC related

features (Figure 3-4C) not observed in the spectrum of bare silica (Figure 3-4A). The absorptions observed at 1644 cm^{-1} can be attributed to O-H bending vibrations, while absorptions at 1000-1100 cm^{-1} can be attributed to C-O vibrations.[226] The absorptions at ~1200 cm^{-1} are attributed to the S=O stretching arising from the sulfate ester group of sulfuric acid which was used during the processing of CNC. For bare silica particles, the vibrations at 3380 cm^{-1} are attributed to the O-H stretching of hydroxyl groups while absorptions observed at 1644 cm^{-1} are attributed to presence of residual water. Features at 1100 cm^{-1} are assigned to the Si–O–Si asymmetric stretching while vibrations at 953 cm^{-1} are assigned to the silanol groups and absorptions at 800 cm^{-1} are assigned to the Si-O-Si symmetric stretching.[227]

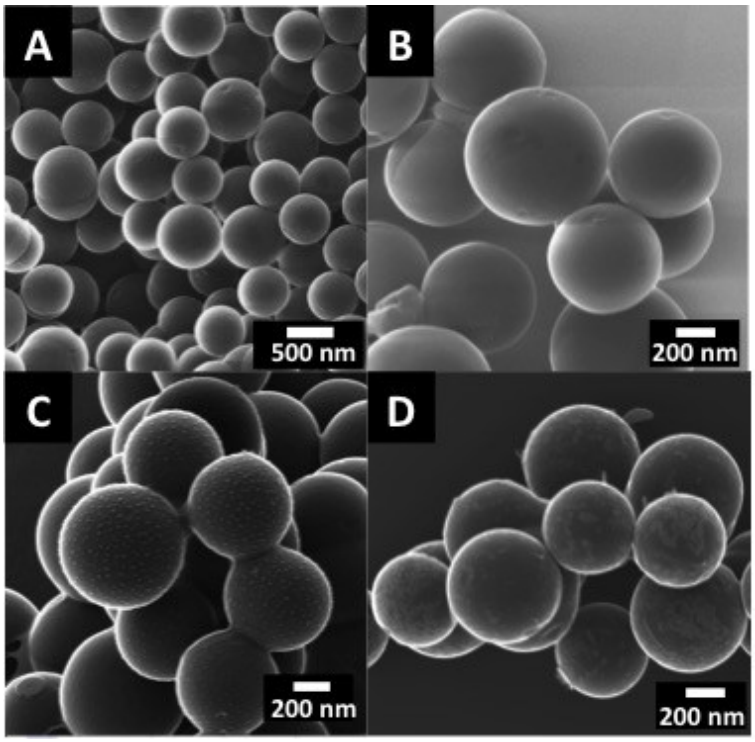

Figure 3-2: (A, B) HIM images of coated silica particles before annealing. (C, D) HIM images of coated silica particles after annealing.

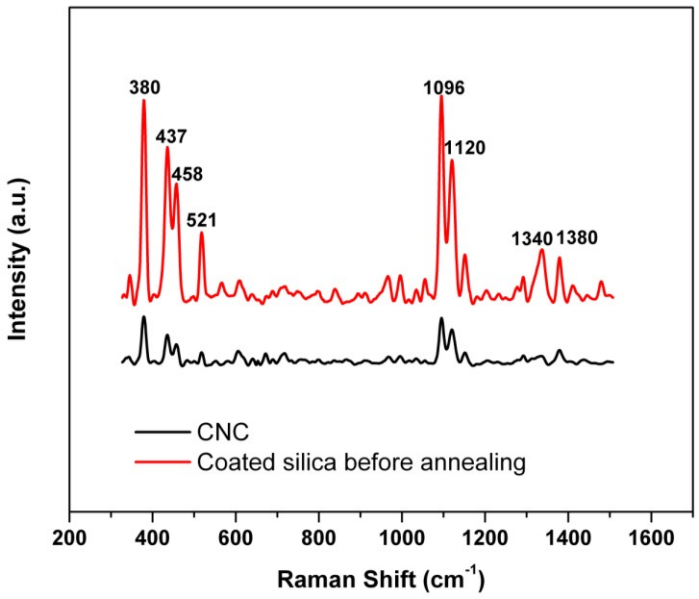

Figure 3-3: Raman spectra of CNC and coated silica particles before annealing control sample.

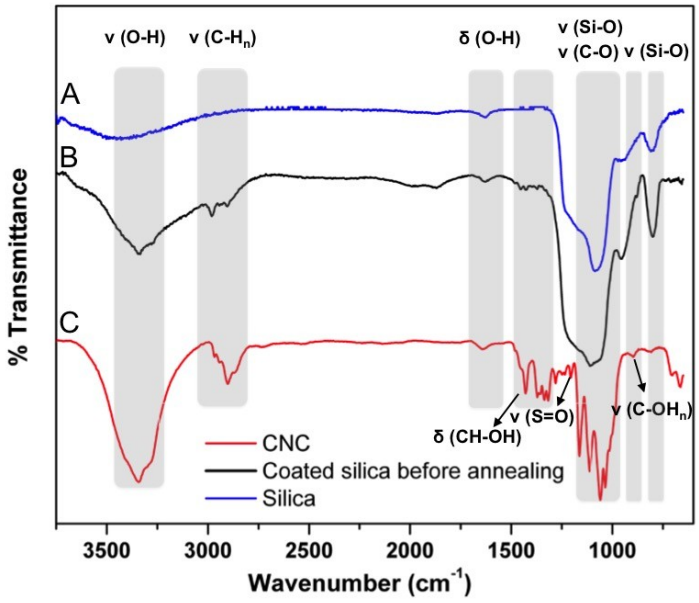

Figure 3-4: FTIR spectra of (A) silica, (B) coated silica before annealing, and (C) CNC.

The product of the annealing was subsequently treated with an alcoholic HF solution to remove the silica core. After etching for 1 hour, a black powder was obtained which, upon drying led to uniformly shaped hollow mesoporous carbon spheres (HCS) that were further investigated by electron and helium ion microscopy (Figure 3-5). As shown in Figure 3-5 E and F, some partial spheres arising from an incomplete coating of some silica particles may give insight into sphere formation and the deposition of CNC onto the silica surfaces.

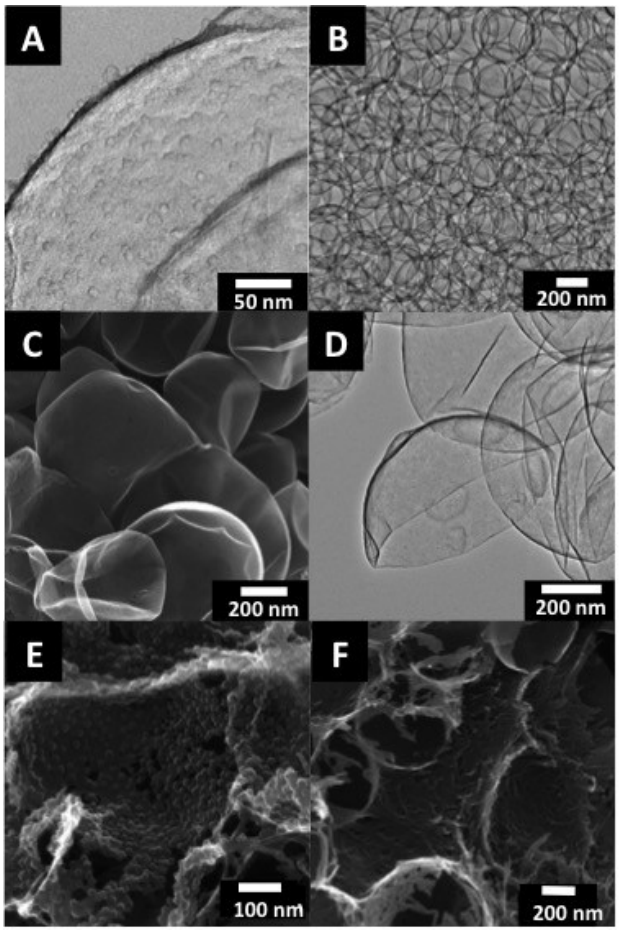

Figure 3-5: (A, B) Bright field TEM images of HCS. (C-F) HIM images of HCS.

To gain further insight into the structure of the HCS they were evaluated using high resolution TEM (HR-TEM). No obvious long-range ordered structure was detected consistent with the material being amorphous (Figure 3-6). The amorphous nature of the HCS was further confirmed by selected area electron diffraction (SAED) that showed dispersed diffraction rings (inset Figure 3-6(a)).

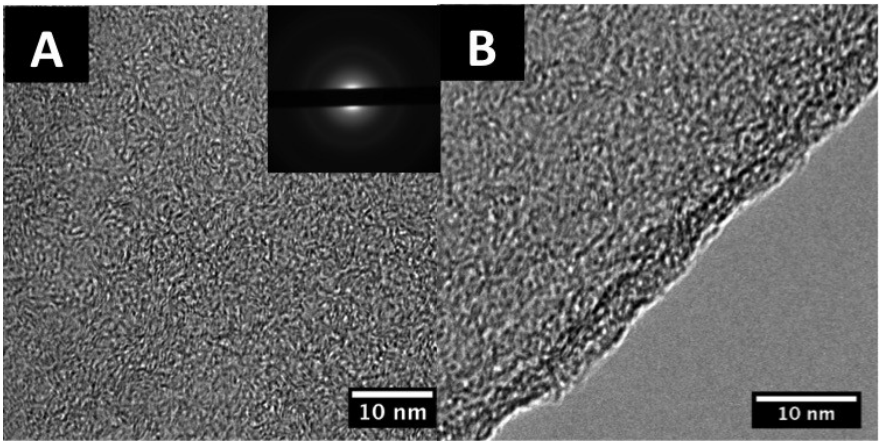

Figure 3-6: HR-TEM images of HCS (A) and (B).

To gain insight into the elemental composition and speciation of HCS particles, X-ray photoelectron spectroscopy (XPS) was performed. The survey spectrum confirms the presence of C and O and trace amounts of Si (<1%) (Figure 3-7A). No other metals were detected either at the sensitivity limit of the instrument. The C1s region of the high-resolution XP spectrum provides insight into the environment of the C in the HCS particles (Figure 3-7B). Three components centered at 284.8, 285.8, and 286.8 eV were obtained upon peak deconvolution. The peak at

284.8 eV is consistent with a graphitic structure (sp^2 C-C) while the emissions at 285.8 and 286.8 eV suggest the presence of C-O and C=O, respectively.[228]

The EDX spectra of HCS and coated silica reveal the elemental composition of the particles consistent with that of the XPS analysis (Figure 3-7C). The prominent Si signal in the EDX spectrum of coated silica sphere was reduced to a trace signal after HF etching confirming the removal of silica core. (n.b., The Cu signal originated from the sample supports for both XPS and EDX techniques).

X-ray powder diffraction pattern for HCS shows two broad features centered at $2\theta \approx 29°$ and 43° reflections that are consistent with the material being amorphous (Figure 3-7D).[124]

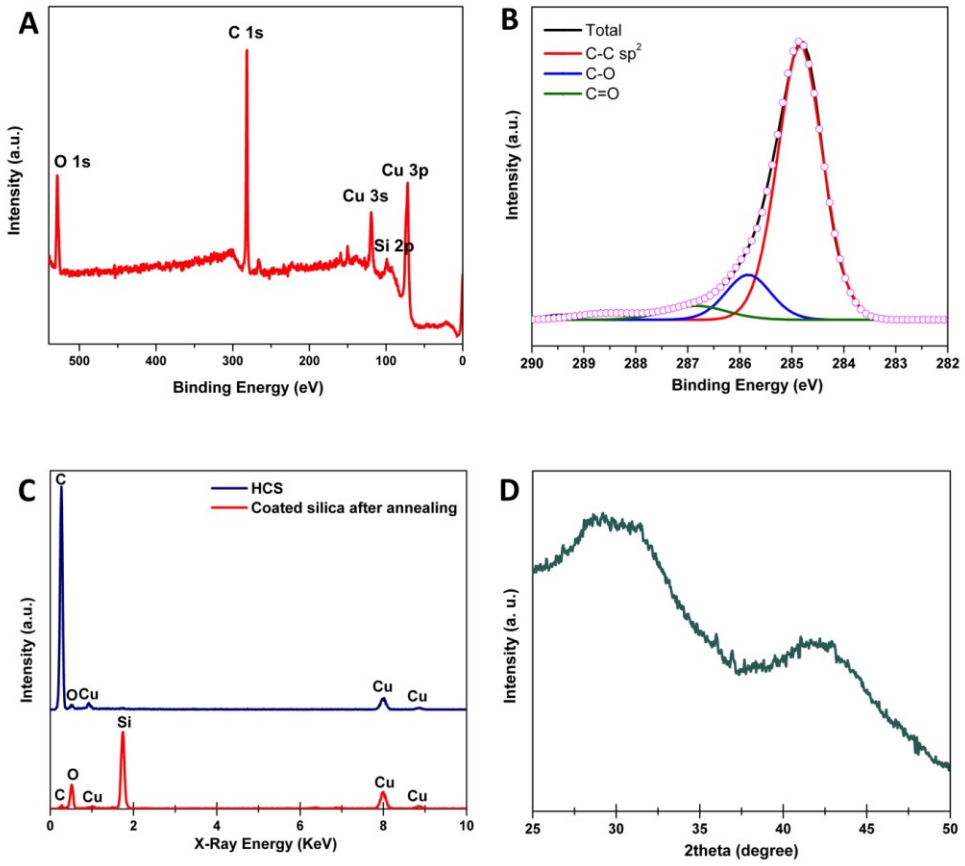

Figure 3-7: (A) Survey XP spectrum of HCS. (B) C1s region of the High-resolution XPS spectrum of HCS. (C) EDX spectra of HCS and coated silica after annealing. (D) XRD pattern for HCS.

FTIR spectra for coated silica after annealing particles show a strong absorption at 1120 cm^{-1}, which is assigned to the Si-O-Si asymmetric stretching (Figure 3-8A), while the absorptions at 800 cm^{-1} can be assigned to Si-O-Si symmetric stretching vibrations. As expected, these features decreased significantly after HF etching to remove the silica core (Figure 3-8A). The vibrations at 2800-

2900 cm^{-1} and at 1452 cm^{-1} are attributed to the stretching and bending vibrations of -C-H groups. The spectra also confirm the presence of oxygen-containing groups (*e.g.*, C=O, O-H) owing to absorptions at 1635 cm^{-1} are attributed to C=O and vibrations are 3300-3600 for O-H stretching. The presence of C=O species was further confirmed in the C1s region of the high-resolution XP spectrum of HCS.

The Raman spectrum for HCS shows two spectral features at 1331 and 1578 cm^{-1} that correspond to the D band and G band, respectively (Figure 3-8B). The D band arises from the A_{1g} breathing mode from sp^3 carbon components, while the G band corresponds to an in-plane stretching of bonds involving sp^2 carbon atoms.[202] Based upon these observations and the HR-TEM data (Figure 3-6), we conclude that HCS contains a mixture of graphitic and amorphous carbon.

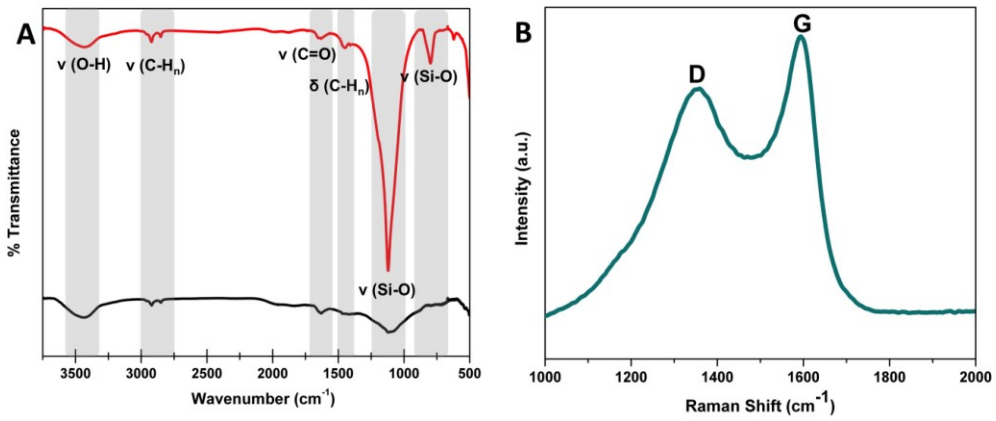

Figure 3-8: (A) FTIR spectra of HCS (black) and coated silica after annealing (red). (B) Raman spectrum of HCS.

Nitrogen sorption analysis was used to evaluate the porosity the HCS particles. The corresponding isotherms (Figure 3-9) show an open hysteresis loop at high relative pressure, consistent with the materials being mesoporous.[229] Evaluation of HCS indicates they possess porosity made up of uniform mesopores of diameters *ca*. 2 nm (calculated from desorption branch of the isotherm), and a high degree of microporosity. The Brunauer-Emmett-Teller (BET) surface area for HCS is 187 m^2g^{-1} and the pore volume is 0.2 cm^3g^{-1}.

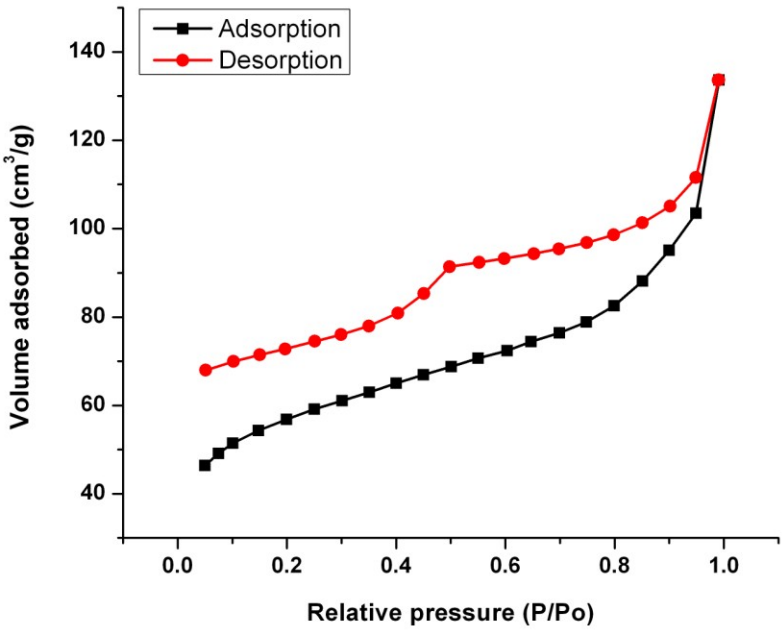

Figure 3-9: Nitrogen adsorption-desorption isotherms for HCS.

4-NP is one of the most prevalent organic pollutants in agricultural and industrial waste waters.[230,231] Therefore, developing an effective approach to remove this pollutant is very important. Catalytic conversion of the nitro functionality to aminophenol is considered as an effective and environmentally friendly method for this purpose. Similarly, the "nitro to amino" conversion is of practical importance for aniline and acetaminophen production.[232] In the industrial production of aniline, benzene is first nitrated with a concentrated mixture of sulfuric acid and nitric acid at around 60 ˚C to obtain nitrobenzene which is then hydrogenated at around 300 ˚C using a metal catalyst. In this context, developing an effective metal-free catalyst for this conversion is of great interest. To address these challenges various nanoparticle systems have been investigated, for example, metallic nanoparticles (gold, silver and platinum) are currently used as catalysts for this purpose.[231,233,234] (NB. In Chapter 5, Section 5.3, decorated silica particles with gold nanoparticles (SiO_2@GNPs) have been investigated as a catalyst for this particular conversion.) However, several recent studies have focused on exploring the use of metal-free systems.[222] Graphene, N-doped graphene and graphene oxide have been explored, however, these materials are costly and often involve challenging synthetic protocols.[222,235,236]

Taking into account all these considerations, the HCS catalytic reduction of 4-NP was investigated by monitoring the reduction of 4-NP using UV-Vis spectroscopy. The 4-NP exhibits a characteristic absorption feature at 317 nm which shifts to 400 nm upon addition of $NaBH_4$ because of the formation of 4-

nitrophenolate ions (equations 3-1 and 3-2; Figure 3-10), while formation of 4-AP is evidenced by appearance of an absorption peak at 300 nm as shown in Figure 3-11.

231,234,237

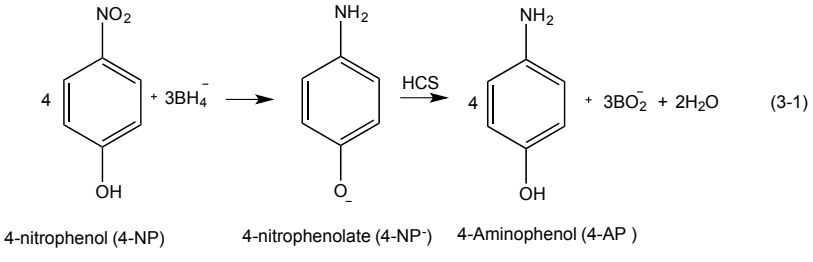

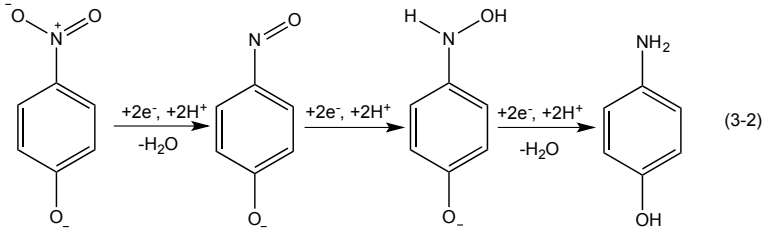

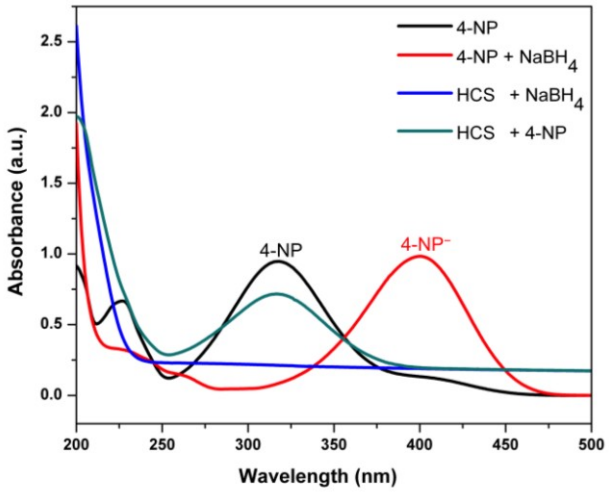

Figure 3-10: UV-vis spectra of 4-NP (1×10^{-4} M), 4-NP (0.5×10^{-4} M) in presence of $NaBH_4$, HCS in presence of $NaBH_4$ and HCS in presence of 4-NP (0.5×10^{-4} M).

The reduction reaction was carried out both in the absence (control) and presence of HCS. It was observed the yellow color of the 4-nitrophenolate solution remains for at least one week in the absence of HCS indicating a very slow or negligible reduction. However, in the presence of HCS, the yellow color disappears within 19 minutes (Figure 3-11A). As the absorption peak of 4-NP^- ions at 400 nm decreases the 4-AP absorption peak at 300 nm concomitantly increases indicating formation of 4-AP. In addition an isosbestic was observed at 327 nm indicating the conversion of 4-NP to 4-AP (Figure 3-11B). Monitoring the intensity of these features can provide insight into the kinetics of the reaction, *e.g.*, type of reaction and reaction rate *etc*. This analysis afforded a pseudo-first order reaction with a rate constant of 4.7 x 10^{-3} s^{-1} (Figures 3-11C and 3-11D). The present reaction kinetics are similar to those previously reported for hydrothermally prepared graphene oxide (HGO), however they differ from those of N-doped graphene and N-doped carbon where the later two followed pseudo-zero order kinetics.[222,235,236] The catalytic performance of HCS was much higher than that of previously reported HGO and other carbon-hybrid metal nanoparticles as presented in the Table 3-1.[235,238–241] We assume that the enhanced catalytic activity of HCS arises as a result of its mesoporous structure, high surface area and the oxygenated functional groups that facilitate the adsorption of 4-NP^- and $NaBH_4$ on the surface of the catalyst as it has been previously reported for HGO.[235] Although the exact mechanism is still under investigation, the reaction can be discussed in terms of the Langmuir-Hinshelwood (LH) mechanism in which two molecules adsorb on neighboring sites and the

adsorbed molecules undergo a bimolecular reaction.[242,243] Borohydride ions react with the surface of the HCS and transfer a surface-hydrogen species to the surface of the HCS.[244] 4-NP molecules are also adsorbed on the surface of the HCS. The reduction of 4-NP, which is the rate-determining step, occurs by the reaction of adsorbed 4-NP with the surface-hydrogen species. 4-AP as the reduction product detaches from the surface and creates a free surface, thus allowing the catalytic cycle to start again and continue (Figure 3-12).[243]

The induction time period, t_0, is required for the initial adsorption of 4-NP at the active sites of the catalyst.[222,243] We compared our HCS catalytic performance with other related catalysts in terms of ratio between 4-NP to $NaBH_4$, rate constant (k) and activity parameter (K) which is the rate constant divided by the weight of the catalyst used (Table 3-1).

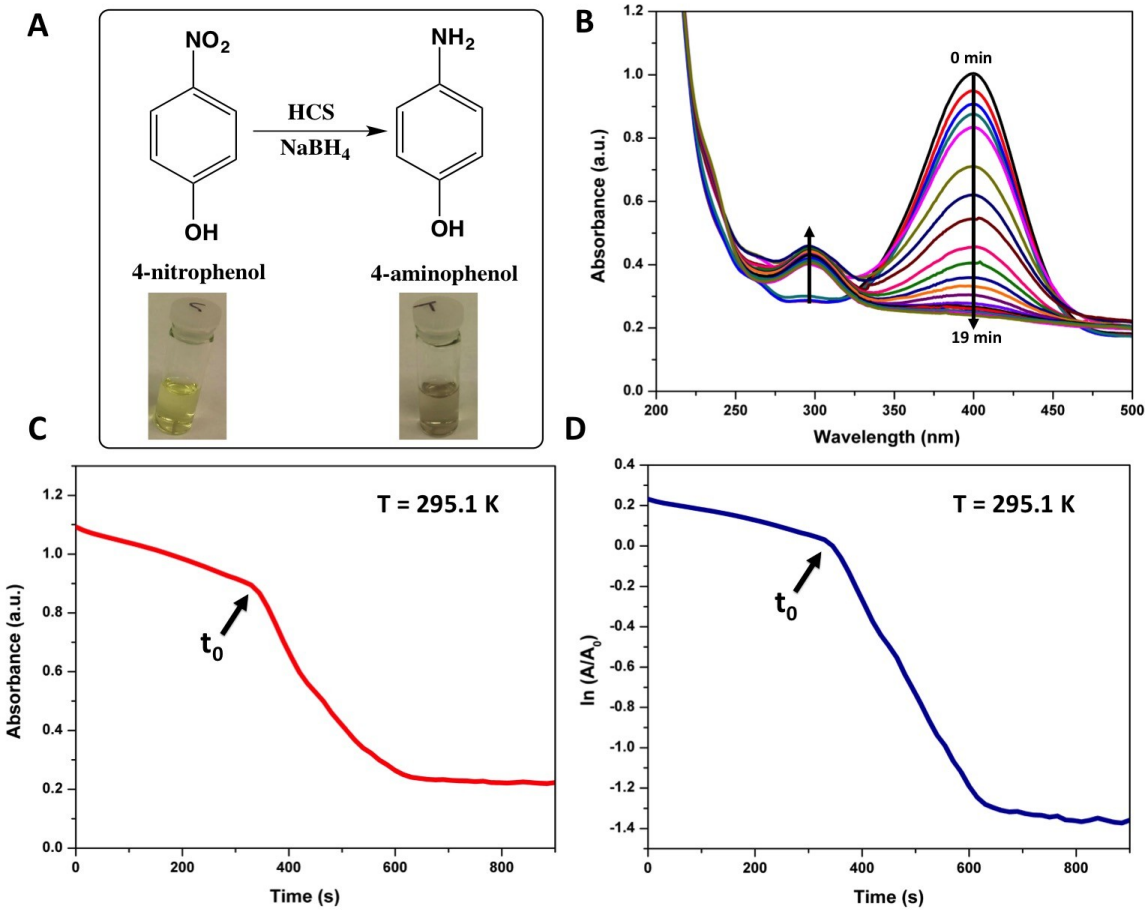

Figure 3-11: (A) Schematic for chemical catalysis from 4-NP to 4-AP using HCS as catalyst. (B) Time dependent UV-vis spectra for the reduction of 4-NP over HCS. (C) and (D) Time curves of the absorbance at 400 nm measured for the HCS catalyst.

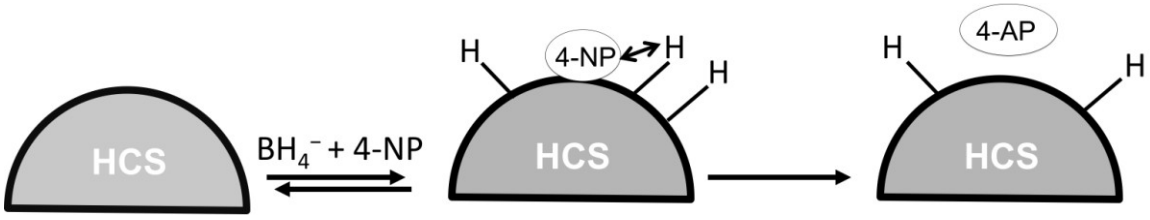

Figure 3-12: Schematic of reduction of 4-NP by borohydride in the presence of HCS.

Table 3-1: A comparison of HCS catalytic performance to other related catalysts

Catalyst	4-NP:$NaBH_4$ molar ratio	Rate constant k (s^{-1})	Activity parameter K (s^{-1} g^{-1})	Reference
HGO	1:200	2.45×10^{-3}	15.3	235
CNC@PDA–AgNP	1:317	4.25×10^{-3}	1.69	238
Au/graphene hydrogel	1: 71.4	3.17×10^{-3}	31.7	239
AgNP/Carbon sphere	1:142.85	1.69×10^{-3}	1.69	240
Ag-Au/Carbon sphere	1:142.85	6.46×10^{-3}	6.46	241
Pd/g-C_3N_4	1:12.50	7.29×10^{-3}	291.6	245
HCS	1:100	4.7×10^{-3}	52.22	This work

HGO: hydrothermally graphene oxide
CNC@PDA–AgNP: Nanocrytalline cellulose polydopamine silver nanoparticles
Pd/g-C_3N_4 : Palladium nanoparticles supported on mesoporous graphitic carbon nitride (g-C_3N_4)

3.4 Conclusions

In summary, we have successfully synthesized hollow mesoporous carbon spheres (HCS) using cellulose nanocrystals (CNC) as carbon precursor. We have found that the presence of trisodium citrate as a mediating agent is necessary for the formation of HCS. The resulting materials show outstanding catalytic activity towards reduction of 4-NP to 4-AP. The reaction rate followed pseudo-first order kinetics with k value of 4.7×10^{-3} s^{-1} and activity parameter of 52.22 $s^{-1}g^{-1}$, which approaches to that of metallic counterparts.

Chapter 4:

Microwave-assisted Synthesis of N-doped Carbon Coated Fe_3O_4 Nanorods as Superior Oxygen Reduction Electrocatalyst in Alkaline Solution[3]

[3] The reported electrochemistry was performed by Davari, E.

4.1 Introduction

Developing high performance electrocatalysts for the oxygen reduction reaction (ORR) is an essential part of establishing efficient fuel cells and metal-air batteries as discussed in Chapter 2, Section 2.1.[206,246]

Pt-based catalysts are very effective in promoting ORR. However, their high cost and limited resources present challenges for their practical application.[182,247–249] Extensive research effort has been expended toward establishing highly active, affordable, alternative precious metal-free electrocatalysts.[250] Because of their low cost, abundance, and environmental compatibility non-precious transition metals[251,252] and metal oxides (*e.g.,* spinels and perovskites)[253–257] as well as nitrogen doped (ND)- carbon species[187,258] have been investigated.

Transition metal oxides (*e.g.,* Co_3O_4, MnO_2, Fe_3O_4 etc.) are available in high quantities at low cost. Their promising ORR catalytic activity makes them suitable alternatives to noble metal systems.[259] However, unmodified oxides usually suffer from limited ORR activities and low stability as a result of their low electrical conductivity and propensity to aggregate.[260]

Recently, researchers have turned their focus to carbon-supported Fe_3O_4 nanocrystals as potential ORR electrocatalysts. Fe_3O_4 possesses an inverse spinel (Fd3m) structure (Chapter 1, Figure 1-29) and a comparatively high electrical conductivity (200 Ω^{-1} cm^{-1}).[261] This crystal structure also provides redox active surface sites for O_2 adsorption.[261,262] Recent studies suggest Fe_3O_4 is also resistant to

chemical degradation under alkaline conditions commonly used for ORR reactions.[262,263] The ORR activity of Fe_3O_4 nanocrystals has been further tuned by coating particles with ND MPC that lowers the ORR activation energy.[264] As discussed in Chapter 2, ND HMC exhibits high ORR and OER activities as well as superior stability in alkaline electrolytes when compared with baseline Pt/C catalysts. Clearly, coupling the properties of ND MPC and Fe_3O_4 nanocrystals offers a promising avenue by which these ORR catalysts may be improved by limiting nanocrystal degradation. Different synthetic methods for preparing α-Fe_2O_3 nanorods have been developed and were summarized in Chapter 1, Section 1.5.1. In this chapter, the synthesis of α-Fe_2O_3 nanorods *via* a new microwave-based approach followed by coating with polydopamine (α-Fe_2O_3@PDA) is demonstrated. Subsequent heating of α-Fe_2O_3@PDA induces the formation of Fe_3O_4 nanorods coated with ND mesoporous carbon (ND-Fe_3O_4@mC). These materials were evaluated for the ORR electroatalytic activity as a function of ND mesoporous carbon coating thickness.

4.2 Experimental

4.2.1 Reagents and Materials

Iron (III) chloride hexahydrate (99.9%) and sodium hydroxide (98.8%) were purchased from Fisher. Dopamine hydrochloride, pluronic F127 and 2-amino-2-hydroxymethyl-propane-1,3-diol (Tris) were purchased from Sigma-Aldrich and used as received. Pt-C (40%), Nafion solution (5% w/w in water) and 1-propanol (99.99%) were purchased from Alfa Aesar. Carbon black (CB) (Vulcan) was purchased from CABOT. Isopropanol was purchased from Sigma-Aldrich. Potassium hydroxide was purchased from Fisher and used as received. Pure argon and oxygen were purchased from Praxair. Acetone and ethanol (100%) were purchased from Fisher.

4.2.2 Synthesis of α-Fe_2O_3 Nanorods

In a typical synthesis aqueous NaOH (6.0 M; 9 mL) was added slowly to an aqueous solution of $FeCl_3.6H_2O$ (2.0 M; 10 mL) with stirring. Water (1 mL) was added to the above solution and stirred for and additional 15 minutes at room temperature. Then, 6 mL of the Fe^{3+} solution were transferred to microwave reactor vial along with a stir bar and sealed and transferred to a Biotage Initiator microwave synthesizer. The microwave reactor was programmed for 60 minutes at 150 °C (5 °C/sec). The resulting red precipitate was isolated by discarding the clear supernatant. Then transferred to centrifuge tube using water and washed three times and collected by centrifugation (10,000 rpm for 20 min) and then dried under

nitrogen for 1 hour. The yield was 42%. The product was characterized using TEM and XRD.

4.2.3 Synthesis of ND-Fe_3O_4@mC

In a typical synthesis of ND-Fe_3O_4@mC, to 50 mg of α-Fe_2O_3 nanorods in 12.5 mL deionized water, 25 mg (0.002 mmole) of triblock copolymer pluronic F127 was added. Then 15 mg (0.12 mmole) of 2-amino-2-hydroxymethyl-propane-1,3-diol (tris) was added. Subsequently, dopamine hydrochloride (50 mg, 0.3 mmole) solid was added and the mixture was stirred at room temperature for 2, 4, or 12 hours. The resulting polydopamine coated iron oxide particles (α-Fe_2O_3@PDA) were collected by centrifugation at a speed of 10000 rpm for half an hour and washed three times using ethanol (25 mL) and dried in vacuo. The resulting dark grey powders were placed in a quartz boat and transferred to a quartz tube furnace and heated to 400 ˚C (heating rate of 5 ˚C/min) where it remained for 3 h followed by cooling to room temperature. All heating and cooling were performed in pure argon atmosphere (flow rate was ca. 2 bubbles/sec). The yields for 2, 4, and 12 hours were 46.2%, 48.3% and 52.1%, respectively. The resulting black powder was characterized using TEM, HR-TEM, EDX, XRD, Raman, TGA, and N_2 sorption.

4.2.4 Preparation of Bare Fe_3O_4 Nanorods

For this purpose, 20 mg of ND-Fe_3O_4@mC-2 was heated at 300 ˚C for 30 min under air atmosphere (heating rate 10 ˚C/min) to burn off the carbon coating. The obtained materials were characterized using HR-TEM, XRD and TGA.

4.2.5 Preparation of Hollow Carbon Nanorods

To dissolve the Fe_3O_4 nanorods core, 10 mg of ND-Fe_3O_4@mC-2 was treated with 6 M HCl to dissolve the Fe_3O_4 core to obtain hollow carbon nanorods. The obtained materials were characterized using HR-TEM.

4.2.6 Electrochemical Measurements

Electrochemical properties of the synthesized materials were measured in a conventional three-electrode assembly with a Bio-logic potentiostat (SP-300) and rotating disk electrode (RDE) (Pine Instruments Co, AFMSRCE). Hg/HgO (1 M NaOH, 0.098 V *vs.* NHE at 25 °C) was used as the reference electrode and Pt coil was used as the counter electrode. Catalyst-modified glassy carbon (GC) was used as the working electrode. The catalyst ink was prepared by mixing catalyst and Vulcan XC-72 carbon black (CB) (catalyst/carbon: 1/1.5) into a solution containing 0.7 ml isopropanol and 0.2 ml of Nafion (5% w/w in water and 1-propanol dispersion, ≥ 0.92 meq/g exchange capacity) and ultrasonicated for 45 min to form a homogenous suspension. Prior to coating the catalysts onto the glassy carbon (GC) working electrode, the surface of the electrode was polished with 0.3 μm and 0.05 μm

alumina slurry followed by washing with acetone, ethanol and deionized (DI) water. Subsequently, 7 µl of the aliquot was drop-coated on the surface of the RDE GC electrode (0.196 cm^2), to reach a mass loading of 0.1 mg cm^{-2}, and dried under a lamp light in the lab. For comparison, commercial Pt-C catalyst (40 wt%, Alfa Aesar) was also prepared with the same method and the same loading. Before cyclic voltammetry (CV) and RDE measurements, the electrolyte (0.1 M KOH) was saturated with high purity O_2 or Ar. CV curves were acquired at a potential scan rate of 10 mV s^{-1} from -0.7 to 0.7 V *vs.* Hg/HgO. Linear sweep voltammograms (LSV) were acquired at a potential scan rate of 10 mV s^{-1} from -0.8 to 0.2 V *vs.* Hg/HgO in an O_2-saturated electrolyte at various rotation speeds (100 - 1600 rpm). The RDE technique was also used to obtain the intrinsic ORR activity of the catalysts by generating the Koutecky-Levich (K-L) plots using the following relationships (Equations 4-1, 4-2, and 4-3):

$$\frac{1}{j} = \frac{1}{j_k} + \frac{1}{j_l} = \frac{1}{B\omega^{1/2}} + \frac{1}{j_k} \qquad (4\text{-}1)$$

$$B = 0.62nFC_o(D_o)^{2/3}\nu^{-1/6} \qquad (4\text{-}2)$$

$$j_k = nFkC_o \qquad (4\text{-}3)$$

where, j, j_k and j_l are the measured, kinetic- and diffusion-limiting current densities, respectively, ω is the angular velocity of the electrode ($\omega = 2\pi N$, N is the linear rotation), n is the number of electrons transferred during ORR, F is the Faraday constant (F = 96,485 $Cmol^{-1}$), C_o is the bulk concentration of O_2 ($C_o = 1.2 \times 10^{-3}$ mol L^{-1}), D_o is the diffusion coefficient of O_2 in the KOH electrolyte ($D_o = 1.9 \times 10^{-5}$ cm^2

s^{-1}), ν is the kinematic viscosity of the electrolyte (ν = 0.01 cm^2 s^{-1} in 0.1 M KOH) and k is the electron-transfer rate constant.[265] Chronoampermetry tests were done at a constant potential of -0.3 V *vs.* Hg/HgO for 2000 s. Long term stability of the catalysts was evaluated using repetitive CV cycling for 5000 cycles at a scan speed of 100 mV s^{-1} from -0.7 to 0.2 V *vs.* Hg/HgO. In order to standardize the comparison, the ORR onset potential was set at the potential where the current was 10 % of the limiting current at 1600 rpm for the O_2 saturated LSV curves. IR correction was made for all experiments, in order to minimize the error caused by the resistance of the electrolyte, using the following equation (Equation (4-4)),

$$E_{true} = E_{measured} - iR_u \qquad (4\text{-}4)$$

where i is the cell current and R_u is the uncompensated resistance which was determined from impedance spectroscopy (EIS) measurements.

4.2.7 Materials Characterization and Instrumentation

Transmission electron microscopy (TEM) was performed using a JEOL 2010 transmission electron microscope equipped with a LaB_6 thermionic emission filament operated at an accelerating voltage of 200 kV. Samples for TEM analysis were prepared by placing a drop of a dilute ethanol suspension of the material of interest onto a carbon-coated, 200-mesh Cu grid and drying at room temperature. High-resolution (HR) TEM images were acquired using a Hitachi-9500 transmission electron microscope operating at an accelerating voltage of 300 kV and processed using Gatan ImageJ software (Version 1.46r). Samples were prepared by drop

casting dilute ethanol suspensions of the sample of choice onto holey carbon-coated copper grids (400 mesh) placed on a piece of filter paper.

X-ray photoelectron spectroscopy (XPS) analyses were performed using a Kratos Axis Ultra instrument operating in energy spectrum mode at 210 W. Samples were prepared by drop coating a solution of prepared materials onto a Cu foil substrate to yield thin films. The base and operating chamber pressure were maintained at 10^{-7} Pa. A monochromatic Al Kα source (λ = 8.34 Å) was used to irradiate the samples and the spectra were obtained with an electron takeoff angle of 90°. To minimize sample charging, a charge neutralizer filament was used when required. Survey spectra were collected using an elliptical spot with major and minor axis lengths of 2 and 1 mm, respectively, and 160 eV pass energy with a step of 0.33 eV. CasaXPS software (VAMAS) was used to interpret high-resolution spectra. All spectra were internally calibrated to the C 1s emission (284.8 eV). After calibration, a Shirley-type background was applied to remove most of the extrinsic loss structure. The FWHM for all the fitted peaks was maintained below 1.2 eV.

Nitrogen adsorption-desorption isotherms were measured at -196 ˚C with a Quantachrome Autosorb-1 adsorption analyzer. Prior to adsorption measurements, samples were degassed at 250 ˚C under vacuum for 2 h. The data were analyzed using Brunauer-Emmett-Teller (BET) theory and Barrett-Joyner-Halenda (BJH) method.[201] The specific surface area was determined from the linear portion of the BET plot and the total pore volume was calculated from the amount adsorbed at a

relative pressure of about P/P_o=0.995. The pore size was determined using BJH method.

Thermogravimetric analysis (TGA) was performed using a Mettler Toledo Star TGA/DSC system. The Fe_3O_4@mC samples were placed in a Pt pan and heated in N_2 atmosphere from 30 to 800 °C at 10 °C min^{-1}.

X-ray diffraction analysis was performed using a Rigaku Geigerflex 2173 diffractometer equipped with a Co Kα radiation source (λ = 1.79 Å). Crystallinity of all samples was evaluated using mounted samples on a silicon plate inside an aluminum holder.

Raman spectra of the particles were measured with a Renishaw inVia Raman microscope. The excitation wavelength was 514 nm. The laser power at the sample was about 1.93 ± 0.04 mW. Samples were prepared by mounting the powder on Al foil.

4.3 Results and Discussion

As discussed in Section 4.1, carbon-supported Fe_3O_4 nanocrystals are potential ORR electrocatalysts. ND mesoporous carbon coated Fe_3O_4 nanorods (ND-Fe_3O_4@mC) used in the present study were prepared using crystalline α-Fe_2O_3 nanorods obtained *via* a hydrothermal synthesis in a laboratory microwave (Figure 4-1).

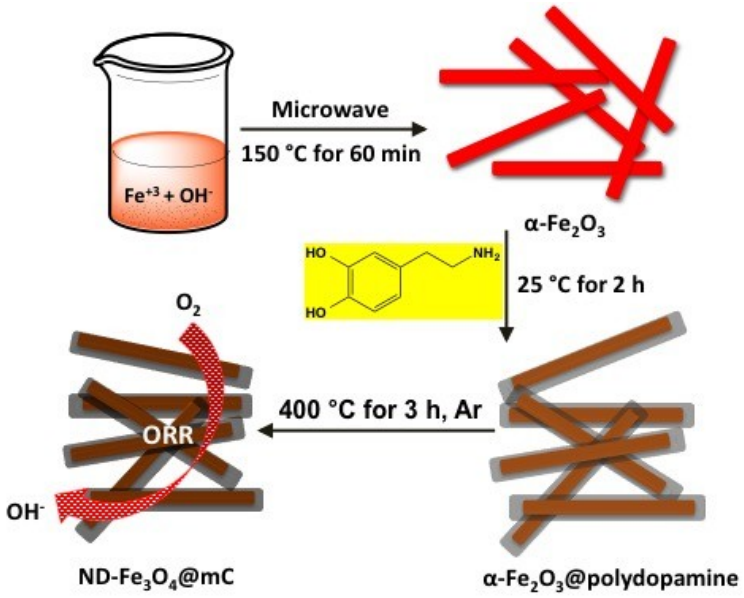

Figure 4-1: Illustration of the preparation process for ND-Fe_3O_4@mC nanorods from as prepared α-Fe_2O_3 nanorods.

The preparation has three stages: i) synthesis of α-Fe_2O_3 nanorods, ii) coating of as-prepared α-Fe_2O_3 nanorods with polydopamine, and iii) carbothermal reduction of the polydopamine coated α-Fe_2O_3 nanorods to yield ND-Fe_3O_4@mC.

Briefly, α-Fe_2O_3 nanorods were prepared in aqueous solution upon slow addition of NaOH (6.0 M) solution to aqueous $FeCl_3 \cdot 6H_2O$ (2.0 M) with stirring. After 15 minutes the solution was transferred to a microwave vial and heated in a microwave reactor for 60 minutes at 150 °C. The procedure yielded red α-Fe_2O_3 nanorods that were purified upon repeated washing with ethanol followed by drying in *vacuo* at room temperature. The as-prepared α-Fe_2O_3 nanorods were subsequently coated with dopamine-derived ND mesoporous carbon using a modification of a literature procedure.[258] The resulting dark grey particles were collected by centrifugation, repeated washed with ethanol, dried at room temperature in *vacuo* and subsequently heated to 400 ˚C for three hours in Ar followed by cooling to room temperature. The final product obtained from this multi-step procedure consisted of ND-Fe_3O_4@mC nanorods.

The structure and morphology of the α-Fe_2O_3 nanorods and as-prepared ND-Fe_3O_4@mC nanorods were investigated using transmission electron microscopy (TEM). The precursor α-Fe_2O_3 nanorods were 141 ± 44.8 nm long with diameters of 14 ± 3.4 nm (Figure 4-2A). A representative high-resolution TEM (HR-TEM) image (Figure 4-2A inset) shows continuous lattice fringes along the long axis of the nanorods consistent with the nanorods being single crystal. The observed *d*-spacing of 0.25 nm is consistent with values reported for the (110) spacing of pure hexagonal α-Fe_2O_3.[266]

Following carbonization the nanorod morphology is preserved (Figures 4-2B and C). A distinct amorphous shell (thickness = 1.5 ± 0.22 nm) that is presumably carbon was observed for samples that had been exposed to dopamine for 2 hours during the second stage of the fabrication procedure followed by carbonization (*i.e.,* ND-Fe_3O_4@mC-2). Representative HR-TEM images (Figure 4-2D) again show continuous lattice fringes indicating that ND-Fe_3O_4@mC-2 nanorods are single crystals with the *d*-spacing of 0.25 nm that are consistent with (311) lattice spacings of cubic Fe_3O_4.[267] The transformation of the α-Fe_2O_3 precursor to cubic Fe_3O_4 was confirmed using X-ray powder diffraction (*vide infra*).

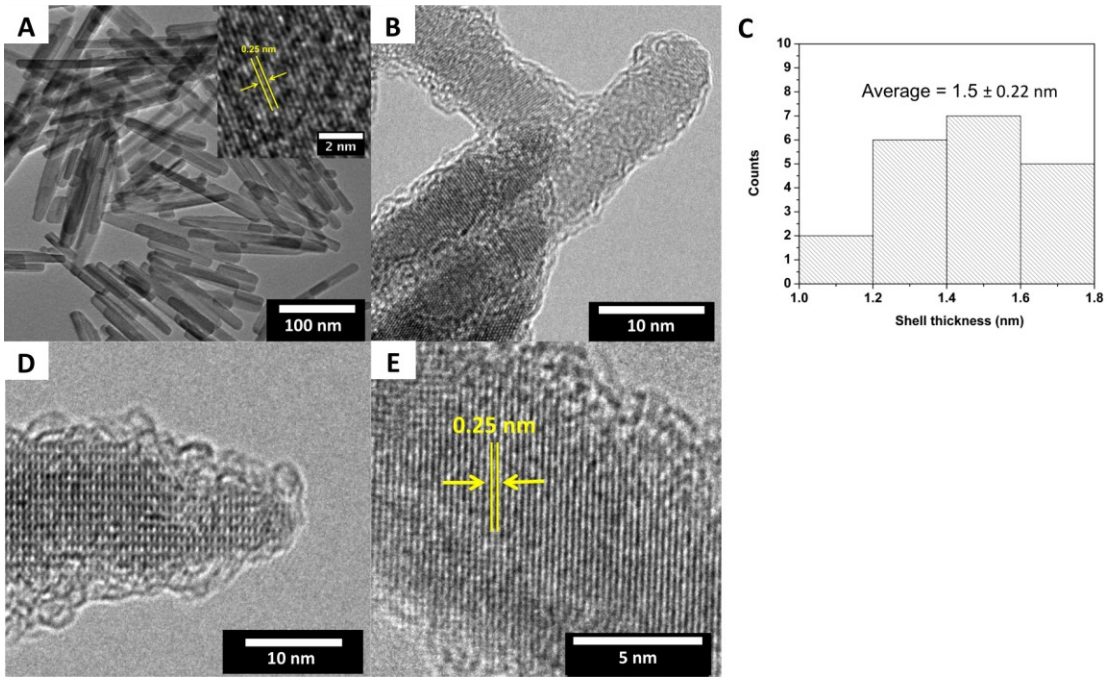

Figure 4-2: (A) Bright field TEM image of α-Fe_2O_3 nanorods (Inset: HR-TEM image of the same sample). (C) Carbon shell thickness distribution of ND-Fe_3O_4@mC-2 nanorods. (D-E) HR-TEM images of ND-Fe_3O_4@mC-2 nanorods.

The thickness of the carbon shell was varied by defining the dopamine coating time between 4 (ND-Fe_3O_4@mC-4) and 12 hours (ND-Fe_3O_4@mC-12), while keeping all other parameters fixed (Figure 4-3). Distinct amorphous shells (thickness = 2.58 ± 0.12 nm and 3.5 ± 0.37 nm) were observed for samples that had been exposed to dopamine for 4 hours (*i.e.,* ND-Fe_3O_4@mC-4) and 12 hours (*i.e.,* ND-Fe_3O_4@mC-12), respectively.

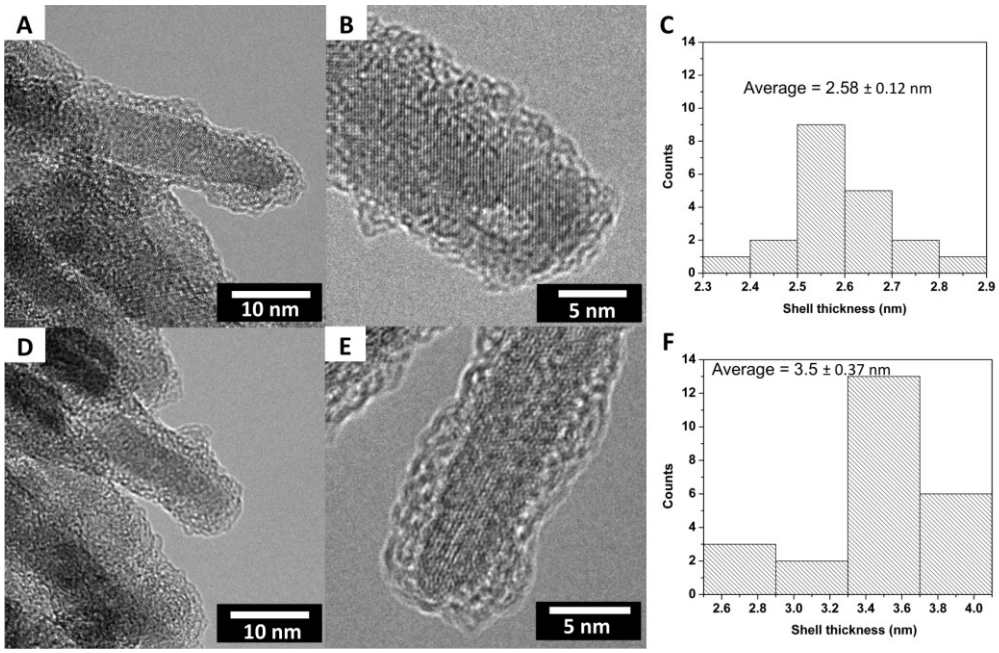

Figure 4-3: (A, B) HR-TEM images of ND-Fe_3O_4@mC-4 nanorods. (C) Carbon shell thickness distribution of ND-Fe_3O_4@mC-4 nanorods. (D, E) HR-TEM images of ND-Fe_3O_4@mC-12 nanorods. (F) Carbon shell thickness distribution of ND-Fe_3O_4@mC-12 nanorods.

The carbon content was determined by thermogravimetric analysis (TGA) for samples obtained from different coating times (Figure 4-4). As expected, the highest carbon content (*i.e.,* 38.3 wt %) was noted for the sample obtained from the longest coating time (*i.e.,* 12 hours) with the carbon layer thickness of 3.5 ± 0.37 nm. For samples obtained from 2 and 4 hour coating times the weight percent carbon was 14.5 wt % and 20.8 wt %, respectively.

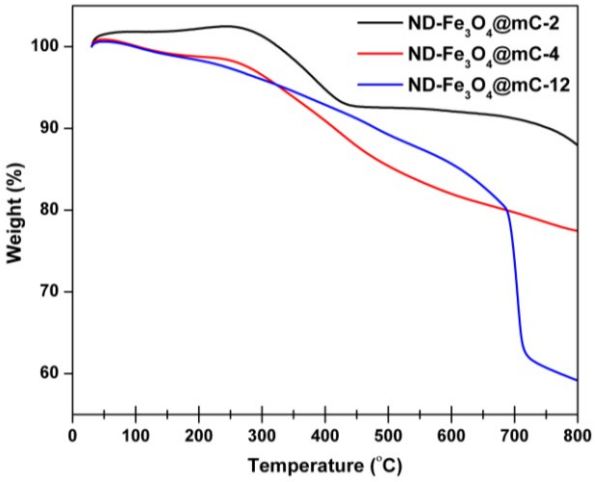

Figure 4-4: TGA curves for ND-Fe_3O_4@mC nanorods with different coating times (heating rate 10 ˚C/min, atmosphere N_2).

Nitrogen sorption analysis was used to evaluate the porosity of the carbon shell for the samples obtained from different coating times. The specific surface area, pore volume, and average pore diameter of the carbon shells are summarized in Table 4-1. The corresponding isotherms (Figures 4-5A-C) show a distinct hysteresis loop at high relative pressure, consistent with the materials being mesoporous.[229] Evaluation of ND-Fe_3O_4@mC-2 nanorods indicates it possesses porosity made up of uniform mesopores of diameters *ca.* 3.8 nm, a Brunauer-Emmett-Teller (BET) surface area of 121 $m^2\ g^{-1}$ and pore volume of 0.54 $cm^3\ g^{-1}$.

Table 4-1: Textural properties of ND-Fe_3O_4@mC nanorods with different coating times

Catalyst	BET surface area ($m^2\ g^{-1}$)	Pore radius (nm)	Pore volume ($cm^3\ g^{-1}$)
ND-Fe_3O_4@mC-2	121	1.9	0.54
ND-Fe_3O_4@mC-4	120	1.7	0.57
ND-Fe_3O_4@mC-12	130	1.7	0.52

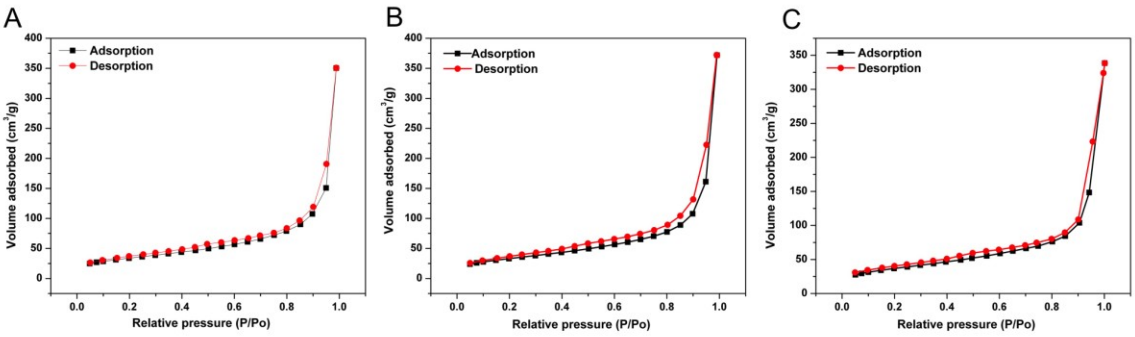

Figure 4-5: Nitrogen adsorption-desorption isotherms for (A) ND-Fe_3O_4@mC-2 nanorods, (B) ND-Fe_3O_4@mC-4 nanorods and (C) ND-Fe_3O_4@mC-12.

X-ray diffraction (XRD) patterns for ND-Fe_3O_4@mC-2 and α-Fe_2O_3 nanorods are shown in Figure 4-6A. The XRD pattern of the precursor nanorods agrees well with α-Fe_2O_3 (JCPDS no.89-8103).[268] In contrast, the pattern obtained for ND-Fe_3O_4@mC-2 nanorods is consistent with pure Fe_3O_4 (JCPDS no.65-3107), indicating that the α-Fe_2O_3 nanorod precursors transform into the face-centered cubic phase of magnetite upon carbothermic reduction.[269] Figure 4-7A and 4-8A show corresponding XRD patterns for ND-Fe_3O_4@mC-4 and ND-Fe_3O_4@mC-12, respectively, which is similar to that of ND-Fe_3O_4@mC-2. The conspicuous absence of reflections arising from graphite in the XRD pattern are consistent with the carbon layer being amorphous and is in agreement with HR-TEM and Raman analyses (Figure 4-9). The Raman spectra for all three samples show features at 1331 and 1578 cm^{-1} that correspond to the D band and G band, respectively. The D band arises from the A_{1g} breathing mode from sp^3 carbon components, while the G peak corresponds to in-plane stretching of bonds involving sp^2 carbon atoms.[202]

To gain insight into the elemental composition of the presented nanorods we employed energy-dispersive X-ray (EDX) analysis and X-ray photoelectron spectroscopy (XPS). EDX (Figures 4-6B, 4-7B and 4-8B) and survey XPS (Figure 4-10, 4-11 and 4-12) analyses of ND-Fe_3O_4@mC-2, ND-Fe_3O_4@mC-4 and ND-Fe_3O_4@mC-12 indicate the nanorods contain only N, C, O and Fe at the sensitivity of the methods that confirms the presence of Fe and O from the core and ND carbon from the shell (n.b. The Cu signal observed arises from the supports).

The Fe 2p region of the high-resolution XP spectrum of ND-Fe_3O_4@m C-2, ND-Fe_3O_4@mC-4 and ND-Fe_3O_4@mC-12, give the oxidation state of the Fe atoms in the nanorods (Figures 4-6C, 4-7C and 4-8C). The signal is not intense for all three samples and we assume it is resulted from carbon coating. Peak deconvolution yields three components centered at 710.5, 713, and 723.3 eV that are confidently assigned to Fe^{+3} $2p_{3/2}$, Fe^{+2} $2p_{3/2}$ and Fe^{+2} $2p_{1/2}$, respectively.[270] These emissions confirm the reduction of Fe^{3+} to Fe^{2+} due to thermal treatment and are consistent with the formation of Fe_3O_4.[270]

Furthermore, the N 1s region of the high-resolution XPS spectrum of all three samples (Figures 4-6D, 4-7D and 4-8D) indicates two forms of nitrogen are present: pyrrolic N (399.9 eV) and pyridinic N (398.1 eV).[271] Both are catalytically active site for oxygen reduction.[272]

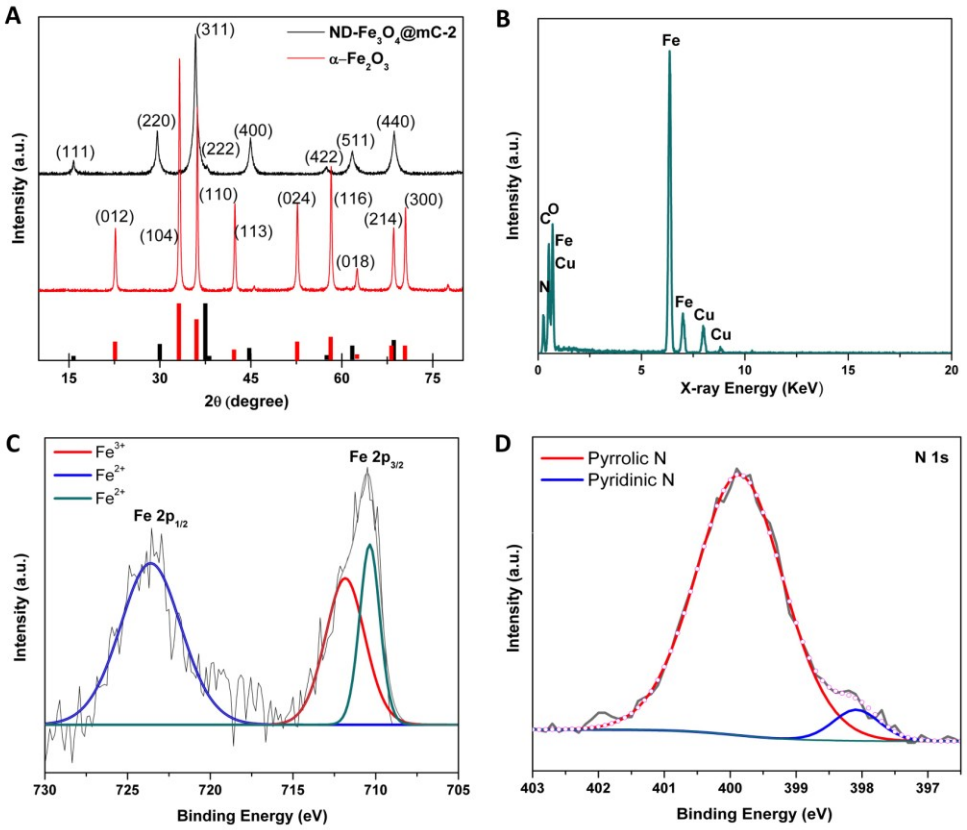

Figure 4-6: (A) XRD patterns for ND-Fe_3O_4@mC-2 and α-Fe_2O_3 nanorods. (B) EDX spectrum from ND-Fe_3O_4@mC-2 nanorods. (C, D) High-resolution XPS spectra for ND-Fe_3O_4@mC-2 nanorods: (C) Fe 2p; (D) N 1s.

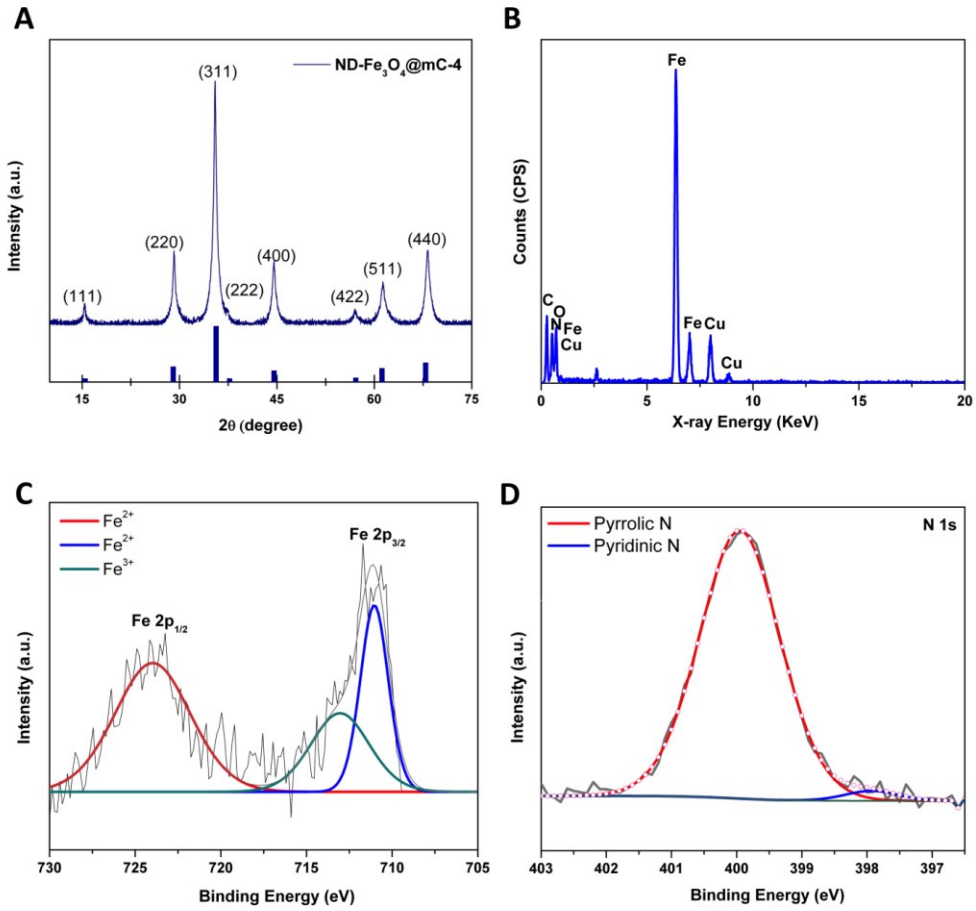

Figure 4-7: (A) XRD patterns for ND-Fe_3O_4@mC-4 and. (B) EDX spectrum from ND-Fe_3O_4@mC-4 nanorods. (C, D) High-resolution XPS spectra for ND-Fe_3O_4@mC-4 nanorods: (C) Fe 2p; (D) N 1s.

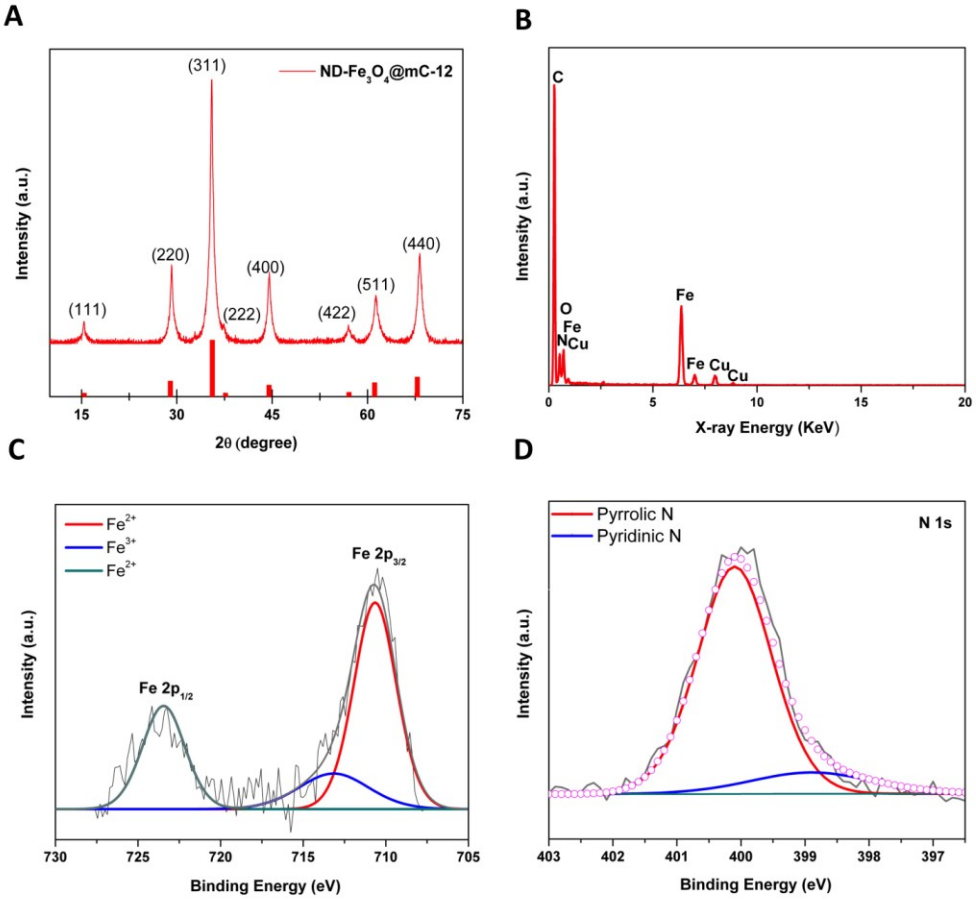

Figure 4-8: (A) XRD patterns for ND-Fe_3O_4@mC-12. (B) EDX spectrum from ND-Fe_3O_4@mC-12 nanorods. (C, D) High-resolution XPS spectra for ND-Fe_3O_4@mC-12 nanorods: (C) Fe 2p; (D) N 1s.

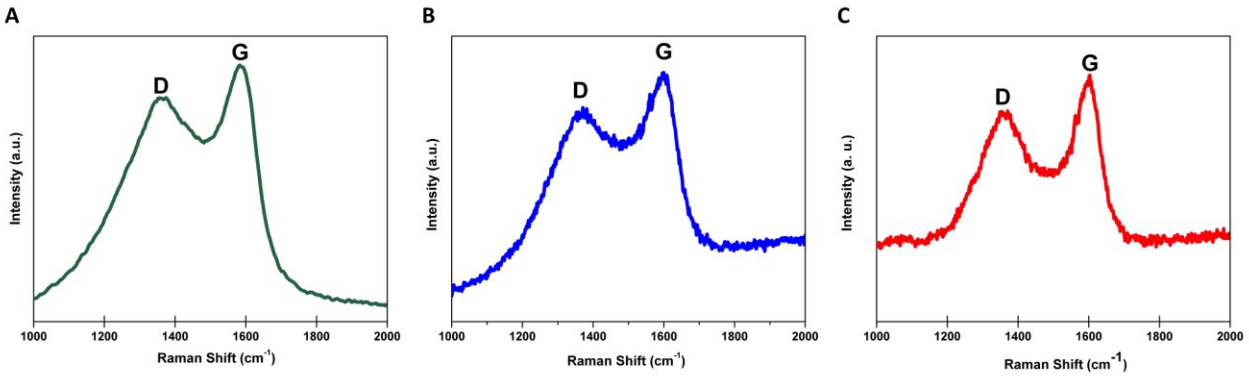

Figure 4-9: Raman spectra for (A) ND-Fe_3O_4@mC-2, (B) ND-Fe_3O_4@mC-4 nanorods, and (C) ND-Fe_3O_4@mC-12 nanorods.

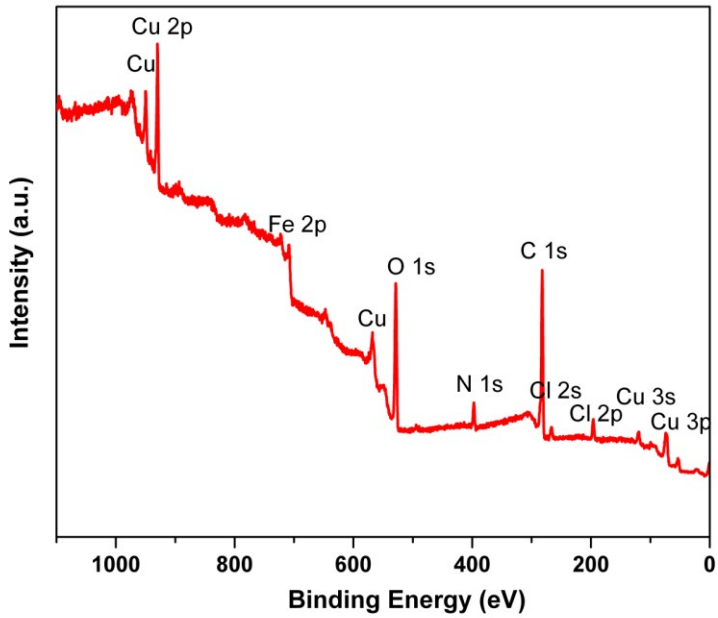

Figure 4-10: XPS survey spectrum for ND-Fe_3O_4@mC-2 nanorods.

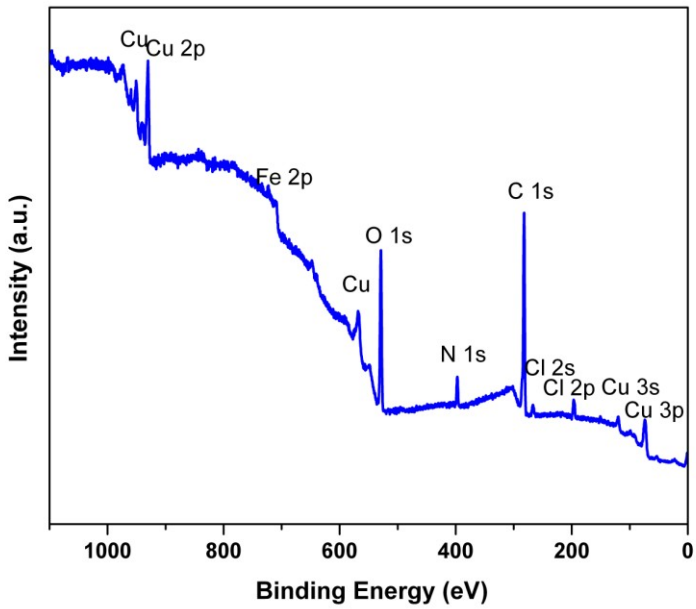

Figure 4-11: XPS survey spectrum for ND-Fe_3O_4@mC-4 nanorods.

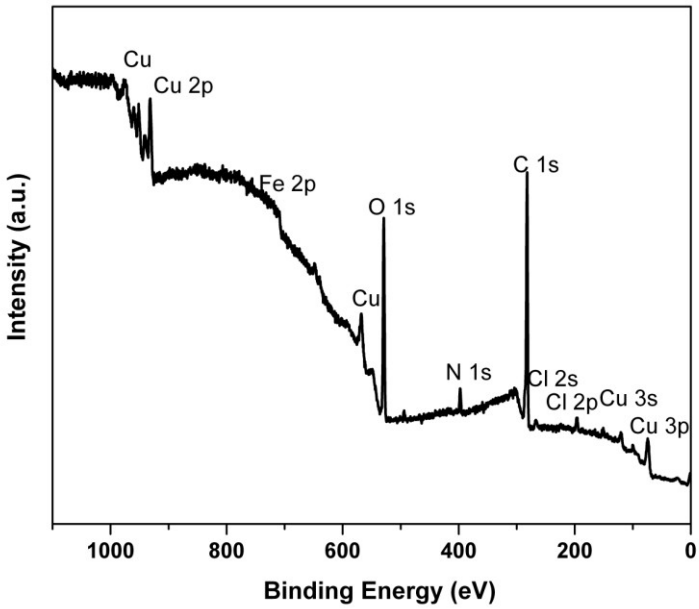

Figure 4-12: XPS survey spectrum for ND-Fe_3O_4@mC-12 nanorods.

In addition the C1s region of the high-resolution XPS spectra for all three samples exhibits three main components (Figure 4-13). The emissions may be assigned to of sp^2 C-C (284.57 eV), as well as C-O and C-N (285.45 eV) and C=N/C=O (288.2 ± 0.1 eV) species.[228]

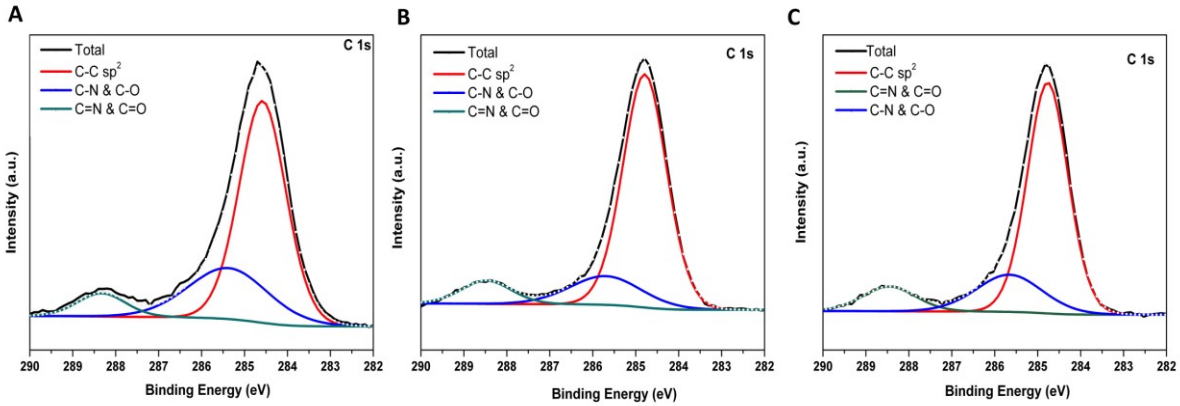

Figure 4-13: High-resolution C 1s XPS spectra for (A) ND-Fe_3O_4@mC-2 nanorods, (B) ND-Fe_3O_4@mC-4 nanorods and (C) ND-Fe_3O_4@mC-12 nanorods.

The ND-Fe_3O_4@mC samples exhibited ORR catalytic activity. Figure 4-14 shows the cyclic voltammograms (CV) results recorded in Ar and O_2-saturated 0.1 M KOH for ND-Fe_3O_4@mC-2, ND-Fe_3O_4@mC-4, and ND-Fe_3O_4@mC-12 at 10 mV s^{-1}. Featureless voltammetric currents are observed in the Ar-saturated electrolyte, which are shown within the potential range of -0.7 to 0.7 V *vs.* Hg/HgO. The increase in the current at 0.6 V arises as a result of the oxygen evolution reaction (OER). An irreversible cathodic peak is present in the O_2-saturated CVs indicating that ORR occurs for ND-Fe_3O_4@mC-2 (-0.21 V *vs.* Hg/HgO), ND-Fe_3O_4@mC-4 (-0.23 V *vs.* Hg/HgO), and ND-Fe_3O_4@mC-12 (-0.24 V *vs.* Hg/HgO). No other cathodic or anodic

wave is present indicating all ND-Fe_3O_4@mC samples are stable toward oxidation and reduction cycling. This is consistent with other reports, carbon supports or coatings hinder the oxidation and reduction of Fe-based catalysts in alkaline solutions.[265,273,274] Quasi-rectangular voltammograms afford electrochemical characterization of the surface area of the mesoporous carbon shell, which is in consistent with the BET results. Also, the higher degree of hydrophilicity for the C-N bond (Figure 4-13) present in ND-carbon shell results in a larger CV baseline current in comparison to the non-doped carbon shell.[274]

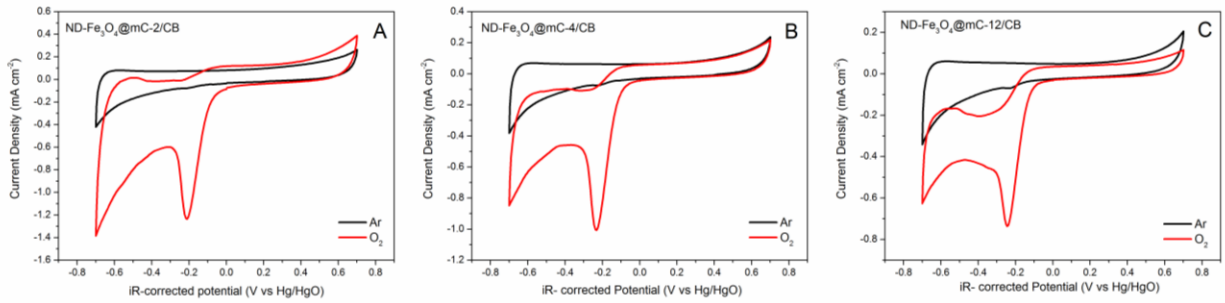

Figure 4-14: CVs for (A) ND-Fe_3O_4@mC-2/CB, (B) ND-Fe_3O_4@mC-4/CB and (C) ND-Fe_3O_4@mC-12/CB in Ar-saturated and O_2-saturated 0.1 M KOH at 10 mV s^{-1}.

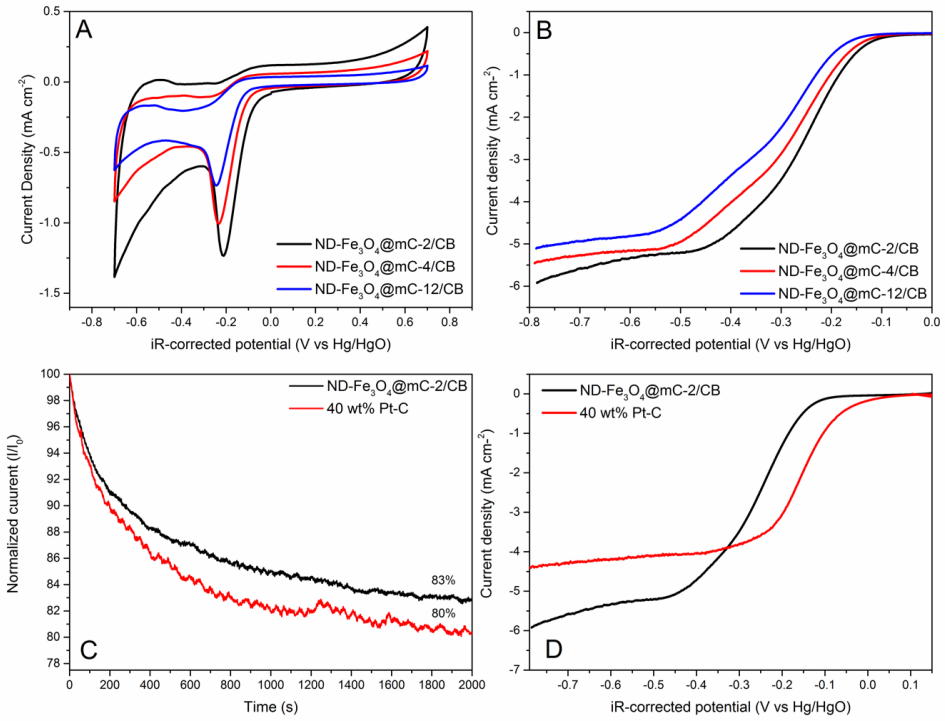

Figure 4-15: (A) CVs for ND-Fe_3O_4@mC-2/CB, ND-Fe_3O_4@mC-4/CB and ND-Fe_3O_4@mC-12/CB at 10 mV s^{-1}. (B) LSV curves for ND-Fe_3O_4@mC-2/CB, ND-Fe_3O_4@mC-4/CB, and ND-Fe_3O_4@mC-12/CB at 1600 rpm and 10 mV s^{-1}. (C) Current–time (i-t) chronoamperometric responses for ND-Fe_3O_4@mC-2/CB and 40 wt% Pt-C at -0.3 V vs Hg/HgO at 1600 rpm. (D) LSV curves for ND-Fe_3O_4@mC-2/CB and 40 wt% Pt-C at 1600 rpm and 10 mV s^{-1} (O_2-saturated 0.1 M KOH was used for all the experiments).

Figures 4-15A and B presents a comparison of the CV and linear sweep voltammetry (LSV) results in O_2-saturated solutions for the three samples (all measurements were repeated for at least three times). There is an increase in the ORR onset potential and the ORR peak current density as the carbon coating time is decreased from 12 to 2 hours. ND-Fe_3O_4@mC-2 (i.e., thinnest carbon coating) shows the most positive onset potential (-0.135 V *vs.* Hg/HgO) and half wave potential (-0.261 V *vs.* Hg/HgO); this is also seen in the CV results. At -0.7 V, the limiting currents (i_l) are -5.59 mA cm^{-2} (ND-Fe_3O_4@mC-2), -5.28 mA cm^{-2} (ND-Fe_3O_4@mC-4) and -4.93 mA cm^{-2} (ND-Fe_3O_4@mC-12) indicating ND-Fe_3O_4@mC-2 is the best ORR catalyst among the three. This indicates that the catalytic activity is determined by the carbon shell thickness on the surface of the Fe_3O_4 core. Table 4-2 summarizes the ORR onset potentials and half wave potentials for the three samples.

Table 4-2: Oxygen electrode catalyst activities

Catalyst	ORR onset potential (V)	ORR $E_{1/2}$ (V)	Average *n*
ND-Fe_3O_4@mC-2/CB	-0.135	-0.261	3.32
ND-Fe_3O_4@mC-4/CB	-0.161	-0.286	2.76
ND-Fe_3O_4@mC-12/CB	-0.182	-0.312	2.62

n: average number of electrons transferred. $E_{1/2}$: half-wave potential.

LSV curves and Koutecky-Levich (K-L) plots for each sample are provided in Figure 4-16. Employing the K-L equations,[205] the average number of electrons transferred (n) at different potentials is 3.32, 2.76, 2.62 for ND-Fe_3O_4@mC-2, ND-Fe_3O_4@mC-4, and ND-Fe_3O_4@mC-12, respectively. The n value for ND-Fe_3O_4@mC-2 is similar to those reported for other Fe_3O_4-based catalysts, however samples with thicker coatings have somewhat lower n values (Table 4-3).[260,273–275] These results suggest that for all catalysts investigated ORR is proceeding *via* both accepted pathways (*i.e.,* 2-electron and 4-electron). The 4-electron pathway is dominant at more negative potentials for the ND-Fe_3O_4@mC-2 sample, which has the thinnest carbon shell and it indicates that ORR is happening much easier on the ND-Fe_3O_4@mC-2 compared to the other two catalysts.

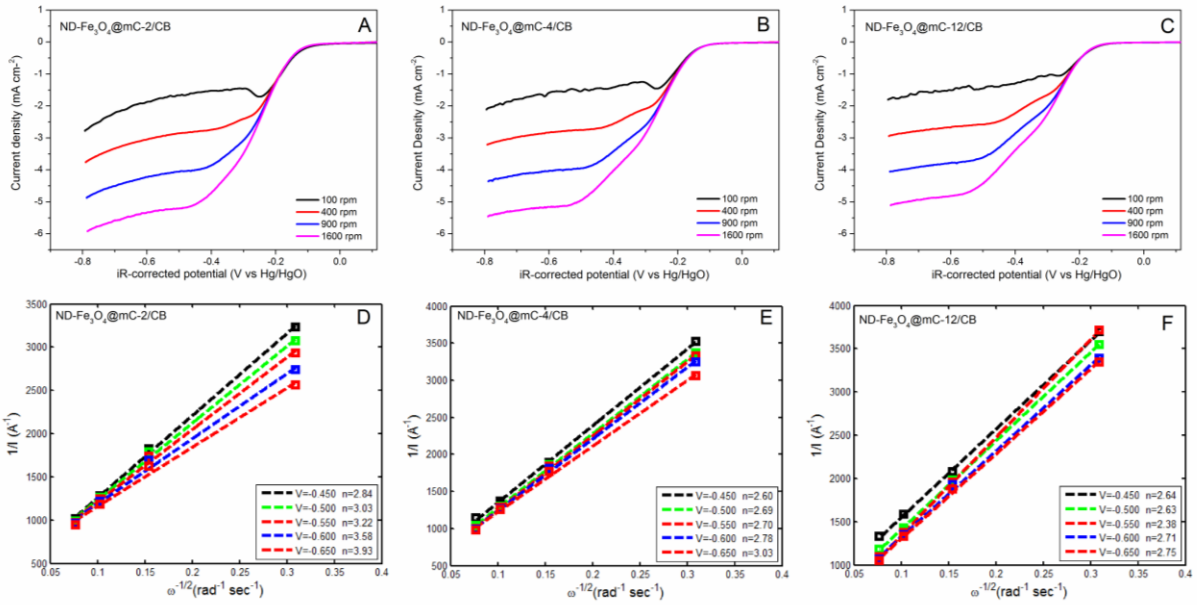

Figure 4-16: LSV curves for (A) ND-Fe_3O_4@mC-2/CB, (B) ND-Fe_3O_4@mC-4/CB and (C) ND-Fe_3O_4@mC-12/CB in O_2-saturated 0.1 M KOH at 10 mV s^{-1} at indicated rotation rates. K-L plots for (D) ND-Fe_3O_4@mC-2/CB, (E) ND-Fe_3O_4@mC-4/CB and (F) ND-Fe_3O_4@mC-12/CB. The number of electrons transferred (n) is calculated for different potentials.

Table 4-3: Comparison of ORR activity for ND-Fe_3O_4@mC with various non-precious metal catalysts in the recent literature

References	Materials	Onset potential (V *vs.* Hg/HgO)	$E_{1/2}$ (V *vs.* Hg/HgO)	i_l at 1600 rpm (mA cm^{-2})	Mass loading (mg cm^{-2})	Average n
This study	ND-Fe_3O_4@mC-2	-0.135	-0.261	5.59	0.1	3.32
[274]	Fe_3O_4-CN_x	0.024	-0.244	~4.00	ND	3.40
[273]	Fe@ Fe_3O_4	0.136	ND	5.79	0.2	2.50-3.50
[271]	Fe_3O_4/N-GA	-0.091	ND	~4.50	ND	3.09-3.80
[260]	Fe_3O_4/graphene	-0.258	ND	~4.00	ND	ND

*ND: not determined

i_l: limiting current density. n: average number of electrons transferred. $E_{1/2}$: half-wave potential.

In order to evaluate the short-term time-drifting stability of the catalysts, current time chronoamperometric responses for the best performing catalyst (ND-Fe_3O_4@mC-2) are compared with the baseline 40 wt % Pt-C catalyst in a O_2-saturated 0.1 M $KOH_{(aq)}$ at 1600 rpm. Figure 4-15C shows a continuous O_2 reduction at -0.3 V *vs.* Hg/HgO for ND-Fe_3O_4@mC-2 results in a 17% loss in normalized current density after 2000 s. The corresponding current density loss for 40 wt % Pt-C catalyst under the same conditions is slightly higher at 20 %. Based on this observation, the short term stability of present ND-Fe_3O_4@mC-2 is comparable to the standard commercial 40 wt% Pt-C baseline catalyst. LSV analysis performed at 1600 rpm (Figure 4-15B) provides further insight. Comparing data for ND-Fe_3O_4@mC-2 with that obtained for 40 wt % Pt-C it is noted that the ORR onset potential for ND-Fe_3O_4@mC-2 is only 88 mV more negative than the baseline catalyst. However, the i_l is increased by 14% for ND-Fe_3O_4@mC-2 relative to the Pt-C system – this indicates superior ORR performance for ND-Fe_3O_4@mC-2 when compared at same mass loading.

The long-term performance of the best performing catalyst (ND-Fe_3O_4@mC-2) was evaluated using repetitive CV analysis (from -0.7 to 0.2 V vs. Hg/HgO in O_2-staurated 0.1 M KOH) for 5000 cycles. As shown in Figure 4-17, there is an obvious decrease (~30% at the peak potential -0.34 V) in the ORR performance after the first 500 cycles. However, the ORR current density and onset potential do not change over the next 4500 cycles. These results indicate high long-term ORR stability of ND-Fe_3O_4@mC-2 after 25 hours CV test in O_2-saturated alkaline solution.

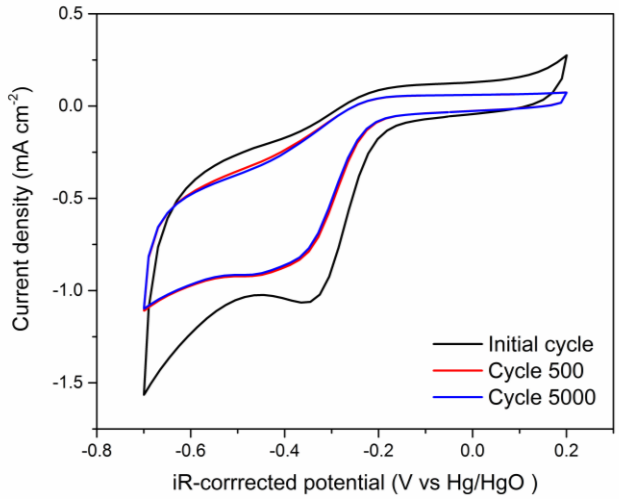

Figure 4-17: CV curves for ND-Fe_3O_4@mC-2 cycled in O_2-saturated 0.1 M KOH at 100 mV s^{-1}.

Despite decades of research on ORR using Fe-oxide based catalysts with carbon supports, the catalyzed ORR mechanism and the active sites on the Fe-based catalysts are not fully understood.[251,273,274] The ORR activity for ND-Fe_3O_4@mC is believed to originate from different sources: i) Nitrogen on the surface of the carbon shell on the nano-sized Fe_3O_4 core provides ORR active sites and seems to be one of the main reasons for the effectiveness of the catalyst.[251,273,274] ii) The conductive and high surface area carbon shell and the presence of hydrophilic C-N bonds further enhance ORR.[264,274] iii) Oxygen chemisorption is facilitated by the Fe_3O_4 nanorods by reducing the ORR activation energy.[264] Therefore, the activity of ND-Fe_3O_4@mC is optimized for a 2-hour coating time. Thicker carbon layer may block the ORR active sites present on the Fe_3O_4 surface and inhibit further access of the electrolyte to the

core. Thinner carbon coating layers (<2 hours coating time) increase the chance of Fe_3O_4 nanoparticles agglomeration and are likely to form non-uniform carbon shells.

4.4 Investigation of Component Synergies

To better understand the function of Fe_3O_4 nanorods as core and carbon as shell, and to clarify if there is any synergistic effect between Fe_3O_4 core and carbon shell, bare Fe_3O_4 nanorods and hollow carbon shell were also prepared. For this purpose, ND-Fe_3O_4@mC-2 was heated at 300 ˚C for 30 min under air atmosphere (heating rate 10 ˚C/min) to burn off the carbon coating. HR-TEM images (Figure 4-18 A and B) show no carbon coating on the surface of nanorods. The XRD pattern after the burning off the carbon is shown in Figure 4-18 C that reveals the appearance of characteristic peaks of α-Fe_2O_3 upon oxidation of Fe_3O_4 under the air. However, Fe_3O_4 is still the dominant phase. The carbon content was determined by thermogravimetric analysis (TGA) for the sample obtained after burning off the carbon shell (Figure 4-14 D). As expected, the carbon content for ND-Fe_3O_4@mC-2 nanorods (*i.e.,* 14.5 wt %) decreased substantially after burning off the carbon layer to a value of 1.5 wt %. Although, carbon is still present, it is much lower than other samples and comparing its electrochemical performance to other prepared catalysts help us understand if there is any synergic effect between Fe_3O_4 nanorods as core and carbon as shell.

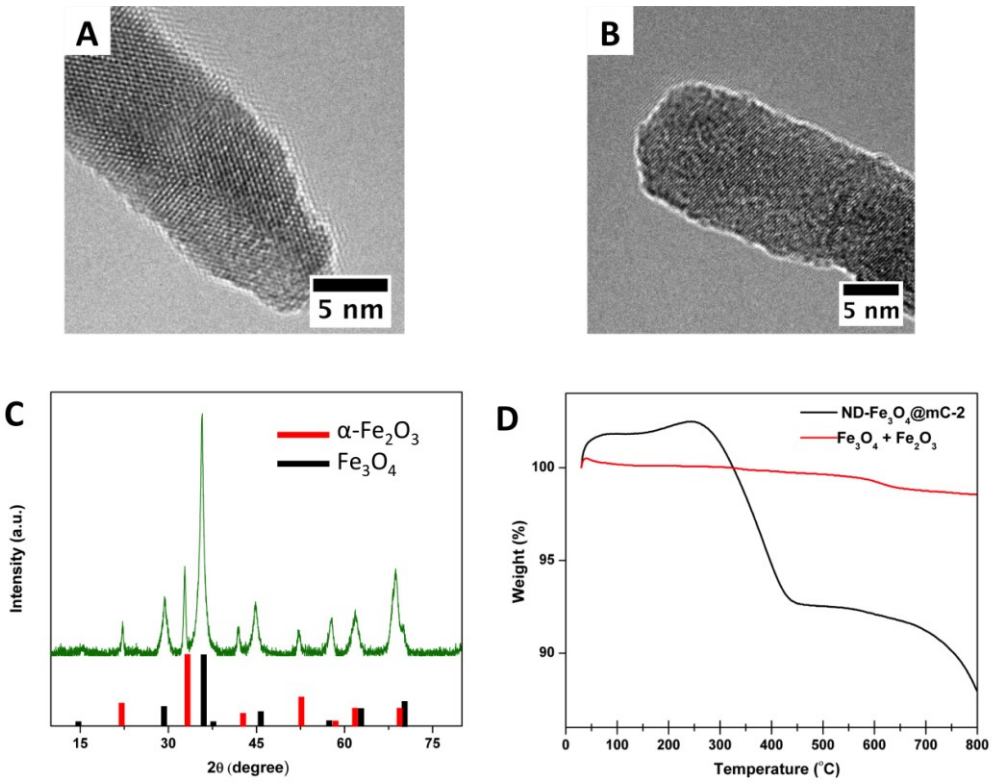

Figure 4-18: (A, B) HR-TEM images of ND-Fe_3O_4@mC-2 nanorods after burning of the carbon coating. (C) XRD pattern for ND-Fe_3O_4@mC-2 nanorods after burning of the carbon coating. (D) TGA curves for ND-Fe_3O_4@mC-2 nanorods before (black) and after (red) burning off the carbon shell (heating rate 10 ˚C/min, atmosphere N_2).

ND-Fe_3O_4@mC-2 was also treated with 6 M HCl to dissolve the Fe_3O_4 core to obtain hollow carbon nanorods. However, HR-TEM images of the sample after acid treatment (Figure 4-19) reveal that the structure collapsed during treatment. The obtained carbon material is also considered as a reference for comparing with other carbon coated samples for future electrochemical test. Although the morphology

was not preserved during acid treatment, the obtained carbon material could be a good reference to be compared to the other samples.

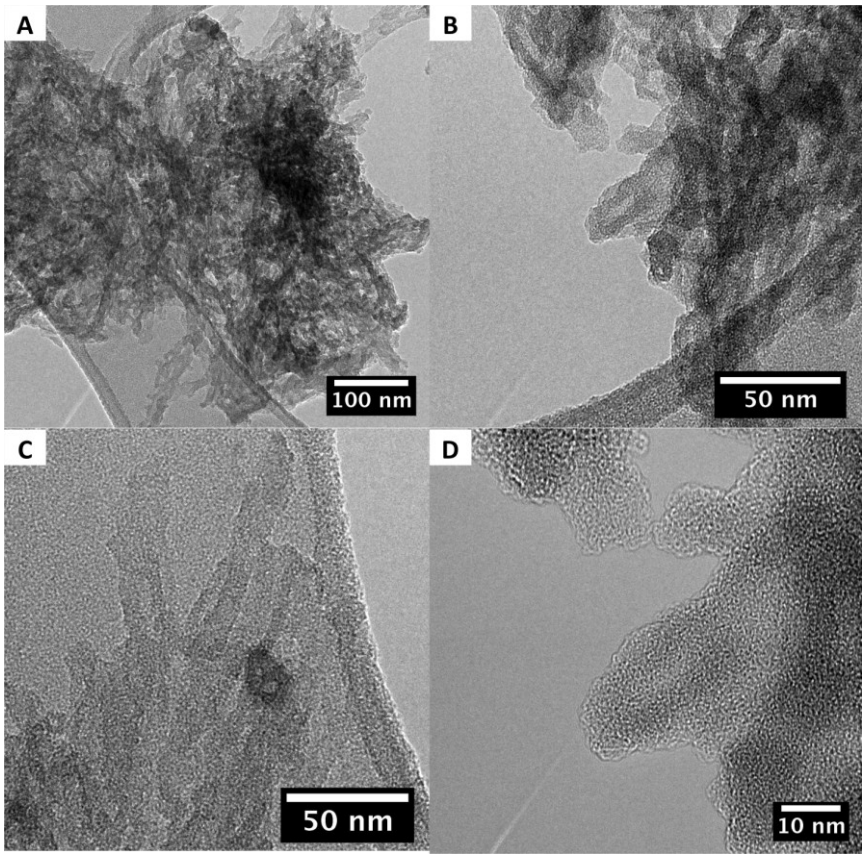

Figure 4-19: (A-D) HR-TEM images of ND-Fe_3O_4@mC-2 nanorods after acid treatment to dissolve Fe_3O_4 core.

The electrochemical performances of bare Fe_3O_4 nanorods and hollow carbon structures were investigated using CV and linear sweep voltammetry (LSV). However, the results were inconclusive and investigations to obtain a conclusive

result regarding the synergistic effect between bare Fe_3O_4 and hollow carbon are in progress.

4.5 Conclusions

In summary, Fe_3O_4 nanorods coated with a ND mesoporous carbon shell (ND-Fe_3O_4@mC) have been successfully prepared using a new microwave-assisted method. The resulting materials were tested for ORR and the effect of carbon shell thickness on ORR activity of the electrocatalyst was studied. The results demonstrate the best electrocatalyst performance is realized when thinner nitrogen doped carbon shells are used; ND-Fe_3O_4@mC-2 (onset potential -0.135 V *vs*. Hg/HgO) in an alkaline electrolyte, i_l (-5.59 mA cm^{-2}). These materials show excellent long-term stability (up to 5000 cycles) in alkaline solutions and initial studies indicate these are promising materials for ORR.

Chapter 5:

Synthesis and Characterization of Gold/Silica Hybrid Nanostructures

5.1 Introduction

Interest in nanoparticles can, in part, be attributed to the exquisitely adjustable properties of these small materials that are different from those of their corresponding bulk materials.[276–278] Metal nanoparticles such as gold and silver show intriguing properties leading to applications in catalysis,[279] optics,[280] magnetism,[281,282] and sensors.[283] The surface plasmon resonance (SPR) effect for conductive nanoparticles leads to outstanding optical properties, with a spectrally sensitive response to their shape, size, metal composition and environment.[284] As discussed in Chapter 1, Section 1.6.1, gold nanoparticles (GNPs) exhibit a strong absorption band in the visible region (400-700 nm) and a distinct color. This absorption is due to the surface plasmon resonance (SPR), which is defined as resonance of the electromagnetic field with the collective oscillation of electrons in the conduction band (see Chapter 1, Figure 1-38). Briefly, when a metal particle is exposed to light, the oscillating electromagnetic field of the light induces a collective coherent oscillation of the free conduction band electrons in the metal. This induced oscillation around the particle surface leads to charge separation with respect to the ionic lattice, forming a dipole oscillation along the direction of the electric field of the light. The amplitude of the oscillation reaches a maximum at a specific frequency and is referred to as surface plasmon resonance (SPR). In nano regime, when the nanoparticle size is comparable to or smaller than the wavelength of light this phenomenon is termed localized surface plasmon resonance (LSPR). The SPR band

intensity and wavelength depends on several factors including metal type, particle size, shape, and structure, as well as composition and dielectric constant of the surrounding medium; it is generally described and understood using Mie theory.[285,286]

Gold nanorods (GNRs) show two distinct LSPR bands: transverse and longitudinal (Figure 5-1).[287] The transverse band (typically located at ca. 525 nm) is weak and corresponds to light absorption/scattering along the short axis of the GNRs. The longitudinal band correspond to light absorption/scattering along the long axis of GNRs. This band is much stronger and tunable from the visible to near infrared (NIR) regions as the aspect ratio (length/radius) of the nanorods is changed.[175]

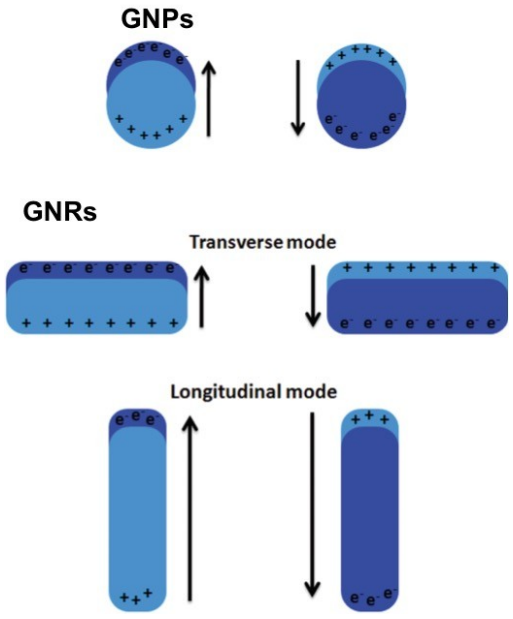

Figure 5-1: Pictorial illustration of surface plasmon resonance in spherical GNPs and GNRs.[287] Reprinted (adapted) with permission from ref 287.

GNPs/GNRs can also convert the light adsorbed into heat *via* a series of nonradiative processes. The El-Sayed group has studied this process (known as the photothermal effect) extensively.[285] In this effect, the energy transformation process starts by an increase in the temperature of the electrons to ~1000 K as a result of increased electron-electron collisions. The electrons subsequently transfer the thermal energy to the lattice in the form of phonons (i.e., lattice vibrations) resulting in a hot lattice with temperature rises on the order of few tens of degrees. Depending on the energy content of the system, three subsequent processes can occur: 1. The lattice can cool off by passing heat to the surroundings *via* phonon-phonon relaxation. 2. The lattice heat can lead to particle melting. 3. The heat content can cause particle ablation. The release of heat via phonon-phonon relaxation can be sufficient to destroy physically adsorbed or chemically attached cancer cells and forms the basis for photothermal cancer treatment. In order for the first relaxation process dominates continuous wave (CW) lasers are used to excite the electron oscillations.[285]

Several methods have been developed and reported for synthesis of GNPs. As mentioned in Chapter 1, Section 1.6, Michael Faraday prepared GNPs via the reduction of an aqueous solution of chloroaurate ($HAuCl_4$) with phosphorus dissolved in carbon disulfide.[288] Later in 1915, Turkevich developed one of the most popular methods for GNPs synthesis using citrate reduction of $HAuCl_4$ in boiling water (Figure 5-2 and Equation (5-1)).[289,290] This method provides GNPs with diameters of ~20 nm. Citrate ions act as a reducing and capping agent. Although the

particles prepared *via* this method are monodispersed, the low yield and restriction of using only water as the solvent are the main drawbacks. Later, Frens achieved control over GNPs size by changing the seed ratio of gold salt to sodium citrate.[291]

$$2AuCl_4^- + 3Na_3C_6H_5O_7 \longrightarrow 2Au + 3Na_3C_5H_6O_5 + 8Cl^- + 3H^+ + 3CO_2\uparrow \quad (5\text{-}1)$$

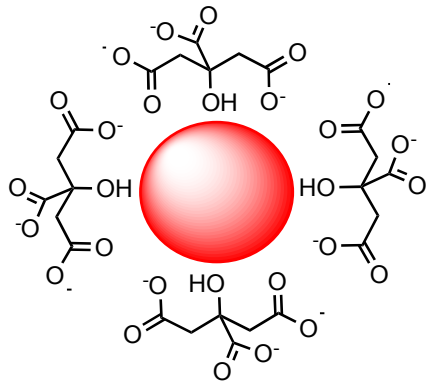

Figure 5-2: Synthesis of citrate capped GNPs *via* Turkevich method.

In 1994, Brust and Schiffrin reported a two-phase synthetic strategy utilizing strong thiol-gold interactions to protect GNPs with thiol ligands (Figure (5-3) and equations (5-2) and (5-3)).[292] In Brust method, $AuCl^{4-}$ is transferred from aqueous phase to toluene using the surfactant tetraoctylammonium bromide (TOAB) and then reduced by sodium borohydride ($NaBH_4$) in presence of dodecanthiol. Compared to Turkevich method, this approach provides smaller GNPs in the range of 1.5 - 5 nm that are stabilized by dodecanthiol ligands that render them compatible with organic solvents.

$$AuCl_4^-(aq) + N(C_8H_{17})_4^+(C_6H_5Me) \rightarrow N(C_8H_{17})_4^+ AuCl_4^-(C_6H_5Me) \quad (5\text{-}2)$$

$$mAuCl_4^-(C_6H_5Me) + nC_{12}H_{25}SH(C_6H_5Me) + 3me^- \rightarrow (Au_m)(C_{12}H_{25}SH)_n(C_6H_5Me) + 4mCl^-(aq) \quad (5\text{-}3)$$

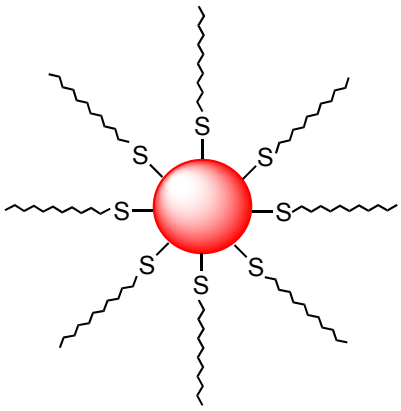

Figure 5-3: Synthesis of dodecanthiol-capped GNPs *via* Brust-Schiffrin method.

One of most common synthetic approaches that offer substantially more control over GNP size involves seeded growth (or seed mediated growth). Compared to the previous approaches, this method offers compatibility with water, room temperature synthesis and requires only a small number of (cost-effective) reagents. To achieve seeded growth, small gold particles are prepared first and then used as seeds (nucleation sites) for the preparation of larger size particles. An understanding of role of the seeds can be drawn from the LaMer model for burst nucleation discussed in Chapter 1, Section 1.1.

In 2001, Murphy *et al.* reported the synthesis of uniformly sized GNPs in the size range of 5 - 40 nm.[293] They used 3.5 nm diameter citrate capped GNPs prepared using a sodium borohydride reducing agent as seeds. During the growth stage, a

weak reducing agent (ascorbic acid (AA)) was used to reduce more gold precursor and offers more control over the growth condition.

Later, Murphy *et al.* showed that through systematic variation of experimental parameters and introducing a capping agent to the system, different shape of GNPs (rod, rectangle, cube, triangle and starlike) can be achieved.[294]

During the growth stage cetyltrimethylammonium bromide (CTAB) was used as a surfactant/capping agent; ascorbic acid (AA) and in some cases small quantity of $AgNO_3$ was introduced to their system. They showed that the morphology and dimension of the GNPs depend on several parameters including: the concentration of the seed particles, CTAB, AA, and Au^{3+}. The authors believed that the formation of different shapes of GNPs resulted from the interplay between the faceting tendency of the stabilizing agent and the growth kinetics. It is believed that the fine gold seeds produced in the presence of CTAB are faceted with the most stable {111} faces exposed.[294,295] Considering this fact, CTAB molecules bind more strongly to the {100} as less stable face compared to {111}. As a result, lower CTAB and higher AA concentration condition favor the faster formation and deposition of Au^0 onto the {111} faces, which leads to the formation of {100} faces and producing cubic shapes nanoparticles. They showed that by increasing CTAB concentration rectangular to cylindrical rod-shapes are formed. The proposed mechanism of surfactant-directed metal nanorods growth is shown in Figure 5-4.[175] The role of $AgNO_3$ is not understood yet, however, El-Sayed *et al.* proposed that silver ions could assist in the template elongation by pairing with Br^- ion of CTAB.[296]

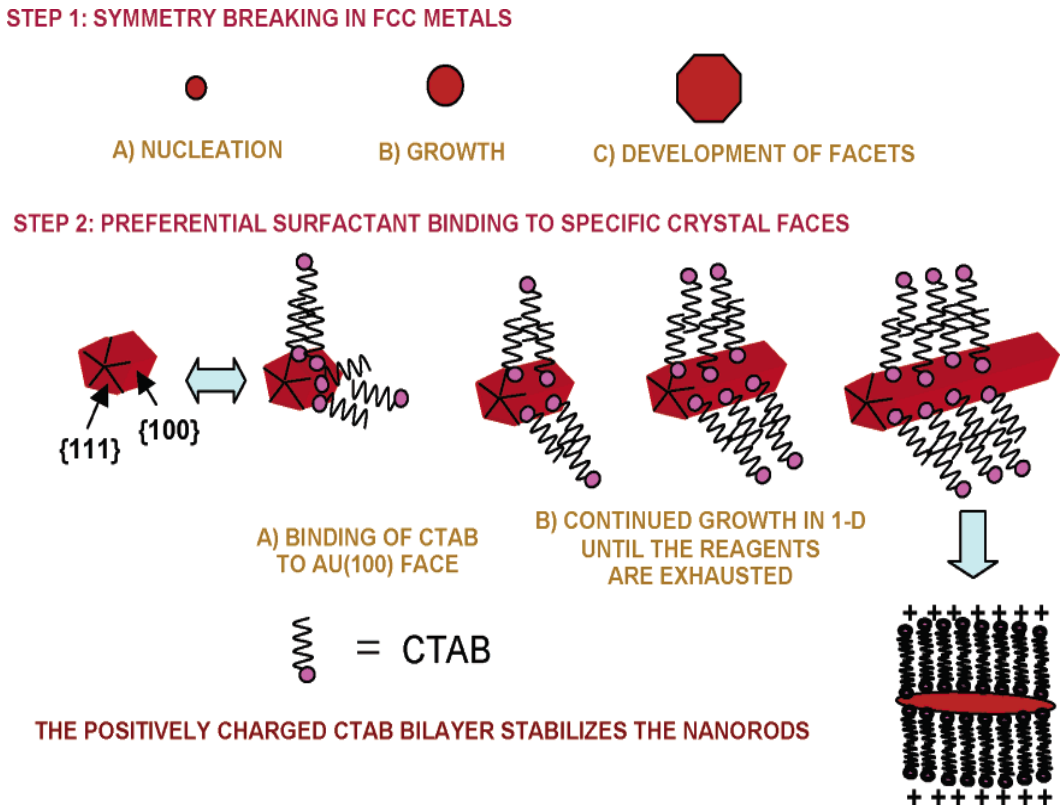

Figure 5-4: Surfactant-directed metal nanorod growth mechanism proposed by Murphy et al.[175] Reprinted (adapted) with permission from ref 175.

Among all the methods proposed for GNRs synthesis, the seed-mediated method developed by the Murphy group is the most popular. Figure 5-5 shows a detailed schematic of using this method for synthesis of GNRs.[297]

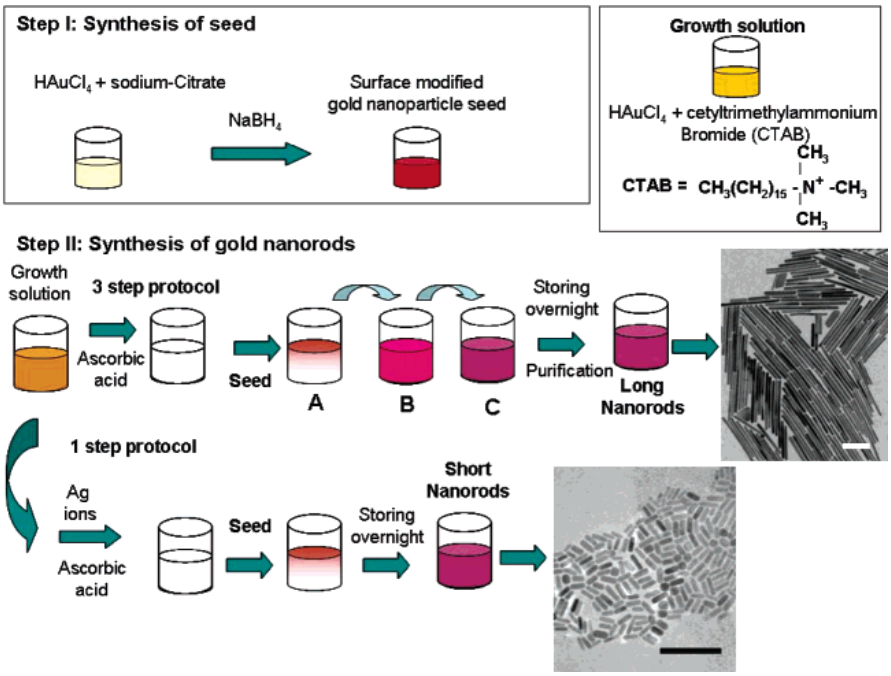

Figure 5-5: Schematic illustration of the seed-mediated growth of GNRs. Scale bars represent 200 nm.[297] Reprinted (adapted) with permission from ref 297.

This preparation involves two steps: first, $HAuCl_4$ is reduced to form seed particles, to achieve this a strong reducing agent (*i.e.*, $NaBH_4$) is used. In the second step, more metal salt and surfactants are introduced to the system. In the presence of a milder reducing agent (AA), metal is deposited onto the seeds leading to the formation of nanorods or nanowires. The surfactants act as growth directing agents and are crucial to the formation of nonspherical shapes.

The Korgel group explored the role of the commonly used growth directing agent CTAB; they evaluated the synthesis of GNRs *via* seed-mediated method using CTAB obtained from ten different suppliers. They suggested that CTAB obtained from a particular supplier contains different level of impurities that either induces

or disrupts nanorods formation. More details about their findings can be found in their report in 2008.[298]

The combination of photothermal effects and the tailorable surface chemistry the GNPs/GNRs surfaces has led to extensive study of these particles in a variety of applications. As a case in point, biological applications include targeted cell ablation and targeted drug delivery.[299]

In case of GNRs, their optical tunability brings several advantages. First, the independently accessible NIR LSPR extinction is consistent with the transparent window of human tissue and facilitates widespread biophotonics applications.[300] Second, the strong LSPR band makes GNRs very sensitive to changes in dimension/morphology, environment as well as interparticle distance.[301] Moreover, LSPR tunability can improve the efficiency of fluorescence quenching and enhancement in bioimaging and biosensing applications.[302] GNRs also have potential applications in in NIR photothermal cancer treatment, and in biosensing and bioconjugation for DNA detection.[303]

In this Chapter, photocatalysis induced/promoted heating arising from the photothermal response of of GNRs will be discussed. Photothermal heating of GNPs/GNRs has been used previously to promote reactions.[304] Most chemical reactions are described by the Arrhenius equation (equation 5-4) so increasing temperature can accelerate them.[242,305]

$$k = Ae^{-\frac{E_a}{RT}} \qquad (5\text{-}4)$$

The other important aspect is the localized heating on the catalysts provides more energy in comparison to those powered by bulk heating methods.[306]

There are several examples of using GNPs being used as nanoscale heat sources in heterogeneous catalytic reactions. The plasmonically driven catalytic conversion of CO to CO_2 by irradiating GNPs/Fe_2O_3 composite has been studied using a 532 nm laser excitation source.[307] GNPs were first irradiated with light corresponding to plasmon resonance frequency in a dilute $Fe(CO)_5$/CO gas environment to deposit crystalline Fe_2O_3 *via* plasmon resonant chemical vapor deposition (PRCVD). Then, the catalytic activity of GNPs/Fe_2O_3 composite was evaluated in purified CO. The CO_2 and O_2 concentrations were monitored during light exposure and after certain time an increase in CO_2 concentration and a decrease in O_2 concentration observed as they are produced and consumed in this reaction (equation (5-5)):

$$2CO + O_2 \longrightarrow 2CO_2 \quad (5\text{-}5)$$

The temperature was estimated to be 330 ℃. Interestingly, they observed no changes

in the CO_2 concentration when only GNPs or Fe_2O_3 alone was irradiated. They conclude that this reaction is not driven only by the thermal heating of the gold nanoparticles but also relies on the interaction of these two materials. Also, they showed that the plasmonically driven catalytic reaction rate is several orders of magnitude higher than that obtained under uniform heating with no irradiation.

Radical species are often produced by traditional heating. Localized photothermal heating can be applied for inducing radical reactions. In another report, GNPs functionalized by a new thiol-functionalized enediyne ligand and then was irradiated by light (514 nm). The heat produced was then transferred to the organic ligand layer, initiating enediyne cyclization and generating surface radicals that lead to subsequent polymerization (Figures 5-6 and 5-7).[308]

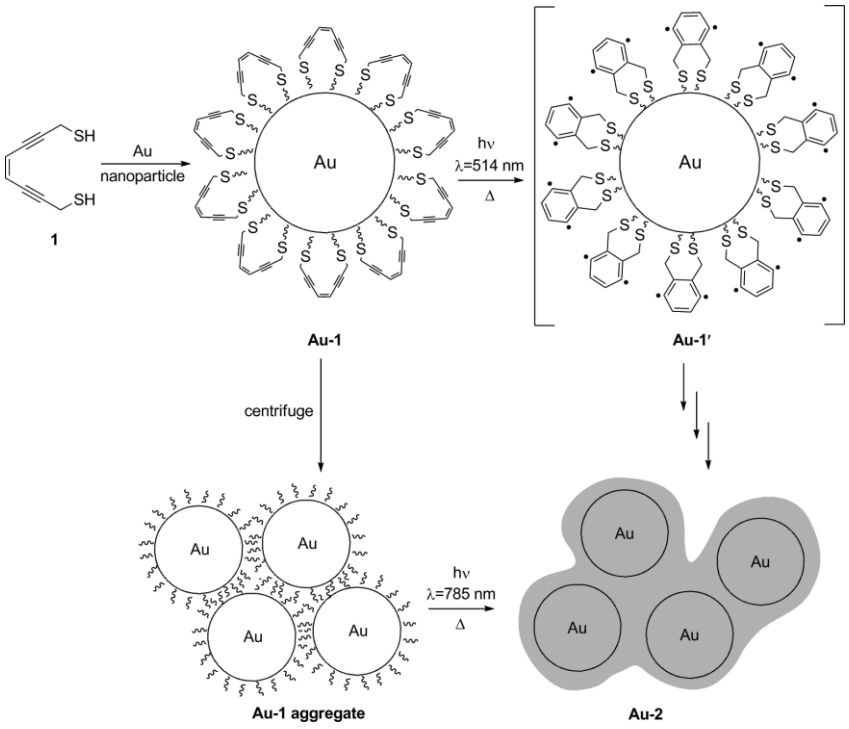

Figure 5-6: Preparation of Au−1 conjugates from citrate-stabilized nanoparticles via ligand exchange. By heating via irradiation this material, Bergman-type cyclization occurs which leads to the formation of Au−1′ followed by polymerization and coating of GNPs (Au−2). In another way, Au−1 can be centrifuged to obtain Au−1 aggregate first and then irradiated.[308] Reprinted (adapted) with permission from ref 308.

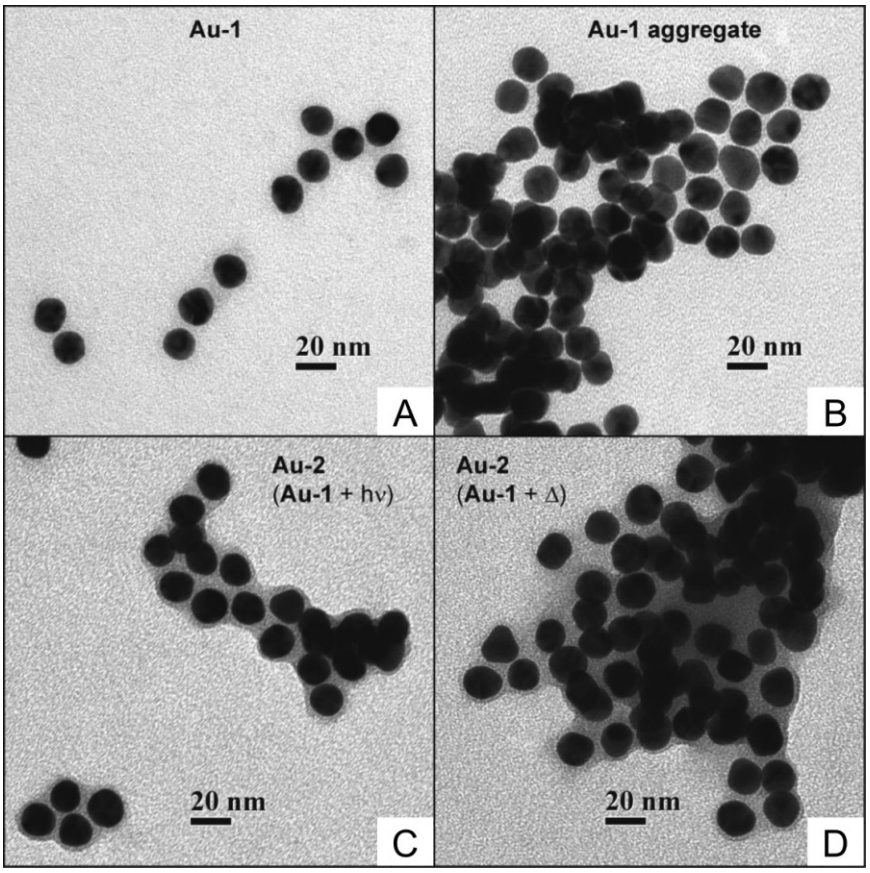

Figure 5-7: TEM images of spherical GNPs (A). Au-1 aggregates (B). Au-2 (Au-1 + hν) (C). Au-2 from direct heating of Au-1 at 50 °C for 8 h.[308] Reprinted (adapted) with permission from ref 308.

Halas *et al.* showed that by focusing solar illumination of absorptive nanoparticles (metal) water vapor is generated without the need of heating the fluid volume.[309] In their study, SiO_2/Au nanoshells were prepared and placed in a transparent tube. A small thermocouple was inserted into the fluid volume. The tube was then partially immersed in an ice bath. Then, the tube was illuminated and the

steam pressure and temperature was monitored. Solar illumination lead to increased pressure over the solution within 5 seconds as a result of steam generation (Figure 5-8).[309]

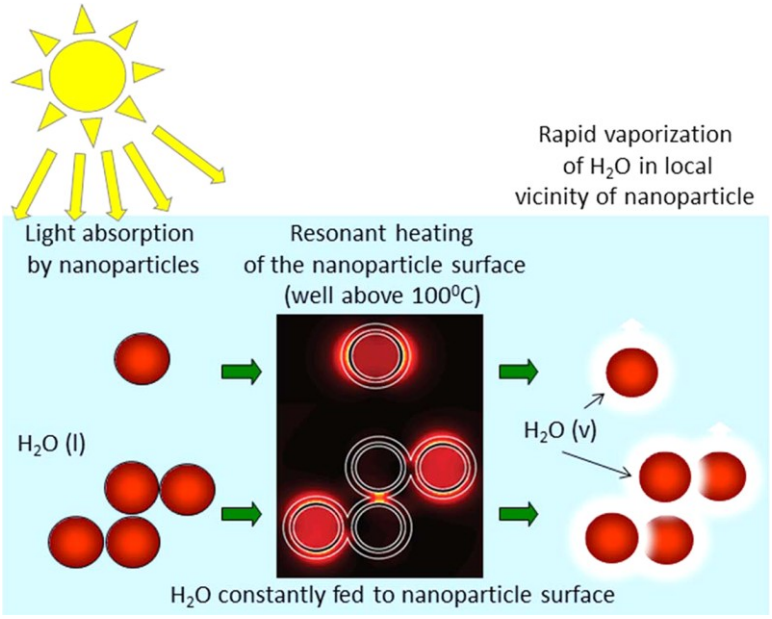

Figure 5-8: Schematic illustration of steam generation upon solar illumination of nanoparticles.[309] Reprinted (adapted) with permission from ref 309.

This group also showed that absorptive nanoparticle can be used to separate liquids *via* a solar-based distillation process. They showed that distillate fractions are significantly richer in the more volatile component in comparison to those of conventional distillation using thermal heat source.[309]

For bio-applications GNRs need to be highly stable, biocompatible, sensitive, and targetable.[310,311] Unfortunately cytotoxicity and low stability remain as two

problems, which limit the practical application of GNRs. During the synthesis *via*, seed-mediated growth method, GNRs are usually coated with a bilayer of cetyltrimethylammonium bromide (CTAB) and CTAB-coated GNRs have been proved to be cytotoxic to human cells.[312] Moreover, an unstable surface CTAB bilayer can easily induce aggregation of CTAB-coated GNRs, especially in acidic, alkaline and electrolyte mediums.[313] After aggregation, GNRs lose their unique optical properties and cannot be taken up by cells anymore. One solution is to deposit an additional coating on the surface of CTAB-coated GNRs.[310] A suitable coating is easy to firmly deposit on the surfaces of CTAB-coated GNRs and also it should be stable and chemically and physically inert. Moreover, it should be nontoxic and biocompatible. It should provide a platform that can be easily modified with functional groups for further conjugation with biomolecules. Optical transparency to excitation and emission light is another parameter that should be considered. It also should not affect the GNRs unique LSPR band properties.[310] Silica meets the requirement of a suitable coating. The relationship between the thickness of the silica shell and the red-shift of the LSPR peak can be investigated. Silica-coated GNRs provides a platform to further introduce various kinds of biomolecules onto the surface [310] The potential biocompatibility and stability of silica-coated GNRs make them promising candidates as optical probes for early diagnosis of cancer cells based on wavelength-selective LSPR enhanced scattering.[314]

5.2 Experimental

5.2.1 Reagents and Materials

$HAuCl_4.3H_2O$ (99.9%), $NaBH_4$ (99%), ascorbic acid (AA) (99%), cetyl trimethylammonium bromide (CTAB) (99%), $AgNO_3$ (99%), and hydroquinone were purchased from Sigma-Aldrich. 3-aminopropyl-trimethoxysilane (APTMS, 95%) and trisodium citrate was purchased from Sigma. Tetraethoxysilane (TEOS) (≥ 99%) was purchased from Sigma-Aldrich and used as received. Ammonium hydroxide (30%) was purchased from Caledon Laboratories. Isopropanol was purchased from Sigma-Aldrich. 4-nitrophenol was purchased from Sigma-Aldrich and used as received. Milli-Q water (18.2 MΩ) was used for making all the solutions and all the solutions were prepared fresh daily as needed.

5.2.2 Gold Nanorod Synthesis

A seed-mediated growth procedure was employed to prepare nanorods used in the present study.[315] Gold seeds were synthesized using a literature procedure.[315,316] In a typical procedure 0.250 mL of an aqueous 0.01 M solution of $HAuCl_4 \cdot 3H_2O$ was added to 7.5 mL of a 0.10 M CTAB solution in a test tube. The solutions was mixed by inversion and the solution appeared bright brown-yellow. Following mixing, 0.600 mL of an aqueous 0.01 M ice-cold $NaBH_4$ solution was added all at once, followed by rapid inversion mixing for 2 min. (Note: Hydrogen gas (H_2) is produced and the mixture must be vented.) The test tube containing the reaction mixture was kept in a water bath maintained at 25 °C until needed. This

seed solution can be used within 2 h and 1 week of its preparation. Appropriate quantities of CTAB (0.1 M) solution, water, $HAuCl_4 \cdot 3H_2O$ (0.01 M), $AgNO_3$ (0.01 M), ascorbic acid (AA) (0.1 M), and seed solution were added sequentially in the order listed to a test tube and mixed gently by inversion after each addition. The seed solution was always added after the addition of AA. For example, in a typical synthesis of 46 ± 4.5 nm × 15 ± 1.5 nm nm nanorods (Length/width aspect ratio ~ 3), 4.75 mL of 0.10 M CTAB, 0.200 mL of 0.01 M $HAuCl_4 \cdot 3H_2O$, and 0.030 mL of 0.01 M $AgNO_3$ solutions were added sequentially to a test tube, followed by gentle mixing by inversion after each addition. The resulting solution was brown-yellow. Subsequently, 0.032 mL of 0.10 M AA was added to the brown-yellow solution became colorless following addition and mixing. Finally, 0.010 mL of seed solution was added, and the reaction mixture was gently mixed for ~ 10 s and left undisturbed for at least 3 h. The same seed solution has been used for synthesis of long nanorods. For nanorods with 85 ± 7.5 nm and 11 ± 7.5 nm dimensions (Length/width aspect ratio ~ 7.5) hydroquinone (0.1 M) is used as reducing agent instead of AA.[316] The materials were characterized using TEM and UV-vis spectroscopy.

5.2.3 Encapsulation of Gold Nanorods (short and long) with Non-porous Silica Shell

Encapsulation of GNRs in a non-porous silica shell was achieved using a modified literature procedure.[317] In a typical experiment, 1.0 mL of the gold nanorod solution (0.2 x 10^{-9} nM; See: Appendix A for the procedure to determine concentration) was added to 5.0 mL of isopropanol with continuous stirring using a magnetic stir bar. Aqueous ammonium hydroxide (125 μL; 30 %) and predetermined volumes of TEOS (1 to 30 μL; 4.5 × 10^{-3} to 0.13 mmoles) were added to the to the GNR solution with stirring for 2 h. The amount of TEOS added defines the thickness of the silica shell on the GNR. The mixture was then left undisturbed and aged for 20 h at 4 ℃. The resulting light purple solution was

centrifuged (10000 rpm, 10 min) and the solid washed three times with ethanol. The materials were characterized by TEM and UV-vis spectroscopy.

5.2.4 Encapsulation of Short Gold Nanorods with Porous Silica Shell

Coating short GNRs with porous silica shell was achieved using a modified literature procedure.[311] In a typical synthesis, the pH of 3.0 mL GNR solution was adjusted to 10 upon addition of 30% ammonium hydroxide. The concentration of GNRs was estimated as stated in Appendix A. Subsequently, predefined quantities of TEOS (10 to 1000 μL of the 10 mM solution) were added with stirring and the mixture was stirred for at least 12 hours. The resultant light purple solution was centrifuged (6000 rpm, 12 min) and the solid was resuspended by sonication and washed three times with ethanol. The materials were characterized by TEM and UV-vis spectroscopy.

5.2.5 "Decoration" of Silica Particles with Gold Nanoparticles (Silica@GNPs)

Spherical silica particles were prepared using the Stöber method with TEOS as the silica source.[318] For a typical synthesis, 40 mL of 0.2 M TEOS was added to a mixed solution of 50 % ethanol (80 mL) and ammonium hydroxide (33 %, 4 mL) and then stirred for 3 hours at ambient temperature. The solution was centrifuged three times at 10000 rpm for 30 min to collect the particles.

The as-synthesized spherical silica particles were functionalized by refluxing 50 mg of the as-synthesized silica particles with 3 mL of APTMS (0.01 moles) in

anhydrous toluene for 3 hours in an Ar atmosphere. The particles were isolated by centrifugation (10000 rpm, 20 min), resuspended by sonication and washed with ethanol 3 times to remove excess reagent. Finally, the APTMS-functionalized particles were re-dispersed in ethanol.[317,319] The materials were characterized by FTIR.

A modified literature procedure was used to prepare silica@GNPs.[318] An aqueous solution of 2.5 mM $HAuCl_4 \cdot 3H_2O$ and 2.5 mM trisodium citrate was prepared and added to APTMS-functionalized silica particles. Then, 0.6 mL of freshly ice-cold prepared $NaBH_4$ (0.1 M) was added to the solution. The solution was stirred for 2 hours at room temperature after which the particles were collected by centrifugation (10000 rpm, 20 min), resuspended by sonication and washed with DI water for at least three times. The product was characterized with TEM and UV-vis spectroscopy.

5.2.6 Catalytic Reduction of 4-nitrophenol (4-NP) by Silica@GNPs

The catalytic reduction of 4-NP was studied using a variant of a literature procedure.[233,320] Typically, a standard quartz cuvette was charged with 0.8 mL of aqueous $NaBH_4$ solution (1.0 mM) and 1.0 mL of 4-NP aqueous solution (0.1 mM). Following this, 200 μL of aqueous suspension of silica@GNPs (5 mg/mL) was

introduced into the cuvette. UV-vis absorption spectra were recorded every 5 min in the range of 200 - 800 nm at 25°C.

5.3 Results and Discussion

The catalytic and photothermal properties of GNPs/GNRs are well known.[242] The possibility of combining the photothermal response of GNPs with traditional thermally active catalysts could open the door to a new class of efficient, recoverable reactive hybrid catalysts. The present Chapter outlines the preparation of a series of silica encapsulated gold nanomaterials (*i.e.,* nanorods and nanoparticles) designed for this type of application.

Two classes of gold nanorods (*i.e.,* short and long) were used as seeds on which non-porous and porous silica shells were grown. The morphology of the short GNRs prepared using a seed-mediated method (Figure 5-9) are shown in in Figures 5-10 A and B. The images reveal an average length and width of 52 ± 5.7 and 19 ± 2.5 nm, respectively; this corresponds to an aspect ratio of 2.8 ± 0.5 (Figure 5-10 C). The absorbance spectrum of these GNRs shows a weak feature at 525 nm and a more intense plasmon resonance peak at 757 nm (Figure 5-10 D); these optical absorptions are attributed to the transverse and longitudinal plasmon bands of the GNRs, respectively.

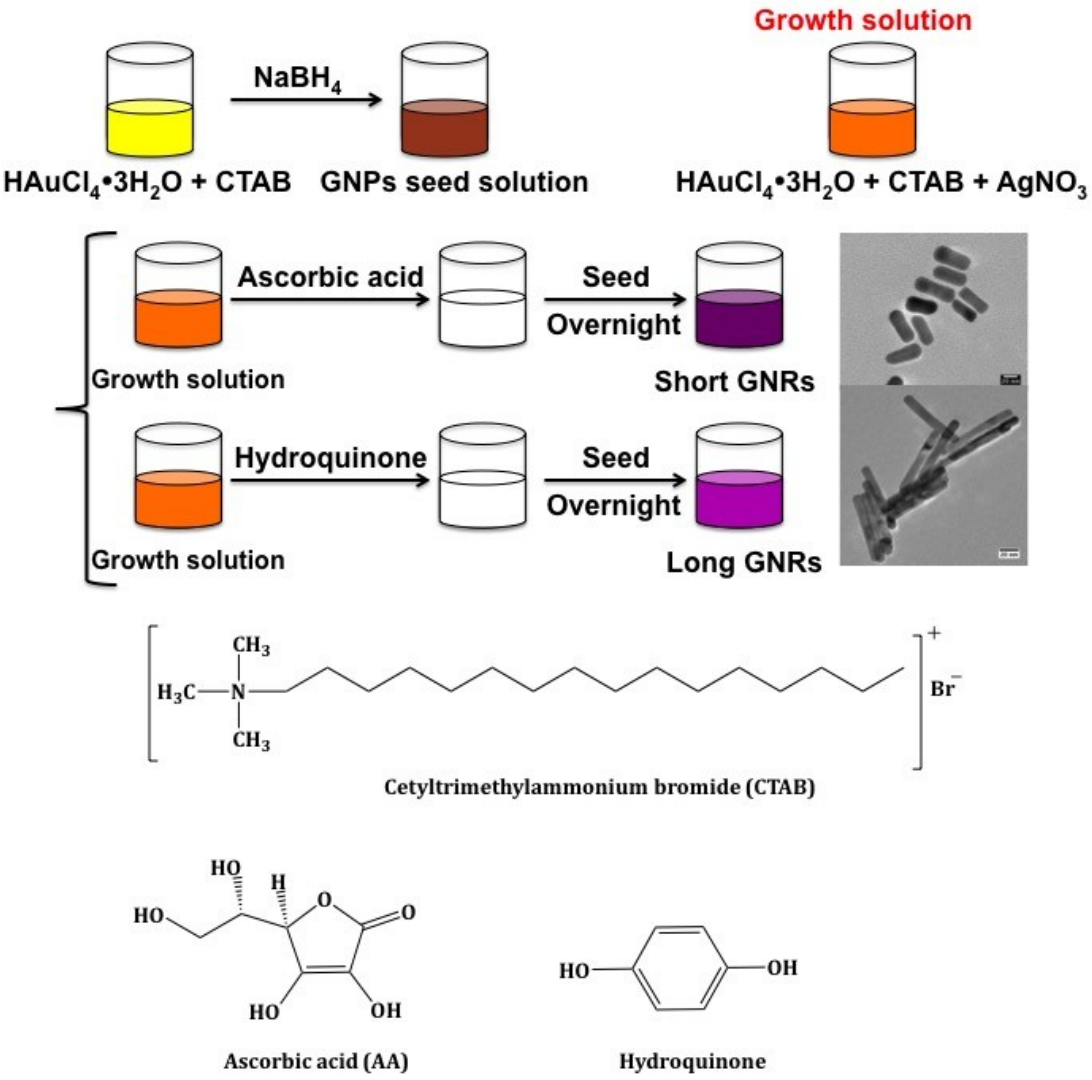

Figure 5-9: Pictorial representation of GNRs (short and long) synthesis *via* seed-mediated growth method.

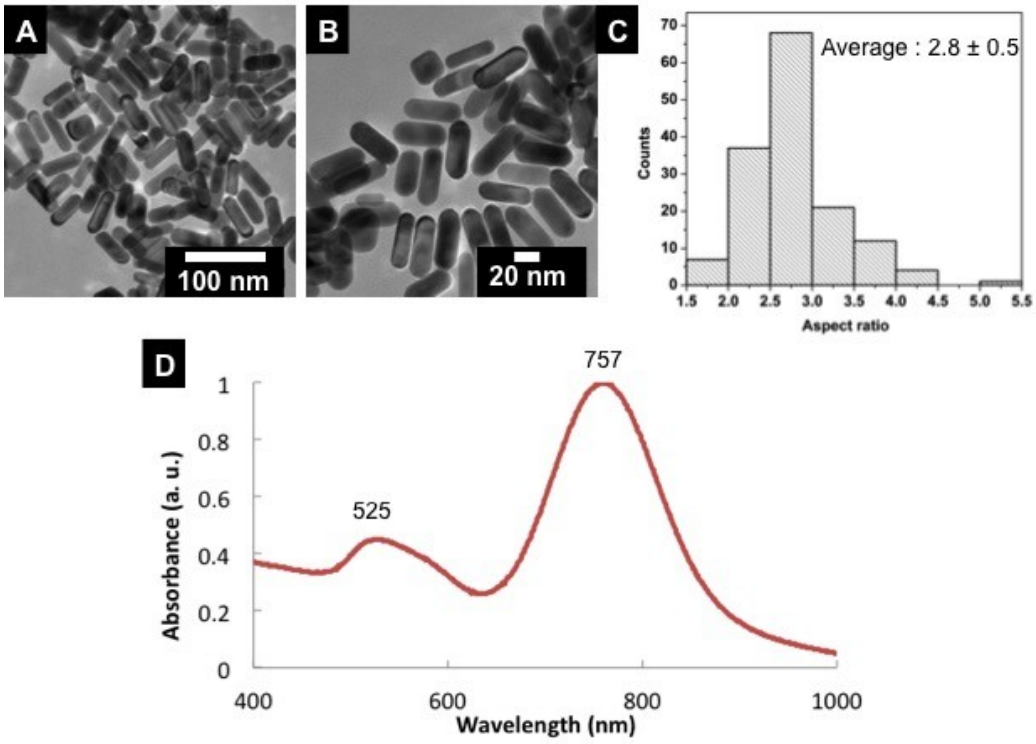

Figure 5-10: TEM images of short GNRs prepared in aqueous solution (A, B). Aspect ratio distribution of short GNRs (C). Absorbance spectrum obtained from an aqueous dispersion of these GNRs (D).

Long GNRs were prepared *via* a modified seeded growth procedure similar to that used for the short GNRs and employing hydroquinone as the reducing agent. The morphology of the long GNRs are shown in Figures 5-11 A and B. The images reveal an average length and width of 85 ± 7.5 and 12 ± 2.1 nm, respectively, corresponding to an aspect ratio of 7 ± 1.65 (Figure 5-11 C). The absorbance spectrum of these nanorods (Figure 5-11 D) shows transverse (509 nm) and longitudinal (1059 nm) plasmon bands.

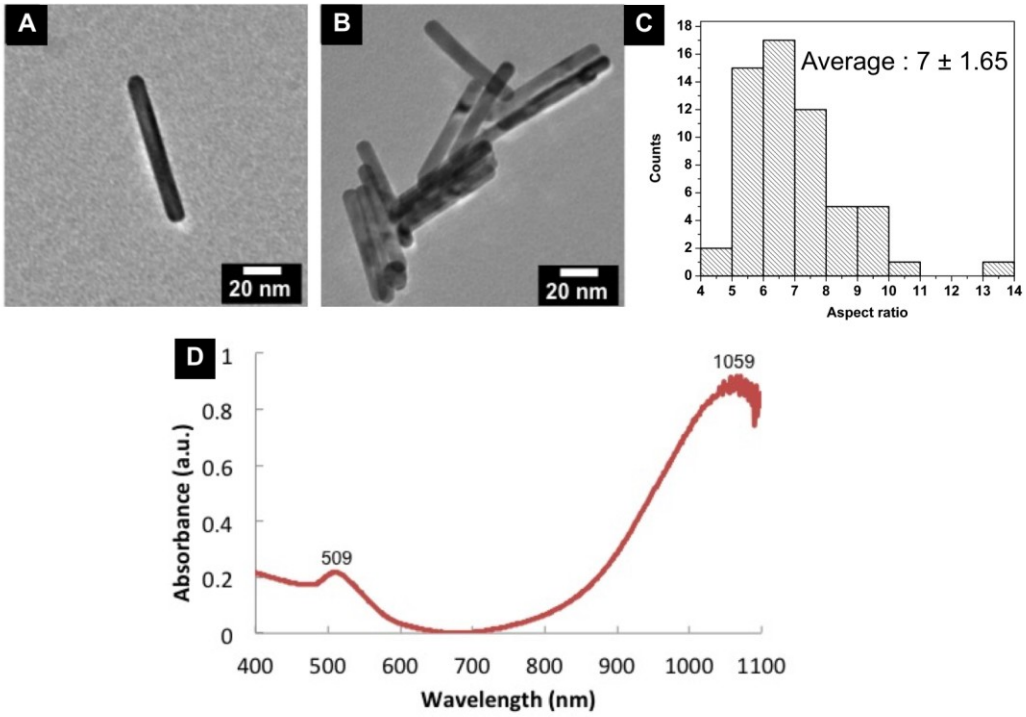

Figure 5-11: TEM images of long GNRs prepared in aqueous solution (A, B). Aspect ratio distribution of long GNRs (C). Absorbance spectrum obtained from an aqueous dispersion of these GNRs (D).

A standard sol-gel process involving hydrolysis and condensation of TEOS in a water-isopropanol solvent mixture was used to prepare silica-coated GNRs. To achieve a uniform non-porous coating on the GNRs, it was necessary to remove excess CTAB from the as-prepared GNRs. To achieve this, solutions of AuNRs were centrifuged to isolate a pellet of GNRs that were re-dispersed into water. TEM imaging (Figures 5-12 A and 5-13 A) clearly shows the GNR core and reveals an average shell thickness is 51.94 ± 6 and 44.05 ± 3.45 nm for short and long GNRs, respectively. SEM imaging of short silica-coated GNRs (Figure 5-12 B) is consistent

with the present TEM analysis and indicates the coated particles possess a pseudospherical morphology.

The absorbance UV-Vis spectra of silica-coated GNRs and original NRs are shown in Figure 5-12 C and 5.13 C. Introducing the silica coating onto the NRs does not affect the transverse plasmon band. However, the longitudinal plasmon band is red-shifted in both cases (*i.e.*, short GNRs, 16 nm; long GNRs 21 nm). The extent to which the longitudinal plasmon band is red-shifted depends on the silica shell thickness. The largest shift is observed for the sample with the thinnest shell thickness suggesting NRs bearing thinner shells are more sensitive to the surrounding environment.[301] The longitudinal surface plasmon band responds to changes in the local refractive index surrounding the GNPs as discussed in Section 5.1.

Zeta potential analysis was performed on the present particles to gain insight into the surface charge of the parent GNRs and those coated with silica. CTAB coated nanorods showed values of +13.8 (short) and +17.8 (long) mV consistent with the surfaces being coated with cationic CTAB. Coating NRs with silica resulting in the zeta potential shifting to -14.0 (short) and -19.3 (long) mV consistent with the surface of the silica being anionic.

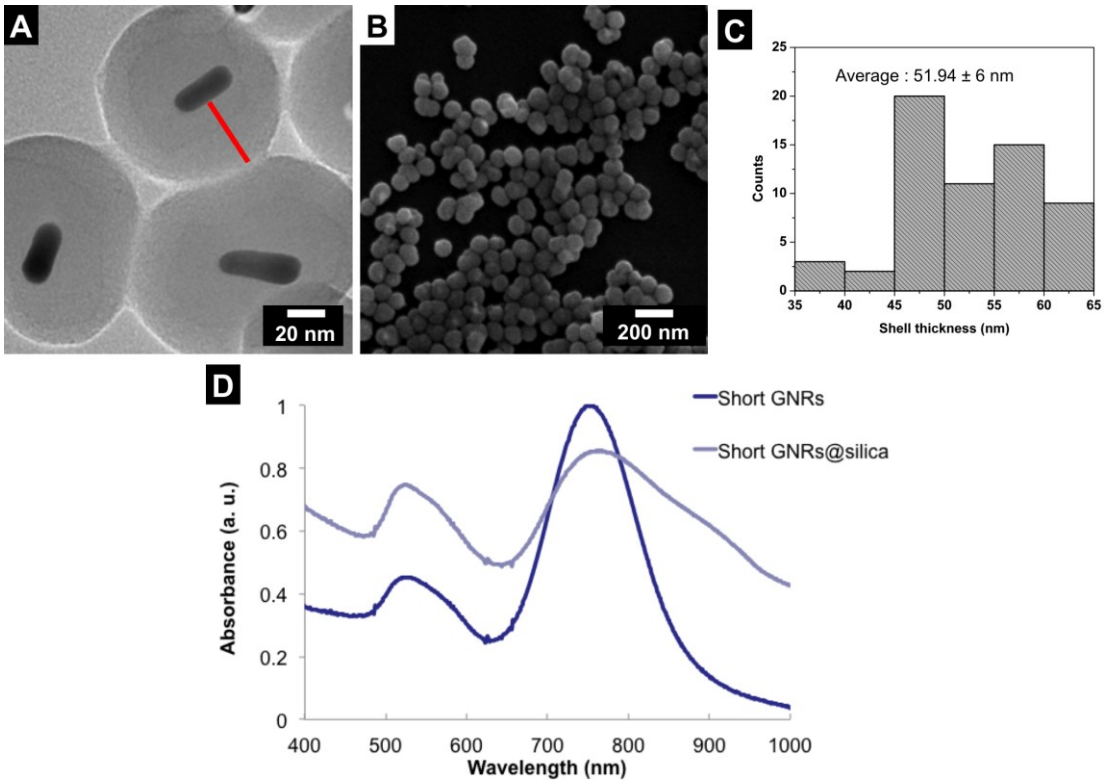

Figure 5-12: (A) TEM image of non-porous silica-coated short GNRs. (B) SEM image of non-porous silica-coated short GNRs. (C) Silica shell thickness distribution of non-porous silica-coated short GNRs (The measurements was performed perpendicular to the long axis of the GNRs as indicated in A). (D) Absorbance spectrum obtained from an aqueous dispersion of these GNRs.

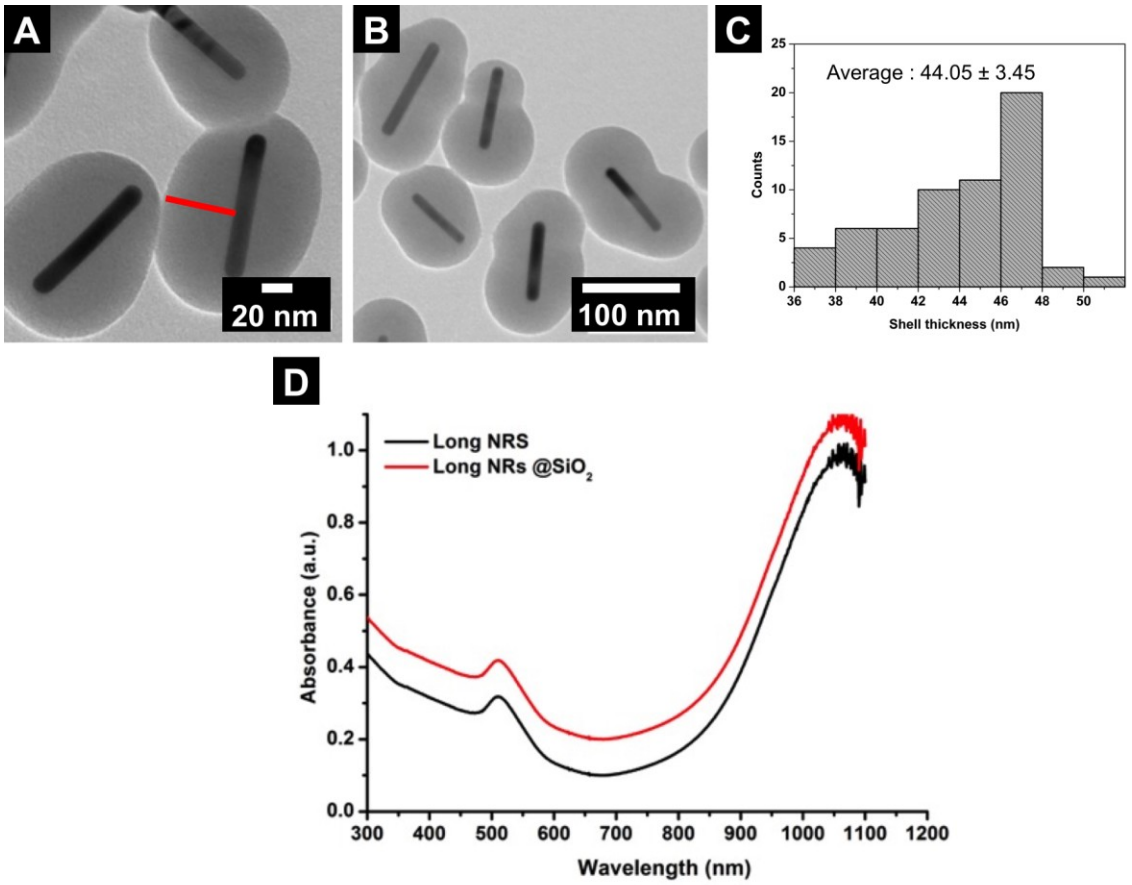

Figure 5-13: (A, B) TEM images of non-porous silica-coated short GNRs. (C) Silica shell thickness distribution of non-porous silica-coated long GNRs (The measurements was performed perpendicular to the long axis of the GNRs as indicated in A). (D) Absorbance spectrum obtained from an aqueous dispersion of these GNRs.

A similar procedure was used to prepare porous silica-coated GNRs, however having CTAB present during the sol-gel reaction produces a porous coating. TEM analysis (Figures 5-14 A and B) shows an average shell thickness is 16 ± 1.63 nm and contrast in the image suggests the shell is porous. The normalized UV-vis spectra of porous silica-coated short GNRs and original GNRs is shown in Figure 5-5 C. Similar to the non-porous silica coated GNRs, the transverse plasmon band is less affected by the silica coating (porous), however, the longitudinal plasmon band is red-shifted by 25 nm *vs.* 16 nm for non-porous coatings consistent with the thinner porous shell affording greater interaction between the GNRs and the surrounding solvent.[301]

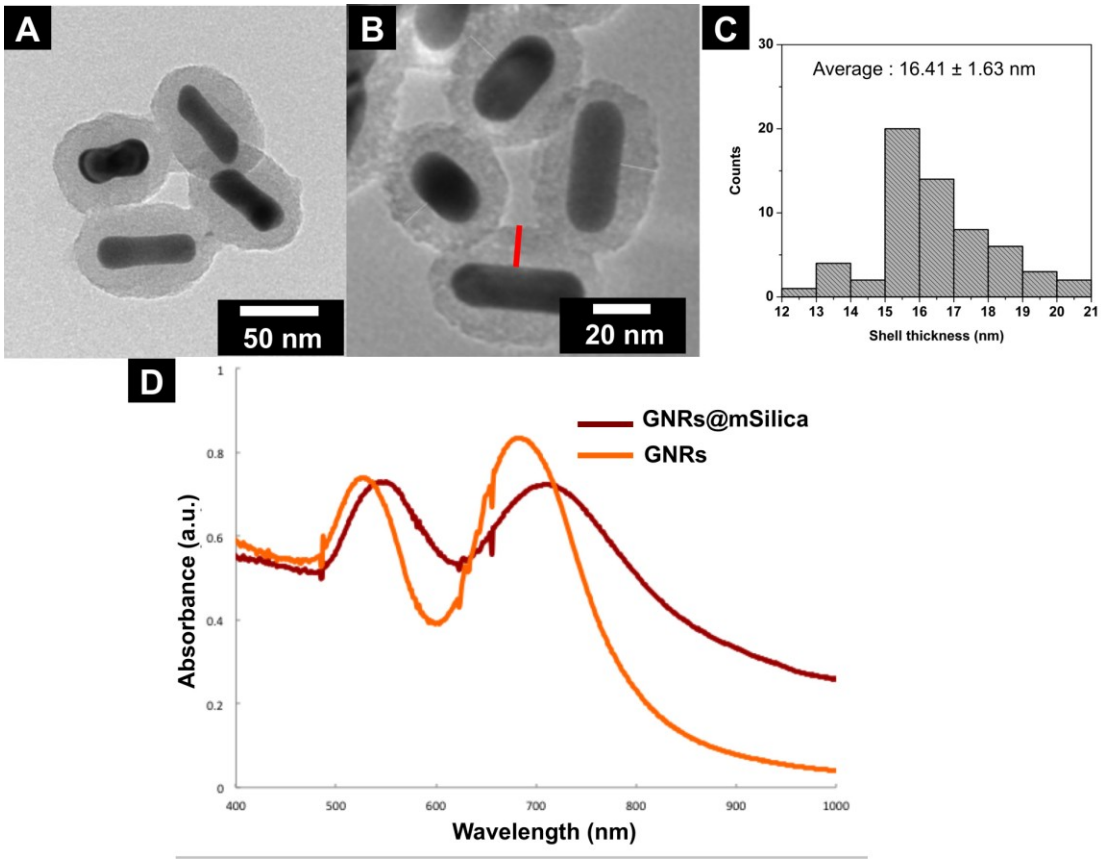

Figure 5-14: (A, B) TEM images of porous silica-coated short GNRs. (C) Silica shell thickness distribution of porous silica-coated short GNRs (The measurements was performed perpendicular to the long axis of the GNRs as indicated in B). (D) Absorbance spectrum obtained from an aqueous dispersion of these GNRs.

Another attractive hybrid structure consisting of AuNPs docked onto the surface of silica particles could also offer photothermal catalyst activation. To prepare these nanosystems the surface of Stöber silica beads was functionalized with 3-aminopropyltrimethoxy silane (Figure 5-15). Subsequently GNPs were prepared by reduction of $HAuCl_4$ with $NaBH_4$ (Figure 5-15).

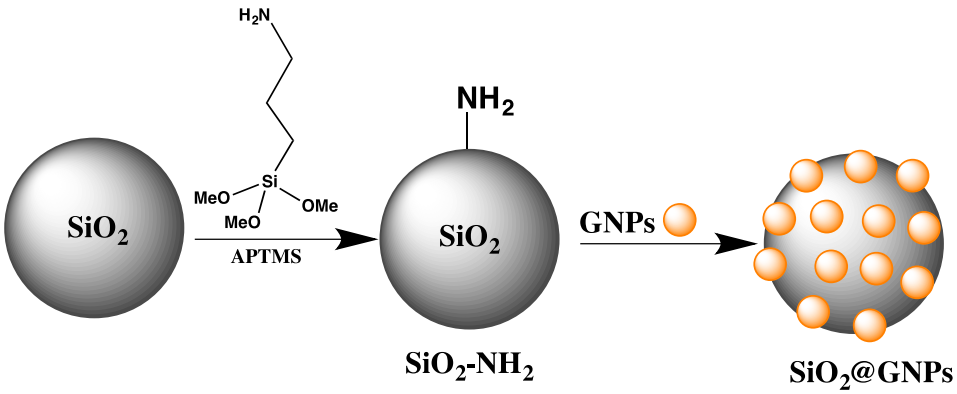

Figure 5-15: An illustration of the deposition of GNPs onto silica particles.

The FTIR spectrum of APTMS-functionalized particles is shown in Figure 5-16. The band at 1100 cm^{-1} is assigned to the Si-O-Si asymmetric stretch. In addition, the bands at 950 and 793 cm^{-1} are assigned to the characteristic silanol Si-OH stretching and Si-O-Si bending modes, respectively. The broad bands centered at 3350 cm^{-1} are assigned to O-H and N-H stretching modes. The peak at 1628 cm^{-1} is the result of functionalization and is assigned to the N-H bending mode.

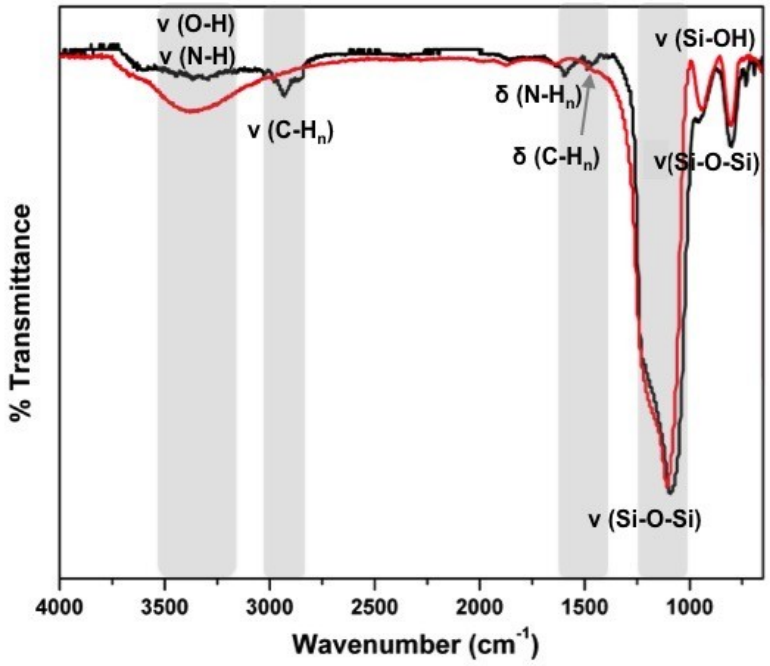

Figure 5-16: FTIR spectra of bare silica (red) and APTMS-functionalized silica particles before adding GNPs (black).

TEM was performed to show the presence of GNP$_S$ (d < 10 nm) attached to the surface as a result of successful functionalization (Figures 5-17 A and B) Moreover, the silica particles take on a pale violet color upon incorporation of the GNPs (Figure 5-17 C). Consistent with this change in physical appearance, the UV-vis spectrum of silica@GNPs (Figure 5-17 D) shows a low intensity band 545 nm arising from characteristic plasmon resonance of GNP. Note that, the presence of large silica particles and the resulting scattering that raises the baseline and limits effective observation of the GNP-based plasmon absorption.

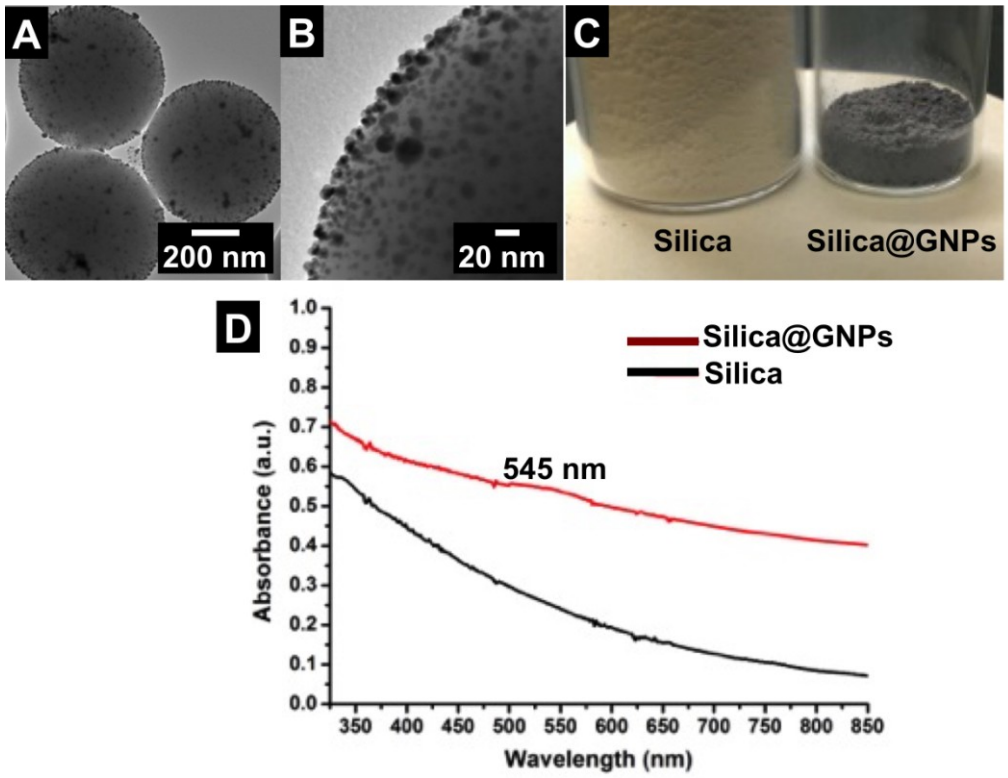

Figure 5-17: (A, B) TEM images of silica@GNPs. (C) Physical appearance of silica NPs and silica@GNPs. (D) Absorption spectra obtained from aqueous dispersion of silica NPs and silica@GNPs.

The catalytic performance of decorated silica particles for the reduction of 4-nitrophenol (4-NP) to 4-aminophenol (4-AP) model reaction was investigated (Figure 5-18).[243,321] In a typical reaction silica@GNPs were combined with 4-NP and an excess of $NaBH_4$ reducing agent. A large excess of $NaBH_4$ is used and the order of the reaction is considered to be pseudo-first order.[320] The reaction progress was monitored by measuring the time-dependent UV-vis absorption spectra of 4-NP and 4-AP (Figure 5-19).

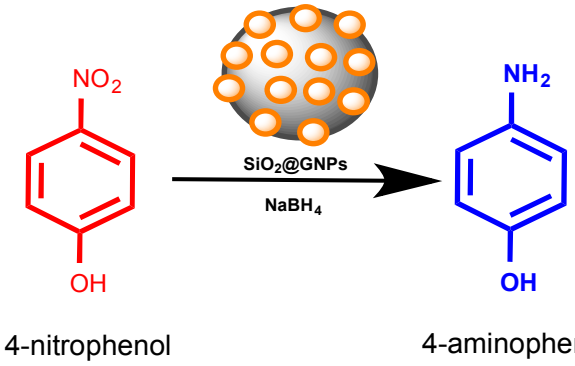

Figure 5-18: Illustration of 4-NP reduction by $NaBH_4$ using SiO_2@GNPs as catalyst.

In alkaline aqueous $NaBH_4$, the absorption peak at 317 nm for 4-NP exhibits red-shift at 400 nm due to formation of 4-nitrophenolate ions. The reduction reaction does not proceed readily in the absence of a catalyst; in fact, the 400 nm absorption remains unaltered even if the mixture is heated to 50 ℃ (Figure 5-20).

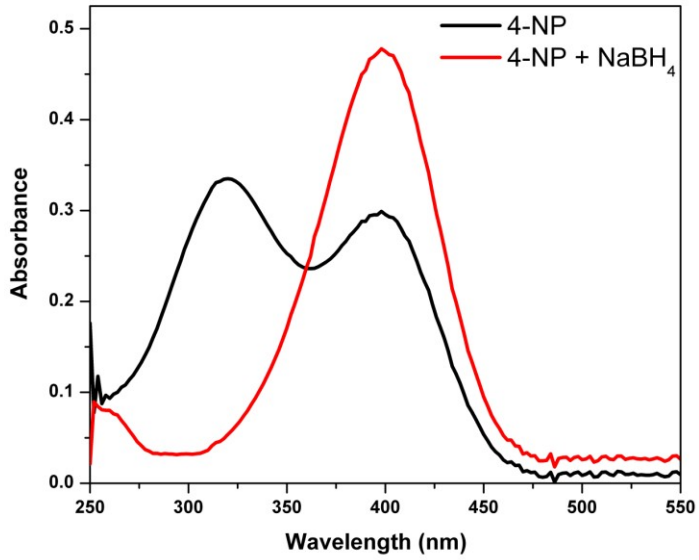

Figure 5-19: UV-vis spectra for 4-NP and 4-NP in alkaline $NaBH_4$.

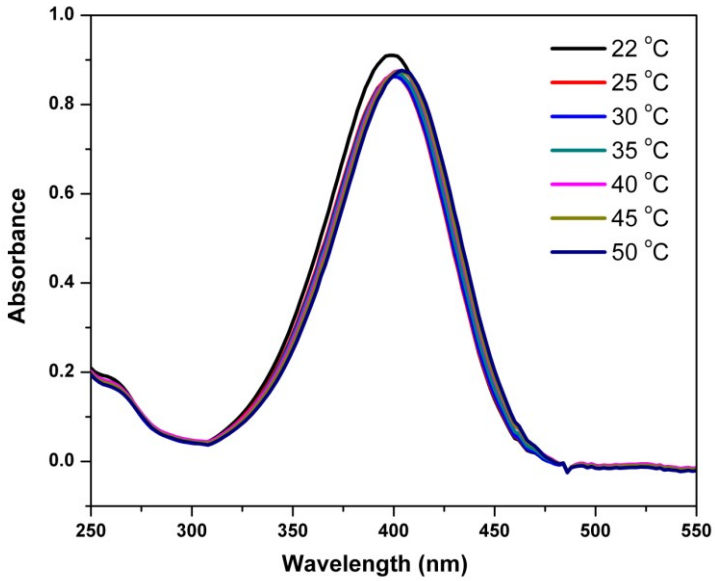

Figure 5-20: UV-vis spectra for monitoring 4-NP reduction by $NaBH_4$ in the absence catalyst at indicated temperatures.

Introducing catalytic quantity (5 mg/mL) of silica@GNPs could facilitate the 4-NP to 4-AP reduction. Upon the silica@GNP catalyst at room temperature the absorption arising from the 4-NP at 400 nm decreases in intensity and new feature at 300 nm appear consistent with the formation of 4-AP (Figure 5-21).[322] This observation indicates that silica@GNPs does catalyze the reduction reaction. Note: Silica induced scattering limits detailed evaluation of the 4-AP absorption.

A plot of ln A_0/A_t *vs*. time provides an estimate of the pseudo-first order rate constant ($k_{obs} = 8.2 \times 10^{-3}$ min^{-1}) (Figure 5-22; A_t: absorbance at 400 nm at time t, A_0: absorbance at 400 nm at t = 0). While the k value is comparable to that of metallic nanoparticles counterparts and the silica@GNPs do show catalytic activity, a complete quantitative study was not undertaken.

The reaction can be discussed in terms of the Langmuir-Hinshelwood (LH) mechanism in which two molecules adsorb on neighboring sites and the adsorbed molecules undergo a bimolecular reaction.[242,243] Here, borohydride ions react with the surface of the GNPs and transfer a surface-hydrogen species to the surface of the GNPs.[244] 4-NP molecules are also adsorbed on the surface of the GNPs. The reduction of 4-NP, which is the rate-determining step, occurs by the reaction of adsorbed 4-NP with the surface-hydrogen species. 4-AP as the reduction product detaches from the surface and creates a free surface and the catalytic cycle can start again and continue (Figure 5-23).[243]

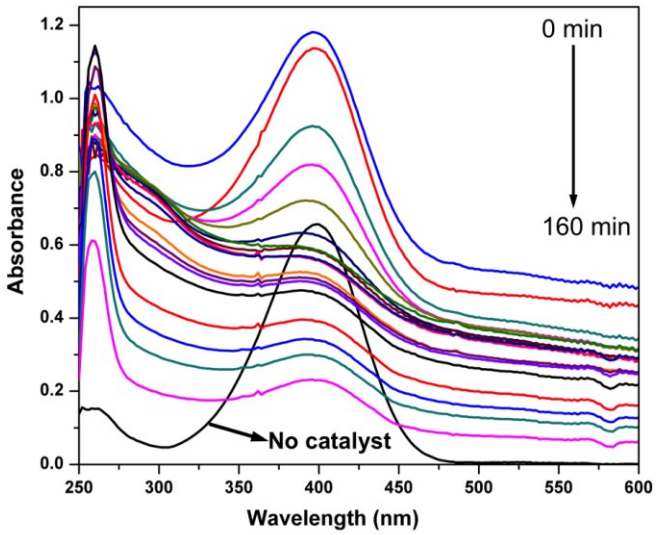

Figure 5-21: Time-dependent UV-vis spectra for monitoring 4-NP reduction by $NaBH_4$ catalyzed by silica@GNPs.

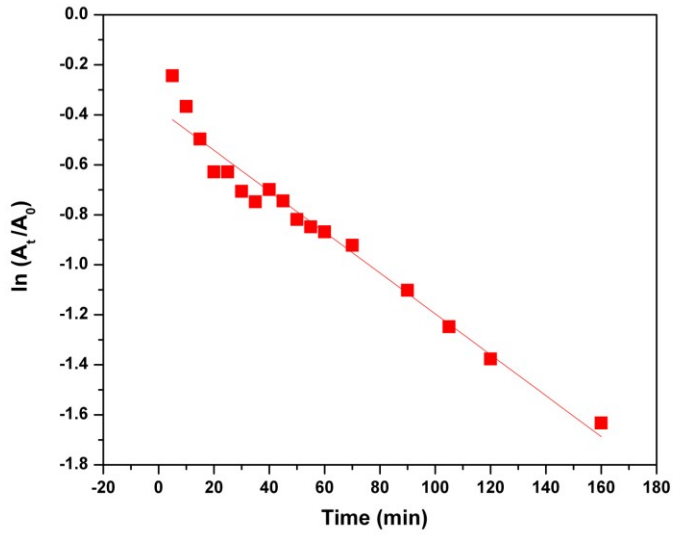

Figure 5-22: Plot of the variation of ln (A_t/A_0) vs. time for the reduction of 4-NP by $NaBH_4$ in the presence of silica@GNPs.

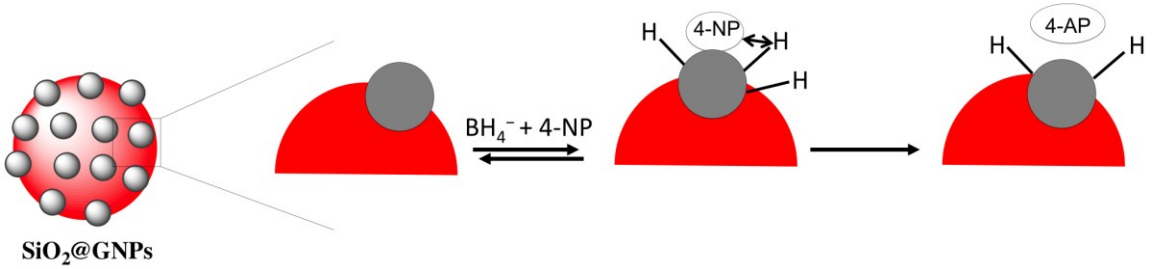

Figure 5-23: Reduction of 4-NP by borohydride in the presence of GNPs (gray spheres).[243] Reprinted (adapted) with permission from ref 243.

To investigate the impact of the photothermal response of GNPs on the observed reactivity, the same reaction was performed while illuminating with a green laser flashlight (532 nm). This reaction is known to be endothermic.[323] However, in a detailed kinetic analysis of this reaction done by Ballauff *et al.* it has been shown that adsorption constant of borohydride is not affected by temperature.[324] So based on their findings and our observations we speculate upon photothermal exposure and subsequent increase in local temperature, partial hydrolysis of BH_4^- occurs as a side reaction that leads to a shift in its concentration. As a result the reaction seems to be stopped (Figures 5-24) and qualitative evaluation suggests it is affected adversely by exposure to green light.

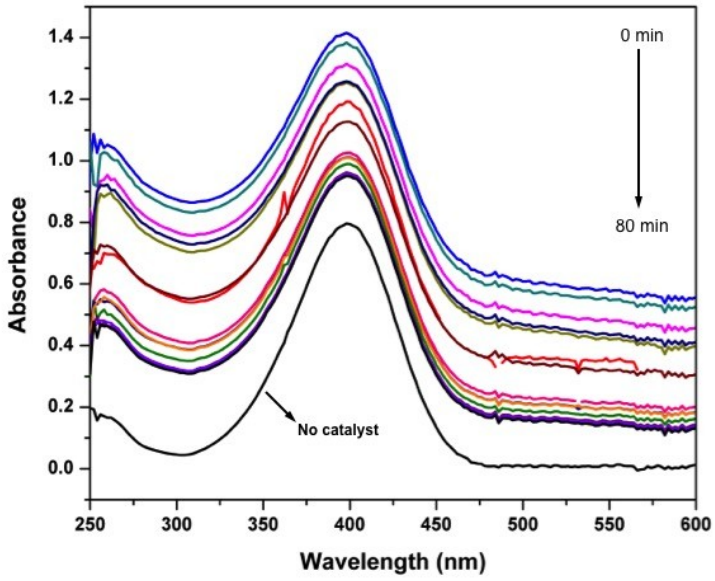

Figure 5-24: Time-dependent UV-vis spectra for monitoring 4-NP reduction by $NaBH_4$ catalyzed by silica@GNPs in presence of green laser (532 nm).

5.4 Conclusions

Different morphologies of gold nanostructures (short and long nanorods and gold nanoparticles) were synthesized with tunable aspect ratios. In scalable synthetic procedures, as-synthesized materials were used to and make new hybrids upon coating with silica (non-porous and porous) into the system. The resulting structures were characterized using TEM and UV-vis spectroscopy. The optical properties as a function of aspect ratio were investigated.

The resulting silica@GNPs hybrids show catalytic activity toward 4-NP reduction, however photochemical exposure did not result in any change in activity.

Future work may include immobilizing different sizes of GNPs on different sizes of silica (different sizes) as support and studying their catalytic activity for nitrophenol reduction. It is also reasonable that GNRs (short/long) coated within a mesoporous silica shell could serve as photoreponsive supports for known catalytic systems. However, in defining target catalytic cycles it is important to consider the thermodynamics (*i.e.*, exo or endothermic) of the reactions because the present results suggest photothermal response can suppress reactivity.

Chapter 6:

Conclusions and Future Directions

6.1 Conclusions

The thesis has been divided into four chapters based on the research projects carried out using different materials with one common underlying goal: to explore the synthesis of "designer" nanomaterials and their eventual application to catalysis. The chapters have been organized based upon the materials used and the catalytic application targeted; high surface area mesoporous carbon (Chapter 2 and Chapter 3), Iron oxide nanorods (Chapter 4) and gold nanoparticles (Chapter 5). Synthesis, characterization and application of these novel materials were investigated in detail. In short, the materials synthesized in Chapter 2 and Chapter 4 were investigated as electrocatalyst for ORR/OER reactions. While Chapter 3 and 5 present the applications of the materials as catalyst for 4-NP conversion to 4-AP.

The objectives of studies presented in Chapter 2 were to synthesize N-doped hollow mesoporous carbon (HMC) by carbonization of polymerized dopamine and further investigate their application as an electrocatalyst. The synthesis was optimized to obtain high surface area mesoporous carbon and characterized in detail to gain further insight into structure-property relationships. The electrochemical performances of the resulting HMC were tested as electrocatalyst by investigating oxygen reduction/evolution reaction (ORR/OER). The HMC exhibited high ORR and OER activities as well as superior stability in alkaline electrolytes when compared with benchmark Pt/C catalysts. We believe that the unique structure of the porous shell provide abundant active sites for oxygen

adsorption and desorption that also facilitate the diffusion of reactants during the catalytic processes. Furthermore, the performance of HMC was also evaluated in a proto-type zinc-air battery (ZAB), which exhibited a small charge–discharge voltage polarization of 0.89 V, and high stability over repeated cycling. The results reveal that when used as a bifunctional catalyst to construct the air electrode for ZAB, N-doped HMC outperformed the state-of-art Pt/C counterpart. The high surface area and N-doped active sites boost the diffusion-limiting current and long-term stability. Thus, HMC is a promising high performance alternative to precious metal bifunctional electrocatalysts in Zn–air batteries (ZAB).

In Chapter 3, the objective was to develop a new type of hollow mesoporous carbon sphere (HCS) obtained using a much more cost-effective and abundant carbon precursor; cellulose nanocrystals (CNC) and investigate its catalytic performance. The synthetic protocol was obtained and the effect of different reagents was studied in detail. It was determined that the presence of trisodium citrate as a mediating agent is necessary for the formation of HCS. The HCS was characterized using different techniques (TEM, HR-TEM, HIM, XRD, XPS, EDX, Raman and IR) to understand the structure and later tune the properties for intended catalytic application. The catalytic performance of the HCS was evaluated by investigating the catalytic conversion of 4-nitrophenol (4-NP) to 4-aminophenol (4-AP). The HCS exhibited outstanding catalytic activity towards reduction of 4-NP to 4-AP, the conversion was completed in minutes as compared to weeks when similar reaction was carried out in absence of HCS. The kinetics of the reaction were

further studied; the reaction rate followed pseudo-first order kinetics with k value of 4.7 x 10^{-3} s^{-1} and activity parameter of 52.22 $s^{-1}g^{-1}$, approaching that of their metallic counterparts.

In Chapter 4, the objective was to synthesize Fe_3O_4 nanorods coated with a N-doped mesoporous carbon shell (ND-Fe_3O_4@mC) by using a new microwave-assisted method and investigate their potential for ORR applications. The effect of carbon shell thickness on ORR activity of the electrocatalyst was studied in detail. It was determined the nanorods exhibit their highest ORR activity when coated with the thinnest nitrogen doped carbon shell tested in current study. The ND-Fe_3O_4@mC-2 exhibited an onset potential -0.135 V *vs*. Hg/HgO) in an alkaline electrolyte, i_l (-5.59 mA cm^{-2}). These materials show excellent long-term stability (up to 5000 cycles) in alkaline solutions and preliminary results studies indicate these are promising materials for ORR.

In Chapter 5, the objective was to synthesize core-shell plasmonic nanostructures of different morphologies and investigate their photochemical characteristics. To achieve this goal, gold nanostructures of different morphologies (nanoparticles, short and long nanorods) were synthesized. Furthermore, scalable synthetic protocols were developed for the synthesis of hybrid nanostructures by coating them with either porous or non-porous silica shells. The resulting structures were characterized using TEM and UV-vis spectroscopy and optical properties were evaluated as a function of aspect ratio as well. The resulting silica@GNPs hybrids

were investigated as a catalyst for catalytic conversion of 4-NP to 4-AP. However upon photochemical exposure the reaction rate decreased.

6.2 Future Directions

6.2.1 Developing New Hybrid Anode Materials for LIBs

Lithium ion batteries (LIBs) are used all over the world as power sources for different types of portable electronic devices. Despite rapid acceptance, improving the power density and discharge voltage is still the focus of intense research.[325] Developing new anode materials with higher specific capacity that meets all the requirements is of great importance. Of the various materials employed till date, porous carbons (800-1100 $mAhg^{-1}$), silicon (4200 $mAhg^{-1}$) and transition metal oxides (500-1000 $mAhg^{-1}$) have gained prominence and are considered promising anode materials.[326] In Chapter 2 and 3, mesoporous carbons (MPCs) were prepared using two different carbon precursors. These materials possess the required features to make them suitable for anode materials, including: availability, stability in thermal, chemical and electrochemical environment, reasonable cost, and more importantly excellent lithium intercalation and de-intercalation reversibility.[327–330] Further, it has been demonstrated that carbon coating on anode active materials for LIBs can improve the performance by reducing the electrolyte decomposition. Moreover, the carbon coating can prevent unwanted changes in morphology and properties of anode materials, for example, oxidation of the core materials.[326]

One of the most promising anode materials for LIBs is silicon with high specific capacity of 4200 $mAhg^{-1}$; this is 10 times higher than the capacity of graphite.[331,332] Silicon, as the second abundant element can be applied in large amounts and at low cost. Although Si has some clear advantages, there are also substantial limitations. First, significant volume changes (300 - 400%) upon Li insertion/extraction lead to loss of Si particle morphology and decreased lithiation capacity.[333] Another limitation is a solid-electrolyte interphase (SEI) film that forms upon decomposition of the organic electrolyte. This interface may result in the reduction of the electronic conductivity of the electrode.[333,334] One approach to address these challenges is to reduce the size of silicon to nanometer scale to minimize the influence of material degradation. Unfortunately, this approach leads to an increased contact between the nanoparticles and the electrolyte thus increasing the influence of the SEI interface. We propose to address these challenges by synthesizing hybrid materials consisting of Si core (tens of nanometer scale) and mesoporous carbon shells derived from either dopamine or CNC (Figure 6-1). In this engineered nanostructure, the carbon shell will support the silicon core, thus minimizing the influence of Li cycling induced expansion/contraction while also providing a barrier for electrolyte diffusion thereby minimizing the SEI formation. Wang *et al.* reported the synthesis of Si/C composite as anode materials for LIBs by dispersing SiNCs (80 nm) in carbon aerogel and subsequent carbonization. The materials showed good cyclability and lithium storage capacity.[335] The electronic conductive of such carbon shell could be enhanced by doping with appropriate

elements. Similarly, the high surface area of mesoporous carbon shell is also electronically conductive and in the case of mesoporous carbon shell high surface area is expected to further improve the performance of the electrode.

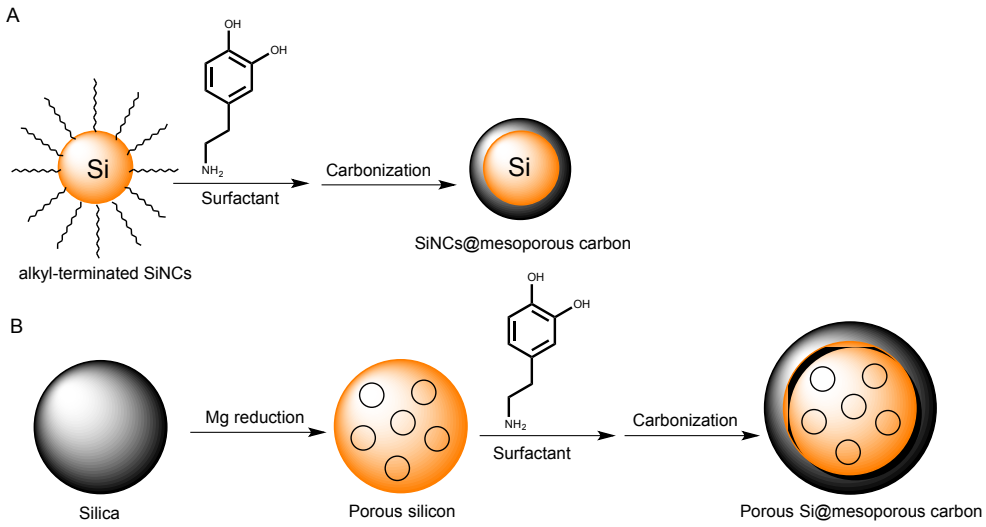

Figure 6-1: Proposed synthetic procedures to prepare Si/C hybrid materials. (A) Alkyl-terminated SiNCs coated with dopamine in the presence of a surfactant and then carbonized to obtain SiNCs coated with mesoporous carbon shell, (B) porous Si is obtained via Mg reduction of silica and then coated with dopamine in the presence of a surfactant and then carbonized to obtain porous Si coated with mesoporous carbon shell.

Transition metal oxides (*e.g.,* Fe_2O_3, Fe_3O_4) are another group of promising anode materials for LIBs. They are non-toxic, naturally abundant and are cost effective. For example, hematite and magnetite provide theoretical capacity of 1007

and 926 $mAhg^{-1}$, respectively. However, these materials also suffer from poor cycling performance due to limitations such as, low electrical conductivity, low diffusion of Li-ions, and high volume expansion and particle aggregation during the operation. Numerous approaches have been employed to overcome these limitations, including changing the morphology and porosity of the oxides. Mesoporous carbon shells could be employed to stabilize the structure and improve the performance of such materials as well as carbon coating. As demonstrated in Chapter 4, magnetite nanorods could be coated with mesoporous carbon shells with exquisite control over shell thicknesses and morphology. It is proposed to employ hematite and magnetite coated nanorods with a mesoporous carbon shell as anode material for LIBs. The effect of nanorods morphology, composition (hematite *vs.* magnetite) and shell thickness are expected to influence the performance of anode material, thus needed to be optimized for application in LIBs

6.2.2 Enhancement of SiNC Photoluminescence by GNPs/GNRs

SiNCs are semiconductor nanoparticles that offer numerous of advantages over other semiconductor nanoparticles, they are abundant, non-toxic, biocompatible and exhibit size and ligand dependent photoluminescence.[336] They have potential applications in sensors, bioimaging, optical devices, photovoltaics and batteries. However, due to the indirect band gap nature of SiNCs they are often considered as poor optical materials.[337]

Plasmonic metal nanoparticles (*e.g.,* gold and silver) are known to alter the emission rate of photoluminescent SiNCs.[338] Biteen *et al.* observed a four-fold enhancement in SiNC photoluminescence with nanoporous gold.[339] There are also other reports of using gold nanodsiks, silver nanodisks and silver nanotriangles for this purpose.[338,340,341] The optical modification (enhancement or quenching) strongly depends on the distance between the metal nanoparticles and SiNCs. Moreover, fabrication of such coupled structures that exhibit photoluminescence enhancement is very challenging and in many cases the results could be misinterpreted where photoluminescent enhancement maybe arising from uncoupled SiNCs instead of plasmonic nanoparticles.[342]

Thus a close controlled attachment of plasmonic nanoparticles is warranted for PL enchantment of SiNCs. As discussed in Section 6.2.2, CNC provide a platform for such a nanoparticles attachment. A hybrid structure consisting of gold and silicon nanoparticles onto the surface of CNC can be designed and studied for PL enhancement. Moreover, In Chapter 5, it has been demonstrated gold nanorods (GNRs) with low and high aspect ratio could be synthesized with exquisite control on aspect ratio and would be an interesting material to investigate for direct attachment of SiNCs for PL enchantment. All proposed approaches are shown in Figure 6-2.

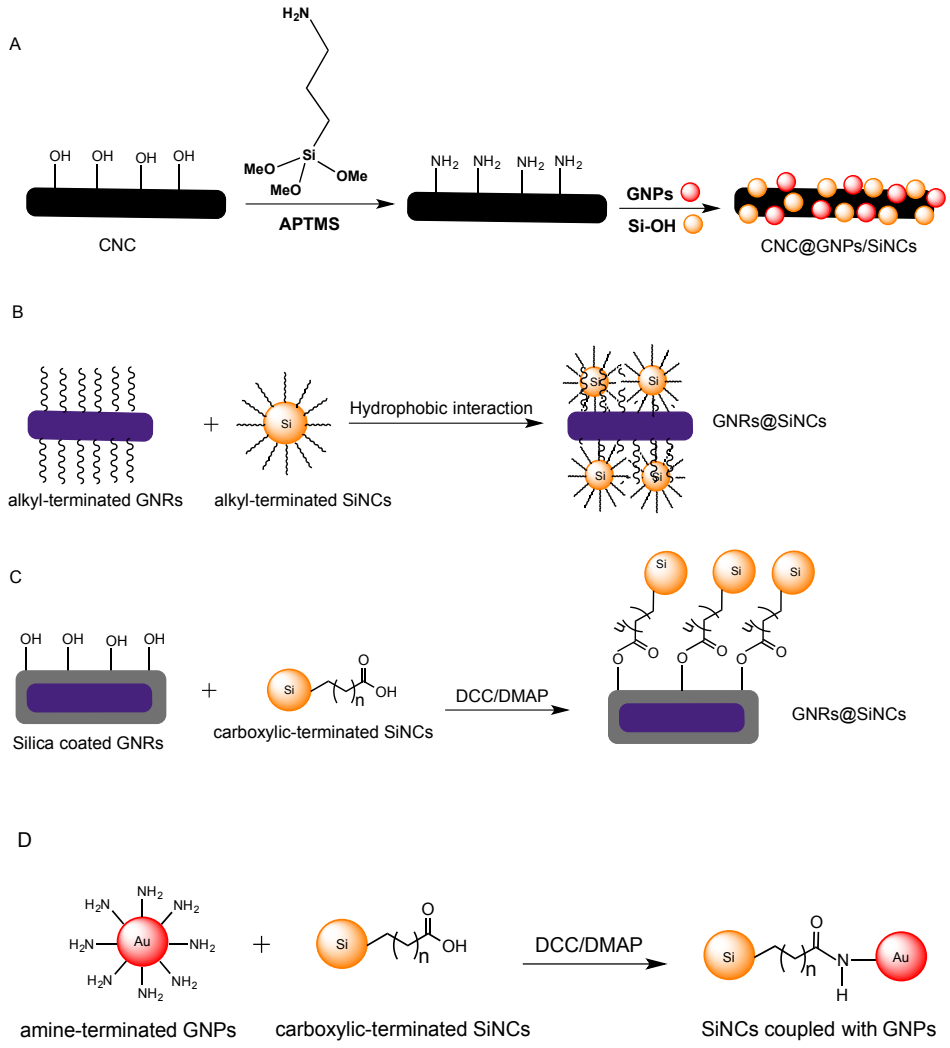

Figure 6-2: Proposed synthetic approaches to prepare hybrid CNC/GNPs/SiNCs and GNRs@SiNCs structures. (A) CNC is functionalized with APTMS to obtain amine-terminated CNC. Then, GNPs and hydroxyl-terminated silicon nanoparticles will be introduced to it. (B) Attachment of alkyl-terminated SiNCs on the surface of alkyl-terminated GNRs *via* hydrophobic interactions. (C) Covalent attachment of SiNCs on the surface of silica coated GNRs *via* Steglich esterification using dicyclohexylcarbodiimide (DCC) as the coupling reagent and 4-dimethylaminopyridine (DMAP) as the catalyst. (D) Covalent attachment of SiNCs on the surface of amine-terminated GNPs *via* Steglich esterification using DCC as the coupling reagent and DMAP as the catalyst.

6.2.3 CNC-based New Hybrid Materials

CNC has gained prominence as a new class of renewable nanomaterial.[109] Its properties and some of its applications have been discussed in Chapters 1 and 3. The surface chemistry of CNC closely matches that of silica, thus, hydroxyl groups on the surface provide a robust platform for adding a variety of functional groups to CNC.[343] As discussed in Chapter 5, GNPs are well known well for their photothermal characteristics. It is proposed to incorporating such metallic nanoparticles (*e.g.,* gold) onto the surface of CNC thus may provide a robust, scalable and cost-effective heterogeneous catalysis system that can be applied in a variety of endothermic reactions (Figure 6-3). For example, as discussed in Chapter 5, such a hybrid catalyst can be applied to enhance 4-NP conversion to 4-AP by employing photothermal effect of gold nanoparticles.

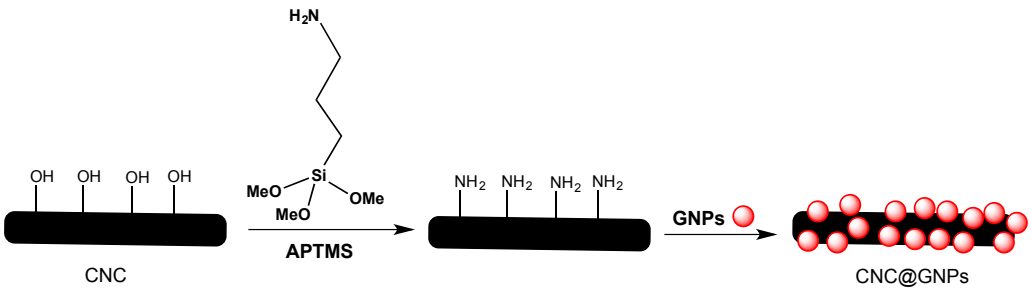

Figure 6-3: Schematic illustration of synthetic approach for making CNC@GNPs.

6.2.4 Plasmonic-induced Surface Functionalization of SiNCs

Hydride terminated SiNCs are prone to oxidation. To protect the surface of SiNCs, different surface functionalization methods have been developed in our group including: thermal, photochemical, catalytic and radical initiated hydrosilylation.[336] In both thermal (190 °C) and radical initiated (60-80 °C) hydrosilylation, adequate heat is required to initiate and complete these functionalization reactions. As discussed in Chapter 5, radical species are produced by thermal energy;[308] thus, localized photothermal heating is proposed as energy source for inducing such radical reactions. It is proposed that by incorporating GNPs in reaction vessels containing SiNCs, an initiator and functionalization ligand and by applying proper wavelength lasers, sufficient localized heated could be generated could lead to surface functionalization of SiNCs. Such an approach is very useful for ligands or initiators, which are sensitive to high temperatures (Figure 6-4).

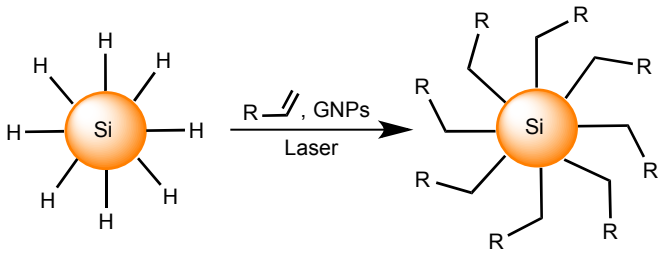

Figure 6-4: Schematic illustration of plasmonic-induced surface functionalization of SiNCs in presence of GNPs and a suitable laser. The local heat is produced upon photothermal effect of GNPs to induce the functionalization.

6.2.5 Dopamine/SiNCs Hybrid Functional Materials

In dye-sensitized solar cells (DSC), light is absorbed by a sensitizer, which is anchored to the surface of semiconductor (*e.g.* TiO_2). Charge separation occurs at the interface through photo-induced electron injection from the dye into the conduction band of the semiconductor. Then, carriers are transported in the conduction band of the semiconductor to the charge collector.[344] Polydopamine (PDA) has been used as sensitizer in polymer-sensitizer solar cells for the absorption of UV light.[345,346]

Recently, polymer-SiNCs hybrid materials have gained much of attention in solar cell research field.[347–349] For example, hybrid SiNCs/poly(3- hexylthiophene) (P3HT) have shown promising efficiencies.[350–354] In this regard, a core-shell structure of SiNCs@PDA is proposed which would create an interface between SiNCs and PDA. The optoelectronic properties of the resulted hybrid material can be studied in a systematic manner by altering the size of SiNCs and PDA shell thickness.

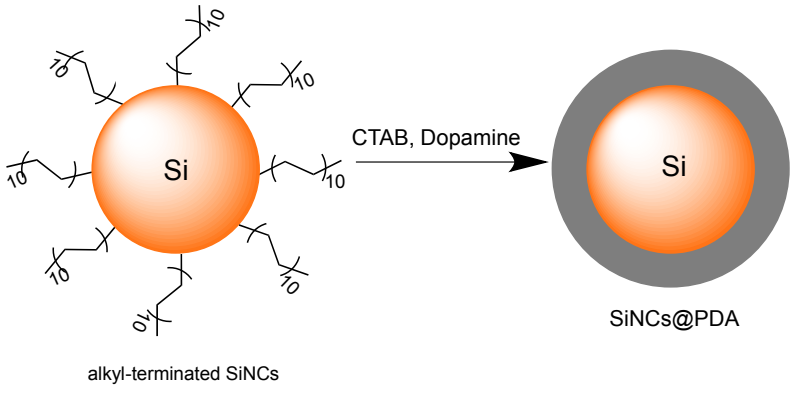

Figure 6-5: Schematic illustration of synthetic approach for making hybrid SiNCs@PDA.

6.2.6 High Surface Area Carbon Network

High surface area carbon nanostructures can be prepared by using inorganic hard templates as discussed in Chapter 1. Mesoporous silica is usually used as sacrificial template for making high surface area carbon nanostructures. Silica aerogels with high surface area (500-1200 m^2/g) and high porosity (80-90%) can be used as sacrificial template for synthesizing mesoporous carbon structure with high surface area.[355] As discussed in Chapter 2, dopamine as a N-doped carbon precursor provides N-doped carbon that can be used for this purpose. Also, in Chapter 3, CNC has been used as carbon precursor. Incorporating CNC during the synthesis of aerogel can give new optical properties to the aerogel *via* its chiral nematic properties.

References

(1) Cao, G. *Nanostructures & Nanomaterials*; Imperial College Press: London, 2004.
(2) Murashov, V.; Howard, J. *Nanotechnology standards and international legal considerations*; Springer London, 2011.
(3) Ramesh, K. T. *Nanomaterials Mechanics and Mechanisms*; Springer London, 2009.
(4) Qi, W. H.; Wang, M. P. *J. Nanoparticle Res.* **2005**, *7* (1), 51–57.
(5) Schmid, G.; Corain, B. *Eur. J. Inorg. Chem.* **2003**, No. 17, 3081–3098.
(6) Agrawal, D. *Introduction to Nanoscience and Nanomaterials*; World Scientific Publishing: Singapore, 2013.
(7) Liu, J. P. *J. Miner. Met. Mater. Soc.* **2010**, *62*, 1–6.
(8) Leubner, I. H. *Curr. Opin. Colloid Interface Sci.* **2000**, *5* (1-2), 151–159.
(9) LaMer, V.; Dinegar, R. *J. Am. Chem. Soc.* **1950**, *72* (8), 4847–4854.
(10) Vreeland, E. C.; Watt, J.; Schober, G. B.; Hance, B. G.; Austin, M. J.; Price, A. D.; Fellows, B. D.; Monson, T. C.; Hudak, N. S.; Maldonado-Camargo, L.; Bohorquez, A. C.; Rinaldi, C.; Huber, D. L. *Chem. Mater.* **2015**, *27* (17), 6059–6066.
(11) Sun, Y. *Chem. Soc. Rev.* **2013**, *42*, 2497–2511.
(12) Beenakker, C.; Ross, J. *J. Chem. Phys.* **1985**, *83 (9)*, 4710 – .
(13) Bryson, B. *A Short History of Nearly Everything*; Anchor Canada, 2004.
(14) http://www.nobelprize.org/nobel_prizes/chemistry/laureates/1996/.
(15) http://www.nobelprize.org/nobel_prizes/physics/laureates/2010/.
(16) Ravula, S.; Baker, S. N.; Kamath, G.; Baker, G. A. *Nanoscale* **2015**, *7* (10), 4338–4353.
(17) Li, Y. J.; Xu, L.; Liu, H. B.; Li, Y. L. *Chem. Soc. Rev.* **2014**, *43* (8), 2572–2586.
(18) Kroto, H. W.; Allaf, A. W.; Balm, S. P. *Chem. Rev.* **1991**, *91*, 1213–1235.
(19) Tripathi, A.; Saraf, S.; Saraf, S. *Materials (Basel).* **2015**, *8* (6), 3068–3100.
(20) Hirsch, A. *Nat. Mater.* **2010**, *9* (11), 868.
(21) Davis, M. E. *Nature* **2002**, *417* (6891), 813–821.
(22) Hu, Z.; Srinivasan, M. P.; Ni, Y. *Adv. Mater.* **2000**, *12* (1), 62–65.
(23) Kong, Q.; Zhang, L.; Liu, J.; Wu, M.; Chen, Y.; Feng, J.; Shi, J. *Chem. Commun.* **2014**, *50* (99), 15772–15775.
(24) Liang, C.; Li, Z.; Dai, S. *Angew. Chem. Int. Ed. Engl.* **2008**, *47* (20), 3696–3717.
(25) Sircar, S.; Golden, T. C.; Rao, M. B. *Carbon N. Y.* **1996**, *34* (1), 1–12.
(26) Corapcioglu, M. O.; Huang, C. P. *Water Res.* **1987**, *21* (9), 1031–1044.
(27) Liu, S.; Li, H.; Wang, L.; Tian, J.; Sun, X. *J. Mater. Chem.* **2011**, *21* (2), 339–341.
(28) Lee, J.; Yoon, S.; Hyeon, T.; Oh, M.; Bum, K. *Chem. Commun.* **1999**, 2177–2178.
(29) Liu, X.; Zhu, H.; Yang, X. *J. Power Sources* **2014**, *262*, 414–420.
(30) Li, X.; Cao, Y.; Qi, W.; Saraf, L. V.; Xiao, J.; Nie, Z.; Mietek, J.; Zhang, J.-G.; Schwenzer, B.; Liu, J. *J. Mater. Chem.* **2011**, *21* (41), 16603–16610.
(31) Chang, H.; Joo, S. H.; Pak, C. *J. Mater. Chem.* **2007**, *17*, 3078–3088.

(32) Joo, S. H.; Choi, S. J.; Oh, I.; Kwak, J.; Liu, Z.; Terasaki, O.; Ryoo, R. *Nature* **2001**, *412* (6843), 169–172.
(33) Gaffney, T. R. *Curr. Opin. Solid State Mater. Sci.* **1996**, *1* (1), 69–75.
(34) Bansal, R. C.; Donnet, J. B.; Stoeckli, F. *Active Carbon.*; Marcel Dekker: New York, 1988.
(35) Ozaki, J. *J. Slav. Mil. Stud.* **2007**, *35* (7), 1031–1033.
(36) Kowalewski, T.; Tsarevsky, N. V.; Matyjaszewski, K. *J. Am. Chem. Soc.* **2002**, *124* (36), 10632–10633.
(37) Lamond, T. G.; Marsh, H. *Carbon N. Y.* **1963**, *1*, 293–307.
(38) Kyotani, T. *Carbon N. Y.* **2000**, *38* (2), 269–286.
(39) Rand, B.; Marsh, H. *Carbon N. Y.* **1971**, *9* (1), 79–85.
(40) Tamai, H.; Kakii, T.; Hirota, Y.; Kumamoto, T.; Yasuda, H. *Chem. Mater.* **1996**, *8* (2), 454–462.
(41) Oya, A.; Yoshida, S.; Alcaniz-Monge, J.; Linares-Solano, A. *Carbon N. Y.* **1995**, *33* (8), 1085–1090.
(42) Pekala, R. W. *J. Mater. Sci.* **1989**, *24* (9), 3221–3227.
(43) Tamon, H.; Ishizaka, H.; Yamamoto, T.; Suzuki, T. *Carbon N. Y.* **1999**, *37*, 2049–2055.
(44) Gierszal, K. P.; Jaroniec, M.; Kim, T.-W.; Kim, J.; Ryoo, R. *New J. Chem.* **2008**, *32*, 981–993.
(45) Knox, H.; Kaur, B.; Millward, G. R. *J. Chromatogr.* **1986**, *352*, 3–25.
(46) Knox, J. H.; Unger, K. K.; Mueller, H. *J. Liq. Chromatogr.* **1983**, *6*, 1–36.
(47) Kyotani, T.; Nagai, T.; Inoue, S.; Tomita, A. *Chem. Mater.* **1997**, *9* (13), 609–615.
(48) Johnson, S. A.; Brigham, E. S.; Ollivier, P. J.; Mallouk, T. E. *Chem. Mater.* **1997**, *9* (2), 2448–2458.
(49) Vartuli, J. C.; Roth, W. J.; Degnan, T. F. *Dekker Encyclopedia of Nanoscience and Nanotechnology*; Marcel Dekker, 2004.
(50) Kresge, C. T.; Leonowicz, M. E.; Roth, W. J.; Vartuli, J. C.; Beck, J. S. *Nature* **1992**, *355*, 242–244.
(51) Kresge, C. T.; Roth, W. J. *Chem. Soc. Rev.* **2013**, *42* (9), 3663–3670.
(52) Ryoo, R.; Joo, S. H.; Jun, S. *J. Phys. Chem. B* **1999**, *103* (37), 7743–7746.
(53) Kaneda, M.; Tsubakiyama, T.; Carlsson, A.; Sakamoto, Y. **2002**, 1256–1266.
(54) Zhao, D.; Feng, J.; Huo, Q.; Melosh, N.; Fredrickson, G.; Chmelka, B.; Stucky, G. *Science* **1998**, *279* (5350), 548–552.
(55) Jun, S.; Joo, S. H.; Ryoo, R.; Kruk, M.; Jaroniec, M.; Liu, Z.; Ohsuna, T.; Terasaki, O. *J. Am. Chem. Soc.* **2000**, *122* (43), 10712–10713.
(56) Moriguchi, I.; Ozono, A.; Mikuriya, K.; Teraoka, Y.; Kagawa, S.; Kodama, M. *Chem. Lett.* **1999**, 1171–1172.
(57) Meng, Y.; Gu, D.; Zhang, F.; Shi, Y.; Cheng, L.; Feng, D.; Wu, Z.; Chen, Z.; Wan, Y.; Stein, A.; Zhao, D. *Chem. Mater.* **2006**, *18* (4), 4447–4464.
(58) Ma, T. Y.; Liu, L.; Yuan, Z. Y. *Chem. Soc. Rev.* **2013**, *42*, 3977–4003.
(59) Liang, C.; Hong, K.; Guiochon, G. A.; Mays, J. W.; Dai, S. *Angew. Chem. Int. Ed. Engl.* **2004**, *43* (43), 5785–5789.

(60) Liang, C.; Hong, K.; Guiochon, G. A.; Mays, J. W.; Dai, S. *Angew. Chem. Int. Ed. Engl.* **2004**, *43* (43), 5785–5789.
(61) Tanaka, S.; Nishiyama, N.; Egashira, Y.; Ueyama, K. *Chem. Commun. (Camb).* **2005**, No. 16, 2125–2127.
(62) Zhang, F.; Meng, Y.; Gu, D.; Yan, Y.; Chen, Z.; Tu, B.; Zhao, D. *Chem. Mater.* **2006**, *18* (22), 5279–5288.
(63) Bates, F. S.; Fredrickson, G. H. *Phys. Today* **1999**, *52* (2), 32–38.
(64) Zhang, F.; Meng, Y.; Gu, D.; Yu, C.; Tu, B.; Zhao, D. *J. Am. Chem. Soc.* **2005**, *127*, 13508–13509.
(65) Rodriguez, A. T.; Chen, M.; Chen, Z.; Brinker, C. J.; Fan, H. *J. Am. Chem. Soc.* **2006**, *128*, 9276–9277.
(66) Fuertes, A. B.; Alvarez, S. *Carbon N. Y.* **2004**, *42* (15), 3049–3055.
(67) Terrones, M. *Annu. Rev. Mater. Res.* **2003**, *33* (1), 419–501.
(68) Babarao, R.; Dai, S.; Jiang, D. *J. Phys. Chem. C* **2012**, *116*, 7106–7110.
(69) Terrones, B. M.; Redlich, P.; Grobert, N.; Trasobares, S.; Hsu, W.; Terrones, H.; Zhu, Y.; Hare, J. P.; Reeves, C. L.; Cheetham, A. K.; Rühle, M.; Kroto, H. W.; Walton, D. R. M. *Adv. Mater.* **1999**, *11* (8), 655–658.
(70) Strelko, V. V; Kuts, V. S.; Thrower, P. A. *Carbon N. Y.* **2000**, *38*, 1499–1503.
(71) Wright, W. M. *J. Chem. Soc.* **1926**, *129*, 1813–1821.
(72) Matter, P.; Zhang, L.; Ozkan, U. *J. Catal.* **2006**, *239* (1), 83–96.
(73) Sidik, R. A.; Anderson, A. B.; Subramanian, N. P.; Kumaraguru, S. P.; Popov, B. N. *J. Phys. Chem. B* **2006**, *110*, 1787–1793.
(74) Sun, C.; Chen, L.; Su, M.; Hong, L.; Chyan, O.; Hsu, C.; Chen, K.; Chang, T.; Chang, L. *Chem. Mater* **2005**, *17* (4), 3749–3753.
(75) Shao, Y.; Yin, G.; Gao, Y.; Shi, P. *J. Electrochem. Soc.* **2006**, *153* (6), A1093.
(76) Coloma, F.; Sepulvedaescribano, A.; Rodriguezreinoso, F. *J. Catal.* **1995**, *154* (2), 299–305.
(77) Maldonado, S.; Stevenson, K. J. *J. Phys. Chem. B* **2005**, *109* (10), 4707–4716.
(78) Czerw, R.; Terrones, M.; Charlier, J. C.; Blase, X.; Foley, B.; Kamalakaran, R.; Grobert, N.; Terrones, H.; Tekleab, D.; Ajayan, P. M.; Blau, W.; R??hle, M.; Carroll, D. L. *Nano Lett.* **2001**, *1* (9), 457–460.
(79) Strelko, V. V.; Kartel, N. T.; Dukhno, I. N.; Kuts, V. S.; Clarkson, R. B.; Odintsov, B. M. *Surf. Sci.* **2004**, *548* (1-3), 281–290.
(80) Lee, W. H.; Moon, J. H. *ACS Appl. Mater. Interfaces* **2014**, *6* (16), 13968–13976.
(81) Shao, Y.; Sui, J.; Yin, G.; Gao, Y. *Appl. Catal. B Environ.* **2008**, *79* (1), 89–99.
(82) Glerup, M.; Steinmetz, J.; Samaille, D.; Stéphan, O.; Enouz, S.; Loiseau, A.; Roth, S.; Bernier, P. *Chem. Phys. Lett.* **2004**, *387* (1-3), 193–197.
(83) Hammer, P.; Alvarez, F.; Droppa, R.; Jr, R. D.; Hammer, P.; Carvalho, a C. M.; Santos, M. C.; Alvarez, F. *J. Non. Cryst. Solids* **2002**, *299-302*, 874–879.
(84) Hummelen, J. C.; Knight, B.; Pavlovich, J.; González, R.; Wudl, F. *Science (80-.).* **1995**, *269* (5230), 1554–1556.
(85) Glenis, S.; Cooke, S.; Chen, X.; Labes, M. M. *Chem. Mater.* **1994**, *6* (10), 1850–1853.

(86) Maldonado, S.; Morin, S.; Stevenson, K. J. *Carbon N. Y.* **2006**, *44* (8), 1429–1437.
(87) Glerup, M.; Castignolles, M.; Holzinger, M.; Hug, G.; Loiseau, A.; Bernier, P.; Bataillon, P. E.; B-, B. *Chem. Commun.* **2003**, 2542–2543.
(88) Terrones, M.; Kamalakaran, R.; Seeger, T.; Ruhle, M. *Chem. Commun. (Camb).* **2000**, 2335–2336.
(89) Wang, E.-G. *Adv. Mater.* **1999**, *11* (13), 1129–1133.
(90) Terrones, M.; Terrones, H.; Grobert, N.; Hsu, W. K.; Zhu, Y. Q.; Hare, J. P.; Kroto, H. W.; Walton, D. R. M.; Kohler-Redlich, P.; Ruhle, M.; Zhang, J. P.; Cheetham, a K. *Appl. Phys. Lett.* **1999**, *3932* (1999), 25–28.
(91) Yudasaka, M.; Kikuchi, R.; Ohki, Y. *Carbon N. Y.* **1997**, *35* (2), 195–201.
(92) Guo, Q.; Xie, Y.; Wang, X.; Zhang, S.; Hou, T.; Lv, S. *Chem. Commun. (Camb).* **2004**, 26–27.
(93) Cao, C.; Huang, F.; Cao, C.; Li, J.; Zhu, H. *Chem. Mater.* **2004**, *16* (25), 5213–5215.
(94) Lefe, M.; Jaouen, F.; Lefèvre, M.; Dodelet, J. P.; Cai, M.; Lefevre, M.; Dodelet, J. P.; Cai, M.; Lefe, M. *J. Phys. Chem. B* **2006**, *110* (11), 5553–5558.
(95) Jiang, L.; Gao, L. *Carbon N. Y.* **2003**, *41* (15), 2923–2929.
(96) Roy, P.; Soc, R.; Met, J. I.; Vernon, W.; Akeroyd, E.; Desmaison, J.; Billy, M.; Sci, C. R. A.; Dominique, S.; Devillers, B.; Bardoll, J.; Froman, M.; Bell, R.; Roy, C. *J. Electochem. Soc.* **1997**, *144*, 2323–2328.
(97) Alves, M. C. M.; Tourillon, G. *J. Phys. Chem.* **1996**, *100* (95), 7566–7572.
(98) Fournier, J.; Lalande, G.; Co⁄té, R.; Guay, D.; Dodelet, J. *J Electrochem Soc* **1997**, *144* (1), 218–226.
(99) Sirk, A. H. C.; Ampbell, S. A.; Birss, V. I. *Electrochem. Solid-State Lett.* **2005**, *8* (2), A104.
(100) He, P.; Lefevre, M.; Faubert, G.; Dodelet, J. *J. new Mater. Electrochem. Syst.* **1999**, *2*, 243–252.
(101) Wei, G.; Wainright, J.; Savinell, R. *J. New Mater. Electrochem. Syst.* **2000**, *129*, 121–129.
(102) D'Ischia, M.; Napolitano, A.; Pezzella, A.; Meredith, P.; Sarna, T. *Angew. Chemie - Int. Ed.* **2009**, *48* (22), 3914–3921.
(103) Postma, A.; Yan, Y.; Wang, Y.; Zelikin, A. N.; Tjipto, E.; Caruso, F. *Chem. Mater.* **2009**, *21* (14), 3042–3044.
(104) Lee, H.; Dellatore, S. M.; Miller, W. M.; Messersmith, P. B. *Science (80-.).* **2007**, *318* (5849), 426–430.
(105) Lee, H.; Scherer, N. F.; Messersmith, P. B. *Proc. Natl. Acad. Sci.* **2006**, *103* (35), 12999–13003.
(106) Yang, F. K.; Zhao, B. *Open Surf. Sci. J.* **2011**, *3*, 115–122.
(107) Liu, R.; Mahurin, S. M.; Li, C.; Unocic, R. R.; Idrobo, J. C.; Gao, H.; Pennycook, S. J.; Dai, S. *Angew. Chem. Int. Ed. Engl.* **2011**, *50* (30), 6799–6802.
(108) Gao, J. K.; Hou, L. A.; Zhang, G. H.; Gu, P. *J. Hazard. Mater.* **2015**, *286*, 325–333.
(109) Habibi, Y.; Lucia, L. a; Rojas, O. J. *Chem. Rev.* **2010**, *110*, 3479–3500.

(110) Peng, B. L.; Dhar, N.; Liu, H. L.; Tam, K. C. *Can. J. Chem. Eng.* **2011**, *89* (5), 1191–1206.
(111) Ranby, B. G. *Discuss. Faraday Soc.* **1951**, *11* (111), 158–164.
(112) Ranby B. G; E. d, R. *Experientia* **1950**, *6*, 12–14.
(113) Ranby, B. G. *Acta Chem. Scand.* **1949**, *3*, 649–650.
(114) Lam, E.; Male, K. B.; Chong, J. H.; Leung, A. C. W.; Luong, J. H. T. *Trends Biotechnol.* **2012**, *30* (5), 283–290.
(115) Elazzouzi-Hafraoui, S.; Nishiyama, Y.; Putaux, J. L.; Heux, L.; Dubreuil, F.; Rochas, C. *Biomacromolecules* **2008**, *9* (1), 57–65.
(116) Braun, B.; Dorgan, J. R. *Biomacromolecules* **2009**, *10* (2), 334–341.
(117) Habibi, Y.; Chanzy, H.; Vignon, M. R. *Cellulose* **2006**, *13* (6), 679–687.
(118) Habibi, Y.; Lucia, L. A.; Rojas, O. J. *Chem. Rev.* **2010**, *d* (110), 3479–3500.
(119) Favier, V.; Chanzy, H.; Cavaille, J. Y. *Macromolecules* **1995**, *28*, 6365–6367.
(120) Shin, Y.; Exarhos, G. J. *Mater. Lett.* **2007**, *61* (11-12), 2594–2597.
(121) Capadona, J. R.; Shanmuganathan, K.; Tyler, D. J.; Rowan, S. J.; Weder, C. *Science (80-.).* **2008**, *319*, 1370–1375.
(122) Capadona, J. R.; Van Den Berg, O.; Capadona, L. a; Schroeter, M.; Rowan, S. J.; Tyler, D. J.; Weder, C. *Nat. Nanotechnol.* **2007**, *2* (12), 765–769.
(123) Shopsowitz, K. E.; Qi, H.; Hamad, W. Y.; MacLachlan, M. J. *Nature* **2010**, *468*, 422–425.
(124) Shopsowitz, K. E.; Hamad, W. Y.; MacLachlan, M. J. *Angew. Chem. Int. Ed. Engl.* **2011**, *50* (46), 10991–10995.
(125) Tang, Z. H.; He, X.; Song, Y.; Liu, L.; Guo, Q. G.; Yang, J. H. *New Carbon Mater.* **2010**, *25* (6), 465–469.
(126) Lee, N.; Yoo, D.; Ling, D.; Cho, M. H.; Hyeon, T.; Cheon, J. *Chem. Rev.* **2015**, *115* (19), 10637–10689.
(127) Dai, L.; Xue, Y.; Qu, L.; Choi, H.-J.; Baek, J.-B. *Chem. Rev.* **2015**, *115*, 4823–4892.
(128) Mitra, S.; Das, S.; Mandal, K.; Chaudhuri, S. *Nanotechnology* **2007**, *18* (27), 275608.
(129) Cudennec, Y.; Lecerf, A. *Solid State Sci.* **2005**, *7* (5), 520–529.
(130) Rollmann, G.; Rohrbach, A.; Entel, P.; Hafner, J. *Phys. Rev. B* **2004**, *69* (16), 1–12.
(131) Comini, E.; Guidi, V.; Frigeri, C.; Riccò, I.; Sberveglieri, G. *Sensors Actuators, B Chem.* **2001**, *77* (1-2), 16–21.
(132) Iturrondobeitia, A.; Goñi, A.; Orue, I.; Gil de Muro, I.; Lezama, L.; Doeff, M. M.; Rojo, T. *Inorg. Chem.* **2015**, *54* (11), 5239–5248.
(133) Frank, S. N.; Bard, A. J. *J. Phys. Chem.* **1977**, *81* (15), 1484–1488.
(134) Fukazawa, M.; Matuzaki, H.; Hara, K. *Sensors Actuators B* **1993**, *14*, 13–14.
(135) Chauhan, P.; Annapoomi, S.; Trikha, S. K. *Thin Solid Films* **1999**, *346*, 266–268.
(136) Qui, G.; Huang, H.; Genuino, H.; Opembe, N.; Stafford, L.; Dharmarathna, S.; Suib, S. L. *J. Phys. Chem. C* **2011**, *115*, 19626–19631.
(137) Weiss, W.; Zscherpel, D.; Schl, R. *Catal. Letters* **1998**, *52*, 215–220.
(138) Faust, B. C.; Hoffmann, M. R.; Bahnemann, D. W. *J. Phys. Chem.* **1989**, *93* (17),

6371–6381.
(139) Ohmori, T.; Takahashi, H.; Mametsuka, H.; Suzuki, E. *Phys. Chem. Chem. Phys.* **2000**, *2* (15), 3519–3522.
(140) Geus, J. W. *Appl. Catal.* **1986**, *25*, 313–333.
(141) Han, J. S.; Bredow, T.; Davey, D. E.; Yu, a B.; Mulcahy, D. E. *Sensors Actuators B* **2001**, *75*, 18–23.
(142) Friák, M.; Schindlmayr, A.; Scheffler, M. *New J. Phys.* **2007**, *9* (5), 1–15.
(143) Kwei, G.; Dreele, R. Von; Williams, A.; Goldstone, J. A.; Lawson II, A. C.; Warburton, W. K. *J. Mol. Struct.* **1990**, *223*, 383–406.
(144) Yuan, S. M.; Li, J. X.; Yang, L. T.; Su, L. W.; Liu, L.; Zhou, Z. *Appl. Mater. Interfaces* **2011**, *3*, 705–709.
(145) Sun, S. *Science (80-.).* **2000**, *287* (5460), 1989–1992.
(146) Burtea, C.; Laurent, S.; Roch, A.; Vander Elst, L.; Muller, R. N. *J. Inorg. Biochem.* **2005**, *99* (5), 1135–1144.
(147) Miller, M. M.; Prinz, G. A.; Cheng, S. F.; Bounnak, S. *Appl. Phys. Lett.* **2002**, *81* (12), 2211–2213.
(148) Jain, T. K.; Morales, M. A.; Sahoo, S. K.; Leslie-Pelecky, D. L.; Labhasetwar, V. *Mol. Pharm.* **2005**, *2* (3), 194–205.
(149) Chourpa, I.; Douziech-Eyrolles, L.; Ngaboni-Okassa, L.; Fouquenet, J.-F.; Cohen-Jonathan, S.; Soucé, M.; Marchais, H.; Dubois, P. *Analyst* **2005**, *130* (10), 1395–1403.
(150) Prasad, P. V. *Magnetic Resonance Imaging*; Human Press: Totowa, New Jersey, 2006.
(151) Charles, S. W.; Popplewell, J. *Endeavour* **1982**, *6* (4), 153–161.
(152) Shokouhimehr, M.; Piao, Y.; Kim, J.; Jang, Y.; Hyeon, T. *Angew. Chemie - Int. Ed.* **2007**, *46* (37), 7039–7043.
(153) Ma, J.; Lian, J.; Duan, X.; Liu, X.; Zheng, W. *J. Phys. Chem. C* **2010**, *114* (24), 10671–10676.
(154) Lian, J.; Duan, X.; Ma, J.; Peng, P.; Kim, T.; Zheng, W. *ACS Nano* **2009**, *3* (11), 3749–3761.
(155) Gash, A. E.; Tillotson, T. M.; Satcher, J. H.; Poco, J. F.; Hrubesh, L. W.; Simpson, R. L. *Chem. Mater.* **2001**, *13* (Iii), 999–1007.
(156) Woo, K.; Lee, H. J.; Ahn, J. P.; Park, Y. S. *Adv. Mater.* **2003**, *15* (20), 1761–1764.
(157) Zhao, Y. M.; Li, Y. H.; Ma, R. Z.; Roe, M. J.; McCartney, D. G.; Zhu, Y. Q. *Small* **2006**, *2* (3), 422–427.
(158) Wang, X.; Li, Y. *J. Am. Chem. Soc.* **2002**, *124* (12), 2880–2881.
(159) Wang, X.; Zhuang, J.; Peng, Q.; Li, Y. *Nature* **2005**, *437* (7055), 121–124.
(160) Hayashi, H.; Hakuta, Y. *Materials (Basel).* **2010**, *3* (7), 3794–3817.
(161) Almeida, T. P.; Fay, M.; Zhu, Y.; Brown, P. D. *J. Phys. Chem. C* **2009**, *113*, 18689–18698.
(162) Hu, L.; Percheron, A.; Chaumont, D.; Brachais, C. H. *J. Sol-Gel Sci. Technol.* **2011**, *60* (2), 198–205.
(163) V&A Home Page - Victoria and Albert Museum http://www.vam.ac.uk/.

(164) Faraday, M. *Philos. Trans. R. Soc. London* **1857**, *147*, 145–181.
(165) Crystallography timeline | The Royal Institution: Science Lives Here http://www.rigb.org/.
(166) Skrabalak, S. E.; Au, L.; Li, X.; Xia, Y. *Nat. Protoc.* **2007**, *2* (9), 2182–2190.
(167) Mie, G. *Ann. Phys.* **1908**, *330*, 377–445.
(168) Yang, X.; Yang, M.; Pang, B.; Vara, M.; Xia, Y. *Chem. Rev.* **2015**, *115* (19), 10410–10488.
(169) Xia, Y.; Halas, N. J. *MRS Bull.* **2005**, *30* (05), 338–348.
(170) Cobley, C. M.; Chen, J.; Cho, E. C.; Wang, L. V; Xia, Y. *Chem. Soc. Rev.* **2011**, *40* (40), 44–56.
(171) Huang, X.; Neretina, S.; El-Sayed, M. A. *Adv. Mater.* **2009**, *21* (48), 4880–4910.
(172) Dreaden, E. C.; Alkilany, A. M.; Huang, X.; Murphy, C. J.; El-Sayed, M. a. *Chem. Soc. Rev.* **2012**, *41* (7), 2740.
(173) Willets, K. A.; Duyne, R. Van; Van Duyne, R. P. *Annu. Rev. Phys. Chem.* **2007**, *58* (1), 267–297.
(174) Gole, A.; Murphy, C. J. *Chem. Mater* **2004**, *16*, 3633–3640.
(175) Murphy, C. J.; Sau, T. K.; Gole, A. M.; Orendorff, C. J.; Gao, J.; Gou, L.; Hunyadi, S. E.; Li, T. *J. Phys. Chem. B* **2005**, *109*, 13857–13870.
(176) Hu, M.; Chen, J.; Li, Z.-Y.; Au, L.; Hartland, G. V; Li, X.; Marquez, M.; Xia, Y. *Chem. Soc. Rev.* **2006**, *35* (11), 1084–1094.
(177) Osaka, T.; Ogumi, Z. *Nanoscale Technology for Advanced Lithium Batteries*; Springer London, 2014.
(178) Linden, D.; Reddy, T. B. *Lithium-Ion Batteries*; McGraw-Hill: New York, 2002.
(179) Li, Y.; Dai, H. *Chem. Soc. Rev.* **2014**, *43* (15), 5143–5402.
(180) Beck, F.; Rüetschi, P. *Electrochim. Acta* **2000**, *45* (15-16), 2467–2482.
(181) Cheng, F.; Chen, J. *Chem. Soc. Rev.* **2012**, *41* (6), 2172–2192.
(182) Lee, J.-S.; Kim, S. T.; Cao, R.; Choi, N.-S.; Liu, M.; Lee, K. T.; Cho, J. *Adv. Energy Mater.* **2011**, *1* (1), 34–50.
(183) Jörissen, L. *J. Power Sources* **2006**, *155* (1), 23–32.
(184) Neburchilov, V.; Wang, H.; Martin, J. J.; Qu, W. *J. Power Sources* **2010**, *195* (5), 1271–1291.
(185) Shao, Y.; Sui, J.; Yin, G.; Gao, Y. *Appl. Catal. B Environ.* **2008**, *79* (1), 89–99.
(186) Liang, H.-W.; Zhuang, X.; Brüller, S.; Feng, X.; Müllen, K. *Nat. Commun.* **2014**, *5*, 4973.
(187) Li, B.; Geng, D.; Lee, X. S.; Ge, X.; Chai, J.; Wang, Z.; Zhang, J.; Liu, Z.; Hor, T. S. A.; Zong, Y. *Chem. Commun.* **2015**, *51* (42), 8841–8844.
(188) Xu, X.; Tan, C.; Liu, H.; Wang, F.; Li, Z.; Liu, J.; Ji, J. *J. Electroanal. Chem.* **2013**, *696*, 9–14.
(189) Lee, K.; Zhang, J.; Wang, H.; Wilkinson, D. P. *J. Appl. Electrochem.* **2006**, *36* (5), 507–522.
(190) Serp, P. *Appl. Catal. A Gen.* **2003**, *253* (2), 337–358.
(191) Lin, C. F.; Zhang, X.; Lin, H.; Wang, N.; Li, J. B.; Yang, X. Z. *Adv. Mater. Res.* **2006**, *11-12*, 543–546.

(192) Chen, X.; Kierzek, K.; Jiang, Z.; Chen, H.; Tang, T.; Wojtoniszak, M.; Kalenczuk, R. J.; Chu, P. K.; Borowiak-Palen, E. *J. Phys. Chem. C* **2011**, *115* (36), 17717–17724.
(193) Terrones, M. *Annu. Rev. Mater. Res.* **2003**, *33* (1), 419–501.
(194) Terrones, M.; Redlich, P.; Grobert, N.; Trasobares, S.; Hsu, W.; Terrones, H.; Zhu, Y.; Hare, J. P.; Reeves, C. L.; Cheetham, A. K.; Rühle, M.; Kroto, H. W.; Walton, D. R. M. *Adv. Mater.* **1999**, *11* (8), 655–658.
(195) Lei, C.; Han, F.; Li, D.; Li, W.-C.; Sun, Q.; Zhang, X.-Q.; Lu, A.-H. *Nanoscale* **2013**, *5*, 1168–1175.
(196) Yang, L.; Kong, J.; Zhou, D.; Ang, J. M. ing; Phua, S. L. ei; Yee, W. A. ik; Liu, H.; Huang, Y.; Lu, X. *Chem. Eur. J.* **2014**, *20* (25), 7776–7783.
(197) Ai, K.; Liu, Y.; Ruan, C.; Lu, L.; Lu, G. M. *Adv. Mater.* **2013**, *25* (7), 998–1003.
(198) Dasog, M.; Smith, L. F.; Purkait, T. K.; Veinot, J. G. C. *Chem. Commun. (Camb).* **2013**, *49* (62), 7004–7006.
(199) Ru, Y.; Evans, D. G.; Zhu, H.; Yang, W. *RSC Adv.* **2014**, *4* (1), 71–75.
(200) Trotochaud, L.; Young, S. L.; Ranney, J. K.; Boettcher, S. W. *J. Am. Chem. Soc.* **2014**, *136*, 6744–6753.
(201) Brunauer, S.; Emmett, P. H.; Teller, E. *J. Am. Chem. Soc.* **1938**, *60* (1), 309–319.
(202) Yu, X.; Fan, H.; Liu, Y.; Shi, Z.; Jin, Z. *Langmuir* **2014**, *30*, 5497–5505.
(203) Liebscher, J.; Mrówczyński, R.; Scheidt, H. a; Filip, C.; Hădade, N. D.; Turcu, R.; Bende, A.; Beck, S. *Langmuir* **2013**, *29* (33), 10539–10548.
(204) Kinoshita, K. *Electrochemical Oxygen Technology*, 2nd ed.; Wiley: New York, 1992.
(205) Bard, Allen J and Faulkner, L. R. *Electrochemical Method*, 2nd ed.; John Wiley & Sons: New York, NY, 2001.
(206) Song, C.; Zhang, J. In *PEM Fuel Cell Electrocatalysts and Catalyst Layers*; Zhang, J., Ed.; Springer London: London, 2008; pp 89–134.
(207) Yang, D. S.; Bhattacharjya, D.; Inamdar, S.; Park, J.; Yu, J. S. *J. Am. Chem. Soc.* **2012**, *134* (39), 16127–16130.
(208) Ozaki, J.; Anahara, T.; Kimura, N.; Oya, A. *Carbon N. Y.* **2006**, *44* (15), 3358–3361.
(209) Yang, W.; Fellinger, T.; Antonietti, M. *J. Am. Chem. Soc.* **2011**, *133*, 206–209.
(210) Yang, Z.; Nie, H.; Chen, X.; Chen, X.; Huang, S. *J. Power Sources* **2013**, *236*, 238–249.
(211) Shao, Y.; Zhang, S.; Engelhard, M. H.; Li, G.; Shao, G.; Wang, Y.; Liu, J.; Aksay, I. A.; Lin, Y. *J. Mater. Chem.* **2010**, *20* (35), 7491.
(212) Farjami, E.; Rottmayer, M. a.; Jay Deiner, L. *J. Mater. Chem. A* **2013**, *1* (48), 15501–15508.
(213) Zhou, C.; Wu, Q. *Nanocrystals – Synth. Charact. Appl. Prop.* **2012**, 103–120.
(214) Dufresne, A. *Can. J. Chem.* **2008**, *86* (6), 484–494.
(215) Mahmoud, K. A.; Male, K. B.; Hrapovic, S.; Luong, J. H. T. *ACS Appl. Mater. Interfaces* **2009**, *1* (7), 1383–1386.
(216) Roman, M.; Dong, S.; Hirani, A.; Lee, Y. W. *ACS Symp. Ser.* **2010**, 81–91.

(217) Gibis, M.; Schuh, V.; Weiss, J. *Food Hydrocoll.* **2015**, *45*, 227–235.
(218) Thoorens, G.; Krier, F.; Leclercq, B.; Carlin, B.; Evrard, B. *Int. J. Pharm.* **2014**, *473* (1-2), 64–72.
(219) Lam, E.; Hrapovic, S.; Majid, E.; Chong, J. H.; Luong, J. H. T. *Nanoscale* **2012**, *4* (3), 997–1002.
(220) Revol, J. F.; Bradford, H.; Giasson, J.; Marchessault, R. H.; Gray, D. G. *Int. J. Biol. Macromol.* **1992**, *14* (3), 170–172.
(221) Ye, C.; Malak, S. T.; Hu, K.; Wu, W.; Tsukruk, V. V. *ACS Nano* **2015**, *9* (11), 10887–10895.
(222) Kong, X.; Sun, Z.; Chen, M.; Chen, C.; Chen, Q. *Energy Environ. Sci.* **2013**, *6* (11), 3260–3266.
(223) Hadidi, L.; Davari, E.; Iqbal, M.; Purkait, T. K.; Douglas, G.; Jonathan G. C. Veinot. *Nanoscale* **2015**, *7*, 20547–20556.
(224) Agarwal, U. P.; Reiner, R. S.; Ralph, S. A. *Cellulose* **2010**, *17* (4), 721–733.
(225) Wiley, J. H.; Atalla, R. H. *ACS Symp. Ser.* **1987**, *44106*, 151–168.
(226) Silva Filho, E. C.; Santos Júnior, L. S.; Silva, M. M. F.; Fonseca, M. G.; Santana, S. A. A.; Airoldi, C. *Mater. Res.* **2013**, *16*, -79–87.
(227) Musić, S.; Filipović-Vinceković, N.; Sekovanić, L. *Brazilian J. Chem. Eng.* **2011**, *28* (01), 89–94.
(228) Dong, Y.; Pang, H.; Yang, H. Bin; Guo, C.; Shao, J.; Chi, Y.; Li, C. M.; Yu, T. *Angew. Chemie - Int. Ed.* **2013**, *52* (30), 7800–7804.
(229) Kruk, M.; Jaroniec, M. *Chem. Mater.* **2001**, *13* (10), 3169–3183.
(230) Nemanashi, M.; Meijboom, R. *J. Colloid Interface Sci.* **2013**, *389* (1), 260–267.
(231) Pradhan, N.; Pal, A.; Pal, T. *Colloids Surfaces A Physicochem. Eng. Asp.* **2002**, *196* (2-3), 247–257.
(232) Fenger, R.; Fertitta, E.; Kirmse, H.; Thünemann, a. F.; Rademann, K. *Phys. Chem. Chem. Phys.* **2012**, *14* (26), 9343–9349.
(233) Shivhare, A.; Ambrose, S. J.; Zhang, H.; Purves, R. W.; Scott, R. W. J. *Chem. Commun. (Camb).* **2013**, *49* (3), 276–278.
(234) Ghosh, S. K.; Mandal, M.; Kundu, S.; Nath, S.; Pal, T. *Appl. Catal. A Gen.* **2004**, *268* (1), 61–66.
(235) Kong, X.; Chen, Q.; Lun, Z. *J. Mater. Chem. A* **2014**, *2* (3), 610–613.
(236) Yang, Y.; Zhang, W.; Ma, X.; Zhao, H.; Zhang, X. *ChemCatChem* **2015**, *7* (21), 3454–3459.
(237) Pradhan, N.; Pal, A.; Pal, T. *Langmuir* **2001**, *17* (5), 1800–1802.
(238) Tang, J.; Shi, Z.; Berry, R. M.; Tam, K. C. *Ind. Eng. Chem. Res.* **2015**, *54* (13), 3299–3308.
(239) Li, J.; Liu, C.; Liu, Y. *J. Mater. Chem.* **2012**, *22* (17), 8426–8430.
(240) Tang, S.; Vongehr, S.; Meng, X. *J. Phys. Chem. C* **2010**, *114* (2), 977–982.
(241) Tang, S.; Vongehr, S.; Meng, X. *J. Mater. Chem.* **2010**, *20* (26), 5436–5445.
(242) Hervés, P.; Pérez-Lorenzo, M.; Liz-Marzán, L. M.; Dzubiella, J.; Lu, Y.; Ballauff, M. *Chem. Soc. Rev.* **2012**, *41* (17), 5577–5587.
(243) Wunder, S.; Polzer, F.; Lu, Y.; Mei, Y.; Ballauff, M. *J. Phys. Chem. C* **2010**, *114*

(19), 8814–8820.
(244) Zhang, H.; Li, X.; Chen, G. *J. Mater. Chem.* **2009**, *19* (43), 8223.
(245) Zhao, Y.; Tang, R.; Huang, R. *Catal. Letters* **2015**, *145* (11), 1961–1971.
(246) Cheng, F.; Chen, J. *Chem. Soc. Rev.* **2012**, *41* (6), 2172–2192.
(247) Zhang, J.; Zhao, Z.; Xia, Z.; Dai, L. *Nat. Nanotechnol.* **2015**, *10* (5), 444–452.
(248) Morozan, A.; Jousselme, B.; Palacin, S. *Energy Environ. Sci.* **2011**, *4* (4), 1238–1254.
(249) Jörissen, L. *J. Power Sources* **2006**, *155* (1), 23–32.
(250) Nie, Y.; Li, L.; Wei, Z. *Chem. Soc. Rev.* **2015**, *44* (8), 2168–2201.
(251) Bezerra, C. W. B.; Zhang, L.; Lee, K.; Liu, H.; Marques, A. L. B.; Marques, E. P.; Wang, H.; Zhang, J. *Electrochim. Acta* **2008**, *53* (15), 4937–4951.
(252) Jin, Y.; Chen, F. *Electrochim. Acta* **2015**, *158*, 437–445.
(253) Jung, K.-N.; Hwang, S. M.; Park, M.-S.; Kim, K. J.; Kim, J.-G.; Dou, S. X.; Kim, J. H.; Lee, J.-W. *Sci. Rep.* **2015**, *5*, 1–10.
(254) Menezes, P. W.; Indra, A.; Sahraie, N. R.; Bergmann, A.; Strasser, P.; Driess, M. *ChemSusChem* **2015**, *8*, 164–171.
(255) Davari, E.; Ivey, D. G. *MRS Proc.* **2015**, *1777*, 1–6.
(256) Cao, X.; Yan, W.; Jin, C.; Tian, J.; Ke, K.; Yang, R. *Electrochim. Acta* **2015**, *180*, 788–794.
(257) Hardin, W. G.; Mefford, J. T.; Slanac, D. A.; Patel, B. B.; Wang, X.; Dai, S.; Zhao, X.; Ruoff, R. S.; Johnston, K. P.; Stevenson, K. J. *Chem. Mater.* **2014**, *26* (11), 3368–3376.
(258) Hadidi, L.; Davari, E.; Iqbal, M.; Purkait, T. K.; Douglas, G.; Veinot, J. G. C. *Nanoscale* **2015**, *7*, 20547–20556.
(259) Toh, R. J.; Sofer, Z.; Pumera, M. *ChemPhysChem* **2015**, *16* (16), 3527–3531.
(260) Barros, W. R. P.; Wei, Q.; Zhang, G.; Sun, S.; Lanza, M. R. V.; Tavares, A. C. *Electrochim. Acta* **2015**, *162*, 263–270.
(261) Verwey, E. J. W.; Heilmann, E. L. *J. Chem. Phys.* **1947**, *15* (4), 174–180.
(262) Zhu, H.; Zhang, S.; Huang, Y.; Wu, L.; Sun, S. *Nano Lett.* **2013**, *13* (6), 2947–2951.
(263) Wang, R.; Jia, J.; Wang, H.; Wang, Q.; Ji, S.; Tian, Z. *J. Solid State Electrochem.* **2013**, *17* (4), 1021–1028.
(264) Zhu, Y.; Zhang, B.; Wang, D.-W.; Su, D. S. *ChemSusChem* **2015**, *8* (23), 4016–4021.
(265) Su, Y. H.; Jiang, H. L.; Zhu, Y. H.; Yang, X. L.; Shen, J. H.; Zou, W. J.; Chen, J. D.; Li, C. Z. *J. Mater. Chem. A* **2014**, *2* (20), 7281–7287.
(266) Wu, C.; Yin, P.; Zhu, X.; OuYang, C.; Xie, Y. *J. Phys. Chem. B* **2006**, *110* (36), 17806–17812.
(267) Yuan, S. M.; Li, J. X.; Yang, L. T.; Su, L. W.; L, L.; Zhou, Z. *ACS Appl. Mater. Interfaces* **2011**, *3*, 705–709.
(268) Lei, C.; Han, F.; Li, D.; Li, W.-C.; Sun, Q.; Zhang, X.-Q.; Lu, A.-H. *Nanoscale* **2013**, *5* (3), 1168–1175.
(269) Zhou, D.; Yang, L.; Yu, L.; Kong, J.; Yao, X.; Liu, W.; Xu, Z.; Lu, X. *Nanoscale* **2015**,

7 (4), 1501–1509.
(270) Song, K.; Lee, Y.; Jo, M. R.; Nam, K. M.; Kang, Y.-M. *Nanotechnology* **2012**, *23* (50), 505401.
(271) Wu, Z.; Yang, S.; Sun, Y.; Parvez, K.; Feng, X.; Müllen, K. *J. Am. Chem. Soc.* **2012**, *134* (22), 9082–9085.
(272) Gong, K.; Du, F.; Xia, Z.; Durstock, M.; Dai, L. *Science (80-.).* **2009**, *323* (5915), 760–764.
(273) Huang, D.; Luo, Y.; Li, S.; Wang, M.; Shen, Y. *Electrochim. Acta* **2015**, *174*, 933–939.
(274) Yang, H.; Wang, H.; Ji, S.; Linkov, V.; Wang, R. *Int. J. Hydrogen Energy* **2014**, *39* (8), 3739–3745.
(275) Wu, Z.; Yang, S.; Sun, Y.; Parvez, K.; Feng, X.; Müllen, K. *J. Am. Chem. Soc.* **2012**, *134* (22), 9082–9085.
(276) Alivisatos, A. P. *J. Phys. Chem.* **1996**, *100* (95), 13226–13239.
(277) Nie, S. *Science (80-.).* **1997**, *275*, 1102–1106.
(278) Schmid, G. *Chem. Rev.* **1992**, *92*, 1709–1727.
(279) El-sayed, M. a. *Acc. Chem. Res.* **2001**, *34* (4), 257–264.
(280) Eychmüller, A. *J. Phys. Chem. B* **2000**, *104* (28), 6514–6528.
(281) Puntes, V. F.; Krishnan, K. M.; Alivisatos, a P. *Science (80-.).* **2001**, *291* (5511), 2115–2117.
(282) Sun, S. *Science (80-.).* **2000**, *287* (5460), 1989–1992.
(283) Mirkin, C. a; Letsinger, R. L.; Mucic, R. C.; Storhoff, J. J. *Nature* **1996**, *382* (6592), 607–609.
(284) Saha, K.; Agasti, S. S.; Kim, C.; Li, X.; Rotello, V. M. *Chem. Rev.* **2012**, *112* (5), 2739–2779.
(285) Huang, X.; El-Sayed, M. A. *J. Adv. Res.* **2010**, *1* (1), 13–28.
(286) Mie, G. *Ann Phys* **1908**, *25*, 337–445.
(287) Jayabal, S.; Pandikumar, A.; Lim, H. N.; Ramaraj, R.; Sun, T.; Huang, N. M. *Analyst* **2015**, *140* (8), 2540–2555.
(288) Faraday, M. *Philos. Trans. R. Soc. London* **1857**, *147*, 145.
(289) Turkevich, J.; Stevenson, P. C.; Hillier, J. *Discuss. Faraday Soc.* **1951**, *55* (c), 55–75.
(290) Enustun, B. V.; Turkevich, J. *J. Am. Chem. Soc.* **1963**, *85* (21), 3317–3328.
(291) Frens, G. *Nat. Phys. Sci.* **1973**, *241* (105), 20–22.
(292) Brust, M.; Walker, M.; Bethell, D.; Schiffrin, D. J.; Whyman, R. *J. Chem. Soc., Chem. Commun.* **1994**, 801–802.
(293) Jana, N. R.; Gearheart, L.; Murphy, C. J. *Langmuir* **2001**, *17* (37), 6782–6786.
(294) Sau, T. K.; Murphy, C. J. *J. Am. Chem. Soc.* **2004**, *126* (28), 8648–8649.
(295) Petroski, J. M.; Wang, Z. L.; Green, T. C.; El-sayed, M. a. *J. Phys. Chem. B* **1998**, *102* (18), 3316–3320.
(296) Nik, B.; Sayed, a El. *Chem. Mater.* **2003**, *15* (16), 1957–1962.
(297) Gold, O. C.; Nanostructures, S.; Murphy, C. J.; Gole, A. M.; Hunyadi, S. E.; Orendorff, C. J.; Carolina, S. *Inorg. Chem.* **2006**, *45* (19), 7544–7554.

(298) Smith, D. K.; Korgel, B. A. *Langmuir* **2008**, *24* (3), 644–649.
(299) Alkilany, A. M.; Thompson, L. B.; Boulos, S. P.; Sisco, P. N.; Murphy, C. J. *Adv. Drug Deliv. Rev.* **2012**, *64* (2), 190–199.
(300) Huang, X.; El-Sayed, I. H.; Qian, W.; El-Sayed, M. A. *J. Am. Chem. Soc.* **2006**, *128* (6), 2115–2120.
(301) Thomas, K. G.; Barazzouk, S.; Ipe, B. I.; Joseph, S. T. S.; Kamat, P. V. *J. Phys. Chem. B* **2004**, *108* (35), 13066–13068.
(302) Soller, T.; Ringler, M.; Wunderlich, M.; Klar, T. A.; Feldmann, J.; Josel, H. P.; Markert, Y.; Nichtl, A.; Kürzinger, K. *Nano Lett.* **2007**, *7* (7), 1941–1946.
(303) Takahashi, H.; Niidome, T.; Nariai, A.; Niidome, Y.; Yamada, S. *Nanotechnology* **2006**, *17* (17), 4431–4435.
(304) González-Béjar, M.; Peters, K.; Hallett-Tapley, G. L.; Grenier, M.; Scaiano, J. C. *Chem. Commun.* **2013**, *49* (17), 1732–1734.
(305) Sarina, S.; Bai, S.; Huang, Y.; Chen, C.; Jia, J.; Jaatinen, E.; Ayoko, G. A.; Bao, Z.; Zhu, H. *Green Chem.* **2014**, *16* (1), 331–341.
(306) Fasciani, C.; Alejo, C. J. B.; Grenier, M.; Netto-Ferreira, J. C.; Scaiano, J. C. *Org. Lett.* **2011**, *13* (2), 204–207.
(307) Hung, W. H.; Aykol, M.; Valley, D.; Hou, W.; Cronin, S. B. *Nano Lett.* **2010**, *10* (4), 1314–1318.
(308) Walker, J. M.; Gou, L.; Bhattacharyya, S.; Lindahl, S. E.; Zaleski, J. M. *Chem. Mater.* **2011**, *23* (23), 5275–5281.
(309) Neumann, O.; Urban, A. S.; Day, J.; Lal, S.; Nordlander, P.; Halas, N. J. *ACS Nano* **2013**, *7* (1), 42–49.
(310) Cho, Y.; Shi, R.; Ivanisevic, A.; Ben Borgens, R. *Nanotechnology* **2009**, *20* (27), 275102.
(311) Zhan, Q.; Qian, J.; Li, X.; He, S. *Nanotechnology* **2010**, *21* (5), 055704.
(312) Alkilany, A. M.; Nagaria, P. K.; Hexel, C. R.; Shaw, T. J.; Murphy, C. J.; Wyatt, M. D. *Small* **2009**, *5* (6), 701–708.
(313) Ding, H.; Yong, K.; Roy, I.; Pudavar, H. E.; Law, W. C.; Bergey, E. J.; Prasad, P. N. *J. Phys. Chem. C* **2007**, *111*, 12552–12557.
(314) Zhan, Q.; Qian, J.; Li, X.; He, S. *Nanotechnology* **2010**, *21* (5), 055704.
(315) Sau, T. K.; Murphy, C. J.; Commun, M. L. H. C.; Commun, A. C. *Langmuir* **2004**, *20* (11), 6414–6420.
(316) Vigderman, L.; Zubarev, E. R. *Chem. Mater.* **2013**, *25* (8), 1450–1457.
(317) Cong, H.; Toftegaard, R.; Arnbjerg, J.; Ogilby, P. R. *Langmuir* **2010**, *26* (6), 4188–4195.
(318) Ma, Z.; Han, H.; Xue, J. *J. Nanosci. Nanotechnol.* **2009**, *9* (5), 3188–3192.
(319) Zhang, L.; Feng, Y.-G.; Wang, L.-Y.; Zhang, J.-Y.; Chen, M.; Qian, D.-J. *Mater. Res. Bull.* **2007**, *42* (8), 1457–1467.
(320) Ghosh, S.; Patil, S.; Ahire, M.; Kitture, R.; Gurav, D. D.; Jabgunde, A. M.; Kale, S.; Pardesi, K.; Shinde, V.; Bellare, J.; Dhavale, D. D.; Chopade, B. a. *J. Nanobiotechnology* **2012**, *10* (1), 17.
(321) Aditya, T.; Pal, A.; Pal, T. *Chem. Commun.* **2015**, *51* (100), 9410–9431.

(322) Zhang, Y.; Liu, S.; Lu, W.; Wang, L.; Tian, J.; Sun, X. *Catal. Sci. Technol.* **2011**, *1* (7), 1142.
(323) Gu, S.; Wunder, S.; Lu, Y.; Ballauff, M.; Fenger, R.; Rademann, K.; Jaquet, B.; Zaccone, A. *J. Phys. Chem. C* **2014**, *118* (32), 18618–18625.
(324) Bingwa, N.; Meijboom, R. *J. Phys. Chem. C* **2014**, *118*, 19849–19858.
(325) Girishkumar, G.; McCloskey, B.; Luntz, A. C.; Swanson, S.; Wilcke, W. *J. Phys. Chem. Lett.* **2010**, *1* (14), 2193–2203.
(326) Goriparti, S.; Miele, E.; De Angelis, F.; Di Fabrizio, E.; Proietti Zaccaria, R.; Capiglia, C. *J. Power Sources* **2014**, *257*, 421–443.
(327) Kong, J.; Yee, W. A.; Yang, L.; Wei, Y.; Phua, S. L.; Ong, H. G.; Ang, J. M.; Li, X.; Lu, X. *Chem. Commun. (Camb).* **2012**, *48* (83), 10316–10318.
(328) Marom, R.; Amalraj, S. F.; Leifer, N.; Jacob, D.; Aurbach, D. *J. Mater. Chem.* **2011**, *21* (27), 9938.
(329) Qiao, L.; Sun, X.; Yang, Z.; Wang, X.; Wang, Q.; He, D. *Carbon N. Y.* **2013**, *54*, 29–35.
(330) Scrosati, B.; Garche, J. *J. Power Sources* **2010**, *195* (9), 2419–2430.
(331) Wu, H.; Cui, Y. *Nano Today* **2012**, *7* (5), 414–429.
(332) Magasinski, a; Dixon, P.; Hertzberg, B.; Kvit, A.; Ayala, J.; Yushin, G. *Nat. Mater.* **2010**, *9* (4), 353–358.
(333) Teki, R.; Krishnan, R.; Parker, T. C.; Lu, T. M.; Kumta, P. N.; Koratkar, N. *Small* **2009**, *5* (20), 2236–2242.
(334) Szczech, J. R.; Jin, S. *Energy Environ. Sci.* **2011**, *4* (1), 56.
(335) Wang, G. .; Ahn, J. .; Yao, J.; Bewlay, S.; Liu, H. . *Electrochem. commun.* **2004**, *6* (7), 689–692.
(336) Yang, Z.; Gonzalez, C. M.; Purkait, T. K.; Iqbal, M.; Meldrum, A.; Veinot, J. G. C. *Langmuir* **2015**, *31* (38), 10540–10548.
(337) Dasog, M.; De Los Reyes, G. B.; Titova, L. V.; Hegmann, F. A.; Veinot, J. G. C. *ACS Nano* **2014**, *8* (9), 9636–9648.
(338) Goffard, J.; Gérard, D.; Miska, P.; Baudrion, A.-L.; Deturche, R.; Plain, J. *Sci. Rep.* **2013**, *3*, 2672.
(339) Biteen, J. S.; Pacifici, D.; Lewis, N. S.; Atwater, H. A. *Nano Lett.* **2005**, *5* (9), 1768–1773.
(340) Mochizuki, Y.; Fujii, M.; Hayashi, S.; Tsuruoka, T.; Akamatsu, K. *J. Appl. Phys.* **2009**, *106* (1), 1–6.
(341) Biteen, J. S.; Lewis, N. S.; Atwater, H. A.; Mertens, H.; Polman, A. *Appl. Phys. Lett.* **2006**, *88* (13), 0–3.
(342) Muñoz-Rosas, A. L.; Rodríguez-Gómez, A.; Arenas-Alatorre, J. A.; Alonso-Huitrón, J. C. *RSC Adv.* **2015**, *5* (113), 92923–92931.
(343) Moon, R. J.; Martini, A.; Nairn, J.; Simonsen, J.; Youngblood, J. *Cellulose nanomaterials review: structure, properties and nanocomposites.*; 2011; Vol. 40.
(344) Grätzel, M. *J. Photochem. Photobiol. C Photochem. Rev.* **2003**, *4* (2), 145–153.
(345) Mao, W.; Lin, X.; Zhang, W.; Chi, Z.; Lu, R.; Cao, A.-M.; Wan, L. *Chem. Commun.*

2016, *52*, 7122–7125.
(346) Nam, H. J.; Kim, B.; Ko, M. J.; Jin, M.; Kim, J. M.; Jung, D. Y. *Chem. - A Eur. J.* **2012**, *18* (44), 14000–14007.
(347) Herrmann, D.; Niesar, S.; Scharsich, C.; Köhler, A.; Stutzmann, M.; Riedle, E. *J. Am. Chem. Soc.* **2011**, *133* (45), 18220–18233.
(348) Wright, M.; Uddin, A. *Sol. Energy Mater. Sol. Cells* **2012**, *107*, 87–111.
(349) Kim, S.; Jeon, K.; Lee, J. C.; Swihart, M. T.; Yang, M. *Appl. Phys. Express* **2012**, *5* (2), 6–9.
(350) Islam, M. A.; Purkait, T. K.; Veinot, J. G. C. *J. Am. Chem. Soc.* **2014**, *136* (43), 15130–15133.
(351) Islam, M. A.; Purkait, T. K.; Mobarok, M. H.; Hoehlein, I. M. D.; Sinelnikov, R.; Iqbal, M.; Azulay, D.; Balberg, I.; Millo, O.; Rieger, B.; Veinot, J. G. C. *Angew. Chemie Int. Ed.* **2016**, 7393–7397.
(352) Liu, C. Y.; Holman, Z. C.; Kortshagen, U. R. *Adv. Funct. Mater.* **2010**, *20* (13), 2157–2164.
(353) Liu, C.-Y.; Holman, Z. C.; Kortshagen, U. R. *Nano Lett.* **2009**, *9* (1), 449–452.
(354) R., K. U. *Nano Lett.* **2009**, *9*, 449.
(355) Aghajamali, M.; Iqbal, M.; Purkait, T. K.; Hadidi, L.; Sinelnikov, R.; Veinot, J. G. C. *Chem. Mater.* **2016**, *28*, 3877–3886.
(356) Orendorff, C. J.; Murphy, C. J. *J. Phys. Chem. B* **2006**, *110* (9), 3990–3994.

Appendix A:

Procedure to Determine Gold Nanorods Concentration

Procedure to Determine Gold Nanorods Concentration

The concentration of GNRs was estimated using the nanorod aspect ratio and the associated extinction coefficient obtained from an optical spectrum, as outlined by Orendorff and Murphy.[356] In Murphy procedure, purified GNRs with aspect ratios form 2.0 to 4.5 were digested by the addition of aqua regia (1 (nitric acid): 3 (hydrochloric acid)) and then gold concentrations determined using inductively coupled plasma (ICP) atomic emission spectrometer. From their absorption maxima and determined concentrations, molar extinction coefficient was calculated ($A = \varepsilon cb$). There is a linear relationship between the extinction coefficient and nanorods aspect ratio and longitudinal plasmon peak maximum. The data provided by this group could serve as calibration plots for estimating extinction coefficients if nanorods dimensions or plasmon absorbance date are available and could be applied to determine nanorod concentration in solution (Figure A-1).

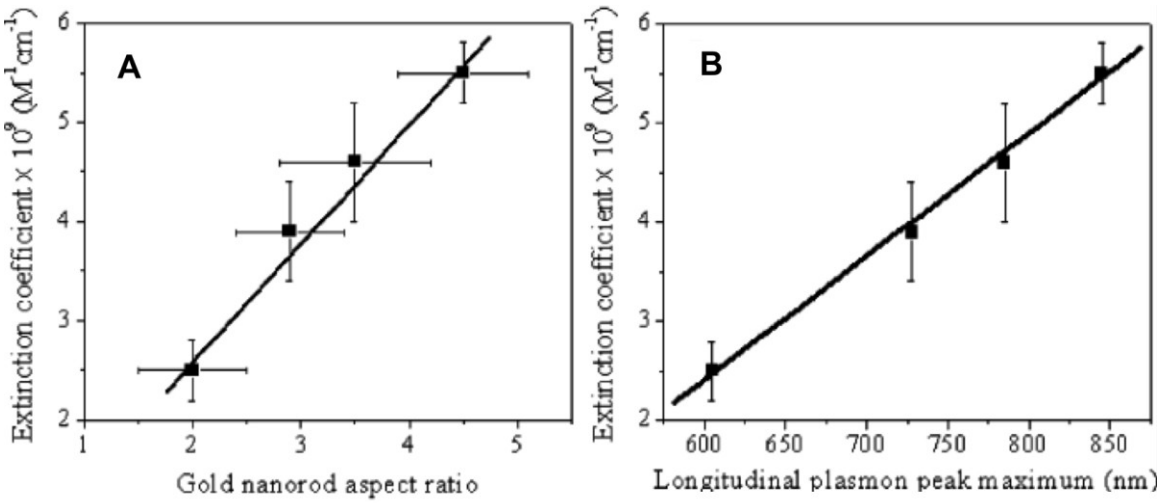

Figure A-1: (A) Plot of extinction coefficient of nanorods (obtained from ICP measurements) vs. aspect ratio for gold nanorods with aspect ratio from 2.0 to 4.5 (determined from TEM). (B) Plot of extinction coefficient vs. longitudinal plasmon peak maximum for gold nanorods with aspect ratio from 2.0 to 4.5.[356] Reprinted (adapted) with permission from ref 356.